UNIVERSITY of CALIFORNIA

Santa Barbara

Plastic Anisotropy and Kink Band Formation in Fine Grained Copper-Niobium Multilayers Produced by Accumulative Roll Bonding

A Dissertation submitted in partial satisfaction of the

requirements for the degree

Doctor of Philosophy

in

Materials

by

Thomas Joseph Nizolek

Committee in charge:

Professor Tresa M. Pollock, Chair
Professor G. Robert Odette
Professor Matthew R. Begley
Professor Michael J. Gordon

December 2016

The dissertation of Thomas Joseph Nizolek is approved.

Professor G. Robert Odette

Professor Matthew R. Begley

Professor Michael J. Gordon

Professor Tresa M. Pollock, Committee Chair

November 2016

Plastic Anisotropy and Kink Band Formation in Fine Grained Copper-Niobium Multilayers Produced by Accumulative Roll Bonding

by

Thomas Joseph Nizolek

Acknowledgements

First and foremost I would like to thank my family, particularly my mother and father. Without the support and guidance from my family, the completion of this dissertation, as well as my graduate, undergraduate, and high school education, would have been impossible. I also owe a debt of gratitude to my grandfather and grandmother for their inspirational demonstration of the importance of knowledge - both technical and otherwise.

My friends, colleagues, and officemates at UCSB have made graduate school a wonderful experience. I thank you for all of the fun we have had, both inside and outside of the lab. I am grateful for my officemates McLean and David, Jackie's help in exploring the complexities of Cu-Nb nanolaminates, and the entire Pollock Group. I am thankful for Rachel's support during the long days spent writing this thesis, and for her help with content and illustration.

I would like to thank Chris Torbet, Deryck Stave, and Kirk Fields for their technical expertise, without which the experimental work described in this thesis could not have been completed. Special thanks are due to Jeff Scott at LANL for his skill and commitment to the improvement of the accumulative roll bonding process. I am grateful to Rod McCabe (LANL) for his help with the *in situ* SEM compression tests and many helpful discussions of twinning, as well

as Bill Mook for conducting the micropillar compression tests.

Professors Bob McMeeking and Matt Begley have shown me the importance and utility of combining continuum mechanics analysis with experimental observations. Their patience and skill in translating between experimental results and mechanics theory is deeply appreciated. The development of an analytical model describing kink band formation would have been impossible without Bob's efforts. I appreciate the many helpful conversations with Matt regarding a fracture mechanics viewpoint of kink band propagation.

I would also like to thank my committee members for their helpful suggestions over the course of my doctoral work. Additionally, guidance from both Nate Mara and Irene Beyerlein during my time at LANL is very much appreciated. I have benefited greatly from Irene's insight and aid with the VPSC model, and Nate's help and advice on the ARB processing and the experimental aspects of research into Cu-Nb nanolaminates.

Finally I would like to thank my advisor, Professor Tresa Pollock, for the support, encouragement, and freedom to explore the many questions uncovered during this investigation into the mechanical properties of Cu-Nb nanolaminates. Her enthusiasm and guidance in pursuing each new question has made my doctoral work immensely interesting and rewarding.

Funding from the Department of Defense, through the NDSEG fellowship, has supported me during much of my doctoral work and is very much appreciated. Additional funding for this research was provided by the the U.C. Lab Fees Research Program #12-LR-238091.

Curriculum Vitæ

Thomas Joseph Nizolek

Education

2010–2016	Ph.D. in Materials, University of California, Santa Barbara, CA, USA.
2006–2010	B.S. in Materials Science and Engineering, Lehigh University, Bethlehem, PA, USA.

Publications

13. **T.J. Nizolek**, R.J. McCabe, J.T. Avallone, N.A. Mara, I.J. Beyerlein, and T.M. Pollock. "Strain Fields Induced by Kink Band Propagation in Cu-Nb Nanolaminate Composites," submitted to *Composites Part A* December 2016.

12. **T. Nizolek**, I.J. Beyerlein, N.A. Mara, J.T. Avallone, and T.M. Pollock. "Tensile Behavior and Flow Stress Anisotropy of Accumulative Roll Bonded Cu-Nb Nanolaminates," *Applied Physics Letters* **108**, no. 5, (2016) 051903. [doi]

11. M. Ardeljan, M. Knezevic, **T. Nizolek**, I.J. Beyerlein, N.A. Mara, T.M. Pollock. "A Study of Microstructure-driven Strain Localizations in Two-phase

Polycrystalline HCP/BCC Composites Using a Multi-scale Model." *International Journal of Plasticity*. **74** (2015) 35-57. [**doi**]

10. J.S. Carpenter, **T. Nizolek**, R.J. McCabe, M. Knezevic, S.J. Zheng, B.P. Eftink, J.E. Scott, S.C. Vogel, T.M. Pollock, N.A. Mara, I.J. Beyerlein. "Bulk Texture Evolution of Nanolamellar Zr-Nb Composites Processed via Accumulative Roll Bonding." *Acta Materialia*. **92** (2015) 97-108. [**doi**]

9. **T. Nizolek**, J.T. Avallone, I.J. Beyerlein, N.A. Mara, T.M. Pollock. "Enhanced Plasticity via Kinking in Cubic Metallic Nanolaminates." *Advanced Engineering Materials*. **17**, no. 6 (2015) 781-785. [**doi**]

8. J.S. Carpenter, **T. Nizolek**, R.J. McCabe, S.J. Zheng, J. Scott, S.C. Vogel, I.J. Beyerlein, N.A. Mara, T.M. Pollock. "The Suppression of Instabilities via Biphase Interfaces During Bulk Fabrication of Nanograined Zr." *Materials Research Letters*, **3**, no. 1 (2015) 50-57. [**doi**]

7. **T. Nizolek**, N.A. Mara, I.J. Beyerlein, J.T. Avallone, T.M. Pollock. "Processing and Deformation Behavior of Bulk Cu-Nb Nanolaminates." *Metallography, Microstructure, and Analysis*. **3**, no. 6 (2014) 470-475. [**doi**]

6. M. Knezevic, **T. Nizolek**, M. Ardeljan, I.J. Beyerlein, N.A. Mara, T.M. Pollock. "Texture Evolution in Two-phase Zr/Nb Lamellar Composites During Accumulative Roll Bonding." *International Journal of Plasticity*, **57**, (2014)

16-28. [doi]

5. M. Ardeljan, M. Knezevic, **T. Nizolek**, I.J. Beyerlein, S.J. Zheng, J.S. Carpenter, R.J. McCabe, N.A. Mara and T.M. Pollock. "A Multi-scale Model for Texture Development in Zr/Nb Nanolayered Composites Processed by Accumulative Roll Bonding." *IOP Conference Series: Materials Science and Engineering*, **63**, no. 1, IOP Publishing, (2014) 012170. [doi]

4. M. Knezevic, I.J. Beyerlein, **T. Nizolek**, N.A. Mara, T.M. Pollock. "Anomalous Basal Slip Activity in Zirconium under High-strain Deformation." *Materials Research Letters*, **1**, no. 3 (2013) 133-140. [doi]

3. I.J. Beyerlein, N.A. Mara, J.S. Carpenter, **T. Nizolek**, W.M. Mook, T.A. Wynn, R.J. McCabe, J.R. Mayeur, K. Kang, S. Zheng, J. Wang, T.M. Pollock. "Interface-driven Microstructure Development and Ultra High Strength of Bulk Nanostructured Cu-Nb Multilayers Fabricated by Severe Plastic Deformation." *Journal of Materials Research*, **28**, no. 2 (2013) 1799-1812. [doi]

2. I.J. Beyerlein, N.A. Mara, J. Wang, J.S. Carpenter, S.J. Zheng, W.Z. Han, R.F. Zhang, K. Kang, **T. Nizolek**, and T.M. Pollock. "Structure-property-functionality of Bimetal Interfaces." *JOM*, **64**, no. 10 (2012) 1192-1207. [doi]

1. **T. Nizolek**. “Metallography of a Modern Pattern-Welded Steel Knife Blade.” *Advanced Materials and Processes*, **166**, no. 2 (2009) 24-26.

Abstract

Plastic Anisotropy and Kink Band Formation in Fine Grained Copper-Niobium Multilayers Produced by Accumulative Roll Bonding

by

Thomas Joseph Nizolek

Metallic nanolaminates are a class of nanocrystalline materials composed of alternating layers of two or more dissimilar metals. These materials offer several advantages over traditional single phase nanocrystalline metals; their lamellar architecture and often immiscible constituent phases provide improved thermal stability and resistance to grain growth, while the nanocrystalline grain size and high interfacial density impart ultra-high strength and hardness. Cu-Nb nanolaminates synthesized *via* thin film deposition techniques have demonstrated extraordinary mechanical properties including strengths in excess of 2 GPa and significant plasticity prior to failure. Yet the limited volumes and film thicknesses ($<$40 μm) of these deposited materials severely limit both mechanical testing and the potential applications of these thin film nanolaminates.

In this work, an accumulative roll bonding (ARB) process was developed

for synthesis of bulk Cu-Nb nanolaminates with layer thicknesses as small as 15 nm (containing over 200,000 individual layers through a 4 mm sheet thickness). The microstructure of these ARB processed nanolaminates differs significantly from previously investigated thin film nanolaminates, with dramatic changes in crystallographic texture, decreases in grain size, and increases in grain aspect ratio occurring throughout the ARB process. The bulk dimensions of these nanolaminates facilitate characterization of mechanical properties, material anisotropy, and deformation mechanisms using a suite of mechanical test methods.

The effects of layer thickness on strength, anisotropy, and deformability are investigated using bulk tensile and compression specimens of ARB Cu-Nb material with layer thicknesses ranging from 1.8 μm to 15 nm. A Hall-Petch type relationship is observed for the materials studied, however significant mechanical anisotropy is present in sub-100 nm nanolaminates. While the in-plane anisotropy is found to result largely from the effects of deformation processing induced crystallographic texture, the lamellar composite structure and grain aspect ratio provides a second source of anisotropy and cause the layer-parallel shear strength to diverge from that expected from a Hall-Petch analysis. The low layer parallel shear strength drives a form of strain localization known as kink banding during layer parallel compression.

Kink bands are determined to be the dominant deformation mechanism during layer parallel compression of nanolaminates with layer thicknesses below 100 nm. A description of the kinematics of kink band formation is developed using observations from post-test microscopy and micropillar compression testing. An analytical model for kink band formation in perfectly plastic anisotropic materials is constructed based on these kinematics. The model predicts the experimentally observed kink band geometry and quantifies the driving force for continued initiation of new kink bands. It is confirmed that kink band formation can occur *via* volume preserving deformation, a result that indicates kinking is a general deformation phenomenon in plastically anisotropic materials. Finally, the phenomenon of kink band propagation is investigated using *in situ* SEM compression tests and digital image correlation (DIC) strain mapping during bulk compression testing. The DIC results provide a quantitative measure of the strain fields in front of a propagating kink band. Analysis of the strain fields indicates similarities between kink bands and mode II cracks, reveals the presence of a stress singularity at the tip of a propagating kink band, and points to a significant additional component to the total energy dissipation during kink band formation.

Contents

List of Figures

List of Tables

Chapter 1

Introduction and Motivation

1.1 Metallic nanolaminates

Metallic nanolaminates, also referred to as 'nanoscale metallic multilayers,' are a class of nanocrystalline materials consisting of alternating layers of two or more dissimilar metals [1]. Formally, the term nanolaminate applies to multilayers in which the individual layer thickness is below 100 nm, thereby satisfying the definition of a 'nanomaterial' (a material having a characteristic microstructural length scale below 100 nm) [2]. Yet multilayers with layer thicknesses above 100 nm may posses grain sizes below 100 nm, satisfying the definition of a nanocrystalline material but technically not that of a nanolaminate. For

the purpose of this work, the term 'multilayers' will be used to refer to lamellar metal-metal composites regardless of layer thickness, while 'nanolaminates' will refer to multilayers with an individual layer thickness below several microns.

Metallic nanolaminates have been shown to exhibit a variety of exceptional properties including ultra high strengths ($>$2 GPa) [1, 3–5], appreciable plasticity prior to failure [5–7], outstanding thermal stability [8–11], and resistance to both shock induced damage [12] and radiation induced damage [13–16]. From a structural materials perspective, the high strength of these materials is particularly attractive, with the maximum strength observed in many nanolaminate systems lying within 30-50% of the theoretical strength [1]. These desirable mechanical and physical properties are attributed to the presence of a high density of heterophase interfaces in nanolaminates, interfaces that influence dislocation motion and point defect interactions [15, 17, 18]. Properties such as thermal stability and radiation damage resistance can exceed even those of the constituent phases in nanocrystalline form [10, 11, 13, 19], further demonstrating the importance of these heterophase interfaces.

While metallic multilayers have been created using a variety of different constituent phase combinations, multilayers consisting of copper (Cu) and niobium (Nb) have received particular attention. Many investigations have focused on the Cu-Nb system due to the limited solid solubility and the absence of

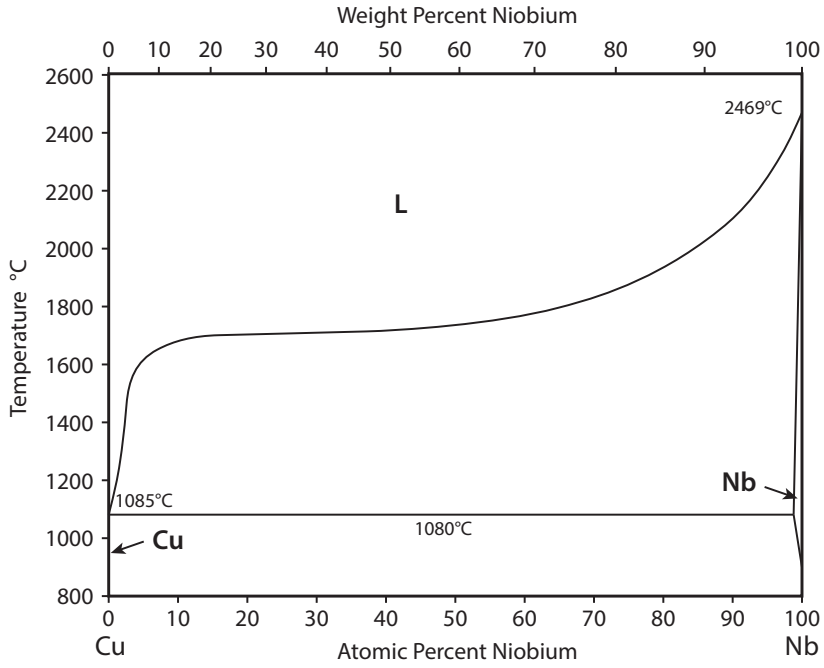

Figure 1.1: Experimentally determined Cu-Nb phase diagram from 0-100% Nb and 800-2600°C . Adapted from Reference [20].

any intermetallic phases: advantageous properties that minimize diffusion induced microstructural changes during thermal exposure or extreme deformation [11, 18]. Figure 1.1 shows the Cu-Nb phase diagram, indicating very limited solid solubility in this system (note that the minimum of the temperature range shown in Figure 1.1 is 800°C).

Another reason that Cu-Nb multilayers are attractive materials for studying the behavior of metallic multilayers is that Cu has a face-centered cubic crystal structure (FCC) while Nb has a body-centered cubic structure (BCC). Thus the deformation behavior of Cu-Nb multilayers can be used to inform

studies of FCC/BCC slip transmission and interface crystallography [18, 21–23]. FCC-BCC composite microstructures occur frequently in industrially relevant alloys such as brasses and dual-phase stainless steels, materials that are of significant technological importance and have motivated previous studies into the co-deformation of FCC-BCC composites [24]. Additionally, prior work on wire drawing of Cu-Nb filamentary composites indicates excellent large strain co-deformation [25, 25], suggesting that the Cu-Nb system is a good system to attempt nanolaminate synthesis through deformation processing, a synthesis technique discussed below.

1.2 Nanolaminate synthesis methods

The three primary synthesis methods for metallic nanolaminates are electrodeposition (ED), physical vapor deposition (PVD), and deformation processing. ED and PVD are both 'bottom up' processes, in which a nanolamellar microstructure is built atom by atom and layer by layer. In contrast, deformation processing is a 'top-down' processing method, where a coarse microstructure is transformed into a nanolamellar microstructure through deformation. Each of these three methods possess certain advantages and drawbacks, as will be discussed in the following sections.

1.2.1 Electrodeposition

Electrodeposition, also known as electroplating, has been used extensively [26–32] to produce biphasic laminated films and sheets, with one of the earliest studies of ED laminate films being the 1921 work of Blum [33]. In electrodeposition, current is passed from an anode to a cathode submerged in an electrolyte containing dissolved metal salts (often sulfate, chlorides, or cyanides) in order to deposit pure metals from the electrolyte solution onto the cathode [34]. The formation of a layered biphasic deposit can be accomplished by either transferring a cathode back and forth between two separate baths, one for each metal to be deposited, or by using a single bath containing two different metal salts and varying current or potential to control which metal is deposited [26].

Metallic multilayers that have been synthesized using ED include Co-Cu [27], Cu-Ni [29], Zn-Ni [35], Co-Au [26], and Co-Ru [26]. For laminates synthesized using the single bath deposition technique, unwanted dissolution of a recently deposited layer may occur when the current or voltage conditions are changed in preparation for the deposition of the next metal, a problem that has been encountered in attempts to deposit Ag-Cu multilayer films [35]. Further, careful chemical control of the electrolyte is needed, and it is not possible to create suitable baths for arbitrary combinations of metals [35, 36]. Dual bath

synthesis eliminates the latter issue, yet introduces additional challenges relating to cleaning the cathode and preventing passivation during transfer between the two plating baths. The transfer process increases the processing time for dual bath multilayer synthesis and, while sometimes automated [35], this transfer process has in many cases discouraged the synthesis of material with truly nanoscale layer thicknesses. Thus while ED synthesis of nanolaminates can be relatively rapid and cost effective for certain systems amenable to single bath deposition (notably Cu-Cr and Cu-Ni), synthesis of nanolaminates of arbitrary composition may require complex and costly dual bath processing and negate the advantages of ED compared to other processing techniques. Additionally, significant layer waviness may occur in the laminate films due to the effects of grain orientation on deposition rate, as shown in Figure 1.2(a).

1.2.2 Physical vapor deposition

Physical vapor deposition (PVD), encompassing the techniques of magnetron sputtering, electron beam evaporation, and molecular beam epitaxy [38], is the most widely used method for synthesizing metallic multilayers [36]. In the case of magnetron sputtering PVD, atoms are removed from a metallic target using an argon plasma and are accelerated towards a substrate using a bias voltage.

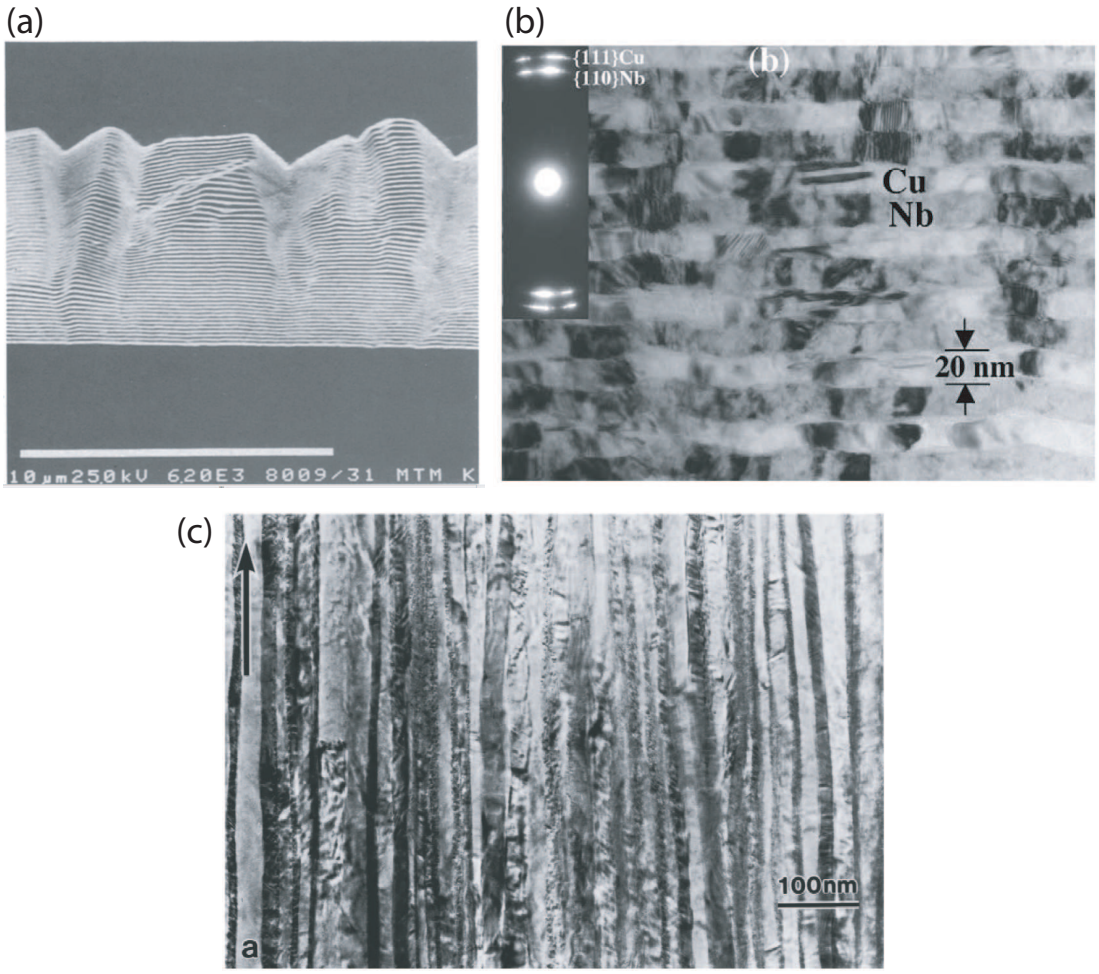

Figure 1.2: Examples of metallic nanolaminates produced by various processing methods. (a) Cross section of an electrodeposition Cu-Ni nanolaminate with a layer thickness 100 nm, reproduced from Reference [31] with permission from The Electrochemical Society. (b) A transmission election micrograph of a cross-sectioned 75 nm physical vapor deposited Cu-Nb nanolaminate from Reference [17], reproduced with permission from Elsevier. (c) A transmission election micrograph of a cold rolled Ag-Fe nanolaminate with a layer thickness of 10 nm reproduced from Reference [37] with permission from the American Institute of Physics.

The substrate, often a silicon wafer, may be heated and rotated during deposition. Deposition of biphasic laminates is accomplished by using two different sputtering targets and either moving the substrate back and forth between the two sources, or by using shutters to blank the sputtering guns in an alternating manner [1]. The advantages of PVD multilayer synthesis include excellent cleanliness (the base vacuum pressure in a PVD systems is typically 10^{-8} torr), precise control of layer thickness and layer thickness uniformity, and the ability to alter substrate temperature during growth. The disadvantages of this technique include significant expense and slow deposition rates (typical deposition rates are $\sim$0.1 nm/s) [36].

PVD processing has allowed for the synthesis of an extremely large variety of metallic laminates; examples of nanolaminates (listing only Cu-X type laminates) include Cu-Nb [11], Cu-Cr [39], Cu-Ni [3], Cu-Co [38], Cu-Mo [40], Cu-Ta [41], Cu-W [42], Cu-V [43], and Cu-Au [44]. An image of a Cu-Nb nanolaminate produced *via* PVD is shown in Figure 1.2(b). The ability to create nearly unlimited combinations of constituent phases, combined with precise layer thickness control, is a tremendous advantage of the PVD process. Yet, the slow deposition rate severely limits the volumes of material that can be produced (synthesis of a 40 μm thick film would require over 100 hours to grow, assuming a deposition rate of 0.1 nm/s). Further, significant layer waviness can

occur during PVD multilayer growth, with the wavelength and amplitude of these undulations increasing with film thickness [36, 45]. The waviness alters the interface crystallography [45], is expected to affect the mechanical response of the multilayers [36], and scales with film thickness. Therefore PVD nanolaminate films thicker than 40 μm are seldom produced.

1.2.3 Deformation processing

The third nanolaminate synthesis method is that of microstructural refinement through deformation processing. Two of the earliest examples of this method are the investigations Sahay [46] and Yasuna [37]. Sahay created brass-steel nanolaminates by diffusion bonding a stack of initially 25 μm foils followed by cold rolling the bonded laminate to create sub-micron layers (layer thicknesses of 400-170 nm) [46]. Yasuna used a similar process but conducted multiple iterations of the stacking, bonding, and rolling procedure to produce Fe-Ag laminates with layer thicknesses as small as 10 nm (Figure 1.2(c)) [37]. While even earlier works explored microstructural refinement of 'in-situ composite' eutectic/eutectoid materials through plastic deformation [47–49] (notably cold drawn/rolled pearlitic steels [48] and rolled Ag-Cu eutectic alloys [49]), the discontinuous pseudo-lamellar structure of these materials stands in con-

trast to the continuous laminates produced by repeated stacking and rolling of elemental foils and will not be discussed further.

Synthesis of metallic nanolaminates through deformation processing was greatly facilitated by the advent of the accumulative roll bonding (ARB) process. This process, the development of which is attributed to Saito, Tsuji, and co-workers [50–53], substituted roll bonding for diffusion press bonding, enabling both bonding of the layers and reduction of the layer thickness to be accomplished in a single step. While initially applied to single phase materials, ARB was successfully used to create Cu-Nb nanolaminates with relatively coarse layers (20-0.2 μm) by Lim in 2009 [54]. Attempts to apply the ARB process to nanolaminate synthesis of other material systems, including Al-steel [55], Al-Ti [56, 57], Al-Cu [58], Al-Zn [59], Cu-Zr [60], Mg-Ti [61], Ni-Cu [62], Ni-Al [63], Zr-Ti, Zr-Ni, and Zr-Al [64], have met with mixed success due to the tendency for layer fragmentation during deformation.

An advantage of the ARB process for nanolaminate synthesis is that, in contrast to PVD or ED methods, bulk sheets of nanolaminates can be produced. The process is industry scalable and uses conventional bulk deformation processing equipment. The disadvantages, or at least complications, are considerable. First, co-deformation is needed to maintain layer continuity during processing and requires that the materials used for nanolaminate synthesis possess sim-

ilar mechanical properties. Secondly, microstructural evolution occurs during processing that is considerably more complex than microstructure formation during PVD nanolaminate synthesis [18]. Third, the extreme strains that are responsible for the microstructural refinement can cause intermixing in some systems [36]. Therefore ARB processing is most readily applied to the synthesis of nanolaminates with constitutive phases that are immiscible.

While the PVD, ED, and ARB synthesis processes have their individual advantages, ARB is the only technique capable of producing truly bulk nanolaminates suitable for structural applications. The Cu-Nb system, with very limited solid solubility and a lack of intermetallics, offers an attractive model system for investigating the potential for ARB synthesis of bulk nanolaminates with layer thickness below 100 nm. While significant prior work has indicated that Cu-Nb nanolaminates synthesized *via* PVD show extraordinary properties, differences in microstructure and mechanical properties may arise from altering the synthesis technique from PVD to ARB. Therefore the practicability of ARB Cu-Nb nanolaminate synthesis, the effects of ARB processing on microstructure, and the resultant mechanical properties and deformation behavior of ARB Cu-Nb nanolaminates will be investigated in this work. In order to provide further context for the results of these investigations, the microstructure, mechanical behavior, and deformation mechanisms reported for PVD nanolaminates will be

summarized in the following section, with particular emphasis on PVD Cu-Nb nanolaminates.

1.3 PVD thin film microstructure and mechanical behavior

The microstructures of thin film nanolaminates, while varying depending on the system, are typically polycrystalline and in-plane isotropic. For the case of Cu-Nb PVD nanolaminates, both phases consist of columnar grains with a strong $\{111\}$ Cu texture and $\{110\}$ Nb texture. That is, the in-plane orientations of each grain in the individual phases is random, but the crystallographic direction normal to the film (the growth direction) is $[111]$ for Cu and $[110]$ for Nb. The copper-niobium interfaces have been found to adopt a Kurjumov-Sachs orientation relationship with $\{111\}_{Cu}\|\{110\}_{Nb}$ $[110]_{Cu}\|[111]_{Nb}$. The in-plane isotropic microstructure of these PVD Cu-Nb films greatly simplifies investigations of the mechanical response, as it limits the anisotropy of the nanolaminate material. Similar columnar grain structures are observed in other PVD films, although the texture and interface crystallography are dependent on the crystal structures of the deposited materials [3, 65].

Due to limitation imposed by the geometry of thin films, the vast majority of mechanical testing that has been conducted on nanolaminates has consisted of nanoindentation. Nanoindentation is capable of determining the hardness, elastic modulus, and (through the use of the empirical Tabor factor relating flow strength to hardness) the flow stress of a material [65–67]. However, it is either difficult or impossible to investigate work hardening, anisotropy, ductility, or deformation mechanisms such as shear localization. Further, the stress state under a nanoindent is complex, and significant experimental evidence has shown that the deformation during nanoindentation can be strikingly inhomogeneous, even in ductile metallic nanolaminates [68–70]. A review of recent mechanical tests, however, has shown that the flow stress estimated from nanoindentation hardness testing is in good agreement with the flow stress determined through micropillar compression normal to the layers and free-standing thin film tensile tests parallel to the layers for the specific case of PVD Cu-Nb nanolaminates [36]. It should be noted that this agreement may be a fortuitous effect of the sample orientations tested and the limited plastic anisotropy of these nanolaminates; certainly in the general case, where pronounced plastic anisotropy may exist, agreement between flow stresses estimated from indentation and tension/compression tests is not guaranteed. Nevertheless, early investigations into the mechanical properties of Cu-Nb multilayers relied exclusively on nanoin-

dentation [71], and dislocation based models for multilayer deformation were developed to fit flow strength data derived from these hardness measurements.

1.3.1 Strength versus layer thickness

An increase in yield strength or flow stress with decreasing layer thickness has been observed in a wide variety of metallic nanolaminates. Figure 1.3 shows a plot of hardness versus the inverse square root of the layer thickness for many nanolaminate systems synthesized *via* PVD, while Table 1.1 shows the tabulated maximum hardness observed in each material system. The trend evident from Figure 1.3 is that small layer thicknesses lead to higher hardnesses and therefore higher flow stresses [67]. Significant differences in hardness are observed across the various systems, with the strength of Ta-V and Co-Mo being substantially higher than other systems with comparable layer thicknesses (Table 1.1). This suggests that other considerations such as interface crystallography, residual stresses, and defects may play an important role in determining the mechanical response of these materials [36].

A clearer picture of the strength versus layer thickness relationship is provided by focusing on a single system: PVD Cu-Nb nanolaminates. Figure 1.4 shows a plot of flow strength versus the inverse square root of the layer thick-

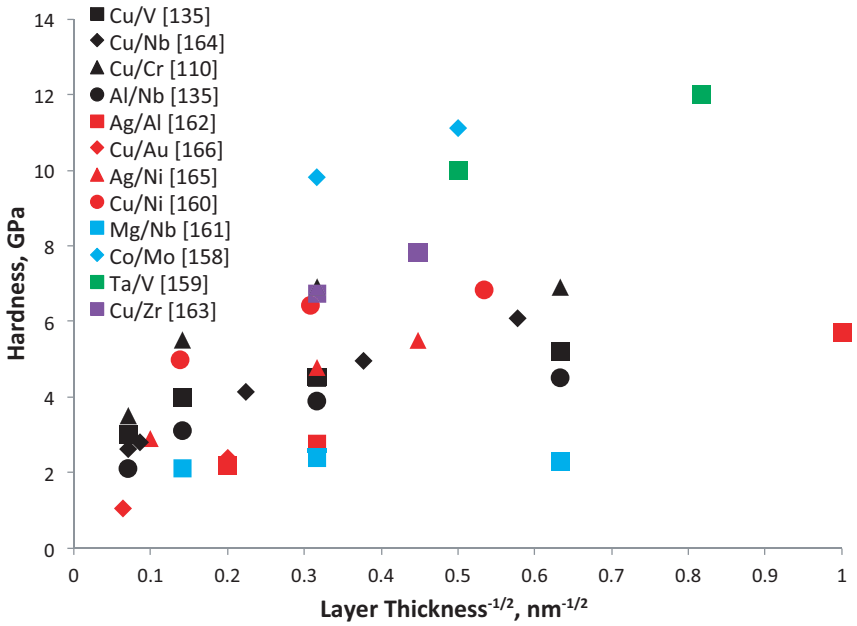

Figure 1.3: A plot of hardness versus inverse square root of the layer thickness for a variety of metallic nanolaminates with equal phase fractions, reproduced from Reference [36] with permission from Springer. For information on the references shown in the figure, refer to the original work.

Table 1.1: Peak hardness observed in various PVD multilayer systems with equal phase fractions. Table adapted from Reference [36] (see Reference [36] for original data sources).

System	Crystal structure	Layer thickness (nm)	Hardness (GPa)	Fabrication method
Al-Ag	FCC/FCC	1.0	5.7	Sputtering
Mg-Nb	HCP/BCC	2.5	2.3	Sputtering
Al-Nb	FCC/BCC	2.5	4.5	Sputtering
Cu-Nb	FCC/BCC	2.5	6.8	Sputtering
Cu-V	FCC/BCC	2.5	5.2	Sputtering
Ag-Ni	FCC/FCC	5.0	5.5	Sputtering
Ta-V	BCC/BCC	1.5	12	Sputtering
Cu-Ni	FCC/FCC	3.0	6.8	Evaporation
Cu-Cr	FCC/BCC	2.5	6.9	Sputtering
Co-Mo	HCP/BCC	4.0	11	Evaporation

ness for PVD Cu-Nb nanolaminates, with data obtained from nanoindentation hardness data. The flow strength of material with layer thicknesses greater than ∼100 nm follows a linear relationship with layer thickness, as shown by the solid line in Figure 1.4. This trend is consistent with the Hall-Petch equation (Equation 1.1) which describes the relationship between the grain size and yield strength of a material [72, 73]. In this equation, σ_y is the material yield strength, σ_0 is an intrinsic stress resisting dislocation motion within a grain, K_y is the Hall-Petch coefficient which provides a measure of the strengthening effect of the boundaries, and d is the grain diameter. Equation 1.1 has been applied to multilayers by substituting the layer thickness h in place of grain diameter [17, 71]. Strictly speaking this equation should apply only to multilayers consisting of single crystalline lamella. Nevertheless many investigators have observed a linear relationship between yield strength and layer size, effectively grouping all non-interphase interface strengthening mechanisms in the σ_0 term.

$$\sigma_y = \sigma_0 + K_y d^{\frac{-1}{2}} \tag{1.1}$$

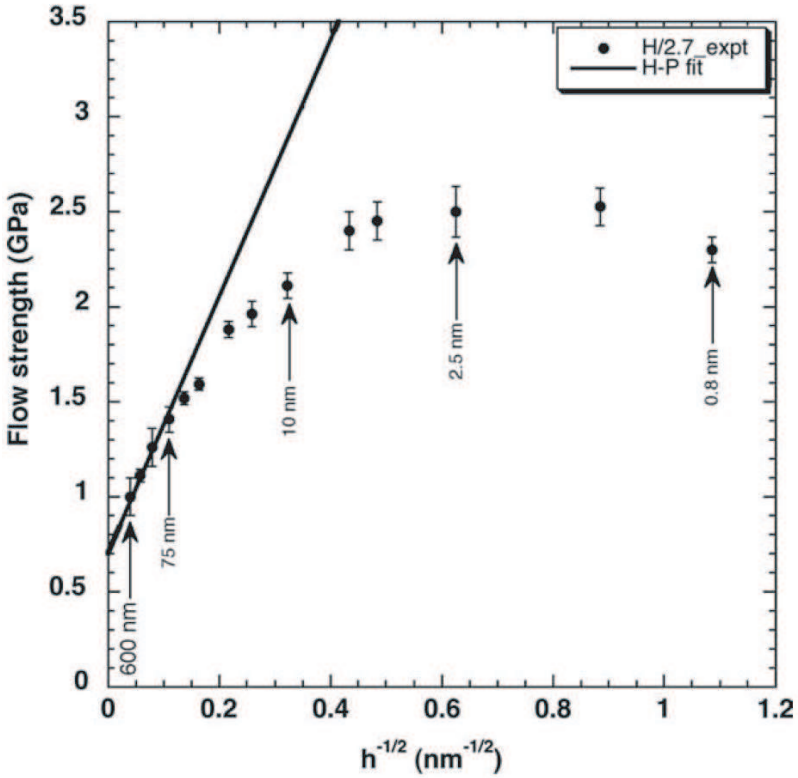

Figure 1.4: Hardness versus layer thickness plot for PVD Cu-Nb nanolaminates, reproduced from Reference [17] with permission from Elsevier. All data obtained from nanoindentation hardness tests.

1.3.2 Dislocation models for sub-100 nm nanolaminates

At layer thicknesses below 100 nm, two alternate dislocation mechanisms have been proposed to explain the strength of nanolaminates. At the finest length scales (layer thicknesses below several nanometers), a plateau in yield strength has been observed, as shown in Figure 1.4. For PVD Cu-Nb multilayers this maximum corresponds to a yield strength of 2.6 GPa and occurs below 5 nm [17]. The insensitivity of yield strength to layer thickness in this regime is attributed to the deformation mechanism of single dislocations crossing Cu-Nb interfaces [17]. The absorption of a single dislocation into the interface results in dislocation core spreading *via* local interfacial shear, and a large applied stress is necessary for further glide into an adjacent layer. The stress required for an interface crossing event has been explored using molecular dynamics simulations and has been found to be in the range of 4-5 GPa [17]. The experimentally observed lower yield stress has been attributed to thermal activation [17].

An additional description of dislocation motion, the confined layer slip (CLS) model, has been proposed to bridge the gap between the dislocation pile-up (Hall-Petch) regime and the dislocation transmission regime. The CLS model is based on the work of Freund and Nix on dislocation motion in thin films [74, 75], and is believed to be operative in nanolaminates with layer thick-

nesses in between 5 and 100 nm [17]. In this model, deformation is attributed to individual dislocation loops gliding within a layer, depositing residual dislocations at the interfaces. The applied stress necessary to propagate a dislocation loop confined within a layer bounded by two identical interfaces is given by an energy balance between the work done by the stress in a film when a dislocation moves and the work required to generate two trailing misfit dislocation segments [17, 75, 76]. In the analysis of Misra [17], the incorporation of a suitable residual dislocation self energy yields Equation 1.2 for the stress required for CLS. In this equation τ_{cls} is the resolved shear stress on the dislocation glide plane, b is the burgers vector, $h^{'}$ is the layer thickness measured parallel to the glide plane, μ is the shear modulus, ν is the Poisson's ratio, and α is a core cut off parameter ranging between 0 and 1 (1 corresponds to a compact dislocation core). Using α =1, it was observed that Equation 1.2 does not provide a good fit for PVD Cu-Nb flow strengths measured *via* nanoindentation [17].

$$\tau_{cls} = \frac{\mu b}{8\pi h'} \frac{4-\nu}{1-\nu} \ln \frac{\alpha h^{'}}{b} \tag{1.2}$$

In order to bring the predicted confined layer slip stress into agreement with the experimental results, Misra *et al.* increased the core cut-off radius to account for dislocation core spreading at the Cu-Nb interface, added an interface stress

term, and incorporated a simplified expression for the interaction of the dislocation loop with pre-existing residual dislocations at the interface. The final result is shown in Equation 1.3, where h is the layer thickness, f is the interface stress, and λ is the spacing of preexisting residual dislocations.

$$\tau_{cls} = \frac{\mu b}{8\pi h'} \frac{4-\nu}{1-\nu} \ln \frac{\alpha h'}{b} - \frac{f}{h} + \frac{\frac{\mu b}{1-\nu}}{\lambda} \tag{1.3}$$

The results were found to be in very good agreement with the observed relationship between flow strength and layer size. It should be noted, however, that the pre-existing dislocation spacing λ behaves as a fitting parameter in this equation.

1.3.3 PVD Cu-Nb nanolaminate anisotropy and deformation behavior

The extensive use of nanoindentation testing has allowed the effects of layer size on hardness and flow strength to be determined and has informed the construction of dislocation based strength models. Yet these tests do not provide information regarding material anisotropy, ductility, or flow localization and failure mechanisms. While information about these aspects of the mechanical behavior of PVD Cu-Nb nanolaminates is limited, a few investigators have con-

ducted micropillar compression tests as well as free-standing thin film tensile tests on PVD Cu-Nb nanolaminates. Mara [77] performed tensile tests of 15 μm thick PVD films of Cu-Nb nanolaminates with a 40 nm layer thickness. High flow strengths of 1.5 GPa were reported with relatively low strains to failure of 3.4%. The low ductility was attributed to the low work hardening rate of the material, with failure occurring nearly at the strain level predicted from the Considère criterion for plastic instability during tension [77].

Micropillar compression tests of PVD Cu-Nb nanolaminates have also been reported. These compression tests have been conducted on pillars with the stress axis aligned with the layer normal direction [5, 78], as well as on pillars in which the layers are inclined by 45° to the stress axis [79]. Layer normal compression tests of a 5 nm PVD Cu-Nb nanolaminate indicated that these materials show excellent deformability in compression, with high strength (2.4 GPa) and large strains to failure ($\sim$25%) reported [5]. The failure mechanism in both 5 and 40 nm layer thickness PVD laminate micropillar specimens was shear band formation, as shown in Figure 1.5 [78]. While mechanical anisotropy of PVD Cu-Nb nanolaminates is limited due to their in-plane isotropic grain morphology and texture, micropillar compression tests conducted at 45° to the layer orientation of 5 nm layer thickness nanolaminates indicated that the layer parallel shear strength of these materials is low [79]. The compressive strength

of these off-axis pillars was ∼1.7 GPa, significantly lower than the compressive strength of pillars compressed normal to the layer orientation (∼2.4 GPa) [79]. The low layer parallel shear strength of these materials is attributed to interface sliding, a mechanism that has been predicted to occur at the atomically flat interfaces in PVD Cu-Nb nanolaminates [80]. These interface shear strength predictions were made using atomistic modeling of perfect Cu and Nb crystals joined together according to the experimentally observed interface orientation relationship. Incremental shear displacements along various directions were applied to the model, and the atomic structure was allowed to relax after each increment. The shear strength was taken to be the stress at which irreversible sliding along the interface occurred [80].

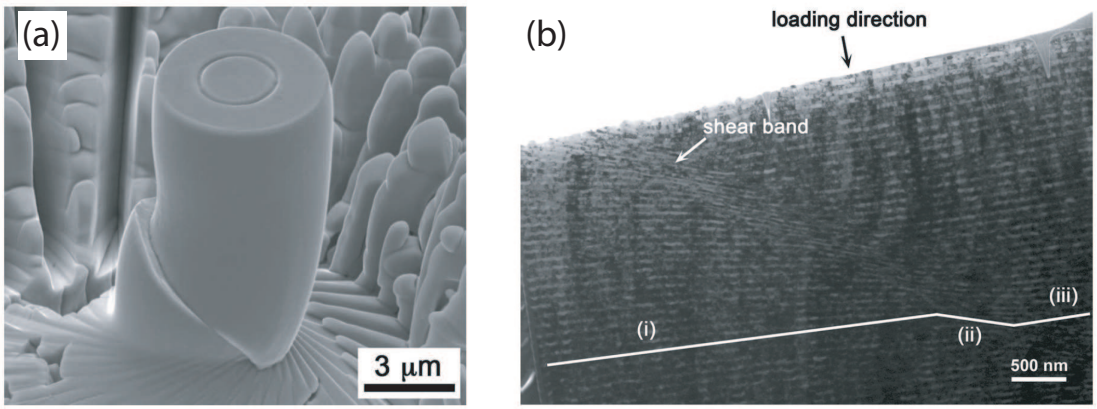

Figure 1.5: Shear band formation in PVD Cu-Nb nanolaminates. (a) shows a 5 nm PVD Cu-Nb micropillar compression specimen tested to failure, reproduced from Reference [5] with permission from the American Institute of Physics. (b) shows a transmission electron micrograph of a shear band in a 40 nm PVD nanolaminate post-test pillar cross-section, reproduced from Reference [78] with permission from the American Institute of Physics.

1.4 Bulk ARB nanolaminates: unresolved issues

While the mechanical testing discussed in the previous section provides insight into the deformation behavior and deformation mechanisms in thin film PVD Cu-Nb nanolaminates, the behavior of ARB processed nanolaminates is expected to be considerably more complex. This expectation is based on consideration of the processing method symmetry elements, the effect of 'top-down' versus 'bottom up' processing, and the relative influence of thermodynamics and kinetics.

The symmetry of a synthesis technique influences the microstructural symmetry in the resultant material. In PVD synthesis of polycrystalline films, line of sight deposition of atoms on a substrate from a sputtering source centered far above the substrate can be expected to produce an in-plane isotropic polycrystalline film (neglecting potential effects of substrate anisotropy). In this idealized scenario [65], the growth flux is uniform, the orientations of the initial clusters or islands of deposited atoms on the substrate is random in-plane, and the resulting grain structure and texture of the polycrystalline film produced as the islands coalesce is also in-plane isotropic. While there may be a distinct out of plane preferred crystallographic orientation and a different out of plane grain diameter (columnar grain height), there is no directionality of the processing

technique from which an in plane anisotropic microstructure could result. In contrast, the idealized plane strain deformation process of rolling can be expected to produce orthotropic symmetry in a rolled polycrystal, both in texture and grain morphology (assuming that the initial polycrystal prior to rolling is isotropic) [81]. This reduction in symmetry, compared to in-plane isotropy, has significant implications for mechanical property determination: the yield stress, flow stress, and strain hardening rate during compression along three orthogonal directions may all be significantly different in an orthotropic material. Small reductions in symmetry lead to significant complications in describing and measuring mechanical properties [81].

The 'top down' nature of deformation processing also indicates that the microstructure and behavior of ARB nanolaminates will be significantly more complex than their PVD counterparts. In PVD, material is deposited until a desired layer thickness is achieved, at which point deposition of the next layer begins. Each layer is built up to the desired thickness using the same deposition parameters. Thus the only difference between a 100 nm layer in a large layer thickness nanolaminate and a 50 nm layer in a smaller layer thickness nanolaminate is that an additional 50 nm of material has been deposited. In that a 100 nm layer contains a 50 nm thick region identical to the 50 nm layer, the resulting structure is required to possess some similarity. In contrast, a top down deformation

process starts with a coarse microstructure and uses a homogeneous deformation to refine the structure. Thus in ARB, a 50 nm layer thickness nanolaminate is produced from a 100 nm layer thickness nanolaminate. The effects of this homogeneous deformation may significantly alter the microstructure of the entire layer, and it is not required that any region within a 100 nm layer posses microstructural similarity to a 50 nm layer. Therefore the effects of layer thickness on mechanical properties may be more pronounced for ARB nanolaminates due to microstructural evolution within the layers during processing.

Finally, the microstructure of ARB nanolaminates evolves during processing through the combined effects of thermodynamics and kinetic processes. While interfacial energy considerations play a role in determining the structure of ARB processed nanolaminates, structure evolution is also expected to be significantly influenced by phenomena such as dislocation nucleation and propagation, recovery, and recrystallization [18]. In low deposition rate PVD film growth, the effects of surface energy and lattice mismatch largely determine the interfacial orientation relationship [18], although surface diffusion during film growth must be considered to explain grain morphology [65]. Nevertheless, the introduction of the effects of dislocation motion and slip system activity during ARB nanolaminate synthesis is expected to lead to more complex microstructures than those observed in PVD nanolaminate films.

In the remainder of this thesis, investigations on the practicability of the ARB process as a means of synthesizing metallic nanolaminates, the microstructure evolution during ARB processing of Cu-Nb nanolaminates, and the mechanical behavior and deformation mechanisms of ARB Cu-Nb nanolaminates will be presented. Microstructural evolution during ARB processing is indeed complex, with changes in crystallography and grain morphology occurring as a function of processing history. Characterization of the mechanical behavior of ARB Cu-Nb nanolaminates with layer thicknesses ranging from 1800 to 15 nm indicates that these microstructural changes strongly influence the strength of the nanolaminates, with significant mechanical anisotropy being observed in sub-100 nm layer thickness materials. This anisotropy drives an unusual form of strain localization known as kink band formation, a phenomenon that will be discussed in detail.

Chapter 2

Experimental and Simulation Procedures

In this chapter, the material compositions, microstructural analysis methods, and mechanical test procedures are given for ARB processed nanolaminates. The techniques used for in-situ compression testing are described, as are the methods and parameters used for mechanical property simulation. While the accumulative roll bonding process itself falls under the category of an experimental procedure, discussion of this process warrants a separate chapter (Chapter 3).

2.1 Compositions of starting materials

Starting materials used for ARB processing of Cu-Nb and Zr-Nb nanolaminates were obtained with as high a purity as practicable given the volumes of material required.

Cu was obtained in the form of cold rolled, 3.17 mm thick sheets conforming to ASTM B170 and UNS C10100 composition standards from Revere Copper Products Inc (Rome, NY, USA). The chemical analysis, as reported by the manufacturer, is listed in Table 2.1. The as-received Cu sheets were cold rolled to a final thickness of either 1 or 2 mm and annealed at 450°C .

Nb was obtained from ATI Wah Chang, Allegheny Technologies (Albany, OR, USA). The Nb was supplied as a fully recrystallized sheet with a thickness of 3.10 mm. The material had a residual resistivity ratio ('RRR' value, an industrially used proxy for purity [82]) of 456-476 and chemical composition as listed in Table 2.2. The Nb sheet was sheared into approximately 15 x 33 cm sections and cold rolled to a thickness of 2 mm in the Sigma facility at Los Alamos National Laboratory (LANL). The material was annealed at 950°C in order to achieve a flow stress comparable to that of the Cu starting material.

Very high purity zirconium, used during ARB synthesis of Zr-Nb nanolaminates, was obtained from David Alexander (LANL, MST-6) as no commercial

suppliers contacted were capable of producing zirconium with the desired purity and dimensions. The material was received in the form of an 80 mm diameter electron beam melted ingot with a length of 100 mm with a chemical composition listed in Table 2.3 (as reported in previous chemical analysis [83]). The ingot was upset forged and clock-rolled (a rolling process in which the rolled material is rotated after every pass to vary the rolling direction) to a thickness of 1 mm with several intermediate annealing steps. The final rolled sheet was annealed at 550°C for 1 hour.

Table 2.1: Impurity concentrations in Cu starting material. All concentrations are given in parts per million by weight.

	Ag	S	Fe	Ni	O	As	Sb	Se	P	Sn	Te
Cu	< 25	< 15	< 10	< 10	< 5	< 5	< 4	< 3	< 3	< 2	< 2

Table 2.2: Impurity concentrations in Nb starting material. All concentrations are given in parts per million by weight.

	Ta	O	Ti	W	Zr	Hf	Mo	Fe	C	N
Nb	110	< 40	< 30	< 30	< 30	< 30	< 30	< 25	< 20	< 20

Table 2.3: Impurity concentrations in Zr starting material. All concentrations are given in parts per million by weight.

	Fe	V	O	Hf	C	Al	N
Zr	< 50	< 50	< 50	35	22	< 20	< 20

2.2 Heat treatments

Annealing heat treatments were conducted on the starting materials for ARB processing, Zr-Nb nanolaminates in between ARB processing steps, and select Cu-Nb nanolaminate mechanical test specimens. Annealing of all starting materials for ARB as well as the Zr-Nb nanolaminates was conducted in a high temperature vacuum furnace (Advanced Thermal Technologies, Inc Brew Associates model 912) with a molybdenum hot zone and argon quench capabilities. Annealing of small mechanical test specimens was conducted at 400°C for 30 minutes in a quartz tube furnace under argon atmosphere with a 10°C heating and cooling ramp rate.

2.3 Microstructural characterization

2.3.1 Metallographic preparation

Metallographic preparation of Cu-Nb nanolaminates is challenging due to the tendency of abrasive media to embed in pure Cu and Nb, the tendency for surface relief between the layers during polishing, and the wide range of layer thicknesses and therefore material hardnesses. Since the quality and accuracy of microstructural characterization, particularly surface sensitive characterization

such as EBSD, is dependent on the quality of the metallographic preparation, the preparation procedure will be given in detail.

All metallographic specimens were mounted in 'cold-mount' metallographic epoxy (Buehler 'Epo-Thin' two part metallographic epoxy). Conventional hot mounting compounds were never used as the elevated temperatures for thermosetting compounds (155°C) was found to induce recrystallization of the severely deformed copper layers in certain specimens.

Rough grinding of the specimens was conducted using silicon carbide metallographic papers (240-1200 grit) with water coolant. Ground specimens were polished using 3 μm polycrystalline diamond suspension (Metadi, Buehler Ltd.) on a low-nap 'TexMet' polishing cloth (Buehler Ltd.). Vibratory polishing was conducted using a 0.3 μm aluminum oxide slurry on a 'MicroCloth' polishing cloth (Buehler Ltd.) for 2 hours followed by vibratory polishing using a 0.05 μm colloidal silica suspension on a 'MasterTex' polishing cloth (Buehler Ltd.) for 30-60 minutes. This procedure was found to yield specimens suitable for all characterization techniques and allowed for the collection of high quality EBSD patterns.

A similar procedure was used for the preparation of Zr-Nb nanolaminates however an additional polishing step using 9 μm diamond suspension was con-

ducted after grinding. Vibratory polishing was found to be extremely helpful for removing surface deformation, however separate colloidal silica suspensions must be used for Zr-Nb and Cu-Nb samples. Attempts to polish Zr-Nb using suspensions previously used for polishing Cu-Nb resulted in a thin surface layer of copper plating out onto the Zr layers.

2.3.2 Light optical microscopy

Light optical microscopy (LOM) was found to be an invaluable tool for the rapid assessment of both bond quality and layer continuity during ARB process development as well as characterization of strain localization in mechanical test specimens. LOM was conducted using a Leica MEF4M inverted metallographic microscope and a Zeiss Axiomat microscope with polarized light capabilities.

While the inherent resolution limitation imposed by the wavelength of light would suggest that light optical microscopy would be unsuitable for the study of nanolaminates with sub-micron layer thickness, metallographically prepared Cu-Nb nanolaminates with layer thickness below 250 nm polarize reflected light. As this polarization is dependent on the orientation of the layers, orientation changes in the layered structure are clearly revealed using cross-polarized light optical microscopy. Thus while the individual layers are not resolvable, informa-

tion regarding the layer orientation can be obtained. The observed polarization of light is attributed to the fine periodic surface relief that occurs during the final polishing of these biphasic materials. Similar effects due to surface relief have been observed in certain etched metals [84] as well as etched lamellar structures such as pearlite [85].

2.3.3 Scanning electron microscopy

Scanning electron microscopy was conducted using an FEI XL-30 scanning electron microscope (SEM) equipped with an FEI backscatter electron (BSE) detector and energy dispersive spectroscopy (EDS) detector. Due to the difference in atomic number between Cu (29) and Nb (41), BSE imaging using an accelerating voltage of 15 kV was found to be the most effective imaging method for analyzing the lamellar structure.

2.3.4 Electron backscatter diffraction

Electron backscatter diffraction (EBSD) is a characterization technique that allows determination and mapping of the crystallographic grain orientation at the surface of a metallographic specimen. EBSD requires a deformation free surface so that backscattered electrons can diffract through a thin surface layer

of the specimen (10's of nm), and form an indexable Kikuchi pattern on a phosphor detector. EBSD analysis was conducted in a FEI XL-30 microscope using an TSL/EDAX Digiview EBSD camera. An accelerating voltage of 20 kV, 50 μm aperture, and 4 $\times$ 4 pattern binning were found to yield acceptable pattern indexing.

2.4 Tensile and compression testing

Tensile specimens with the tensile axis parallel to either the rolling direction (RD) or transverse direction (TD) of the rolled Cu-Nb nanolaminate plates were prepared by electro-discharge machining (EDM) and ground using 15 μm abrasive papers to remove damage from the machining operation. The final gauge dimensions measured 1.25 $\times$ 4.0 $\times$ 14.2 mm as shown in Figure 2.1(a) The specimens possessed a similar gauge length to width ratio as the ASTM standard geometry while conforming to the constraints imposed by available material dimensions. Displacement controlled tensile tests were conducted on a servo-hydraulic load frame using hydraulic wedge grips and a laser extensometer (Electronic Instrument Research model LE-01) for measuring the distance between two retro-reflective tapes applied to the ends of the specimen gauge. The initial strain rate was 10^{-3}s^{-1} and all samples failed within the gauge.

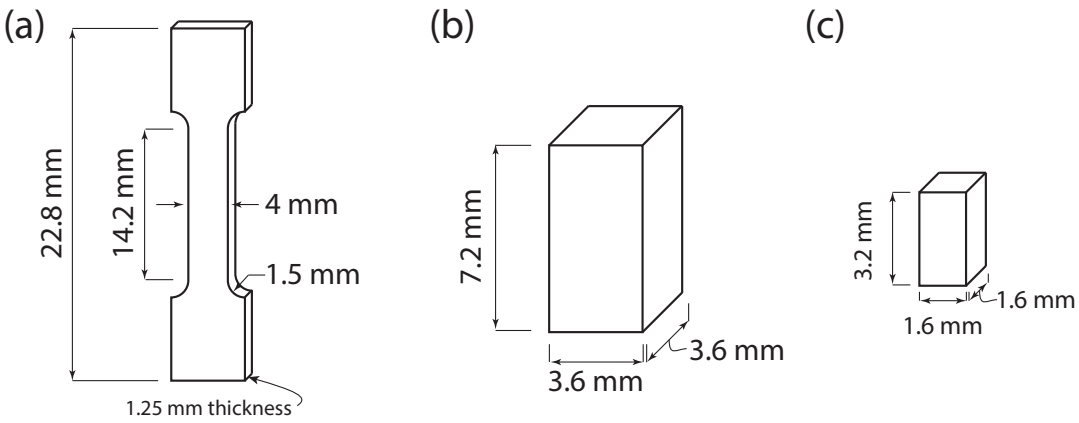

Figure 2.1: Geometry of tensile (a) and compression (b,c) specimens.

Compression specimens with a square cross-section and a 2:1 height to width aspect ratio were EDM cut from the rolled laminate plate at various orientations to allow layer parallel compression tests, layer normal compression tests, and compression tests at various angles to the layered structure. Due to the limited sheet thickness of the rolled material and the desire to use specimens as large as practicable for each orientation, two specimen sizes were used. The largest, shown in 2.1(b), measured $7.2 \times 3.6 \times 3.6$ mm. A scaled geometry, shown in 2.1(c), was used for all layer normal and off-axis compression specimens. All specimens were carefully aligned with respect to the layer orientation and fixtured during machining to ensure good parallelism. Potential damage from the machining operation was removed *via* metallographic polishing. All compression test specimens were annealed at 400°C for 30 minutes in order to strengthen the most recently bonded interfaces and inhibit delamination.

All compression tests were conducted on an MTS servo-hydraulic load frame under displacement control. The initial strain rate was $10^{-3}s^{-1}$ for all specimens with the exception of those used for digital image correlation based strain mapping (see Section 2.6). A molybdenum disulfide lubricant was applied to the specimen ends in order to minimize friction between the specimen and compression platen. Initial compression tests were carried out between one fixed platen and one self-aligning hemispherical tungsten carbide platen in order to eliminate misalignments and promote a uniaxial stress state. Due to the pronounced inhomogeneous deformation exhibited by many of the compression specimens, the self-aligning platen was replaced with a fixed platen for subsequent tests. The rationale for this modification was that if a state of uniaxial compression cannot be maintained due to strain localization, the invariant constraint imposed by rigid non-rotatable compression platens is preferable to that provided by the self-aligning type platens which may rotate during large strain deformation of the specimens. The type of end constraint used will be indicated as the results are presented.

2.5 *In situ* SEM and micropillar compression testing

Two types of SEM compression tests were conducted at Los Alamos National Laboratory: 1) *In situ* SEM compression tests of bulk specimens and 2) micro pillar compression tests conducted on focused ion beam (FIB) milled pedestals.

Specimens for *in situ* SEM compression testing were prepared from 65 and 30 nm Cu-Nb nanolaminate material by EDM cutting, lapping, and polishing using a Multiprep lapping machine (Allied High Tech Products Inc. Compton, CA). The final specimens measured $1 \times 1 \times 2.5$ mm. The compression axis (longest dimension) of the specimens was parallel to the transverse direction of the rolled plates. Specimens were compressed between hardened steel platens using an MTI Instruments Fullam 1000 lb capacity SEM tension/compression sub-stage with a 300 lb capacity load cell and a linear variable differential transformer (LVDT). The stage was driven using a variable output DC power supply. Due to severe compliance of the compression stage, the stress-strain data was not used for analysis. Instead, these tests provided insight into kinematics of kink band strain localization.

The *in situ* stage was loaded into a Philips XL-30 ESEM. Imaging was con-

ducted using the BSE detector, an accelerating voltage of 20 kV, and a scan speed of 3 seconds per frame. While initially intended to provide high magnification images of kink band propagation, significant vibration of the stage limited the working magnification to 2000× and below. Saved images were imported into ImageJ [86] as a stack and aligned.

Micropillar compression tests provided information about kink band formation in specimens with reduced specimen size to layer thickness ratios. Dr. William Mook performed the compression pillar FIB milling and compression testing at Los Alamos National Laboratory. Square cross-section pillars measuring approximately $4 \times 4 \times 10\,\mu$m were FIB milled with the compression axis parallel to the transverse direction of the rolled 65 nm ARB nanolaminates. Compression tests were carried out using an SEM-PicoIndenter in an FEI Helios dual beam SEM.

2.6 Digital image correlation

Compression specimens measuring $7.2 \times 3.6 \times 3.6$ mm were machined from the rolled and annealed laminate plate *via* EDM. The specimens were carefully aligned with respect to the layer orientation, with the compression axis parallel to the transverse direction of the rolled material. Potential damage from the

machining operation was removed on four of the six specimen faces *via* metallographic polishing, with the top and bottom surfaces left in the as-machined condition to prevent edge rounding or loss of parallelism. A speckle pattern was applied to one face of the specimens using toner ink that was fused to the polished surface *via* brief exposure to a heat lamp.

Compression testing was conducted on a MTS servo-hydraulic load frame under displacement control at an initial strain rate of $10^{-4}s^{-1}$. Due to the small specimen size, the need to position specimens centrally on the compression platens, and the lighting requirements of digital image correlation, truncated pyramidal hardened steel pedestals were attached to the compression platens. This allowed for *in situ* imaging of the compression specimens without reflections or shadowing from the large compression platens. A molybdenum disulfide lubricant was applied between the specimens and the compression pedestals to minimize friction.

A laser extensometer (Electronic Instrument Research model LE-01) was used to measure the distance between two retro-reflective tapes attached to the compression pedestals while local strains on the specimen face were obtained from digital image correlation. The digital image correlation (DIC) setup consisted of a Point Grey Grasshopper digital camera, Nikon AF Micro Nikkor 70-180 mm lens, fiber optic light source, and a half-silvered mirror for splitting

the light source beam. This setup allowed for co-axial illumination of the polished specimens, yielding images containing good contrast between the dark toner speckles and reflective specimen surface. Images were acquired every 500 ms using the commercial acquisition software VIC-Snap 2009 (Correlated Solutions Inc.). While the full strain field should in theory require a two camera, 3D DIC set up, the strong anisotropy of the lamellar material combined with the early onset of kink band formation yielded a predominately plane strain deformation with the imaged surface of the specimen remaining within the focal plane of the imaging set up. The compression tests were interrupted once kink band propagation was complete.

2.6.1 DIC analysis

The images collected during compression testing were analyzed using VIC-2D 2009 software (Correlated Solutions Inc.). Based on the image size of 1908 $\times$ 2319 pixels and the speckle pattern, a subset size of 49 $\times$ 49 pixels (102 $\times$ 102 μm) with a step size of 11 pixels (23 μm) was found to produce a good balance between correlation quality and strain resolution. A normalized squared differences correlation criterion was used during analysis. While a local Gaussian decay kernel matrix is required in the software, the minimum kernel of 5

$\times$ 5 steps (55 $\times$ 55 pixels) was applied during the strain calculation [87]. The displacements and Lagrangian strain values were exported from VIC-2D, and all visualization and further analysis was conducted using MATLAB software.

Within the subset used to calculate strain, DIC treats the deformation as affine [87], and therefore significant care must be taken when using DIC on specimens that deform by heterogeneous and localized shear. If the subset used to calculate strain does not deform homogeneously and is instead sheared along a plane by a narrow kink band, correlation of the deformed state to the reference state is either impossible or very poor. The quality of correlation is represented by the 'sigma' value (one standard deviation confidence interval) calculated by the VIC-2D software. While the average sigma values for regions of the specimen that deformed uniformly were 0.012, indicating good correlation, higher values of sigma ($\sim$0.03) and uncorrelated subsets were found to correspond to the location of the kink band as it propagated across the sample. Thus the sigma value provided both a measure of the quality of the correlation and a convenient way to track the location of the kink band.

Calculated strain values for regions with a sigma value above a threshold of 0.018 were discarded. This removed potentially unreliable strain measurements corresponding to the location of the kink band. However additional cleanup of the strain data was needed due to the use of the Gaussian decay kernel during

the strain calculation. While this filter reduces noise in the calculated strain values, it also increases the distance between two truly independent strain measurements. All calculated strain values in the area surrounding the kink band were removed by eroding the neighboring five strain measurements around any region containing a value of sigma greater than the threshold value (removing data within 122 μm of the kink band). All DIC strain maps are presented using the undeformed coordinates of each subset in order to allow calculated rather than interpolated strain values to be shown.

2.7 Mean field polycrystal modeling

The VPSC7 (visco-plastic self-consistent, version 7) code developed at Los Alamos National Laboratory [81, 88] was employed to model the effects of crystallographic texture on plastic anisotropy. In this model, plastic deformation in each grain occurs *via* crystallographic slip, neglecting the effects of elastic deformation, which is a reasonable assumption for large strain deformation. The Taylor or 'full constraints' homogenization approach was used instead of the self-consistent homogenization. This approach ensures compatibility between individual grains and satisfies equilibrium in an average sense (equating the macroscopic stress to the average of the grain level stresses). While a rela-

tively simple approach, the Taylor model was deemed suitable for exploring the mechanical response of Cu-Nb nanolaminates subject to layer parallel tension. Co-deformation of the Cu and Nb phases is required in layer parallel tension and therefore the Taylor homogenization was used to prevent physically unrealistic strain partitioning.

According to prior microstructural and texture analyses [81], the Cu deforms by $\{111\}\ \langle 110\rangle$ slip and the Nb by a combination of $\{110\}\ \langle 111\rangle$ and $\{112\}\ \langle 111\rangle$ slip, respectively. In the model, the resistance to slip evolves with strain according to the Voce hardening law. Four hardening parameters are used: τ_0 is the initial critical resolved shear stress (CRSS), θ_0 is the initial hardening rate, θ_1 is the asymptotic hardening rate, and τ_1 is the difference between the back extrapolated CRSS and the initial CRSS. The parameters for each slip mode in each phase were characterized using nano-indentation hardness data for the individual phases reported by Hansen *et al* [89]. For the two slip modes in the Nb phase, the hardening behavior was assumed identical, an approximation supported by discrete dislocation dynamics simulations [90]. The Voce hardening law parameters for Cu and Nb are given in Table 2.4.

Polycrystal simulations were conducted in order to model the tensile deformation behavior of the 500 nm and 30 nm nanolaminates. Since layer parallel tension requires equal strain in both the Cu and Nb layers, single phase tensile

Table 2.4: Voce hardening parameters for mean field polycrystal simulations.

		τ_0 (MPa)	τ_1 (MPa)	θ_0 (MPa)	θ_1 (MPa)
Cu	$\{111\}\langle 110\rangle$	143	147	1750	25
Nb	$\{110\}\langle 111\rangle$	190	280	2580	25
Nb	$\{112\}\langle 111\rangle$	190	280	2580	25

simulations were conducted and averaged to generate the two-phase composite stress-strain response. All starting models consisted of a polycrystal containing 10,000 Cu or Nb grains with crystallographic orientations assigned based on experimental (EBSD) texture measurements of either the 500 or 30 nm material. Plane strain tensile deformation along either the RD or TD was simulated in increments of 0.5% strain with crystallographic texture updated after each increment.

Chapter 3

ARB Processing

This chapter is devoted to the ARB process and includes discussion of the historical development of ARB, discussion of rolling and surface preparation techniques, and strategies for preventing plastic instabilities during ARB synthesis of nanolaminates.[1] The procedures for ARB synthesis of Cu-Nb and Zr-Nb nanolaminates are described in detail and recommendations for ARB process improvements are presented.

[1] Some material in Chapter 3 is reproduced from *Processing and deformation behavior of bulk Cu-Nb nanolaminates* T. Nizolek, N.A. Mara, I.J. Beyerlein, J.T. Avallone, J.E. Scott and T.M. Pollock, Metallography, Microstructure, and Analysis 2014 [91]

3.1 Historical background

The development of the accumulative roll bonding process is widely attributed to Yoshihiro Saito, Nobuhiro Tsuji, and co-workers [50–53]. In the period from 1998 to 2000, Saito and Tsuji (then a research associate at Osaka University, Osaka, Japan) published a series of papers proposing and describing the ARB process and its application for grain refinement of monolithic aluminum alloys and interstitial free (IF) steels. Saito and Tsuji may have been the first to advocate the process now known as ARB for the exclusive purpose of grain refinement in single phase materials, and the use of moderate processing temperatures (500°C for IF steel [50]) was clearly advantageous for their purpose. However, to state that the processing procedure, rather than the purpose, outlined in the 1998 paper by Saito *et al.* [50] represented a revolutionary or novel concept would be inaccurate. More than 10 years prior to the work of Saito, a nearly identical process was used by Wadsworth *et al.* [92] to create laminates from ultra-high-carbon steel and an Fe-3%Si alloy. The only notable difference in processing procedure was that Wadsworth used a rolling temperature 200°C higher than that used by Saito.

Recognition that ARB could be used to refine grain size to the sub-micron level, combined with the scientific community's growing interest in nanostruc-

tured metals [93], led to a tremendous number of studies focused on ARB and ARB processed materials. For centuries, however, laminated bi-metallic composites and nominally single phase materials have been made through repeated stacking, solid state bonding, and rolling. Prior to the development of the rolling mill, similar processes using forging had been practiced for millennia [94, 95]. Indeed, the stated purpose of Wadsworth's 1986 study [92] was to replicate the ancient (600 AD) process of pattern welding steel using modern methods and materials. It is regrettable that later papers have failed to similarly acknowledge the historical precedents for the ARB process.

3.1.1 Ancient deformation processed laminates

Noteworthy historical examples of laminated structural metals created through repeated stacking, bonding, and deformation processing include the famous Japanese samurai swords, Viking and Merovingian pattern welded knives, Indonesian laminated 'kris' blades, and wrought iron [95–97]. Pre-industrial ferrous materials contained slag and inhomogeneities due to poor metallurgical control and the inability to fully melt pure iron; lamination both improved the chemical homogeneity of the material and refined the iron/slag structure. Additionally, repeated lamination afforded some control over the carbon content

of early ferrous alloys as the carburized or decarburized surface layer could be repeatedly folded into the material to alter the bulk chemistry [92, 95].

Japanese samurai sword steel offers an example of chemical homogenization and control through lamination. Direct reduction of iron ore was achieved by charging a clay furnace with a mixture of iron oxide, sand, and charcoal. After heating, a spongy mass of reduced iron with varying carbon content was obtained [98]. This material was broken into pieces and, based on the appearance of the fracture surfaces, suitable pieces were selected for further processing. These pieces were joined together to form small plates by 'forge welding' (a solid state bonding process in which materials are heated to just below their melting points and hammered together). Subsequent stacking and forge welding of these plates produced a large block of steel which was then repeatedly forged, folded, and forge welded: a process repeated up to 30 times [98]. Initial carbon content inhomogeneity was removed, slag particles in the original sponge iron were refined and dispersed, and the carbon content could be adjusted through control of surface decarburization [94, 98].

While the process used to create Japanese sword steel dates back to as early as 800 AD, a more modern use of repeated stacking, bonding, and deformation processing is found in industrial era production of wrought iron. A spongy mass of low carbon iron and siliceous slag, produced in a puddling furnace,

was forged at high temperatures to expel the molten slag and compact the iron sponge. The product was rolled or hammered into bars 3/4 inches thick by 2 1/2 to 8 inches wide, sheared into pieces, stacked, and welded together [97]. The resulting 180-600 pound composite block was re-rolled to create 'single-refined iron' [97] A more expensive grade of wrought iron with improved mechanical properties due to slag elimination and refinement was created by repeating the shearing, stacking, and lamination process (creating 'double-refined iron') [99]. Remarkably, this method was used for commercial production of wrought iron well into the 20th century, with one of the last facilities in the United States still in operation in 1949 [97].

A final example of a 'primitive' method for creating metal laminated composites is the process used to create decorative 'mokume-gane,' traditionally composed of layers of silver, copper, and gold rich alloys. This process, in use in Japan as early as 1700 AD [95, 100], used diffusion bonding to produce a composite block of material containing distinct layers with contrasting colors. Subsequent forging or rolling refined the layered structure and deliberate surface patterning ensured that multiple layers intersected the sheet surface to provide a 'wood grain' pattern [100]. In contrast to the previously discussed techniques, the purpose of the mokume-gane process was to create a composite material consisting of distinct layers with sharp interfaces. Thus, similarly to

modern scientific laminate processing methods, the motivation for lamination was to create inhomogeneity rather than homogeneity (albeit for aesthetic not technical purposes).

3.1.2 Modern deformation processed laminates

While the use of deformation processing to create laminated materials for research and development increased dramatically after Saito's 1998 paper [50], lamellar composites produced *via* stacking, bonding, and deformation processing were synthesized and studied throughout the latter half of the twentieth century. The majority of the materials produced were either diffusion bonded *via* hot pressing and/or bonded only a single time (without the repeated cutting and stacking steps characteristic of ARB). Thus, conceptually, the pre-ARB scientific laminate processing methods are more tangentially related to ARB than their ancient counterparts. However, the emphasis many of these investigations placed on controlling ductility, strength, and fracture resistance though tailoring the lamellar structure is maintained in modern ARB research.

Notable examples of bi-metallic multilayers synthesized through a single iteration of hot press bonding followed by rolling include the 1979 work of Sherby [101] on ferrous composites and later investigations by both Sherby [102] and

Sahay [46] on UHCS/brass composites. Sahay's work is particularly interesting and prescient: not only do the authors claim 'the first attempt toward the fabrication of nanoscale multilayer composites by cold rolling' but also posit that interfacial effects alter crystallographic texture formation compared to monolithically rolled materials [46]. Synthesis of UHCS/brass multilayers using repeated press-bonding and rolling steps was also investigated and used to explore the fracture behavior of metal laminates [103]. While some investigations replaced press bonding with hot roll bonding, for example the synthesis of Ni-Cu laminates by Choi [104] and Al/304 stainless steel composites by Chawla [105], hot roll bonded multilayers were not as widely studied, presumably due to the relative difficulty in preventing oxidation during hot roll bonding.

The historical precedents for the ARB process, both modern and ancient, are summarized in Table 3.1. While these techniques provided the basis for the present day ARB process, the limited volumes of material and the relatively coarse layers produced speak to the experimental difficulties of fabricating multilayers using these methods. These early processes either required extensive preparation time to prepare a small volume of material *via* hot press bonding or introduced the risk of oxidation during hot roll bonding. The development of the ARB process - dispensing with hot pressing, repeating the stacking and bonding steps, and in many cases using room temperature processing - has en-

Table 3.1: Historical precedents for the modern ARB process (from antiquity to 1998).

Process	Deformation method	Bonding method	Stack and repeat?	Material	Representative Date and Reference
ARB	rolling	roll bonding	yes	Al, IF steel	Saito 1998 [50]
	rolling	roll bonding	yes	UHCS/Fe3%Si	Wadsworth 1986 [92]
Lamination	rolling	roll bonding	no	Al/304 steel	Chawla 1978 [105]
	rolling	roll bonding	no	Ni/Cu	Choi 1990 [104]
	rolling	hot pressing	no	UHCS/Brass	Sahay 1996 [46]
	rolling	hot pressing	no	steel-steel	Sherby 1979 [101]
	rolling	hot pressing	yes	UHCS/Brass	Sherby 1990 [102, 103]
	rolling	hot pressing	yes	Ag/Fe	Yasuna 1997 [37]
Wrought iron prod.	rolling/forging	rolling/forging	yes	Fe/slag	1600-1950 [97]
Monkume-gane prod.	rolling/forging	hot pressing	?	Cu/Ag/Au	1700AD [95, 100]
Pattern welded steel prod.	rolling/forging	rolling/forging	yes	steel/steel	Ancient 600AD [94, 95]
Samurai sword steel prod.	forging	forging	yes	steel/steel	Ancient 700AD [95]

abled vast improvements in both the quantity and quality of metallic multilayers that can be produced.

3.2 ARB procedure

A general description of the ARB process will be given, followed by specific modification that were found advantageous for processing Cu-Nb and Zr-Nb multilayers.

3.2.1 General ARB procedure

The basic ARB process, shown schematically in Figure 3.1 uses an iterative sequence of cleaning, stacking, roll bonding, and cutting to create and refine a lamellar microstructure. Two sheets of the starting materials (for example Cu and Nb) were degreased in an ultrasonic bath of acetone for 10 minutes, and the clean surfaces were wire brushed using a 100 mm (4 inch) diameter rotary wire brush driven using a hand held electric drill. This step both removed native oxide and provided surface roughness to promote cold roll bonding [106]. The sheets were stacked together and cold roll bonded using a 50-60% single pass reduction on a Waterburry Farell rolling mill. This mill, shown in Figure 3.2,

was originally configured for 4-high rolling, but for the purposes of ARB the two primary rolls were removed and the large diameter (16 inch) backing rolls were used as primary rolls. The large roll diameter, direct drive of the rolls, and lack of workpiece lubrication facilitated large single pass rolling reductions. The bonded sheet was then sheared into two pieces, re-cleaned, stacked, and re-bonded to generate a four layer laminate. Through repetition of this procedure, the number of layers was exponentially increased while the final rolled sheet thickness remained nearly constant. Extremely large strains were imparted to the material, with the logarithmic rolling strain given by Equation 3.1, where h_f is the final sheet or layer thickness and h_o is the original sheet or layer thickness.

$$\epsilon = \ln \frac{h_o}{h_f} \tag{3.1}$$

If every ARB step doubles the number of layers, 18 iterations would be required to create a laminate with 262,144 layers (a 15 nm layer thickness, assuming a 4 mm final sheet thickness). The number of layers after each ARB cycle (assuming simple doubling) is simply 2^n, with n being is the number of layers. Considerable setup time, often approaching 60 minutes, is required for cutting and trimming the rolled sheet, adjusting the rolling mill, and degreasing and wirebrushing the material in each ARB cycle. Thus synthesis of a 15 nm layer

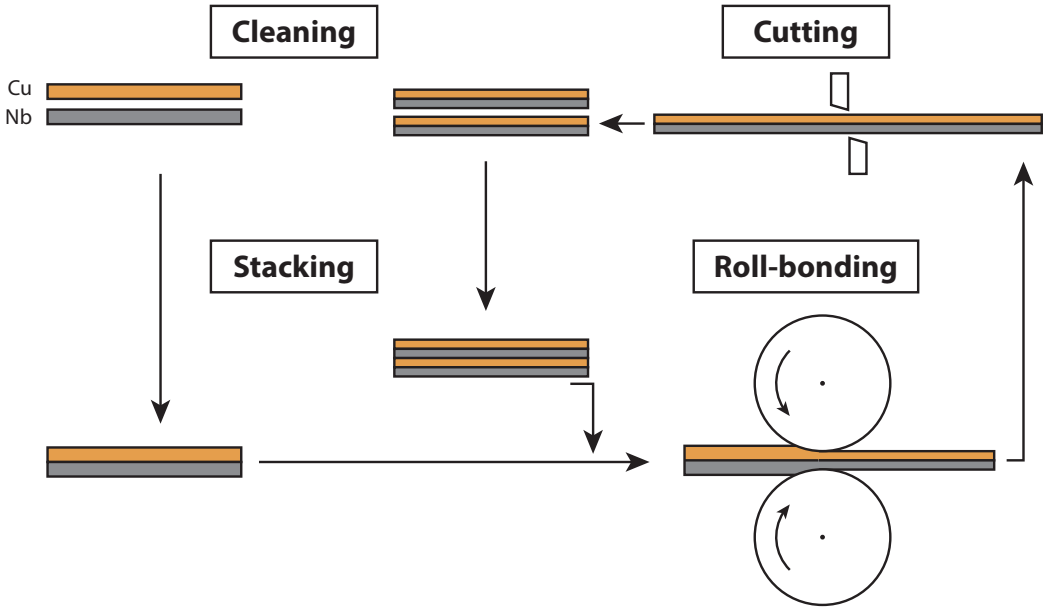

Figure 3.1: Schematic showing steps of the general ARB process.

Figure 3.2: Waterburry Farrel rolling mill at the LANL Sigma Complex used for ARB processing.

thickness nanolaminate using the procedure described above would require approximately 18 hours of processing time.

3.2.2 Multi-stack ARB procedure

The ARB process can be significantly accelerated if, instead of merely doubling the material each ARB step, the material is cut into 3, 4, or 5 pieces and re-stacked. In practice this is accomplished by introducing conventional rolling passes to further thin and elongate the material after each cold roll bonding step. For example, if the starting materials for ARB are 2 mm thick sheets of Cu and Nb, an 8 mm thick stack consisting of four alternating layers of Cu and Nb is roll bonded in the first ARB step. The bonded laminate is now approximately 4 mm thick and is conventionally rolled to a thickness 2 mm using multiple passes. This material can then be sheared onto four pieces and arranged to create another 8 mm stack for the next ARB cycle. Using this method, 262,144 (4^9) layers can be created in only 9 ARB steps ($\sim$9 hours of processing time). The number of layers as a function of ARB processing cycles is given by Equation 3.2, where n is the number of layers, c is the cycle number, s_c is the number of sheets stacked in cycle number c, and c_{last} is the last ARB cycle number.

$$n = \prod_{c=1}^{c_{last}} s_c \tag{3.2}$$

An additional benefit of this procedure is that the number of layers is not restricted to powers of two and therefore specific layer thickness can be achieved by planning out the number of sheets stacked in each ARB step. Further, the progressive decrease in final sheet thickness that would occur during simple doubling if the roll bonding reduction exceeds 50% can be avoided and thus high percent reductions (60%) can be targeted.

3.2.3 Clad ARB procedure

One drawback of the ARB procedure illustrated in Figure 3.1 is that Cu layers and Nb layers are bonded to each other during every ARB bonding step. This means that 1) both Nb and Cu surfaces must be wirebrushed throughout ARB processing, and 2) the Cu-Nb interfaces in the final laminate material have not all experienced the same cumulative rolling strain. The interfaces created in the first ARB cycle have experienced the total cumulative ARB rolling strain while the most recently bonded interfaces have only experienced the rolling strain associated with the last ARB bonding step. This presents a challenge to microstructural characterization as, having characterized the crystallography

of a particular interface, it is not possible to know with certainty how much deformation the adjacent Cu and Nb layers have experienced since they were first joined. The total number of interfaces in the laminate is simply one less than the number of layers. The number of interfaces (n_{int}) in the final laminate that were created at step c is given by Equation 3.3 where c is the ARB cycle number and s_c is the number of sheets stacked at cycle number c.

$$n_{int}^{from\ step\ c} = \begin{cases} (s_c - 1) & c_{last} = 1 \\ (s_c - 1) \prod_{c^*=c+1}^{c_{last}} s_{c^*} & c_{last} > 1 \end{cases} \tag{3.3}$$

The probability (p) that an interface picked at random was created at step number c is given by Equation 3.4.

$$p = \begin{cases} 1 & c_{last} = 1 \\ \dfrac{(s_c - 1) \prod_{c^*=c+1}^{c_{last}} s_{c^*}}{\prod_{c=1}^{c_{last}} s_c - 1} & c_{last} > 1 \end{cases} \tag{3.4}$$

For the simplistic case in which ARB processing is conducted by repeatedly doubling an initial two layer stack of 2 mm Cu and Nb until a 15 nm layer thickness is achieved, Equation 3.4 indicates that the likelihood that an interface selected at random had experienced the cumulative ARB rolling strain of 11.8 (i.e. the interface having been created in the first ARB step) is only 0.5. There

is a probability of 0.25 and 0.13 that this interface experienced a strain of 11.1 and 10.4 respectively. Such a distribution in cumulative strains is undesirable.

In order to avoid these issues, a modified ARB procedure ('clad ARB') was developed in which all Cu-Nb interfaces were created at the first ARB processing step. A 2 mm thick Nb sheet is placed in between two 1 mm thick copper sheets and roll bonded to create a Cu clad sheet of Nb. Throughout subsequent ARB processing, Cu is bonded directly to Cu and the original Cu-Nb ARB interface is simply elongated. This modified ARB process is shown in Figure 3.3 and photomicrographs of the cross-section a Cu-Nb laminate processed using this procedure is shown in Figure 3.4. In addition to eliminating the distribution of Cu-Nb interface cumulative strains, as shown in Figure 3.5, this modified ARB procedure results in exceptionally clean Cu-Nb interfaces. During processing the layers are reduced from 2 mm to 20 nm and the length of the initial Cu-Nb interface is elongated by a factor of 10^5. This means that, even if small oxides or contaminates are present on the initial Cu-Nb interface (for example a hypothetical contamination of 1 oxide particle every 10 μm), by the time the material has been processed to a 20 nm layer thickness the particle spacing would be increased by a factor of 10^5 (a final particle spacing of 1 particle every meter).

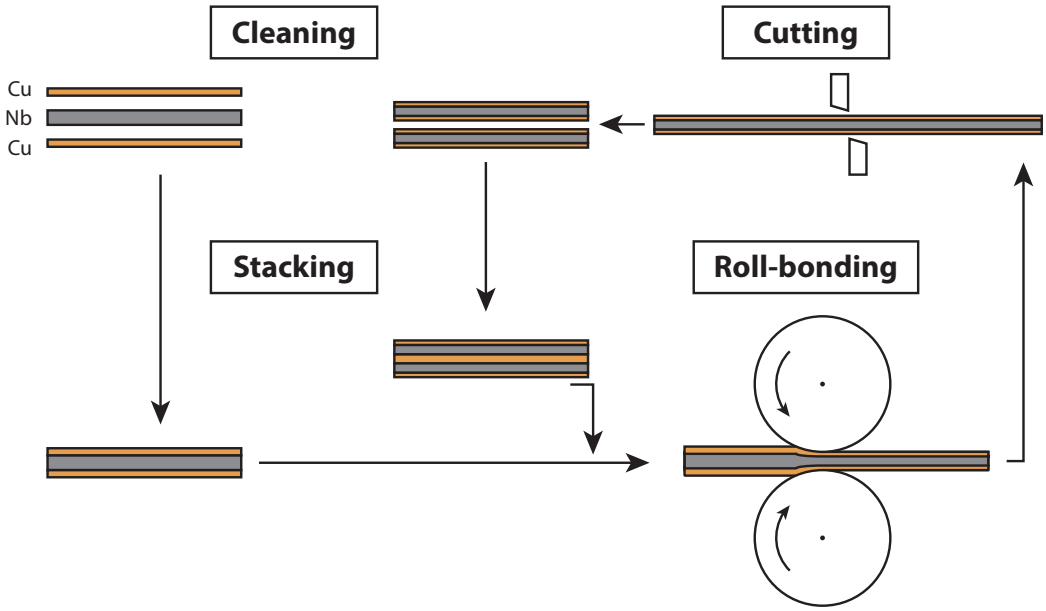

Figure 3.3: Schematic showing steps of the clad ARB process. Reproduced from Reference [91] with permission from Springer.

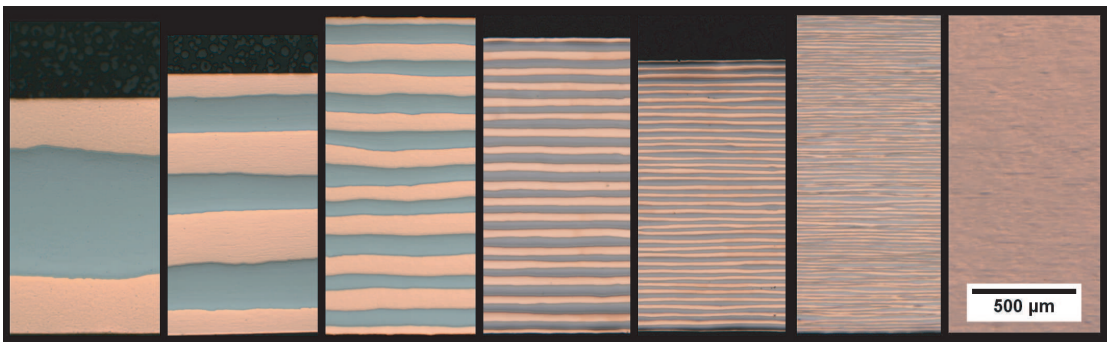

Figure 3.4: Photomicrograph of Cu-Nb sheets at various stages of processing. Reproduced from Reference [91] with permission from Springer.

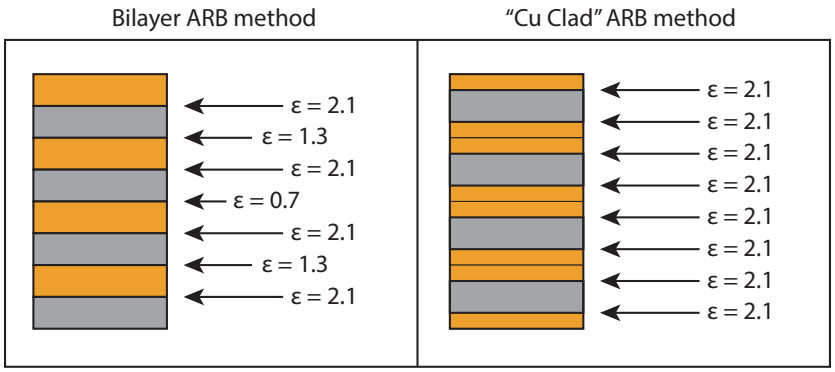

Figure 3.5: Schematic comparing the cumulative strain experienced by the interfaces in bilayer ARB vs Cu clad ARB processed 8 layer laminate.

3.2.4 Specimen synthesis

Using the clad ARB process and stacking multiple sheets per ARB pass, Cu-Nb nanolaminates were synthesized with layer thicknesses of 1800, 500, 245, 140, 65, 30, and 15 nm and a sheet thickness of approximately 4 mm. Table 3.2 gives the number of layers, cumulative rolling reduction, and cumulative rolling strain of each material. All processing was conducted at room temperature and without any annealing steps. A representative rolling schedule, from the synthesis the 30 nm material, is shown in Table 3.3.

Zr-Nb laminates were processed using two different methods: one in which intermediate annealing steps (575 °C for 1 hour) were conducted every other ARB cycle and one in which no annealing steps were conducted. In both cases, the clad ARB process was used and the material was doubled each ARB step. The final thickness of the rolled material ranged from 1.5 to 2 mm and specimens

Table 3.2: Rolling history of ARB Cu-Nb nanolaminate materials.

Layer thickness (nm)	Number of layers	Rolling reduction (%)	Strain, ϵ
1800	2,040	99.91	7.01
500	8,192	99.975	8.29
245	16,384	99.9877	9.01
140	28,224	99.993	9.57
65	65,536	99.9968	10.33
30	163,840	99.9985	11.11
15	248,832	99.9992	11.80

were taken after every ARB cycle. For the material processed using annealing steps after every other ARB cycle (i.e. at 4, 16, 64, etc. layers) specimens were taken both before and after the material was annealed. Thus the samples of Zr-Nb laminates processed with annealing consisted of samples with 4 layers, 4 layers (annealed), 8 layers, 16 layers, 16 layers (annealed), etc. The specimens of Zr-Nb laminates are listed in Tables 3.4 and 3.5.

3.3 Cold roll bonding and surface preparation

Successful ARB synthesis relies first and foremost on the ability to bond separate sheets of material to create a laminate. Thus achieving a strong bond during cold roll bonding is a critical step of the ARB process.

The cold roll bonding (CRB) of metals has been conducted extensively in

Table 3.3: A typical rolling schedule, showing rolling steps during synthesis of the 30 nm Cu-Nb nanolaminate material.

Pass no.	Mill Setting (left, right)	Thickness before	Thickness after	Reduction	Comments
1	50,74	0.320	0.129	60%	4x1=4 lyr
2	30,64	0.129	0.095	26%	
3	27,61	0.095	0.082	14%	
4	30,57	0.328	0.129	61%	
5	30,57	0.129	0.098	24%	
6	30,57	0.098	0.088	10%	
7	30,55	0.088	0.078	11%	
8	30,57	0.312	0.129	59%	4x16=64 lyr
9	30,57	0.129	0.101	22%	
10	30,25	0.101	0.088	13%	
11	35,65	0.352	0.147	58%	4x64=256 lyr
12	30,60	0.294	0.138	53%	2x256=512 lyr
13	25,55	0.138	0.105	24%	
14	25,55	0.105	0.090	14%	
15	25,55	0.090	0.083	8%	
16	30,60	0.332	0.142	57%	4x512=2048 lyr
17	30,60	0.142	0.106	25%	
18	35,55	0.106	0.099	7%	
19	35,55	0.099	0.091	8%	
20	35,63	0.364	0.168	54%	4x2084=8192 lyr
21	35,63	0.168	0.118	30%	
22	35,65	0.118	0.105	11%	
23	30,60	0.105	0.095	10%	
24	30,60	0.095	0.090	5%	
25	25,55	0.090	0.081	10%	
26	30,68	0.324	0.165	49%	4x8192=32768 lyr
27	20,48	0.165	0.120	27%	
28	10,38	0.120	0.096	20%	
29	5,33	0.096	0.085	11%	
30	0,28	0.085	0.073	14%	
31	-5,23	0.073	0.067	8%	
32	12,40	0.335	0.177	47%	5x32768=163840 lyr

Table 3.4: ARB Zr-Nb multilayer materials, processed without any intermediate annealing steps.

Layer thickness (μm)	Number of layers	Rolling reduction (%)	Strain, ϵ
749	2	62.535	0.98
394	4	80.315	1.62
209	8	89.523	2.26
106	16	94.682	2.93
56	32	97.222	3.58
29	64	98.551	4.23
14	128	99.296	4.96
7.5	256	99.623	5.58
3.3	512	99.834	6.40

Table 3.5: ARB Zr-Nb multilayer materials, processed with intermediate annealing steps after every other ARB cycle (at 4, 16, 64, etc. layers). Materials for which samples were removed both prior to and after annealing are indicated with an asterisk (*).

Layer thickness (μm)	Number of layers	Rolling reduction (%)	Strain, ϵ
825	2	58.725	0.88
476*	4	76.188	1.43
234	8	88.253	2.14
127*	16	93.65	2.76
58	32	97.103	3.54
31*	64	98.472	4.18
13	128	99.355	5.04
6.8*	256	99.658	5.68
2.9	512	99.856	6.54
1.5*	1024	99.923	7.17
0.73	2048	99.963	7.91
0.37*	4096	99.981	8.59
0.16	8192	99.992	9.46
0.088	16384	99.9956	10.03

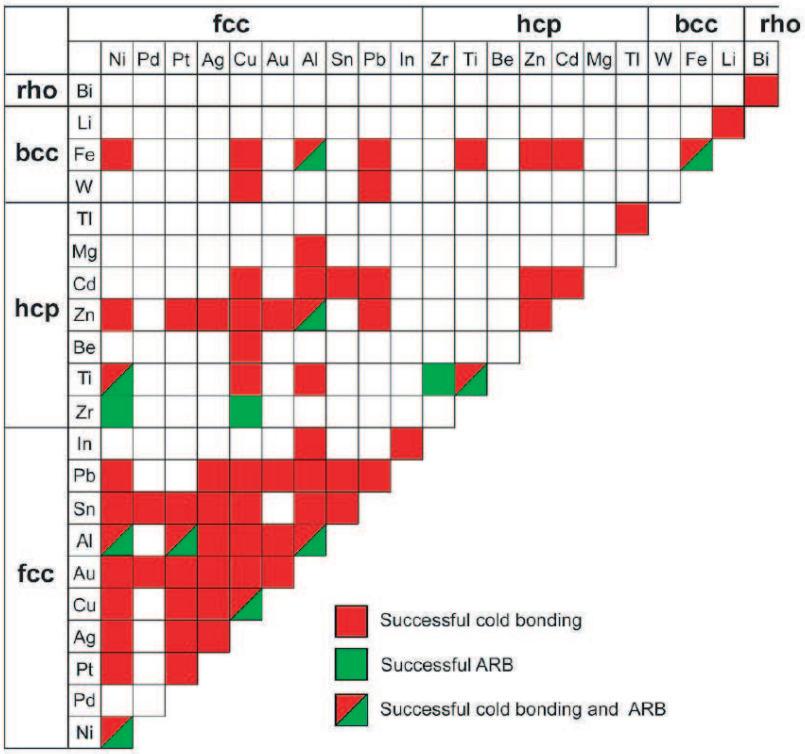

Figure 3.6: A partial list of materials that have been successfully cold roll bonded and/or ARB processed. From Reference [108] and reproduced with permission from Taylor and Francis.

industry to prepare clad materials for application ranging from bi-metallic thermostat metals to composite stainless steel/copper cookware [107, 108]. Figure 3.6 shows a partial list of materials that have been successfully cold roll bonded from Reference [108]. Two main factors influencing the success of CRB and the resultant bond strength are 1) the rolling reduction, and 2) the surface preparation.

3.3.1 Rolling reduction

For a given surface preparation method, bond strength increases with percent rolling reduction. This has been demonstrated for a variety of materials as shown in Figure 3.7 from Reference [108]. For each pair of materials shown in Figure 3.7, a minimum or threshold percent reduction is necessary to achieve bonding. For rolling reductions exceeding this threshold, bond strength increases monotonically with increasing rolling reduction. The influence of rolling reduction on bond strength is attributed to both the pressure generated in the roll gap (forcing the surfaces to be bonded into intimate contact) and elongation of the original interface (breaking up oxide or surface contaminates and exposing virgin material at the interface) [107, 108].

For the purposes of ARB, interfacial bond strength is of limited importance, provided that a bond is achieved, since the strength of the initial bond can be increased by subsequent ARB steps and/or heat treatments. The minimum threshold reduction, however, represents a hard constraint on the ARB process. High threshold reductions for cold roll bonding result in high rolling mill loads and necessitate large roll diameters and/or high workpiece-roll friction.

Figure 3.8 shows the geometry of the roll gap where R is the roll radius, h_o is the initial sheet thickness, and h_f is the final sheet thickness, and Δh is the

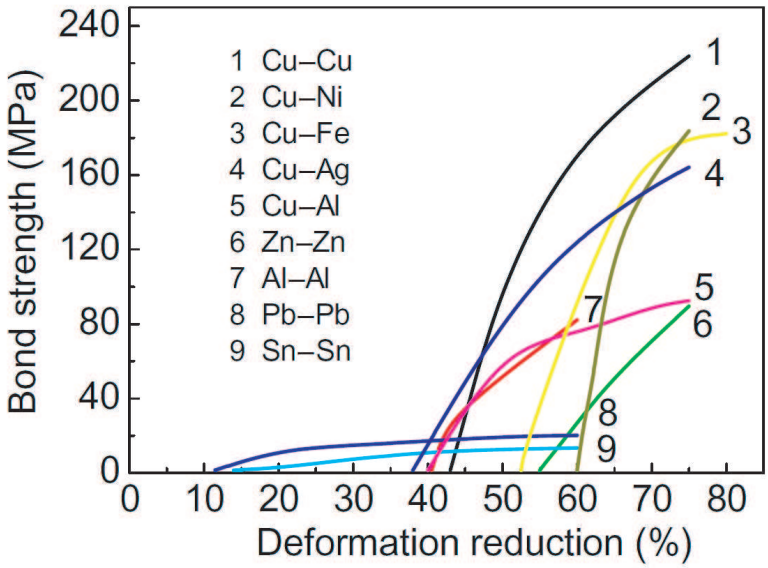

Figure 3.7: Cold roll bond strength as a function of rolling reduction for various materials. From Reference [108] and reproduced with permission from Taylor and Francis.

reduction. The angle α made between the sheet surface plane and the centerline of the rolls is the angle of contact, F is tangential force resulting from friction at the roll entrance, and P_r is the radial force exerted by the rolls on the workpiece. The projected length of the arc of contact (L_p) is given by Equation 3.5 [73].

$$L_p = \left(R(h_o - h_f) - \frac{(h_o - h_f)^2}{4}\right)^{1/2} \approx (R\Delta h)^{1/2} \tag{3.5}$$

The specific roll pressure (p), neglecting frictional effects, is given by Equation 3.6 where P is the rolling load and b is the sheet width (out of plane dimension in Figure 3.8 [73].

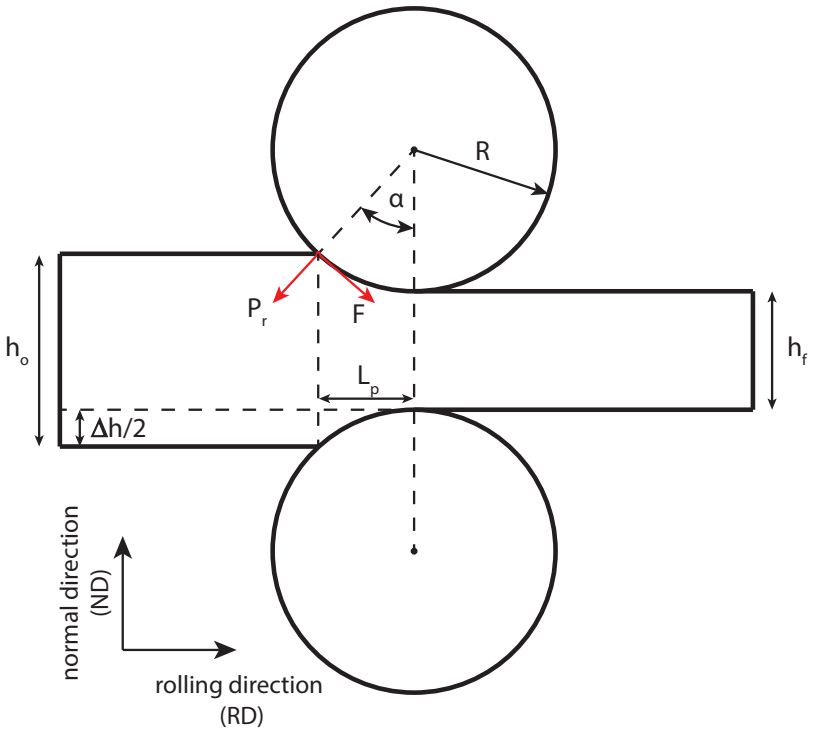

Figure 3.8: Schematic showing roll gap geometry.

$$p = \frac{P}{bL_p} \tag{3.6}$$

From Equations 3.5 and 3.6, an approximation of the rolling load is obtained (Equation 3.7) where σ_o is the plane strain flow stress of the material being rolled. This approximation neglects strain hardening during rolling, as well as the effects of frictional forces in the roll gap.

$$P = \sigma_o b(R\Delta h)^{1/2} \tag{3.7}$$

If friction is included, Equation 3.7 is replaced by Equation 3.8 [109], where μ is the coefficient of friction between the workpiece and the rolls and h_{av} is the average thickness of the material in the roll gap.

$$P = \sigma_o b (R\Delta h)^{1/2} \left(1 + \frac{\mu (R\Delta h)^{1/2}}{2h_{av}}\right) \tag{3.8}$$

For the case of roll bonding two 4 mm thick and 100 mm wide strips of pure Cu to Cu, with a threshold reduction of 43%, a flow stress of 200 MPa, and a coefficient of friction of 0.15, Equation 3.8 indicates that the rolling load on a mill with a roll diameter of 406 mm (16 inches) would be approximately 695,300 N (156,300 pounds force) and scale linearly with sheet thickness and sheet width. For the case of a much stronger material with a flow stress of 1400 MPa and a rolling reduction of 55% (representative of an ARB step conducted on 15 nm Cu-Nb nanolaminate material), the rolling load would exceed 5,800,000 N (1,304,000 pounds force). For this material, the capacity of the Waterburry Farrel rolling mill used for ARB synthesis (1.5 million pounds force) would be reached if ARB was attempted with a sheet width exceeding 115 mm (4.5 inches). Thus ARB synthesis of high flow stress nanolaminates requires a rolling mill with very high load capacities if substantial volumes of material are to be processed at ambient temperature.

An additional effect of the requirement of large threshold rolling reductions is that a rolling mill with suitably large roll diameters and/or high friction roll surfaces must be used. In order for the rolling mill to draw material into the roll gap, the horizontal component of F in Figure 3.8 must exceed the horizontal component of P_r. This condition is shown in Equation 3.9.

$$F \cos \alpha \geq P_r \sin \alpha \tag{3.9}$$

As $F = \mu P_r$ where μ is the coefficient of friction, Equation 3.9 simplifies to Equation 3.10. In order for the rolled sheet to be drawn into the roll gap, $\tan(\alpha)$ must be less than or equal to the coefficient of friction (μ) between the workpiece and the rolls.

$$\mu \geq \tan \alpha \tag{3.10}$$

The maximum reduction that can be obtained for a given roll diameter and friction coefficient is found by expressing $\tan \alpha$ as $\frac{L_p}{R - \frac{\Delta h}{2}}$. Using the approximation for L_p in Equation 3.5 and assuming $R \gg \frac{\Delta h}{2}$, the maximum reduction criterion is given by Equation 3.11 [73].

$$\Delta h_{max} = \mu^2 R \tag{3.11}$$

Assuming $\mu = 0.15$ (cold rolling with non-lubricated rolls [108]) and an initial sheet thickness of 8 mm, the maximum reduction that can be obtained using a rolling mill with 406 mm diameter rolls is 57%. This is approximately the experimentally determined maximum reduction during ARB of Cu-Nb multilayers on the Waterburry Farrel rolling mill with 406 mm diameter rolls. The challenges for ARB synthesis of very thick plates of material are obvious from Equation 3.11: with $\mu = 0.15$, achieving a 57% reduction and a final rolled plate thickness of 25 mm would require a rolling mill with roll diameters of approximately 3 m (9.8 ft). While this suggests the necessity of an extremely large rolling mill, the maximum reduction increases with the square of the coefficient of friction. If μ can be increased to 0.5 (a typical value for hot rolling [73]), a final ARB sheet thickness of 25 mm could be obtained with a roll diameter of only 265 mm (less than the roll diameter of the Waterbury Farrel mill shown in Figure 3.2).

As both the minimum load capacity and roll diameter necessary for ARB scale dramatically with the threshold percent reduction and sheet thickness, large rolling mills are required for the synthesis of even modest sheets of room temperature ARB processed materials. Therefore surface preparation methods that minimize the threshold reduction for bonding are highly desirable.

3.3.2 Surface preparation methods

One strategy that can be employed to minimize the threshold rolling reduction is appropriate surface preparation. Increasing surface roughness and decreasing absorbed surface contaminates enables cold roll bonding to be achieved with lower rolling reductions. Figure 3.9 shows the effect of various surface preparation methods on the threshold reduction and bond strength for Al-Al cold roll bonding. The threshold reduction increases as surface roughness decreases, with polished surfaces failing to bond at almost twice the threshold percent reduction for surfaces roughened by wirebrushing. In addition to roughness, surface cleanliness impacts the threshold reduction for bonding, with the percent reduction increasing after exposure to solvents (as shown in Figure 3.9) or a 15 minute exposure to laboratory atmosphere [108]. This effect is attributed to the formation of surface contaminates or native oxide growth.

The most effective technique for surface preparation prior to cold roll bonding is that of degreasing in acetone followed by wire brushing. This is the method used both for preparation of Cu-Nb and Zr-Nb laminates as well as many other systems reported in literature [108]. The roughness of the wirebrushed surfaces provides asperities that undergo large local deformation during roll bonding, far in excess of the nominal strain induced by rolling. Further,

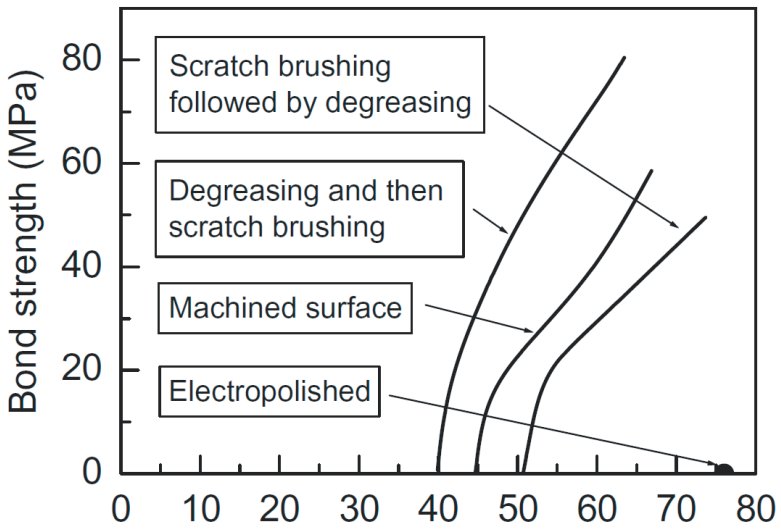

Figure 3.9: Effect of surface preparation on cold roll bonding threshold percent reduction and bond strength for aluminum. From Reference [108] and reproduced with permission from Taylor and Francis.

mechanical interlocking of the asperities may play a role in promoting cold roll bonding, however the relative contributions of these effects has not been thoroughly explored.

3.3.3 Wirebrush generated inclusions

While wirebrushing both removes surface oxides and contaminates and enhances surface roughness, the process can also induce material damage and create loosely adhered burs and debris that can become included in the bonded interface. Initial attempts at ARB synthesis of Cu-Nb nanolaminates were conducted using a 100 mm (4 inch) diameter wire brush with 500 μm diameter bris-

tles and a twisted morphology, shown in Figure 3.10. The wirebrushed surfaces of the Cu and Nb annealed sheets used for the first ARB step showed significant roughness and periodic burrs or clumps of abraded material on the surface (Figure 3.10). While bonding was achieved for all rolling reductions between 51% and 64%, inclusions of either pure Nb or heavily intermixed Nb and Cu were observed in the ARB processed material. These defects, shown in Figure 3.11 caused local distortion of the lamellar structure during rolling and often contained cracks or unbonded regions. EBSD analysis of these defects (Figure 3.12) showed that, even in the case of the pure Nb defects, the grain size of the material within the inclusion was markedly different from that of the surrounding layers, suggesting that these inclusion were material that had been severely plastically deformed by the wirebrush.

Confirmation that the defects shown in Figure 3.11 resulted from the use of an overly aggressive wire brush during surface preparation was obtained by collecting and cross-sectioning fine particulates that were found to accumulate on the workbench where wirebrushing was conducted. These particulates, shown in Figure 3.13, consist of Cu, Nb, or heavily intermixed Cu and Nb and show strong similarities to the inclusions found in the rolled material. While these particles were produced during wirebrushing and ejected from the sheet surface, similar particles were undoubtedly left behind on the sheets as loosely

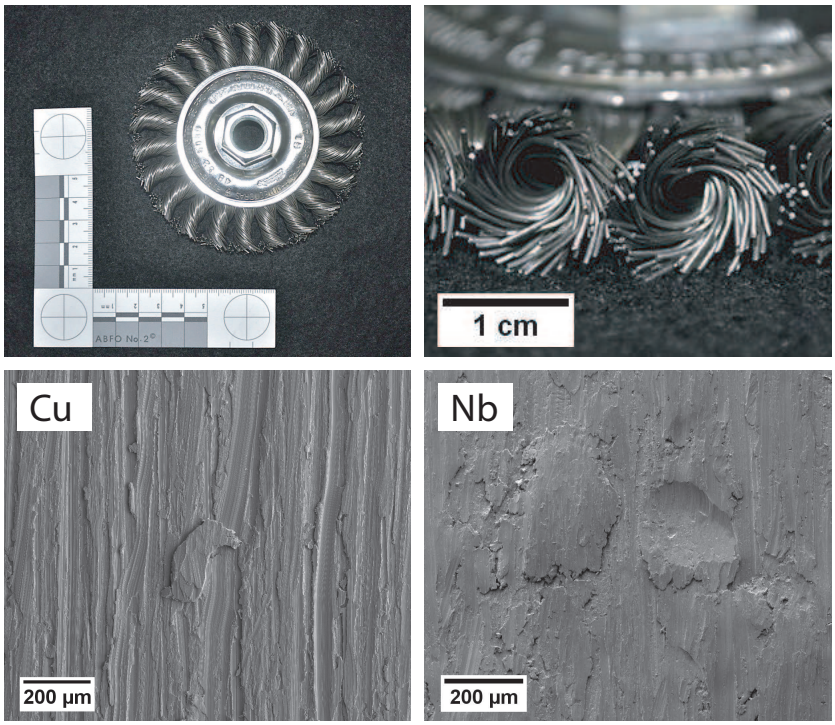

Figure 3.10: Image of the coarse wirebrush and wirebrushed surfaces of Cu and Nb annealed sheets.

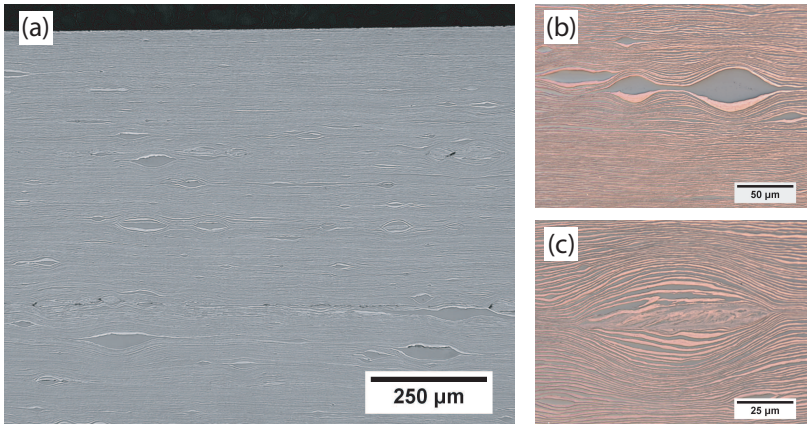

Figure 3.11: Defects observed in a 770 nm Cu-Nb nanolaminate processed using the coarse wirebrush shown in Figure 3.10 during surface preparation.

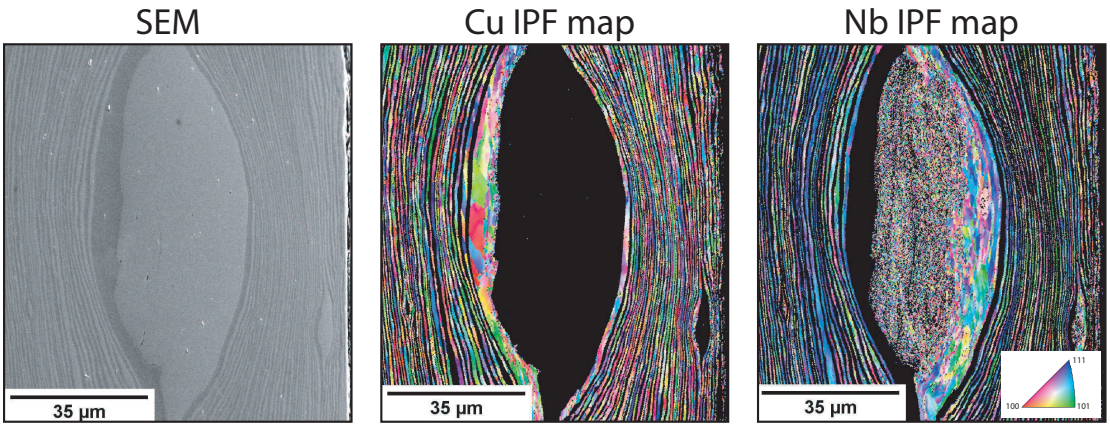

Figure 3.12: EBSD analysis of a Nb inclusion found within an ARB processed 770 nm Cu-Nb nanolaminate.

adhered burrs which became included in the material during subsequent ARB. The presence of many more Nb inclusions than Cu inclusions in the material suggests that the tendency for burr formation is higher in Nb than Cu. This is supported by SEM analysis of the wirebrushed surfaces, shown in Figure 3.10, where it was observed that the wirebrushed Cu appears more cleanly 'cut,' with fewer lumps of abraded material. While pure Nb or Cu defects are formed at coarse layer thickness, intermixed Cu and Nb defects can occur when the layer thickness of the wirebrushed sheets is sufficiently thin that the bristles of the brush penetrate multiple layers.

In order to minimize damage and inclusions resulting from the wirebrushing operation, a less aggressive wirebrush was selected. The wirebrush had straight, radial, bristles with a diameter of 250 μm and is shown in the inset in Figure

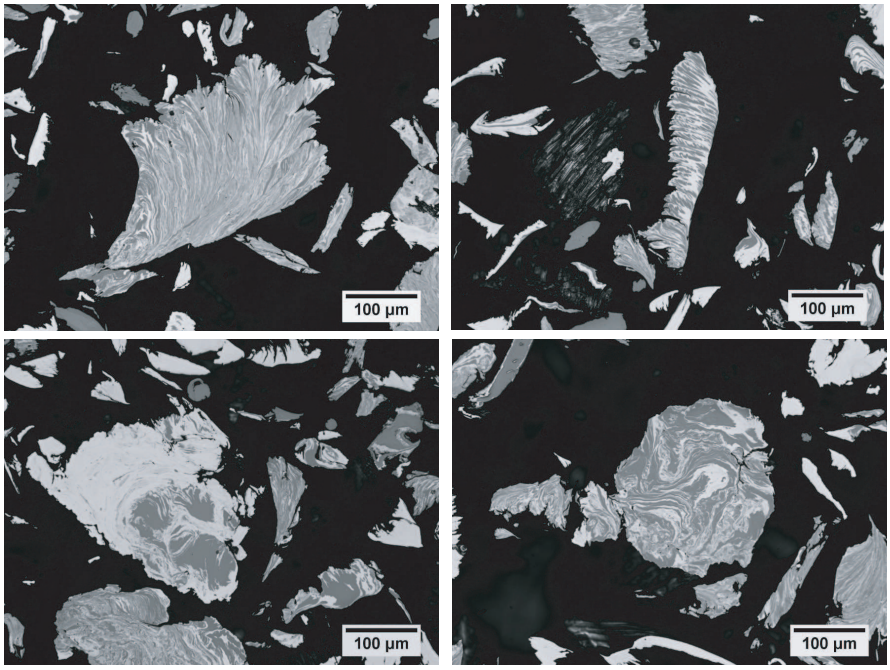

Figure 3.13: Photomicrographs showing cross sectioned particulates formed and ejected from Cu-Nb sheets during wirebrushing.

3.14. The radial bristles are more compliant than twisted bristles, sweeping over the surfaces during wirebrushing as opposed to digging into them. Additionally, implementation of the clad ARB procedure minimized direct wirebrushing of Nb. The formation of pure Nb defects was largely eliminated, as shown in Figure 3.14 which compares the material made using the two different wirebrushes. While some intermixed defects were still observed, the total inclusion content was significantly reduced.

While even less aggressive surface preparation methods were attempted, including wirebrushing with a 75 μm bristle brush, sanding using SiC abrasive

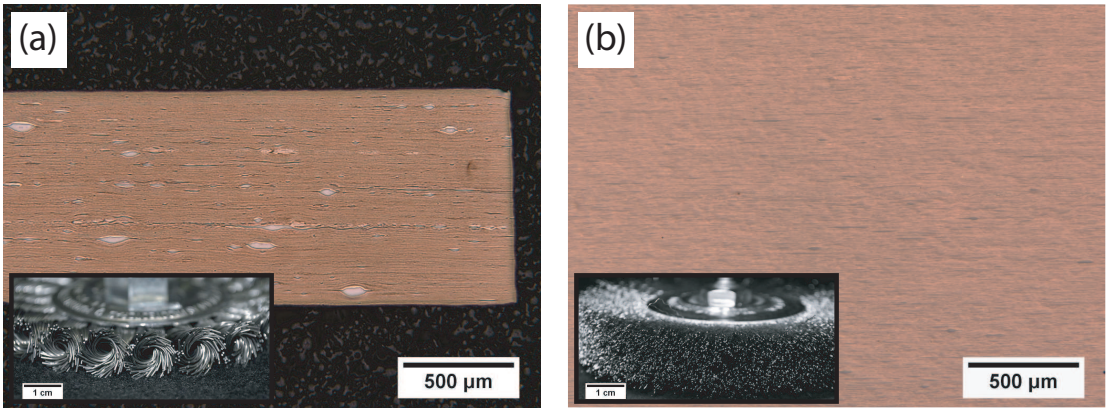

Figure 3.14: Comparison of inclusion content in material processed using a coarse twisted wirebrush (a) and material processed using a fine radial bristle brush (b).

papers, chemical etching, and low pressure grit blasting, the threshold cold roll bonding reductions for materials prepared using these techniques exceed that which could be achieved, and bonding was not obtained. With the constraints of room temperature bonding and targeted threshold reductions of ~50%, less aggressive surface preparation does not appear feasible.

3.4 Plastic instabilities during ARB

While the previous sections detail the equipment, rolling, and surface preparation considerations necessary for the creation of a lamellar composite *via* ARB, successful refinement of the layers to the nanoscale requires that 1) bulk rolled sheet instabilities such as excessive edge cracking, center cracking, and buck-

ling be avoided and 2) layer length scale instabilities such necking, fracture, and shear banding be avoided. While sheet length scale instabilities can be readily detected during processing, they lead to either unacceptable material loss (trimming off edge cracking) or rejection of the entire sheet (center cracking, buckling). The occurrence of layer length scale instabilities may not be evident during processing, yet they can result in loss of layer continuity. While co-deformation and layer refinement is assured during rolling of a continuous lamellar composite, necking or fracture of the layers can allow strain partitioning and inhibit layer refinement.

3.4.1 Sheet length scale instabilities

Edge cracking, buckling, and splitting of cold rolled metals has been explored extensively in the literature and these defects are attributed to stresses arising from inhomogeneous deformation. Inhomogeneous deformation of the workpiece may result from roll deflection under high rolling loads or arise from the natural variation in constraint between the middle and edges of a rolled strip. Figure 3.15 shows typical rolling defects in sheet products, all of which have been observed during ARB processing of nanolaminates.

During rolling, high loads can cause elastic bending of the rolling mill rolls.

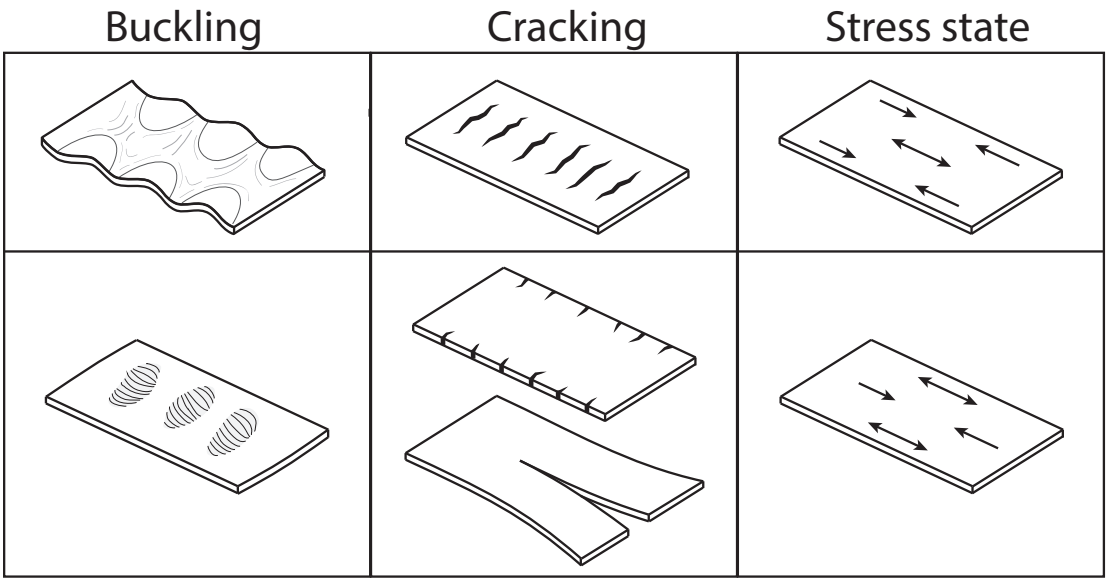

Figure 3.15: Schematic showing several common defects in rolled sheet and strip materials.

If the profile of the rolls are straight (perfectly cylindrical rolls), roll deflection would result in a roll gap wider at the center of the rolls than at the edges (Figure 3.16). This would cause thickness variations in the rolled material, with the rolled sheet being thinner at the edges than in the center. In order to combat this issue, rolling mill rolls are often cambered: the profile of the rolls is slightly 'barrel shaped' to compensate for the roll deflection that occurs under high rolling loads (Figure 3.16). Ideally, the camber of the roll would be selected based on expected loads (a function of material flow strength, width, and percent reduction), yet in practice rolling mills are frequently used for a variety of different materials and rolling conditions. Therefore the rolls may

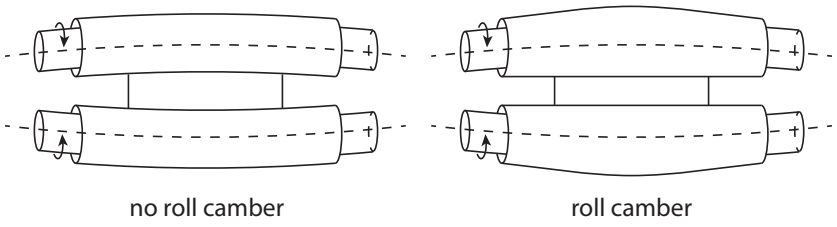

Figure 3.16: Schematic of rolling mill rolls, with and without camber, under high load. Roll deflection is exaggerated.

be over-cambered for some tasks and under-cambered for others. Insufficient camber results in more thinning and elongation at the edges of a rolled sheet than in the center, while over-camber results in the reverse. The inhomogeneous deformation induced by these conditions produces a rolled sheet with edges that are in in-plane compression and the center in in-plane tension along the rolling direction (under-cambered rolls) or edges that are in in-plane tension and the center in in-plane compression (over-cambered rolls). These different residual stress states may manifest themselves through buckling in regions of in-plane compression or cracking in regions of in-plane tension (as shown in Figure 3.15).

While improper roll camber is responsible for many of the commonly observed rolling defects, edge cracking may also be driven by the lack of confinement at the edges of a rolled sheet. If the edges of the sheet are slightly radiused (either deliberately or as a natural result of lateral spread and workpiece/roll

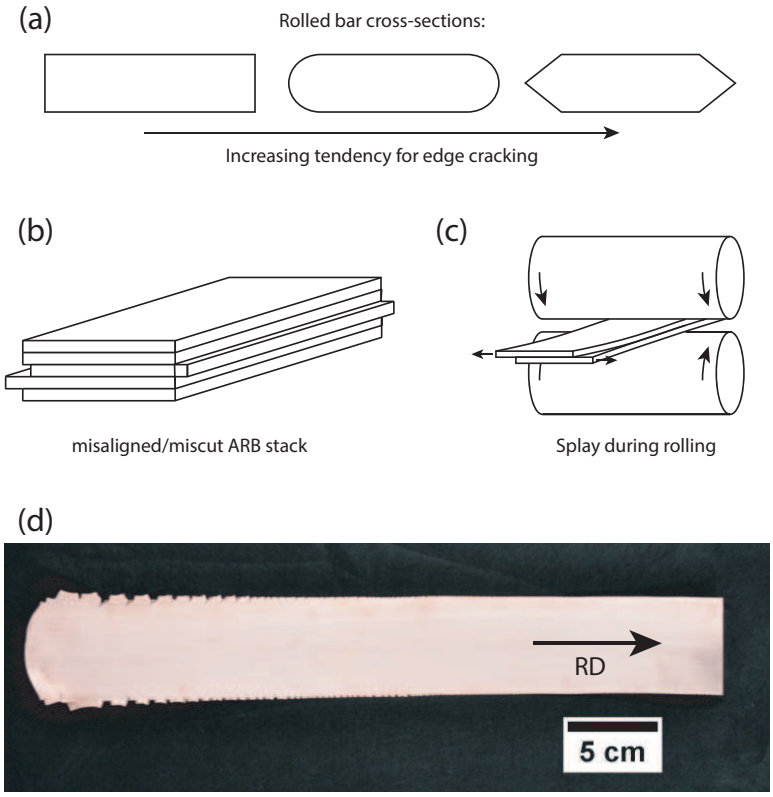

Figure 3.17: (a) Profile of rolled bars showing increasing tendency for edge cracking, adapted from [110]. (b) Overhanging sheet edges due to misalignment/miscutting during ARB, and (c) splay of a bilayer stack during ARB leads to increasing misalignment and edge cracking in the tail of the rolled strip shown in (d)

friction during deformation) edge cracking is exacerbated compared to rolling of a strip with square edges (Figure 3.17(a)) [110]. The sheet edges must elongate in the rolling direction to match the deformation of the rolled sheet, but unlike the bulk of the rolled sheet, these edges are not in contact with the rolls and do not experience the hydrostatic pressure induced by friction during rolling. The tensile stress associated with the elongation of the unconfined edges can induce cracking even in relatively ductile materials when the rolling reduction, and hence elongation, is high. This type of edge cracking is a particularly common problem in ARB processing. When multiple sheets of material are stacked together for cold roll bonding using a large rolling reduction, any misalignment or mismatch in sheet width produces overhanging and unsupported 'fins' that elongate during rolling (Figure 3.17(b)). Cracks can initiate at these edges and propagate inward. A similar result occurs if the stacked sheets 'splay' and shift relative to each other during infeed (Figure 3.17(c)). This splay results in increased edge cracking at the tail of the rolled strip/sheet (Figure 3.17(d)). In order to aid alignment and prevent splay, hardened steel guides were bolted to the rolling mill table, shown in Figure 3.18. This was found to greatly reduce edge cracking and associated material losses.

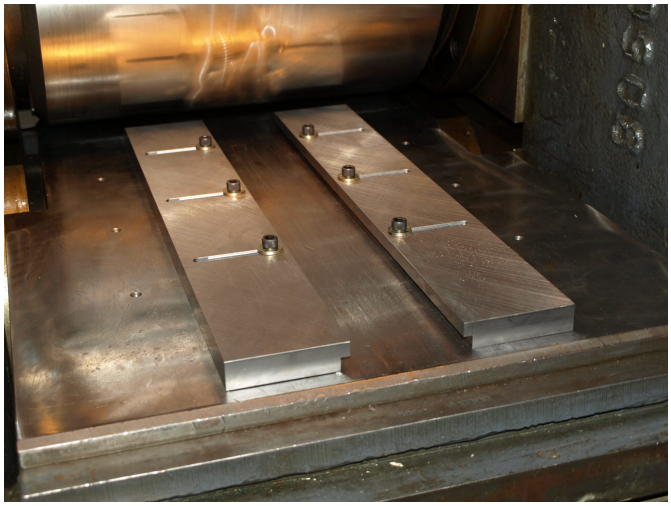

Figure 3.18: Hardened steel guides used to aid alignment of the ARB stack and reduce edge cracking.

3.4.2 Layer length scale instabilities

Plastic instabilities such as shear band formation and necking of individual layers during rolling has been reported in a wide variety of composite systems including Al-steel [55], Al-Ti [56, 57], Al-Cu [58], Al-Zn [59], Cu-Zr [60], Mg-Ti [61], Ni-Cu [62], Ni-Al [63], Zr-Ti, Zr-Ni, and Zr-Al [64]. While Cu-Nb laminates are remarkably stable and resistant to the loss of layer continuity during room temperature ARB, the stability of this system appears to be the exception rather than the rule. Most attempts to synthesize bi-metallic composites *via* ARB have encountered difficulties in maintaining layer co-deformation.

Analysis of layer stability during rolling of laminated bimetallic materials has been conducted by a variety of investigators [55, 111–116]. Prior to the

widespread use of ARB, rolling of clad materials and the pack-rolling of foils motivated these studies. The approaches taken in these studies vary, with authors conducting bifurcation analyses [113, 114], numerical studies [55, 116], and Considère type necking analyses [115]. Most studies have approximated rolling as a plane strain deformation and have found that, in order to satisfy the composite yield criteria, the soft phase is subject to in-plane compression and the hard phase is subject to in-plane tension during rolling [111]. This in-plane tension can drive necking or shear instabilities in the stronger layers.

Both theoretical and experimental studies confirm that necking or fracture occurs in the stronger layer and that both the mismatch in flow stress [55, 115, 116] and the strain hardening of the stronger layers [55, 115] influence co-deformation. Effects of the thickness ratio of the constituents as well as the rolling mill roll gap geometry have also been reported [117, 118]. Yazar [55] predicted that necking can be inhibited by keeping the flow stress mismatch between perfectly plastic constituents to below 2:1, and that with strain hardening this limit may be raised to 5:1. Empirically, a 3:1 flow stress mismatch has been taken as the limit for co-deformation of metal-metal composites [119]. While the role of strain hardening rate has not been thoroughly explored experimentally, studies indicate that high work hardening rates in the hard layer promote flow stability [55, 115, 116]. While strain hardening of the hard layers

may promote stability at low strain levels, unless it is accompanied by commensurate strain hardening of the softer layers it may be expected to actually increase the tendency for localization by increasing the instantaneous flow stress mismatch between the two materials.

Loss of layer continuity due to flow stress mismatch was observed in Zr-Nb laminates that were ARB processed at room temperature without annealing steps. Figure 3.19 shows photomicrographs of the rolled laminates. While layer continuity is preserved in Zr-Nb laminates with layer thicknesses above 100 μm (Figure 3.19(a-d)), further ARB processing induces severe shear localization (Figure 3.19(e-g)). The Zr layers appear cut along very narrow shear bands and the extensive local deformation along these bands is evident in a high magnification image of the 256 layer (7.5 μm) laminate (Figure 3.19(h)).

In an attempt to inhibit shear localization and loss of layer continuity, a second ARB synthesis of Zr-Nb laminates was attempted and periodic annealing steps were introduced after every second ARB cycle (as discussed in Section 3.2.4). The aim of the annealing steps was to both reduce the flow stress mismatch and restore work hardening capacity by reducing the stored dislocation content in the Zr phase. The annealing steps were expected to influence the mechanical properties of Zr more strongly than Nb due to its lower melting point and recrystallization temperature.

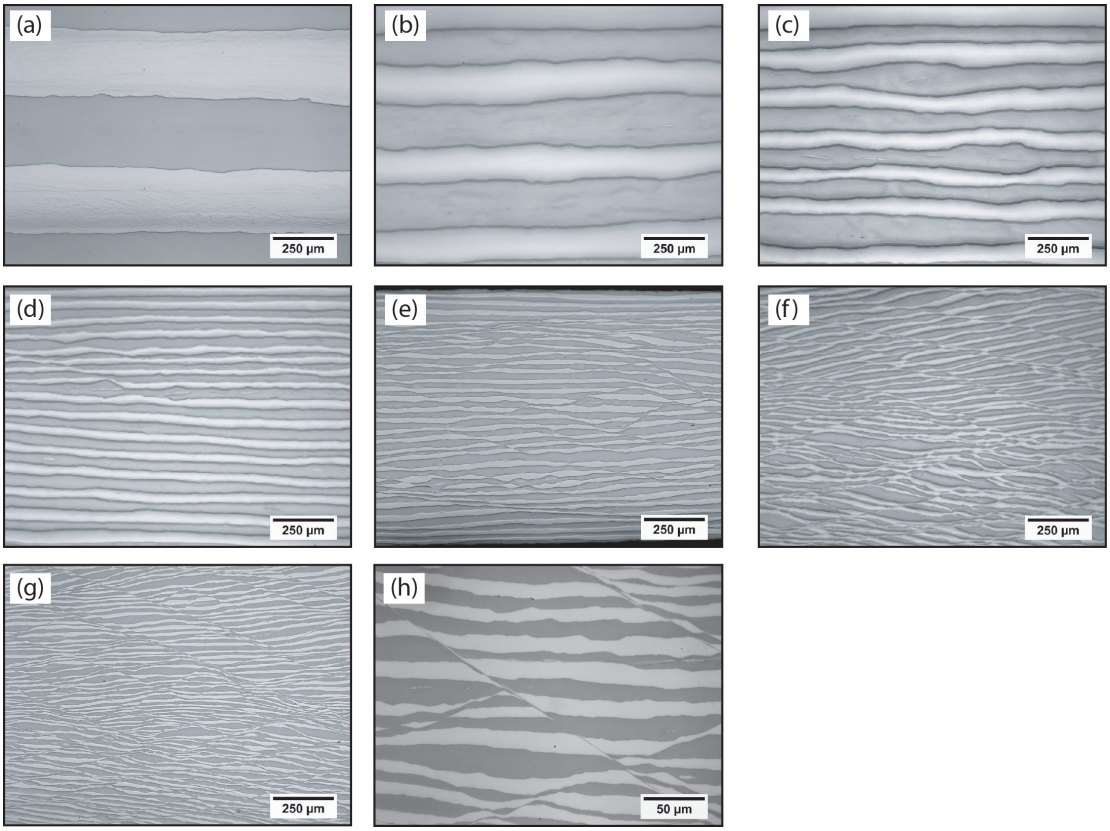

Figure 3.19: Cross section photomicrographs of ARB Zr-Nb laminates processed without intermediate annealing steps. From (a) to (g): 4, 8, 16, 32, 64, 128, and 256 layer material (nominal layer thickness given in Table 3.4). A high magnification image of the shear localization in the 256 layer sample is shown in (h).

Figure 3.20(a-g) shows photomicrographs of these laminates where it can be seen that shear localization is suppressed and layer continuity is maintained. Unlike the material shown in Figure 3.19, the actual layer thickness is well represented by the nominal layer thickness (Table 3.5) as all of the imposed rolling strain is accommodated by thinning of the layers, rather than shear along narrow inclined shear bands. Continued ARB processing using intermediate an-

nealing steps resulted in the successful synthesis of Zr-Nb nanolaminate material with a nominal layer thickness of 88 nm, shown in Figure 3.20(h) [120]. These results demonstrate that periodic annealing steps can be advantageous for reducing the tendency for shear localization and preventing loss of layer continuity.

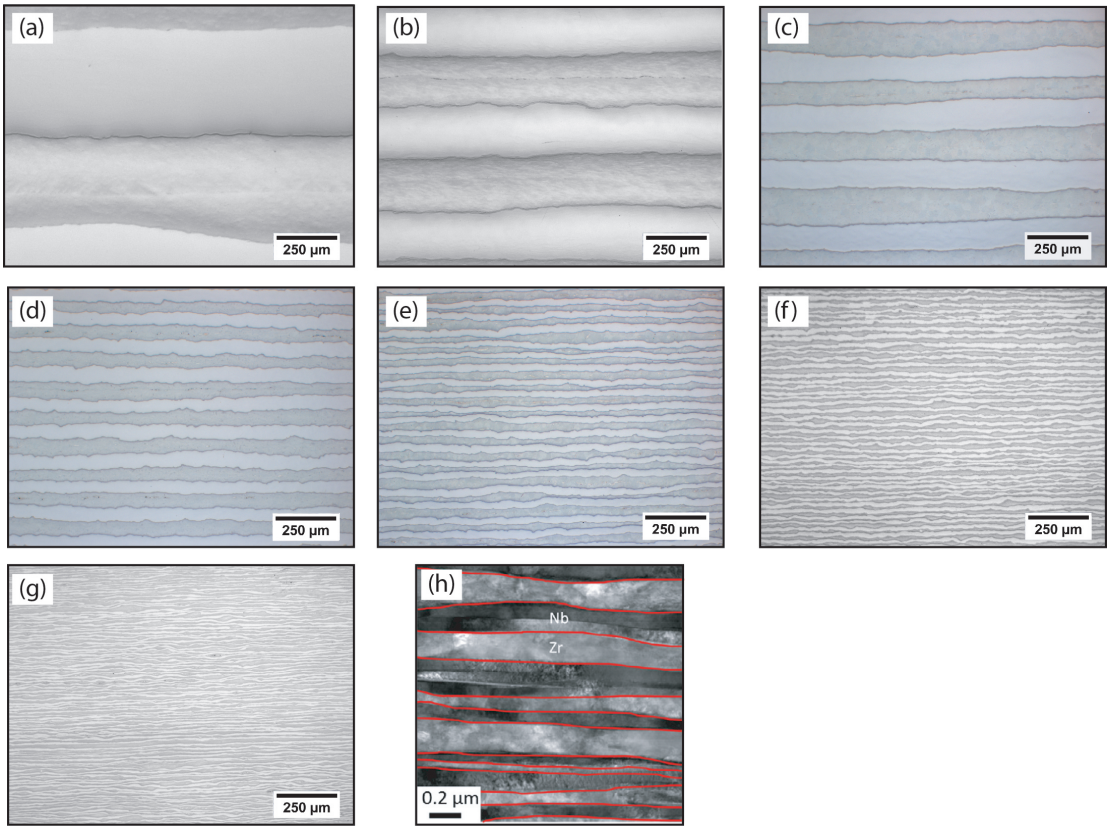

Figure 3.20: Cross section photomicrographs of ARB Zr-Nb laminates processed with intermediate annealing steps. From (a) to (g): 4, 8, 16, 32, 64, 128, and 256 layer material (nominal layer thickness given in Table 3.5). A TEM micrograph (h) shows the continuous layers in the final 88 nm layer thickness nanolaminate. (h) is reproduced from Reference [120] with permission from Elsevier.

3.5 Summary and recommendations for ARB process improvement

While prior laminate processing techniques share conceptual similarities with the ARB process, the ARB method has greatly facilitated the synthesis of multilayer and nanolaminate materials. Laminates containing hundreds of thousands of individual layers and bulk sheet dimensions can be routinely synthesized, even in a research and development environment. New multistack and clad ARB processing routes have increased efficiency and improved material quality, and the surface preparation methods and rolling reductions necessary to achieve consistent cold roll bonding have been explored. While sheet and layer length scale plastic instabilities can lead to material losses and inhibit successful layer refinement, improved rolling mill control and intermediate annealing steps to reduce the constituent phase flow stress mismatch provide promising means of preventing these instabilities.

The prospects for truly industrial scale ARB processing remain daunting, with the greatest obstacles arising from the high flow stresses of nanolaminate metals and the large rolling reductions necessary to achieve cold roll bonding. The unavoidable conclusion from the discussion of threshold reduction and surface preparation methods, rolling mill loads, and the maximum reduction crite-

rion is that industrial scale ARB would require processing at elevated temperatures. No other single modification to the ARB process would afford as many benefits as raising the process temperature.

Among the numerous advantages of hot or warm ARB processing are:

1. Hot ARB would provide dramatic reductions in rolling loads. This reduction stems from both the decreased flow stress of nanolaminate materials at elevated temperatures [77] as well as the lower threshold rolling reductions necessary for hot roll bonding compared to cold roll bonding [121].

2. The minimum rolling mill roll diameter dictated by the maximum reduction criterion (Equation 3.11) would be decreased tremendously. This would result in part due to the smaller threshold reductions necessary for hot roll bonding but would be driven primarily by the increase in the coefficient of friction with increased rolling temperature.

3. Less aggressive surface preparation methods could be used in place of wirebrushing. The decreased emphasis on surface roughness afforded by the substantial decrease in threshold rolling reduction moving from cold roll bonding to hot roll bonding may eliminate the need for wire brushing, further reducing inclusion content and damage.

4. Sheet length scale instabilities driven by roll deflection or improper roll

camber would be reduced. With a decreasing rolling load, roll deflection would be less severe. Further, a decrease in the required roll diameter may allow the use of 4-high or planetary rolling mills which minimize roll deflection through the use of backing rolls.

5. The ability to adjust the rolling temperature may provide means to combat layer length scale instabilities such as shear banding and necking. Stability may be improved by dynamic recovery and the associated increase in work hardening rate or, particularly for laminates composed of materials with different crystal structures, the varying temperature sensitivities of the material flow stresses [122]. Proper deformation temperature selection may enable ARB processing of material combinations that are difficult or impossible to process at room temperature.

While high temperature ARB processing may induce undesirable diffusion, phase transformations, or intermetallic growth in some systems, it would appear well suited for processing laminates with immiscible or low solid solubility phases such as Cu-Nb and Zr-Nb. Further, it may allow materials with inherently low room temperature ductility (e.g. magnesium alloys) to be successfully processed using ARB. While presenting a new set of challenges, including those related to preventing oxidation during bonding and rolling, elevated tempera-

ture ARB processing would remove a host of limitations encountered in room temperature ARB processing. It is therefore recommended that elevated temperature ARB processing be explored for the efficient industrial production of ARB laminates.

Chapter 4

Material Properties and Anisotropy

In this chapter, microstructural characterization and mechanical property evaluations of ARB processed Cu-Nb nanolaminates will be presented. The evolution of microstructure and crystallographic texture with layer thickness will be discussed and related to both the strength and anisotropy of the laminates. Of particular importance is the divergence of the layer parallel tensile strength and layer parallel shear strength as the layer thickness is refined below 250 nm. This anisotropy is responsible for kink band formation, a phenomenon analyzed in Chapter 5.

4.1 Microstructural evolution during ARB

Significant microstructural changes occur throughout the ARB process, with the grain size and crystallographic texture changing as the layer size is reduced. The 30 nm Cu-Nb material, for example, contains Nb grains that are four orders of magnitude smaller than those in the initial Nb plate, with the grain shape having evolved from an equiaxed morphology to one consisting of extremely high aspect ratio grains (RD:ND grain aspect ratios on the order of 80:1) [123]. The crystallographic texture of the annealed starting materials is transformed into a strong deformation texture that, at small length scales, differs from that expected in rolled monolithic Cu or Nb [18, 124]. Finally, a predominant interface orientation relationship between Cu and Nb is observed in the nanoscale laminates [18, 125, 126].

Characterization of the microstructure across the tremendous range of length scales and deformation states (cumulative strains ranging from 0 to $\sim$12) encountered in ARB processed materials has required the use of a suite of advanced characterization tools. Studies detailing the structure of these nanolaminates have employed EBSD [54, 123, 125, 127, 128], precession electron diffraction (PED) [125, 126, 129], SEM [130], scanning transmission electron microscopy (STEM) [7], transmission electron microscopy (TEM) [9, 54, 131], and neu-

tron diffraction characterization techniques [124, 125] and have been carried out by a variety of investigators. The vast majority of these studies (References [7, 9, 123–125, 125, 125, 127, 128, 130, 131]) were conducted on nanolaminates synthesized at Los Alamos National Laboratory using the high purity materials and the methods described in Chapter 3. In order to discuss the microstructural changes that occur during ARB, characterization data from literature sources [123, 126, 129, 132], experimental EBSD investigations into grain structure evolution in coarse multilayer samples (with layer thickness $>20\,\mu$m), and characterization of the final samples used for mechanical testing (with layer thicknesses ranging from 1800 to 15 nm) will be presented.

The microstructures of the starting materials for ARB processing are shown in Figure 4.1, where inverse pole figure (IPF) maps, grain boundary maps, and crystallographic texture pole figures are presented. IPF maps are generated from EBSD analysis, where each point on the map is colored according to the crystallographic direction aligned with a particular sample axis (in this case the ND of the rolled sheet). The crystallographic directions corresponding to the IPF colors are indicated in the key shown on the lower left hand corner of each map. In addition to highlighting the grain structure, IPF colors provide some information about the crystallographic texture; for example the Nb IPF map shown in Figure 4.1 indicates that most grains are oriented such that a $[111]$ direction

lies nearly parallel to the ND axis of the sheet, a result confirmed by the pole figure representations of crystallographic texture. A pole figure (PF) shows the distribution of crystallographic directions projected onto the sample coordinates (with axes RD, TD, and ND for rolled materials, as indicated above the PF color key in Figure 4.1). The intensity of the resulting distribution is colored according 'multiples of random,' and quantifies how 'peaked' or 'sharp' the distribution in crystallographic orientations is compared to randomly oriented grains. All pole figures presented are equal area projections, a projection conceptually similar to the more common stereographic projection, and discussed in detail in Reference [81].

Figure 4.1 indicates that the cold rolling and annealing procedures described in Chapter 2 produce materials with fully recrystallized equiaxed grain structures and typical annealing textures [81]. The Cu has a high density of annealing twins and an average grain size of 17 μm (as calculated from EBSD data, excluding $\Sigma 3$ twin boundaries). The Nb has a much larger grain size of approximately 200 μm and a strong fiber crystallographic texture [81]. It should be noted that gathering statistically significant grain size measurements on such a coarse microstructure is challenging, with only 117 grains present in the large EBSD scan in Figure 4.1. Nevertheless, Figure 4.1 shows that the starting materials possess vastly different initial grain sizes and crystallographic textures.

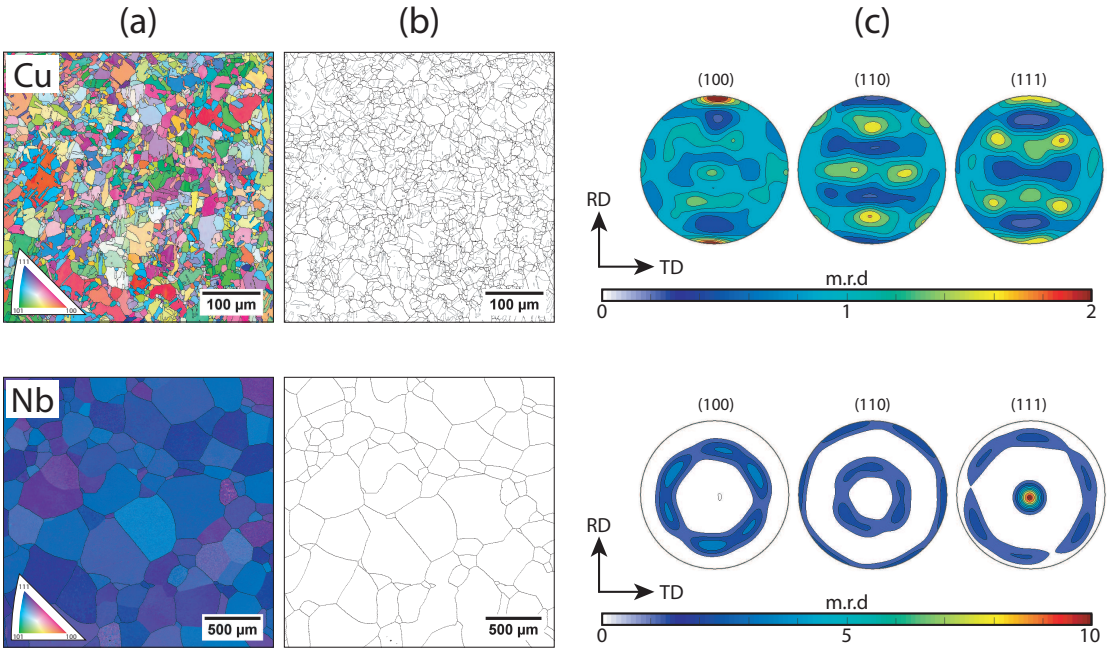

Figure 4.1: The microstructure and texture of the annealed Cu and Nb material used for ARB. (a) shows IPF maps colored with respect to the ND while grain boundary maps where twin boundaries in the Cu are shown in gray (b). Pole figures showing typical FCC and BCC annealing textures for Cu and Nb are presented in (c).

The evolution of the microstructure and texture throughout the initial ARB processing steps (during refinement of the layer thickness from 1 mm to 20 μm) is shown in Figures 4.2, 4.3, and 4.4. EBSD IPF maps of Cu and Nb layers (Figure 4.2) show that at these layer thicknesses, both the Cu and Nb layers are polycrystalline, with most grains unassociated with a Cu-Nb interface. The breakdown of the initial coarse Nb structure is seen in the 500 μm Nb IPF map, where subgrain formation has begun to occur after the rolling strain of 0.69 (as evidenced by the mottled colors within the large Nb grains in Figure 4.2).

The unique grain map (UGM) (a map where the colors have no crystallographic significance, but are used to denote individual grains separated by boundaries with a $>5^\circ$ misorientation) shows only small regions that are significantly misoriented from the original grains. The copper layers in the 500 μm material are spanned by hundreds of individual grains, and have an average grain size of 2.8 μm (computed from a larger scan area than the one shown in Figure 4.2). The IPF maps for the 165 μm Cu-Nb multilayer show that the influence of the large initial grain size of the Nb persists at a rolling strain of 1.8, with the microstructure consisting of clusters of grains and subgrains with similar orientations. Yet, in terms of a reduction in grain size, the 165 μm UGM shows that the Nb now contains many grains misoriented by $>5^\circ$ and that the initially coarse grain structure has been largely refined. Material removed after ARB processing to a 40 μm layer thickness shows Cu and Nb grains that are comparable in size: the average Nb grain diameter is 0.83 μm vs 0.76 μm for Cu.

The crystallographic texture evolution in Cu-Nb multilayers with layer thicknesses ranging from 500 μm to 20 μm is shown in Figure 4.3 and 4.4. These pole figures were calculated from EBSD data collected over large areas, typically $\sim$1 mm^2. A conventional rolled Cu texture forms early on during ARB processing (Figure 4.3), with the weak Cu annealing texture having been transformed into a typical FCC rolling texture [81] at a layer thickness of 500 μm.

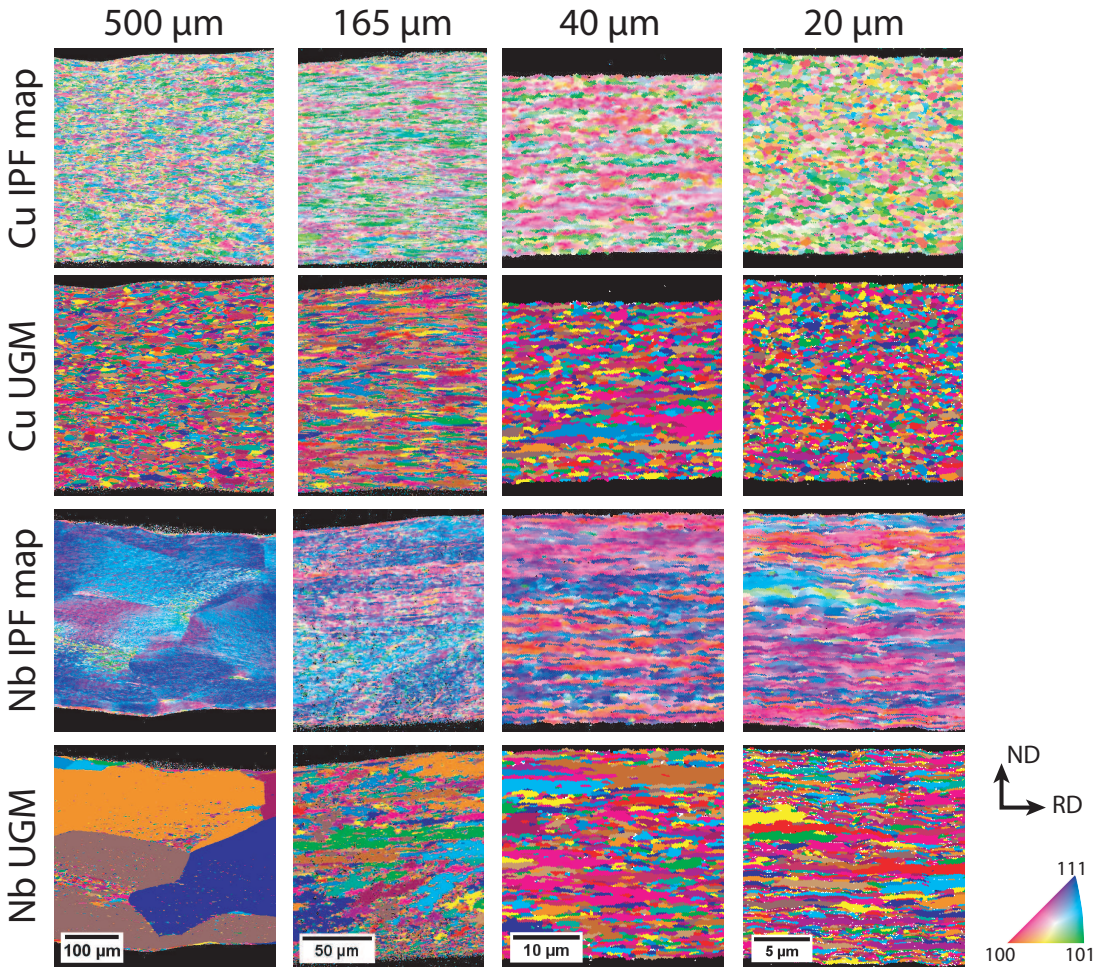

Figure 4.2: EBSD inverse pole figure (IPF) maps and unique grain maps (UGM) for Cu and Nb layers in 500, 165, 40, and 20 μm layer thickness specimens removed during ARB processing (note the different scales). IPF colors are applied with respect to the ND, EBSD scans were conducted on the RD-ND plane. While IPF maps show crystallographic orientation and subgrain formation, UGM (calculated with a grain tolerance of 5°) gives information on grain aspect ratio and size.

This rolling texture persists throughout processing from 500 μm to 20 μm, although some fluctuation in intensity and texture character is evident in Figure 4.3 and is attributed to periodic dynamic recrystallization during rolling. Evidence for this recrystallization is seen in Figure 4.2 where the elongated Cu grains at a 165 μm layer thickness have transformed into the more equiaxed grains seen in the 40 μm and 20 μm layer thickness materials. In contrast to the Cu phase, the initial annealed fiber Nb texture persists to high rolling strains, with a typical BCC rolling texture [81] not emerging until processing to a 40 μm layer thickness (a rolling strain of 3.2).

The microstructure of the Cu-Nb nanolaminate materials with layer thicknesses of 1800, 500, 245, 140, 65, and 30 nm has been characterized using a combination of EBSD, TEM, and PED. These layer thicknesses correspond to the materials used for mechanical testing, as will be discussed in Sections 4.2 - 4.5 As the layer thickness is refined from 1800 nm to 140 nm, the Cu layer grain structure transitions from one in which multiple grains (2-3) span the layers to one in which individual grains span the layers (Figure 4.5). This transition in grain structure for the Cu layers occurs at 245 nm, with the Cu layers spanned by relatively low aspect ratio grains (as shown in Figure 4.5). While the layers of both phases remain polycrystalline in-plane, the aspect ratio of the Cu grains increases as the layer thickness falls below 245 nm.

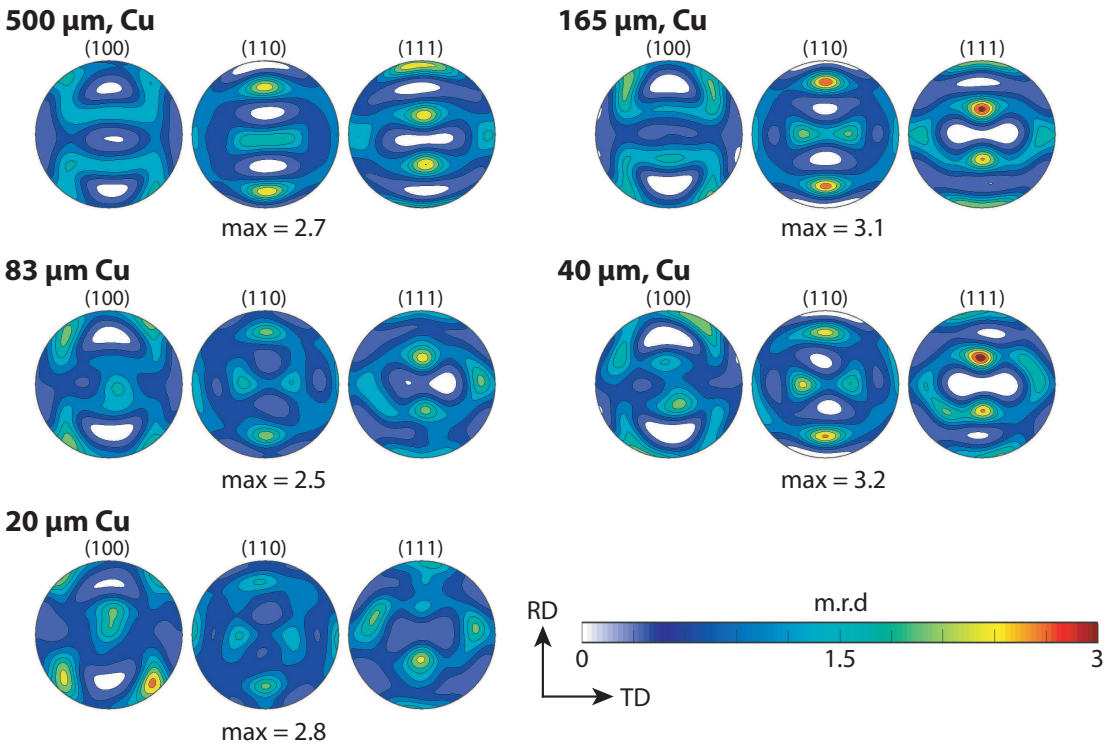

Figure 4.3: Pole figures for the Cu phase in ARB Cu-Nb multilayers with layer thicknesses ranging from 500 μm to 20 μm obtained from EBSD. All PFs shown are equal area projections.

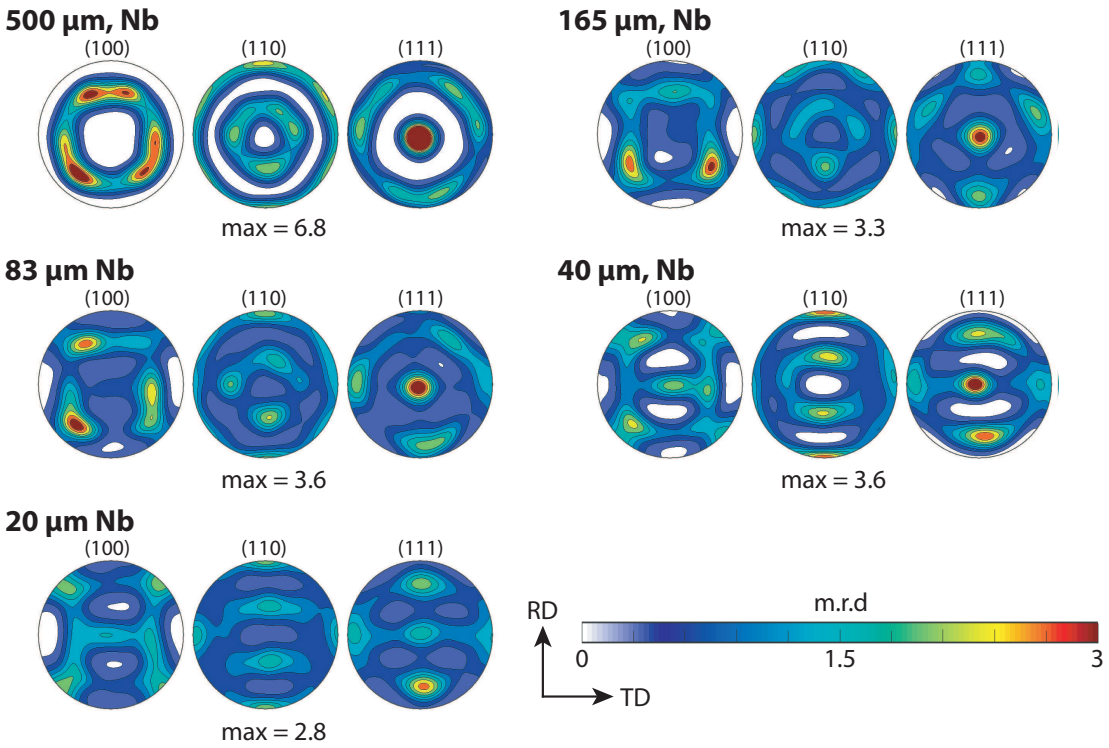

Figure 4.4: Pole figures for the Nb phase in ARB Cu-Nb multilayers with layer thicknesses ranging from 500 μm to 20 μm obtained from EBSD. All PFs shown are equal area projections.

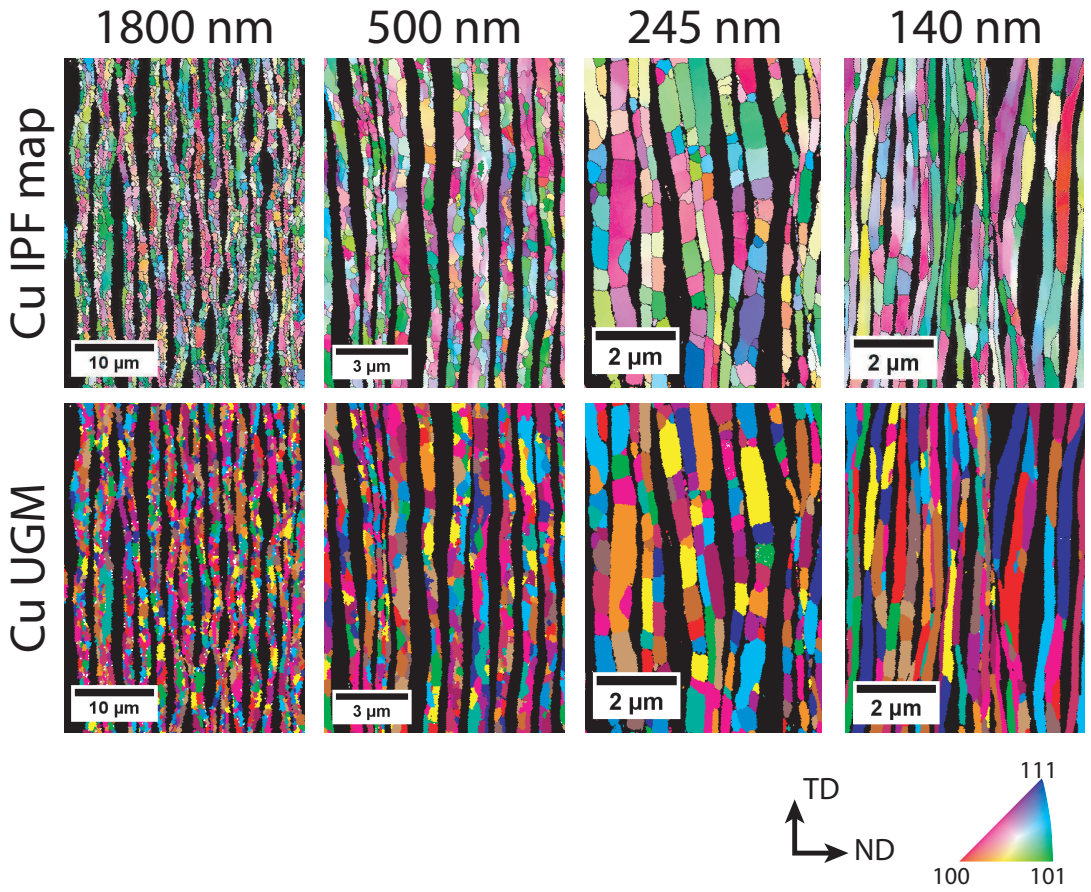

Figure 4.5: EBSD IPF maps and UGM images partitioned to show only the Cu phase in 1800 to 140 nm layer thickness Cu-Nb nanolaminates. The grain structure of the Cu layers evolves from one in which 2-3 grains span the layers at 1800 nm to one in which the Cu layers are spanned by single high aspect ratio grains (as seen at 140 nm). The transition to predominantly single crystal through thickness Cu layers occurs at 245 nm.

Previous studies by Lim and Rollett [54] have indicated that the dislocation density, and therefore the driving force for recrystallization, in the copper layers decreases as the layer thickness is reduced from 20 μm to 200 nm (falling from 1.2×10^{15} m^{-2} to 0.5×10^{15} m^{-2}). A low dislocation density in rolled Cu-Nb com-

posites has also been noted by other investigators [133]. The decrease in dislocation density, combined with the constraint that the critical recrystallization grain nucleus must be smaller than the layer thickness, is believed to suppress conventional recrystallization processes in nanoscale Cu layers [54]. The high aspect ratio grains observed in the 140 nm laminate (Figure 4.5) appear to be a consequence of this phenomenon.

While the Cu layers are spanned by single grains at a layer thickness of 245 nm, the Nb layers still possess multiple grains through thickness as seen in Figure 4.6. While the Nb layers appear discontinuous at 140 nm, this appearance is an artifact of surface relief induced shadowing during EBSD pattern collection. As the collection of Nb microstructural data using EBSD at length scales at and below 140 nm is challenging and often produces images in which the continuity of the layers is not captured, precession election diffraction (PED) must be used for grain orientation mapping in these nanolaminates. This technique was used to produce inverse pole figure maps of the Nb layers in the 30 nm material, and provides better spatial resolution and more accurate representations of the lamellar structure. As evident in the PED IPF map of the 30 nm Nb layers (Figure 4.6), the Nb layers are spanned by single, very high aspect ratio grains. While the very high aspect ratio grains exceed the dimensions of the PED scan presented in Figure 4.6, STEM images of the 30 nm material are shown in

Figure 4.7. The pair of complementary phase contrast and grain contrast STEM images reveal the lamellar microstructure and elongated grain structure of both the Cu and Nb layers over a wide area (1.7 x 1.7 μm). The characterization results for the 140 and 30 nm layer thickness material indicates that the transition from polycrystal to single crystal through thickness Nb layers occurs between 140 and 30 nm.

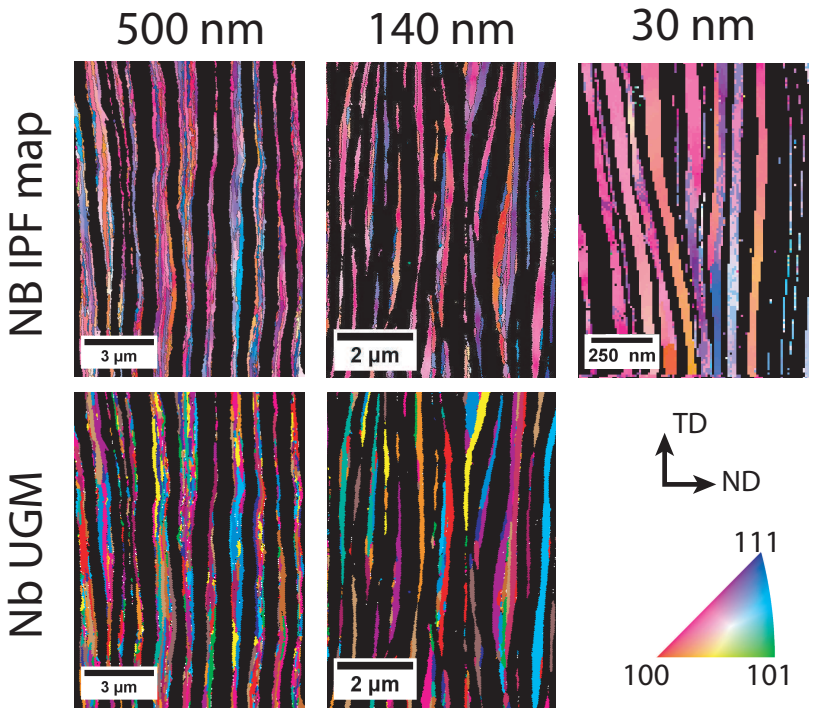

Figure 4.6: EBSD IPF maps and UGM images partitioned to show the Nb phase in 500 and 140 nm layer thickness Cu-Nb nanolaminates and PED IPF image of 30 nm Nb layers. The Nb grains at 500 and 140 nm are more elongated than the Cu grains shown in Figure 4.5, with multiple Nb grains spanning each layer. By 30 nm, the Nb layers are observed to be predominantly single crystal through thickness.

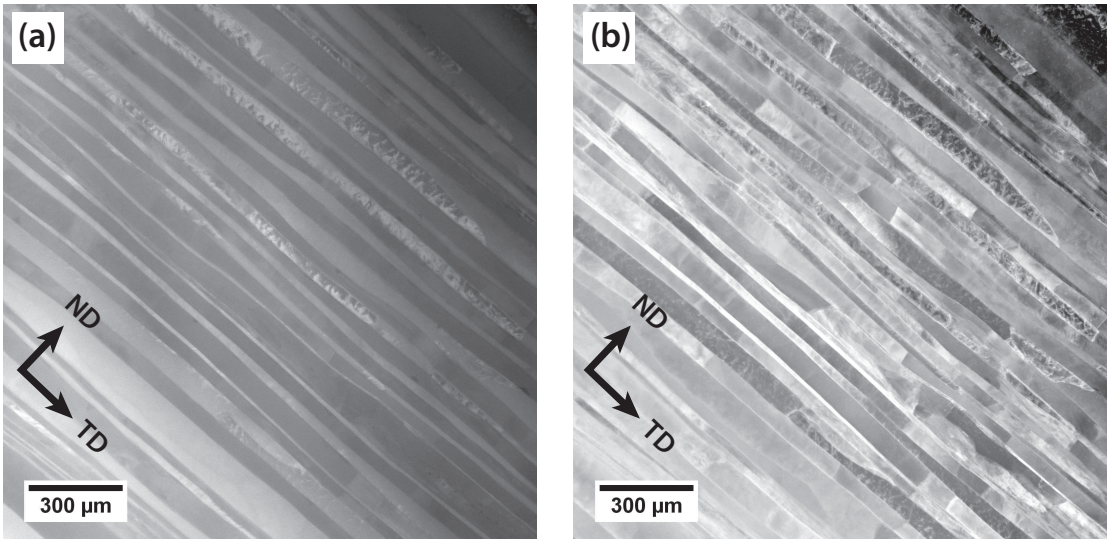

Figure 4.7: STEM images of 30 nm Cu-Nb nanolaminate (TD-ND plane). Phase contrast provided by a 48 mm camera length (a) shows the lamellar phase structure (where Cu appears darker than Nb), while grain contrast (b) obtained using a 480 mm camera length revealed the grain structure. Images courtesy of Jaclyn Avallone, UCSB [134].

The results of the EBSD, PED, and STEM characterization of these materials agree with the grain size data reported by Carpenter [123]. These data are shown in Figure 4.8, where the percent area by phase (i.e. each phase is considered separately) is plotted versus the grain lengths measured along the RD, TD, and ND directions. This experimental data was obtained from EBSD analysis of 20 μm, 8 μm, 714 nm, 135 nm, and 58 nm ARB Cu-Nb nanolaminates. Interestingly, no significant change is seen in the distribution of RD grain lengths as the layer thickness is refined, and only a slight decrease in the TD grain length is observed. The ND grain dimension, however, does decrease as

the layer thickness is refined since the ND grain dimension is constrained by the layer thickness once the layers become single crystalline in the through thickness direction (∼245 nm). The result of a largely invariant RD and TD grain length and a decreasing ND grain length is that the grain aspect ratios increase dramatically as the layer thickness is refined below 245 nm. Calculations based on the peaks in the grain size distributions in Figure 4.8 indicate that grains in both phases exceed aspect ratios of 1:50:5 (ND:RD:TD) at a layer thickness of 58 nm, as shown schematically in Figure 4.8(d) [123].

Figures 4.9 and 4.10 show pole figures representing the crystallographic textures of both the Cu and Nb phase in Cu-Nb nanolaminates with layer thicknesses ranging from 1800 nm to 15 nm. All pole figures were calculated from EBSD data using the MTEX MATLAB package [135], and texture data was collected from the 65, 30, and 15 nm samples using the 'wedge mounting' technique described in Reference [127]. This technique involves mounting and preparing the laminates so that the surface for EBSD analysis intersects the layers at a shallow inclination angle (increasing the apparent layer thickness). The Cu phase at all length scales shows a consistent, strong deformation texture, with the maximum intensity of the pole figures ranging from 2.9 to 4.1 multiples of random. The sharp peaks in the (111) pole figure (indicated with arrows in Figure 4.9) shift slightly and strengthen from 65 nm to 15 nm. The position

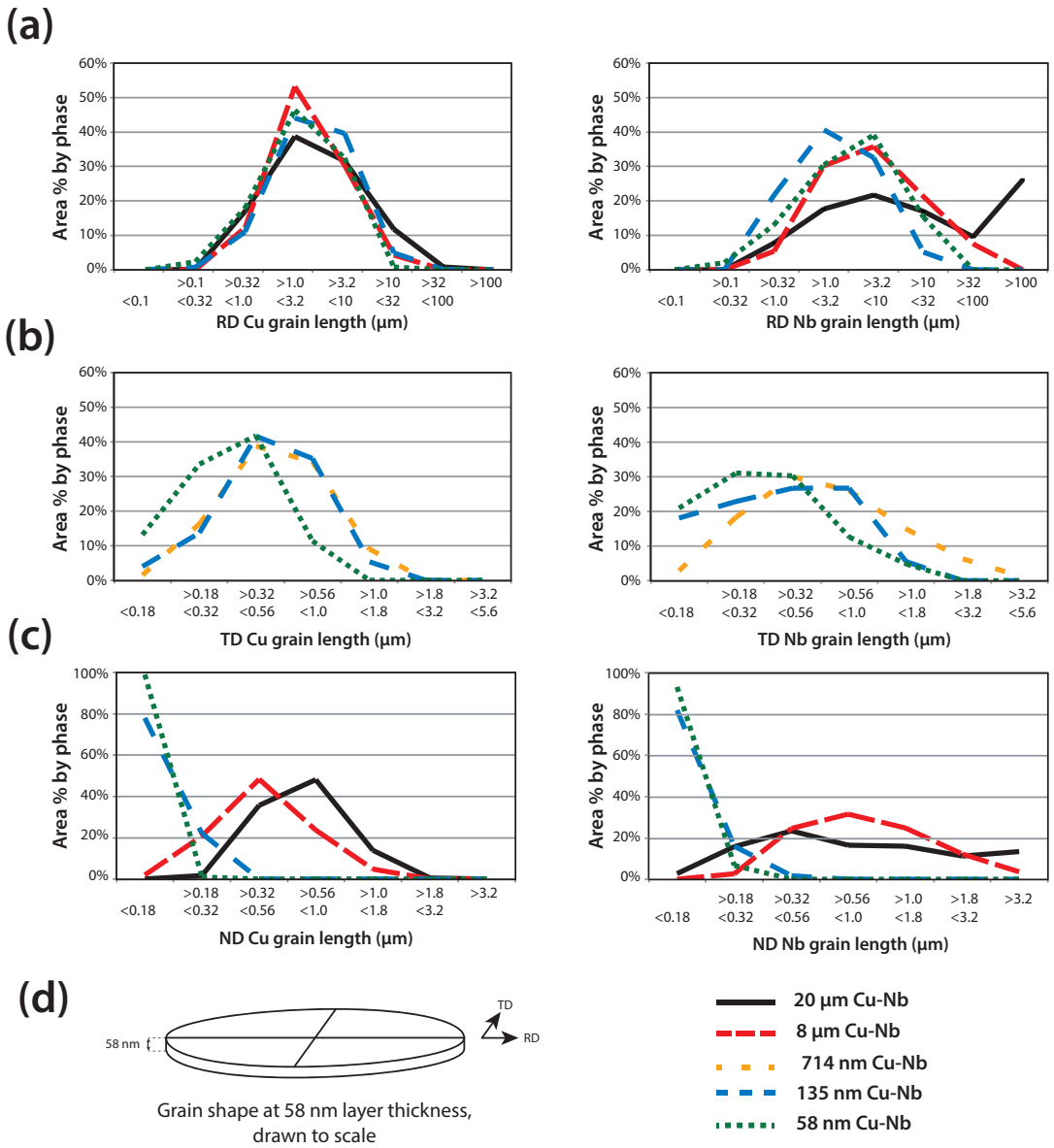

Figure 4.8: Grain size statistics obtained from EBSD for Cu-Nb nanolaminates processed at LANL, adapted from Reference [123]. Plots show percent area by phase of Cu and Nb grains having lengths within the bins of the horizontal axis. Grain lengths along the RD (a), TD (b), and ND (c) are plotted (note the different axis range and bins). (d) shows a schematic of the grain shape in the 58 nm material (drawn to scale): RD and TD grain lengths obtained from peaks in (a) and (b), ND length taken as the layer thickness.

of these peaks implies that the Cu grains are oriented with the $[112]$ crystallographic directions aligned with the ND direction of the rolled plates and represents a departure from a conventional rolled Cu texture [18, 125]. The Nb pole figures (Figure 4.10) show sharp crystallographic textures with intensities that tend to increase as the layer thickness is refined from 1800 μm to 15 nm. These pole figures indicate that Nb grains tend to align with the $[111]$ direction parallel to the TD and the $[110]$ direction parallel to the RD. As pointed out in Reference [128], the Nb pole figures indicate that there are two symmetric texture components (the texture peaks could be reproduced using only two Nb grains: the $[110]$ direction of each grain would be aligned with the rolling direction, with each grain tilted in opposite directions about the RD axis). Comparison of these Nb textures to those of the coarse laminates (Figure 4.4) shows a major difference in the (111) pole figures, where the $[111]$ peaks previously aligned along the RD-ND plane have split into two peaks (indicated by arrows in the 15 nm pole figure). This peak splitting is not observed in rolled monolithic Nb and has been attributed to the high density of Cu-Nb interfaces in these materials and their effect on slip system activity [18]. While all of the materials with layer thicknesses ranging from 1800 to 15 nm possess a strong crystallographic texture, the texture in material with layer thickness $<$100 nm is generally stronger than that in materials with layer thickness $>$100 nm. The texture data presented

in Figures 4.9 and 4.10 will serve as inputs into the polycrystal modeling efforts discussed in Section 4.2.

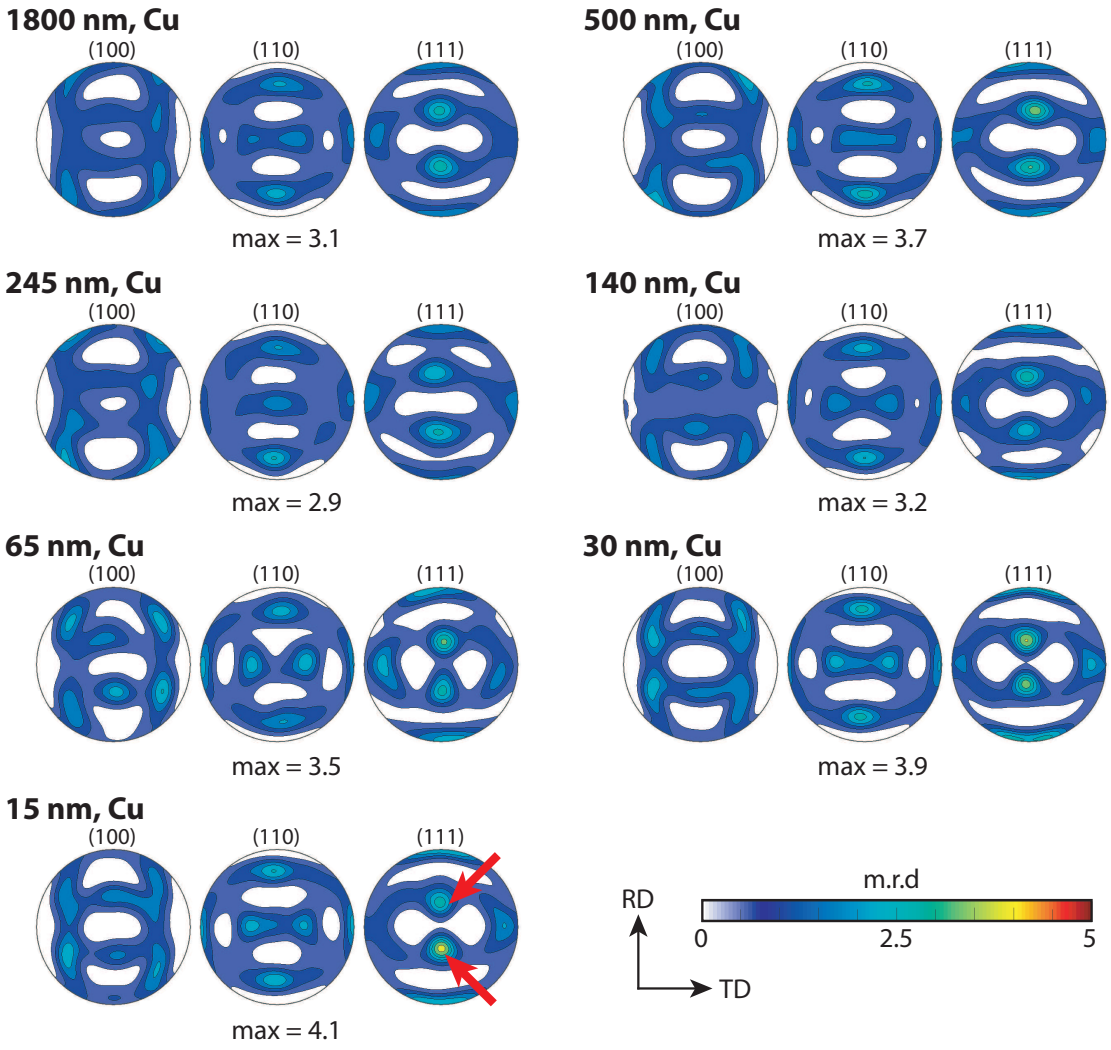

Figure 4.9: Pole figures for the Cu phase in ARB Cu-Nb nanolaminates with layer thicknesses ranging from 1800 to 15 nm obtained from EBSD. All PFs shown are equal area projections.

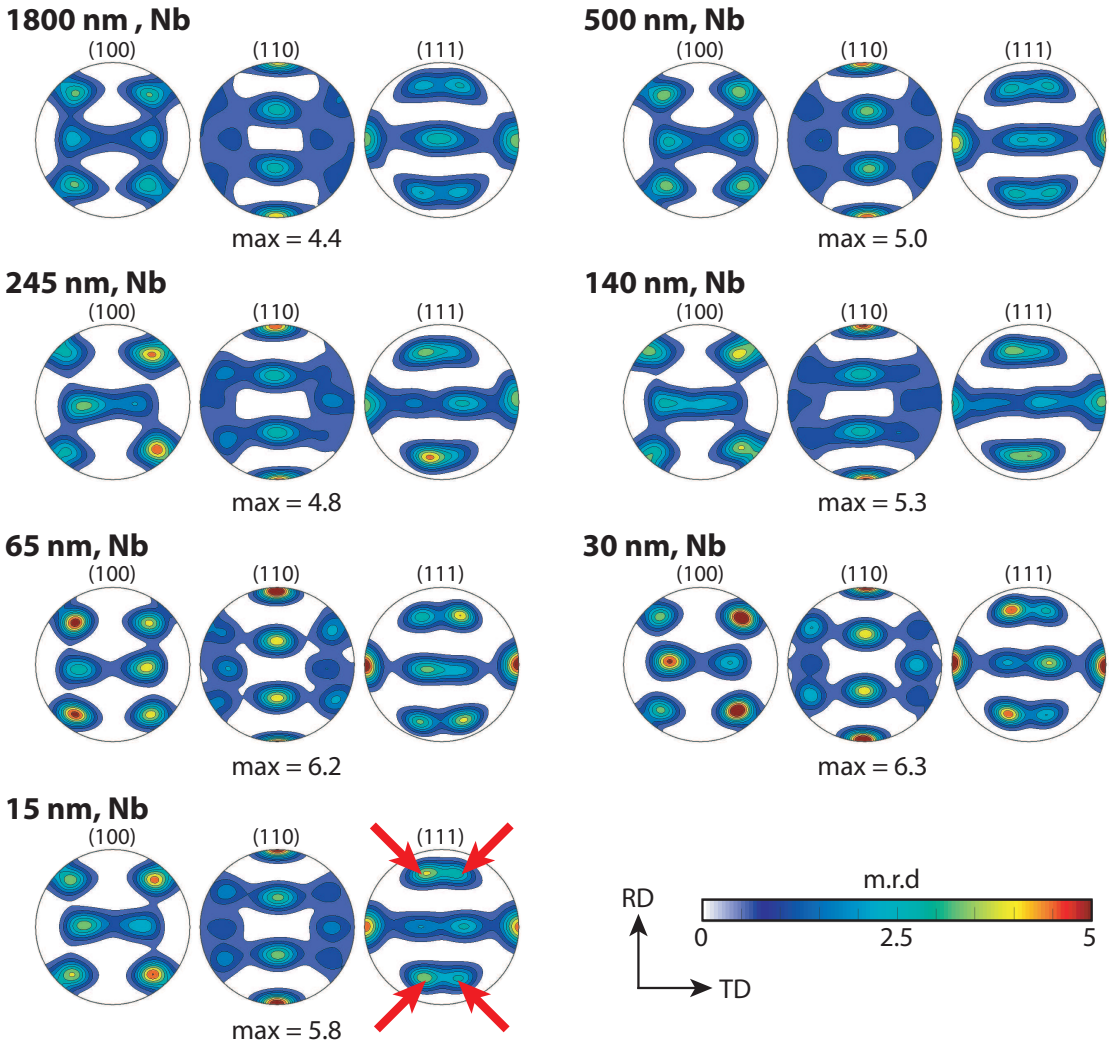

Figure 4.10: Pole figures for the Nb phase in ARB Cu-Nb nanolaminates with layer thicknesses ranging from 1800 to 15 nm obtained from EBSD. All PFs shown are equal area projections.

Finally, it should be noted that a strong interfacial crystallographic orientation relationship develops during ARB processing. The presence of such a relationship is suggested by the strong crystallographic textures of the single

phases, but requires spatially resolved crystallographic data to prove. Lee [126] used EBSD analysis and developed automated heterophase interface character distribution (HICD) software to show that the interface relationship in ARB Cu-Nb nanolaminates with layer thicknesses ranging from 600 to 200 nm was predominantly a Kurdjumov-Sachs (K-S) $\{112\}_{fcc}\|\{112\}_{bcc}$ $[111]_{fcc}\|[110]_{bcc}$ relationship. This technique used large sample areas, enabling statistically significant interface distributions to be obtained [126]. Additional studies using high resolution TEM imaging and PED have confirmed that this relationship persists during continued ARB processing and is therefore a stable, preferred interface [125, 129, 136]. Liu [129] found that the fraction of interfacial area possessing the $\{112\}_{Cu}\|\{112\}_{Nb}$ relationship increases from 23% to 32% as the layer thickness is decreased from 86 nm to 30 nm. Interestingly, the K-S $\{112\}_{fcc}\|\{112\}_{bcc}$ $[111]_{fcc}\|[110]_{bcc}$ relationship has also been reported in deformed Cu-Nb wire-drawn composites and Ni-Cr alloys, suggesting that it may be a common relationship for deformation processed FCC/BCC composites [18].

Figure 4.11 shows a HRTEM image of a $\{112\}_{Cu}\|\{112\}_{Nb}$ $[111]_{Cu}$ $\|[110]_{Nb}$ interface in an 18 nm ARB Cu-Nb nanolaminate. The interface is ordered and faceted along $\{110\}$ and $\{111\}$ planes. This atomic faceting has been found to strongly influence the interfacial shear strength and mechanisms of interfacial dislocation motion, as will be discussed later in Section 4.5.3.

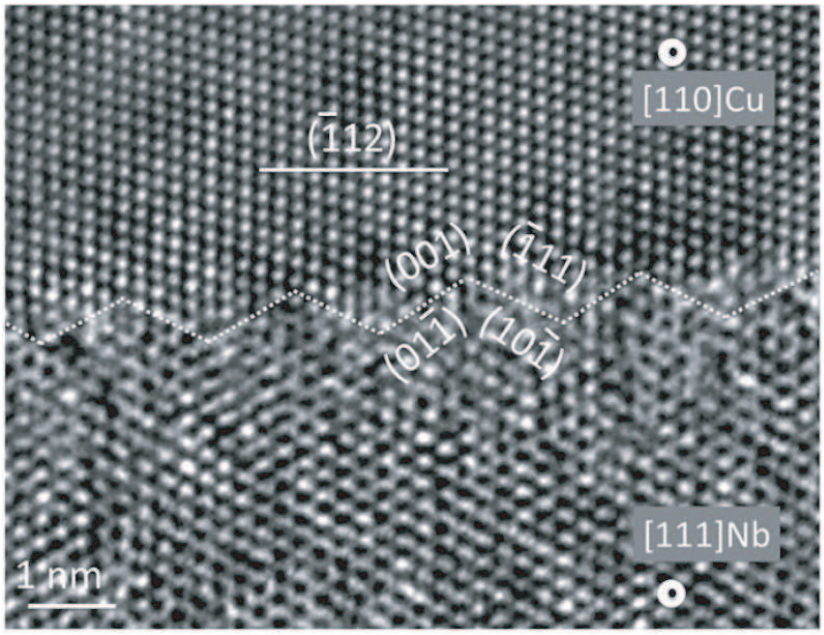

Figure 4.11: HRTEM image of Cu-Nb interface crystallography showing the predominant interface in ARB Cu-Nb nanolaminates. The $\{112\}_{Cu}\|\{112\}_{Nb}$ $[111]_{Cu}\|[110]_{Nb}$ interface type is atomically faceted along $\{110\}$ and $\{111\}$ planes. Reproduced from Reference [23] with permission from the National Academy of Sciences.

An overview of the microstructural changes that occur during the ARB process is shown in Figure 4.12 which compares the 500 nm and 30 nm ARB processed material. Notable changes include the strengthening of the crystallographic texture, refinement of the lamellar structure, and the transition in grain size and aspect ratio (shown in Figure 4.12(a), (b), and (c)). Not shown, but discussed previously is the emergence of a stable and predominant interface crystallography relationship, with over 30% of the interfacial area in the 30 nm material having a $\{112\}_{Cu}\|\{112\}_{Nb}$ $[111]_{Cu}\|[110]_{Nb}$ type interfacial character.

These microstructural changes will be related to the mechanical response of the Cu-Nb nanolaminates in the following sections.

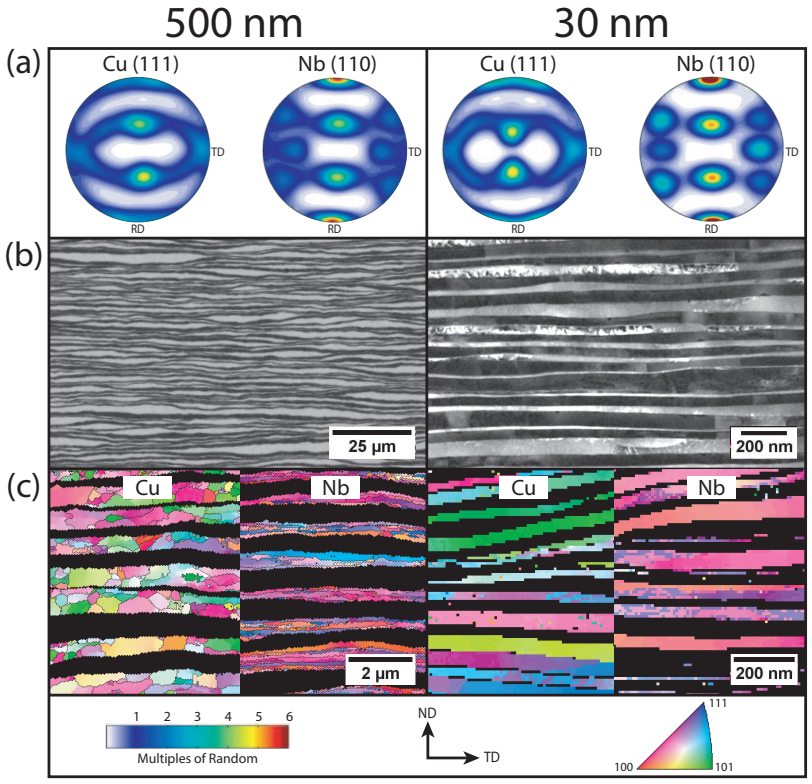

Figure 4.12: Comparison of the 500 and 30 nm Cu-Nb nanolaminate microstructure. (a) Cu (111) and Nb (110) PFs calculated [135] from EBSD data. (b) Backscattered SEM image (500 nm) and high-angle annular dark field STEM image (30 nm) showing Cu (dark) and Nb (light) layers. (c) EBSD IPF maps (500 nm) and PED maps (30 nm) for Cu and Nb. PF scale for (a), transverse direction (TD) and normal direction (ND) sample axes for (b) and (c), and IPF coloring scheme for (c) shown at bottom. Reproduced from Reference [7] with permission from the American Institute of Physics.

4.2 In-plane tensile behavior

The bulk nature of ARB processed Cu-Nb nanolaminates allows for the mechanical properties of these materials to be evaluated using conventional macroscopic tensile and compressive tests.[1] While some micromechanical tests have been conducted on thin film PVD Cu-Nb nanolaminates [5, 78], a thorough exploration of the effects of layer thickness and stress state on deformation behavior and mechanical properties has not been reported. Further, the microstructure of ARB processed Cu-Nb nanolaminates differs substantially from the PVD synthesized material, and likely produces a different mechanical response. Thus the bulk tensile and compressive tests discussed in the following sections offer new information regarding the anisotropy, deformation behavior, and strength of ARB processed Cu-Nb nanolaminates.

4.2.1 Experimental tensile behavior

Bulk tensile testing of ARB Cu-Nb nanolaminates was motivated by the desire to assess the ductility and strength versus layer thickness relationship for these nanolaminate materials. The exploration of the tensile properties of

[1] A substantial amount of material in Section 4.2 is reproduced from *Tensile behavior and flow stress anisotropy of accumulative roll bonded Cu-Nb nanolaminates* T. Nizolek, I.J. Beyerlein, N.A. Mara, J.T. Avallone, and T.M. Pollock, Applied Physics Letters 2016 [7]

nanolaminates has been traditionally hindered by the challenges associated with mechanically testing PVD synthesized thin films [137]. A limited number of studies have explored the tensile behavior of free-standing nanolaminate films [6, 29, 32, 138]; however these investigations have either been restricted to a small range of layer thicknesses, did not report ductility, or attributed low ductility to specimen geometry and film growth flaws. Obtaining reliable tensile property data for nanolaminates with a wide range of layer thicknesses is essential in order to reveal the effects of layer size on constitutive behavior, determine the effects of crystallographic texture on plastic anisotropy, and provide insight into the mechanisms of plastic deformation. Changes in the relationship between layer thickness and strength/anisotropy could indicate a transition from conventional polycrystal plasticity to a regime where proposed nanolaminate deformation mechanisms, such as confined layer slip (CLS) or interface crossing, dominate [17].

Tensile specimens with the stress axis parallel to either the RD or TD axes of the rolled Cu-Nb nanolaminates were prepared and tested as discussed in Section 2.4. The resulting stress-strain curves for select tensile specimens are shown in Figure 4.13 and the yield stress, ultimate tensile strength, and strain-to-failure for all samples are given in Table 4.1. The yield stress at a 0.5% offset is reported since large offsets are typically used for nanocrystalline metals due

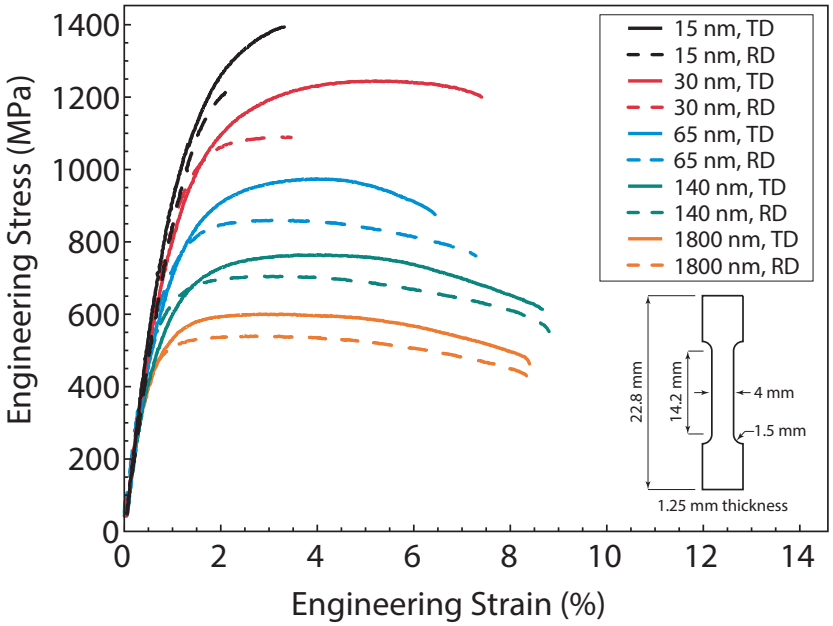

Figure 4.13: Stress-strain curves for select Cu-Nb nanolaminate tensile specimens with layer thicknesses ranging from 1800 to 15 nm (curves for 500 and 245 nm specimens are omitted for clarity). The specimen geometry is shown in the lower inset. Reproduced from Reference [7] with permission from the American Institute of Physics.

to a gradual onset of plasticity [106, 139]. As the layer thickness of the material is reduced, both the yield strength and ultimate tensile strength increase while the strain-to-failure generally decreases. This trend has been observed in many single-phase nanocrystalline materials and is attributed primarily to the diminished work hardening capability of nanocrystalline metals [140, 141]. For all length scales, the TD tensile specimens show appreciably higher flow stresses than the RD specimens, a trend that is particularly apparent for the 65 and 30 nm samples.

Table 4.1: Yield strength at 0.5% offset (σ_y), ultimate tensile strength (UTS), and failure strain (ϵ_f) for tensile specimens. Mean values are listed $\pm$ the standard deviations (given as 'na' if from a single sample); most data collected from 4 samples. Reproduced from Reference [7] with permission from the American Institute of Physics.

h	1800		500		245		140		65		30		15	
(nm)	RD	TD	RD	TD	RD	TD	RD	TD	RD	TD	RD	TD	RD	TD
σ_y	489	527	554	559	592	588	648	601	729	768	952	898	1056	1116
(MPa)	$\pm$17	$\pm$2	na	$\pm$4	$\pm$5	$\pm$7	$\pm$17	$\pm$15	$\pm$16	$\pm$19	$\pm$5	$\pm$35	$\pm$19	na
UTS	539	606	605	652	635	725	714	771	856	951	1085	1238	1179	1395
(MPa)	$\pm$8	$\pm$4	$\pm$6	$\pm$2	$\pm$8	$\pm$20	$\pm$12	$\pm$23	$\pm$7	$\pm$15	$\pm$4	$\pm$8	$\pm$48	na
ϵ_f	8.6	8.2	9.1	7.3	8.0	7.1	8.2	8.5	7.0	5.4	3.2	7.6	2.0	3.3
(%)	$\pm$1.3	$\pm$0.5	na	$\pm$0.8	$\pm$0.4	$\pm$0.8	$\pm$0.8	$\pm$0.1	$\pm$0.3	$\pm$0.6	$\pm$0.2	$\pm$0.3	$\pm$0.1	na

The yield stress is plotted as a function of the inverse square root of the layer thickness in Figure 4.14 in order to determine whether the relationship follows the Hall-Petch equation. This equation (modified from the original [72] by substituting layer thickness for grain diameter) is given in Equation 4.1, where σ_y is the yield stress, h is the layer thickness, and K_y is the Hall-Petch coefficient, and σ_0 is a friction stress for lattice dislocation motion. The relationship between yield strength and layer thickness appears consistent with the Hall-Petch relationship across the range of layer thicknesses investigated, as indicated by the linear fit in Figure 4.14. The Hall-Petch coefficients (K_y) calculated from the RD and TD tensile data are 0.078 and 0.080 MPa m$^{1/2}$ (2480 and 2540 MPa nm$^{1/2}$), values that appear realistic when compared to the reported K_y values for pure Cu and Nb: 0.16 and 0.041 MPa m$^{1/2}$ [142, 143]. While the dislocation pile-ups associated with the Hall-Petch model seem improbable in nanoscale laminates, Figure 4.14 provides empirical support for the use of the Hall-Petch equation for these materials.

$$\sigma_y = \sigma_0 + K_y h^{\frac{-1}{2}} \tag{4.1}$$

As shown in Figure 4.13, there are significant differences in the flow stresses along the RD and TD directions. Due to the increase in strength, the differ-

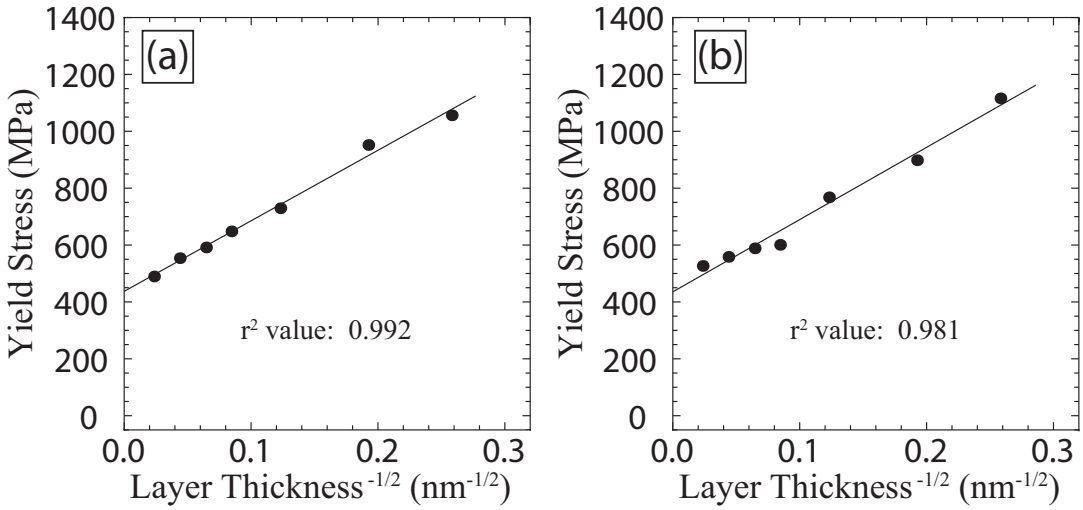

Figure 4.14: Hall-Petch plots for tensile specimens tested parallel to the rolling direction (a) and the transverse direction (b). Plot markers are larger than error bars. Reproduced from Reference [7] with permission from the American Institute of Physics.

ence between the RD and TD samples appears to increase as the layer thickness decreases. However when compared on a percent difference basis, the degree of anisotropy at 2% plastic strain varies between 8% and 13%, and no clear trend with respect to layer thickness is observed. While potential sources of anisotropy include crystallographic texture, grain morphology, and interfacial effects on dislocation motion that may occur at layer thicknesses below 100 nm [81, 144, 145], the invariance of the observed anisotropy across a wide range of length scales suggests that the persistent strong crystallographic texture is responsible for the in-plane tensile anisotropy.

4.2.2 In-plane tensile anisotropy predictions

In order to determine whether the in-plane tensile anisotropy of these nanolaminates can be attributed primarily to the effects of crystallographic texture, full constraints Taylor polycrystal modeling was conducted [81, 88]. The modeling technique, slip systems, and hardening laws used were discussed in Section 2.7. While the model used does not consider strain partitioning between grains or interfacial effects on plasticity, it serves as a means to isolate the effect of crystallographic texture on plastic anisotropy. The mechanical response of both the 500 and 30 nm material subject to plane strain tension along the RD and TD directions was simulated, with the starting texture of each simulation matching that obtained from EBSD analysis of the undeformed nanolaminates.

The simulated stress-strain data for both the individual phases as well as the averaged composite response was analyzed and a measure of the level of anisotropy at 2% plastic strain was obtained using Equation 4.2.

$$\text{anisotropy level} = \frac{\sigma_{TD} - \sigma_{RD}}{\sigma_{TD}} \times 100 \tag{4.2}$$

The anisotropy level is defined as the percent difference between σ_{TD} and σ_{RD}, where positive values indicate $\sigma_{TD} > \sigma_{RD}$. This measure allows the 500 and 30 nm results to be directly compared as it removes any dependence on the

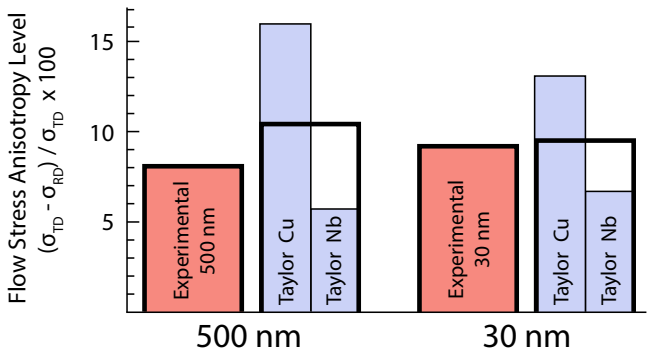

Figure 4.15: Comparison of the predicted single phase (solid blue bars) and composite (bold lines) anisotropy levels with the experimental composite anisotropy level (solid red bars). Reproduced from Reference [7] with permission from the American Institute of Physics.

magnitude of the flow stress.

Both the single phase and composite anisotropy levels predicted by Taylor modeling are shown in Figure 4.15. For both the 500 and 30 nm material, the simulations predict $\sigma_{TD} > \sigma_{RD}$ for the individual phases as well as the composite response. The predicted composite anisotropy levels (10.2% and 9.5%) are found to be in very good agreement with the experimental anisotropy. While the calculated single phase results have no experimental counterparts, they are included in Figure 4.15 as they provide bounds for the composite anisotropy level. That is, regardless of the assigned relative strengths of the single phases, the composite anisotropy is bounded by that of the individual phases.

The qualitative effect of texture on anisotropy revealed by polycrystal modeling ($\sigma_{TD} > \sigma_{RD}$) can be understood by considering how the strain path in RD

and TD tension compare to the rolling process. Since the initial texture consists of crystallographic orientations that are stable during rolling (elongation in the RD and compression along the ND), any deviation from this deformation path requires significant grain distortion and reorientation. Consequently, TD tension leads to higher flow stresses than RD tension as it represents an abrupt strain path change relative to the prior rolling deformation.

The agreement between the predicted and observed experimental anisotropy level is interesting given that, at layer thicknesses below $\sim$100 nm, dislocation motion and deformation mechanisms in metallic nanolaminates are predicted to differ from that of coarse grained polycrystals [17, 146]. Based on the existing models, confined layer slip (where dislocation loops glide parallel to the interfaces) is likely to be operative in the 65, 30, and 15 nm specimens [146]. Yet the polycrystal modeling results show that in-plane anisotropy can be predicted and explained using traditional models that do not account for interfacial effects. This, combined with the relationship between layer thickness and strength that is consistent with Hall-Petch, suggests that confined layer slip, if active, does not substantially alter the plastic response of these ARB Cu-Nb nanolaminates subjected to layer-parallel tension. However, other types of loading, such as layer-parallel shear, may involve deformation modes where such influences become evident.

4.3 Layer normal compressive behavior

Layer normal compression tests were conducted on the Cu-Nb nanolaminates with layer thicknesses ranging from 1800-15 nm. The purpose of this experimental work was to determine the deformability and strain to failure of these materials. Compression perpendicular to the layers is the most common loading orientation for micropillar compression of thin film nanolaminates as it requires little sample preparation aside from gluing the substrate to a stub and focused ion beam milling of the as-deposited film [77, 147, 148]. While only limited micropillar compression tests have been conducted on ARB Cu-Nb nanolaminates, investigators have noted that ND micropillar compression specimens of 18 nm material posses reasonable deformability ($\sim$10%), with final failure resulting from shear band formation [130].

While the previous tensile tests examined the response of Cu-Nb nanolaminates to near plane strain tension (elongation in the RD or TD, contraction along the ND), layer normal compression tests using compression specimens with a square cross-section do not provide the same geometric constraint. Additionally, the materials used for all compression tests were annealed at 400°C for 30 minutes in order to suppress potential delamination. While these factors preclude direct comparison of the tensile and compressive behavior, the results obtained

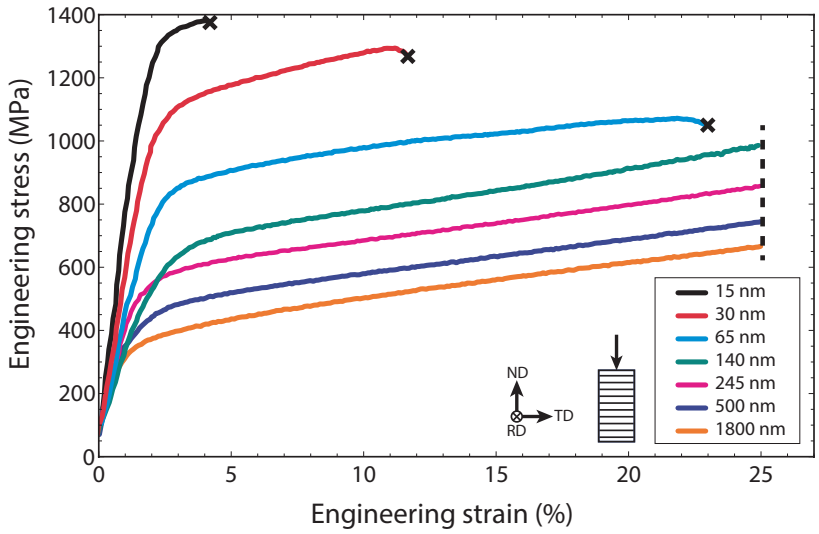

Figure 4.16: Stress-strain curves for specimens compressed along the ND axis. The data for the 15, 30, and 65 nm specimens post failure have been removed for clarity, and the failure point is denoted with an 'x'. All tests were interrupted at 25% strain.

from compression tests for various layer thicknesses and specimen orientations can be safely compared.

Compression specimens with the stress axis aligned with the ND were prepared as discussed in Section 2.4. All specimens were tested at a strain rate of $10^{-3}s^{-1}$ using rigid and non-rotatable compression platens. The deformation behavior of the specimens was monitored using *in situ* imaging and all tests were interrupted at an engineering strain of 25%.

The resulting stress-strain curves are shown in Figure 4.16 (where post-

failure stress-strain data for the 15, 30, and 65 nm specimens have been removed for clarity). As with the tensile tests, a monotonic increase in yield strength and flow stress with decreasing layer thickness is observed. Further discussion of the flow strength versus layer thickness trend is deferred until the end of this chapter, where it will be compared with the results from all compression specimens. While no evidence of failure was seen in the 1800, 500, 245, or 140 nm specimens, the 65, 30, and 15 nm specimens failed prior to the 25% engineering strain at which the tests were interrupted. Figure 4.17 shows the *in situ* images captured during the tests and compares the deformation behavior of the 500, 30, and 15 nm specimens. The 500 nm specimen shows relatively homogeneous compression with the typical barreling associated with friction at the specimen ends. Both the 30 nm and 15 nm specimens show evidence of localized deformation (for example the dark bands across the 30 nm specimen at 10% strain) and fracture. The low deformability of the 15 nm specimen is clear, with multiple fractures occurring after the initial failure strain of 4%.

Similar localized deformation followed by fracture has been observed during ND micropillar compression of 18 nm ARB Cu-Nb laminates [130]. Shear band formation was observed and led to fracture along a shear band at a true strain of 10% (Figure 4.18). While detailed characterization of the failure mechanism in the bulk ND compression tests has not been conducted, the evidence of shear

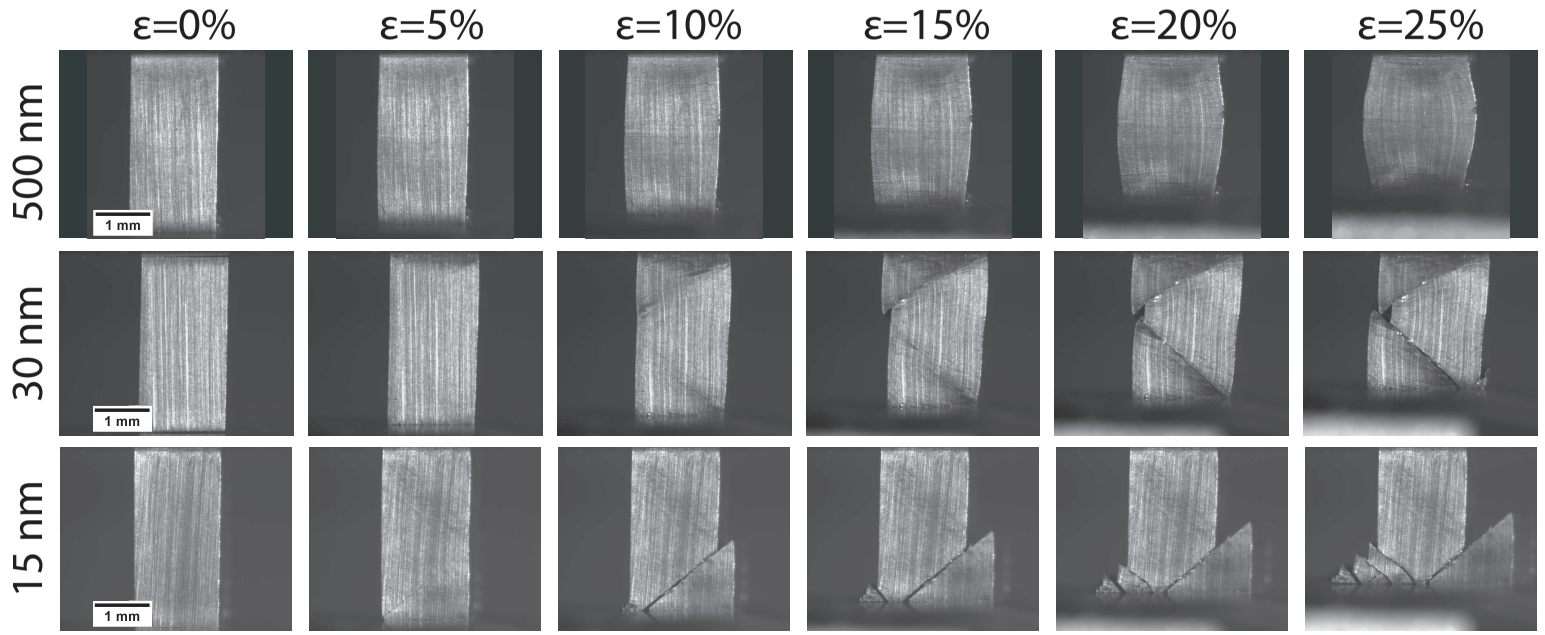

Figure 4.17: *In situ* images for specimens compressed along the ND axis showing specimen deformation at 5% strain increments.

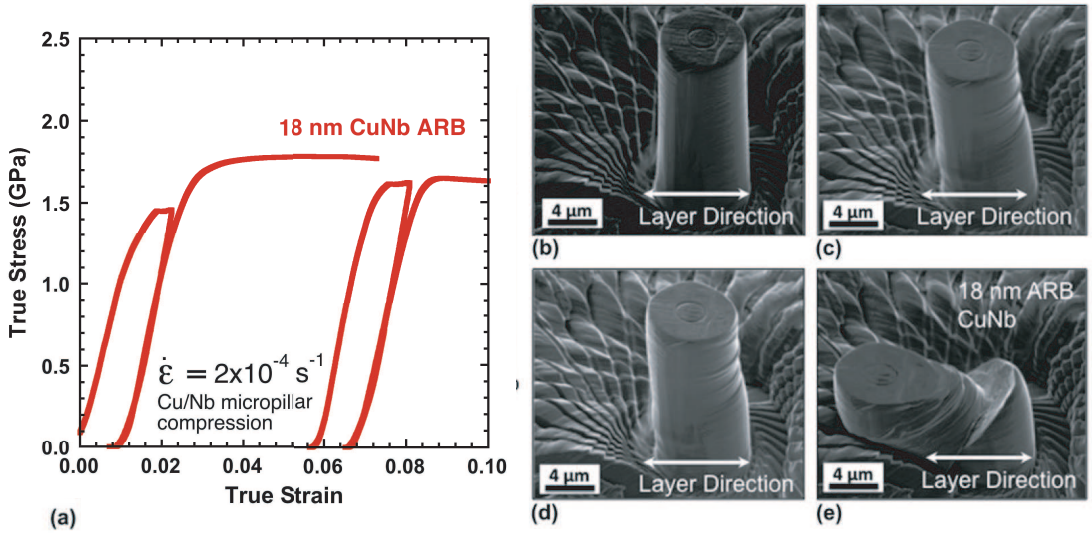

Figure 4.18: Shear band formation in a micropillar compression test of 18 nm ARB Cu-Nb. Compression direction is aligned with the ND axis. The stress-strain plot shows several loading/unloadings during test; failure occurred at a true strain of 10%. Reproduced from Reference [130] with permission from the Cambridge University Press.

localization and fracture along bands inclined near 45° to the loading axis suggests that shear band formation is responsible for the low strain to failure at small layer thicknesses.

4.4 Layer parallel compressive behavior

Layer parallel compression tests were conducted on Cu-Nb nanolaminates with layer thicknesses ranging from 1800 to 15 nm. In contrast to the previous

[1]Some material in Section 4.4 is reproduced from *Enhanced plasticity via kinking in cubic metallic nanolaminates* T. Nizolek, N.A. Mara, I.J. Beyerlein, J.T. Avallone, and T.M. Pollock, Advanced Engineering Materials 2015 [149].

ND compression specimens, no layer parallel micropillar compression tests had been performed for either ARB or PVD Cu-Nb nanolaminates. Thus the results of bulk compression provided the first indication of the mechanical properties and deformation behavior of Cu-Nb nanolaminates subject to layer parallel compression. The response of these materials to layer parallel compression is of particular technological interest as layer parallel compression, combined with layer parallel tension, occurs during bending of sheet metals and therefore should provide insight into the formability of these bulk nanolaminate materials.

The compression specimens were prepared and tested as discussed in Section 2.4. All specimens were compressed to a strain of 25% between one fixed platen and one self-aligning hemispherical tungsten carbide platen with molybdenum disulfide applied to the specimen ends to minimize friction. While this testing configuration aids specimen alignment and promotes a uniaxial stress state, as described in ASTM standard E9-09 [150], efforts to enforce a uniaxial stress state were unsuccessful at large strains due to the occurrence of pronounced strain localization (discussed below).

The stress-strain data from the TD and RD compression specimens are shown in Figures 4.19 and 4.20. As expected, the yield strength and flow stress of the nanolaminates increase as the layer thickness decreases. RD compression specimens show lower flow stresses that the TD compression specimens, a result

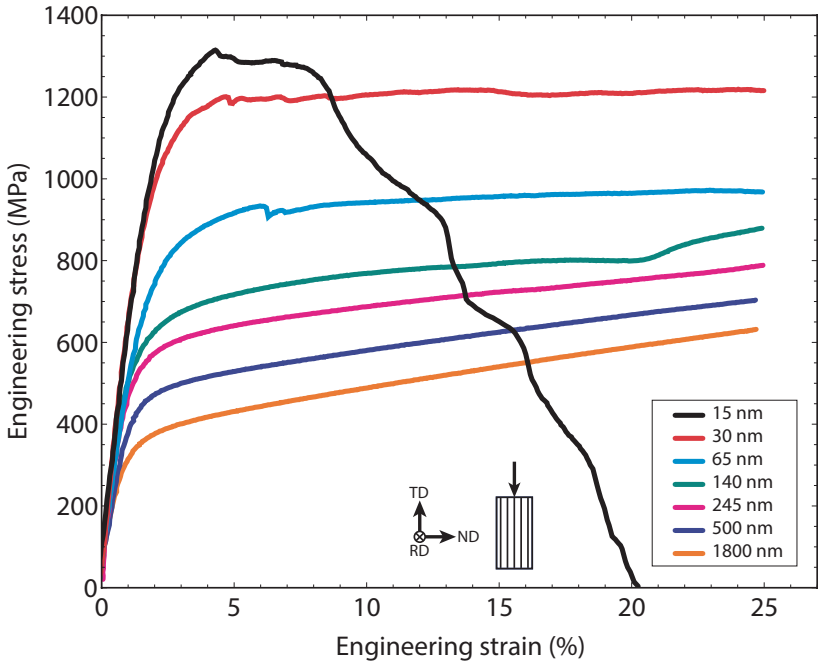

Figure 4.19: Stress-strain curves for specimens compressed along the TD axis. All tests were interrupted at a strain of 25%.

consistent with the tensile data reported in Section 4.2. Discussion of the flow strength versus layer thickness trend is deferred until the end of this chapter, where it will be compared with the results from all compression specimens.

Significant differences between the stress-strain response of the larger layer thickness specimens (1800 or 500 nm samples) and the sub-100 nm specimens are evident in Figure 4.19. While the curve for the 500 nm specimen shows the typical increase in engineering stress with increasing engineering strain (resulting from the increase in cross-sectional area during compression), the stress-strain response of the 30 nm specimen is markedly different. For this specimen,

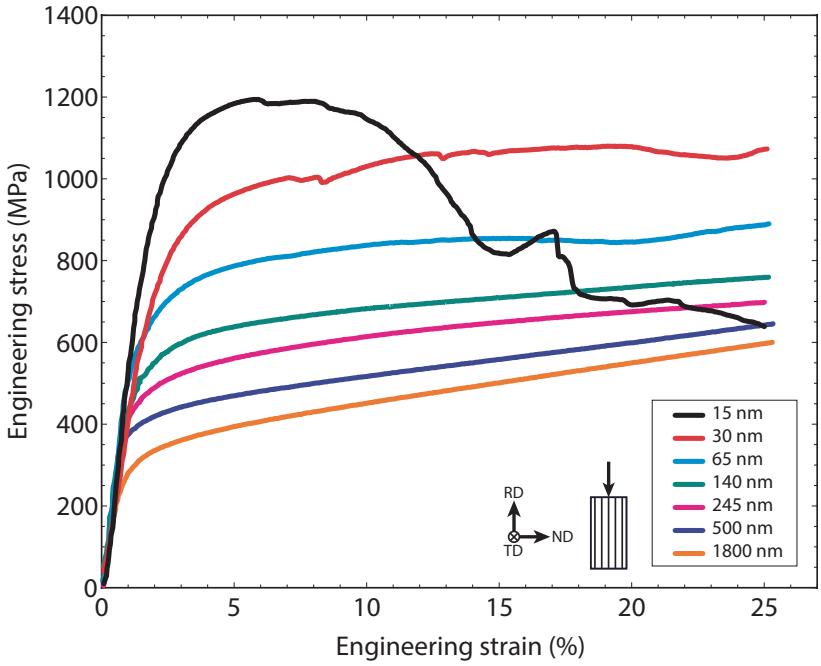

Figure 4.20: Stress-strain curves for specimens compressed along the RD axis. All tests were interrupted at a strain of 25%.

a small perturbation occurs shortly after yield, followed by continued deformation at a near constant stress. Despite this unusual stress-strain response, no evidence of failure is observed for these specimens tested to 25% strain (with the exception of the 15 nm specimens which failed by delamination).

The explanation for the unusual stress-strain response is evident from examination of the *in situ* images from the tests (Figures 4.21 and 4.22): pronounced strain localization occurs in the specimens with sub-100 nm layer thickness. The formation of dark bands traversing the specimens and inclined to the loading axis occurs simultaneously with the small load drops/perturbations in the stress-

strain curves. These bands are observed to broaden with increasing compressive strain, although the formation of additional bands occurs in some specimens (particularly in those compressed parallel to the RD). The transition between homogeneous deformation and deformation localized in bands occurs at a layer thickness of 245 nm, with band formation becoming increasingly pronounced and occurring at lower compressive strains as the layer thicknesses decreases. Thus the formation of these localized deformation bands appears to be dependent on the length scale of the lamellar structure.

The dark bands evident in Figures 4.21 and 4.22 correspond to kink bands: bands of localized shear in which the lamellar microstructure has been uniformly sheared and rotated from its initially vertical orientation. The microstructure of the 65 nm TD compression specimen is shown in Figure 4.23. While the bands of localized deformation appeared dark in Figures 4.21 and 4.22 (due to a small amount of local surface relief), the bands do not correspond to crack formation or obvious material damage. Instead, as shown in Figure 4.23(a) the material within the kink bands remains fully dense. Figure 4.23(c) shows an SEM image of a small kink band in the 30 nm TD specimen where the uniform shear and layer rotation is obvious. Remarkably, despite the extensive local shear strain, the layers in the kinked samples remain continuous across the kink bands and there is no noticeable thinning or thickening of the layers within the

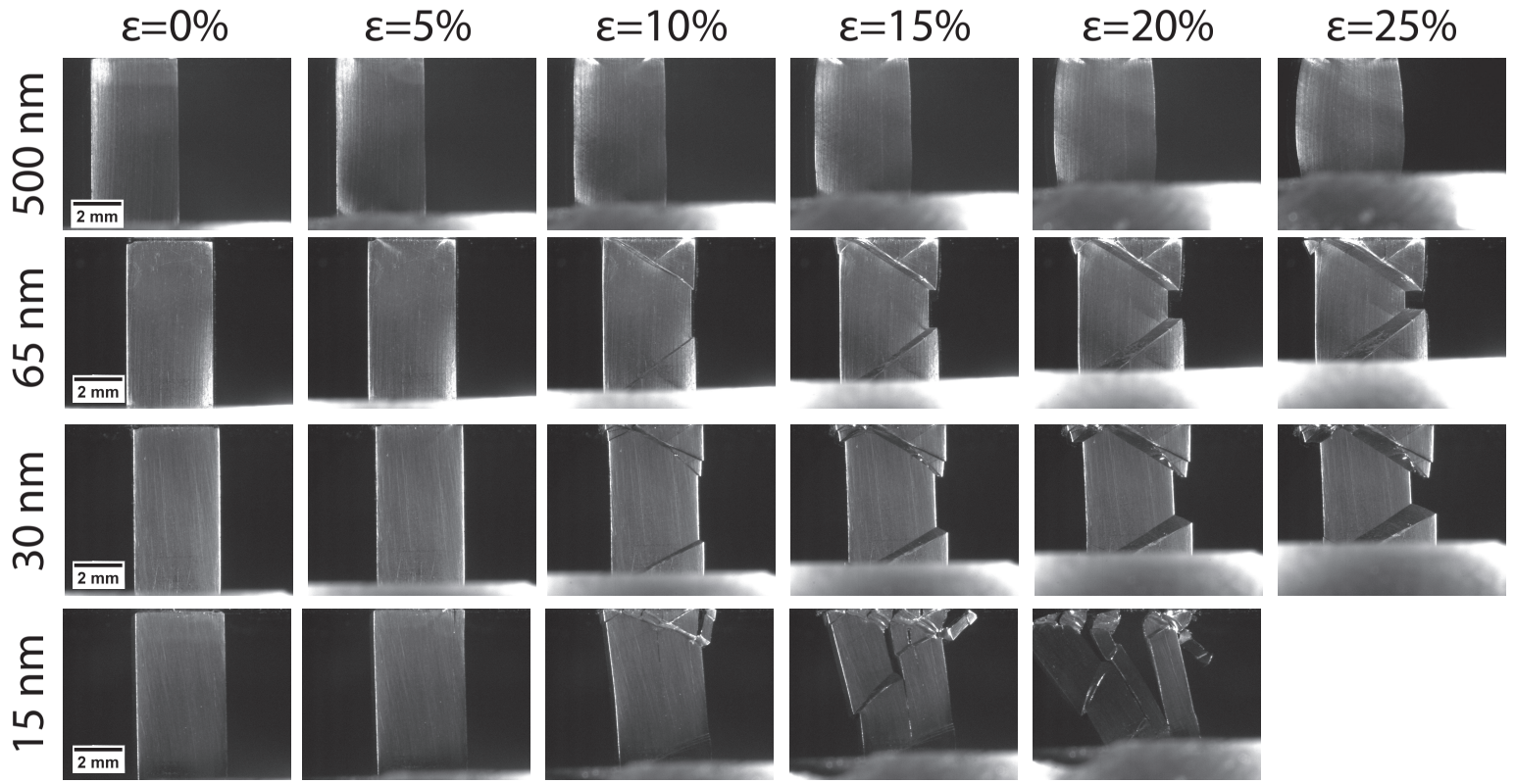

Figure 4.21: *In situ* images for specimens compressed along the TD axis.

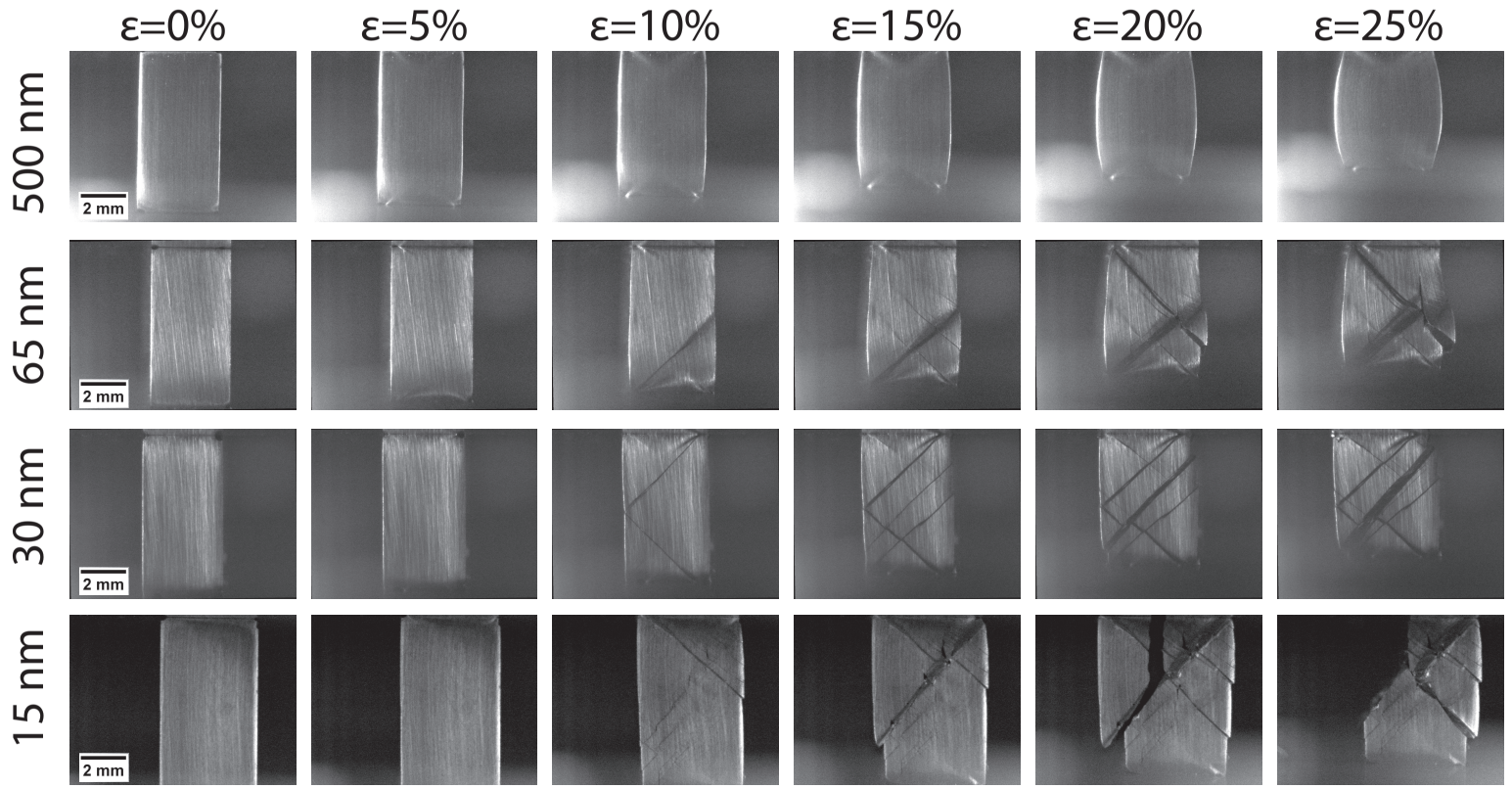

Figure 4.22: *In situ* images for specimens compressed along the RD axis.

kink band. There is no evidence of layer fracture or debonding, even at the boundary of a kink band (Figure 4.23(d)).

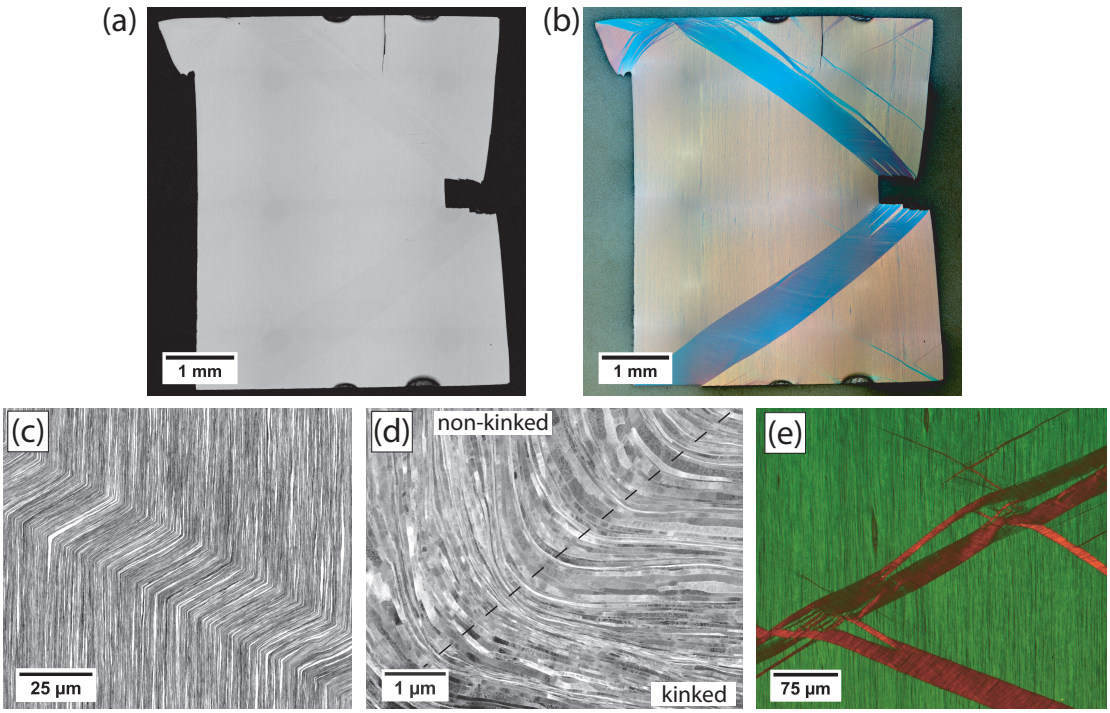

Figure 4.23: Kink bands in the 65 nm and 30 nm TD compression specimens. (a) The polished cross-section of the 65 nm compression specimen shows an absence of cracks along the kink bands which are clearly visible under polarized light illumination (b). (c) The structure of a single kink band in the 30 nm specimen shows a constant shear strain (60%) and layer rotation within the deformation band. (d) STEM image of a kink band boundary in the 30 nm specimen shows layer continuity and a small radius of curvature (1.5 μm). (e) The complex network of kink bands extending through the 30 nm specimen contains both intersections and bifurcations and is revealed using polarized light. The compression direction is vertical in all images. Image reproduced from Reference [149] with permission from John Wiley and Sons.

A full discussion of kink bands and kink band formation is deferred until later, as Chapter 5 is devoted entirely to this phenomenon. However, in order to

conclude the discussion of the mechanical response of the RD and TD layer parallel compression specimens, the angle (β) at which the kink bands form should be noted. Kink band inclination angles for the first kink bands to form in the RD and TD specimens are given in Table 4.2. For the TD compression specimens the kink band inclination angle tends to be shallow, with the angle (β) between the kink band boundary and the layer normal direction (perpendicular to the stress axis) equaling approximately 26° for the first kink band in the 30 nm TD specimen. The result is that there is a large region between the upper and lower kink bands in 4.21 that the initial kink bands can broaden into and consume. This occurs at a near constant stress as evident in Figure 4.19. In contrast, the RD specimens appear to form kink bands at much steeper angles, with the first kink band to form in the 30 nm RD specimen occurring at an angle of approximately 45°. Because the compression specimen height to width ratio is 2:1, these kink bands meet in the middle of the specimen and can only accommodate limited shear strain before the triangular regions of non-kinked material at the specimen ends impinge on each other. This means that, unlike the TD compression specimens, the initial kink bands cannot continue to broaden and additional kink bands, intersecting the original bands, must be formed. The combination of kink band inclination angle and specimen aspect ratio appears to be responsible for the difference in stress-strain behavior for the RD and TD specimens shown

Table 4.2: Range of kink band inclination angles (β) in RD and TD compression specimens. Measurements were conducted on the first kink bands which formed and spanned the entire specimen, as subsequent kink band formation may be influenced by non-uniaxial stress states. Samples where kink band formation could not be clearly observed in the *in situ* images are indicated with 'n.d.' for not distinguishable.

	245 nm	140 nm	65 nm	30 nm	15 nm
β, TD compression	30-38°	32-38°	32-37°	24-27°	21-24°
β, RD compression	n.d.	n.d.	43-45°	44-45°	44°

in Figures 4.19. The hardening that occurs in the RD specimens after formation of the initial kink bands suggests that existing kink bands serve as obstacles and raise the stress required for subsequent kink band formation.

While kink band formation has not previously been reported for nanocrystalline nanolaminates, the layer parallel compression tests indicate that it is a dominant deformation mechanism for Cu-Nb nanolaminates as the layer thickness falls below 100 nm. Kink bands have been reported in other materials systems such as unidirectional polymer matrix fiber composites [151–153], oriented polymers [154], and anisotropic single crystals [155–157] where their occurrence has been linked to the presence of a low layer or fiber parallel shear strength [151, 158–160]. Based on these observations it is expected that the layer parallel shear strength of the nanolaminates which form kink bands should be low, and that the difference between shear strength and layer parallel compressive strength of the laminates may show a dependence on layer thickness

(since the occurrence of kink bands is limited to the sub-250 nm nanolaminates). In order to determine the layer parallel shear strength, compression tests on specimens with layers oriented at 45° to the stress axis were conducted.

4.5 Layer parallel shear strength

To characterize the layer parallel shear strength of Cu-Nb nanolaminates and determine whether the shear strength displays a dependence on layer thickness, compression specimens were machined at a 45° angle to the lamellar structure. While the stress state during compression of these specimens is not one of pure layer parallel shear, shear tests are notoriously difficult to conduct [161, 162]. The limited dimensions of the rolled nanolaminate material precluded many standard specimen geometries such as the Losipescu specimen geometry [162] and thin walled cylinder torsion tests. The 45° off-axis tensile test has been used to explore the shear response of a variety of composite materials and is reported to produce good agreement with shear data obtained from torsion [161], while 45° compressive tests have been used to assess the anisotropy of PVD Cu-Nb nanolaminates [163] as well as Al-SiC nanolaminates [164]. While the 45° compression specimens superimpose the stress states of layer parallel shear and layer normal compression, they provide a convenient geometry for mea-

suring the layer parallel shear strength and produce data that, at the very least, provide a self-consistent measure of layer parallel shear strength and anisotropy.

4.5.1 Experimental layer parallel shear strength

Two sets of specimens were prepared: 1) specimens with the compression axis at 45° to the TD-ND plane (with the maximum resolved shear stress parallel to the RD), and 2) specimens with the compression axis at 45° to the RD-ND plane (with the maximum shear stress parallel to the TD). Both specimen types, referred to as RD45 and TD45 respectively, allow layer parallel shear to occur during compression. All 45° compression specimens were compressed between rigid non-rotatable platens lubricated with molybdenum disulfide. Lubrication is essential for 45° compression tests as any asymmetric shape change driven by layer parallel shear naturally induces sliding at the compression specimen ends. *In situ* imaging was conducted in order to monitor the specimens and observe the shape change of the specimens.

The resulting stress-strain curves for the RD45 and TD45 compression specimens are shown in Figures 4.24 and 4.25. The stress measure for these plots is the compressive engineering stress calculated from the cross-sectional area of the undeformed specimens (the layer resolved shear stress will be half of the

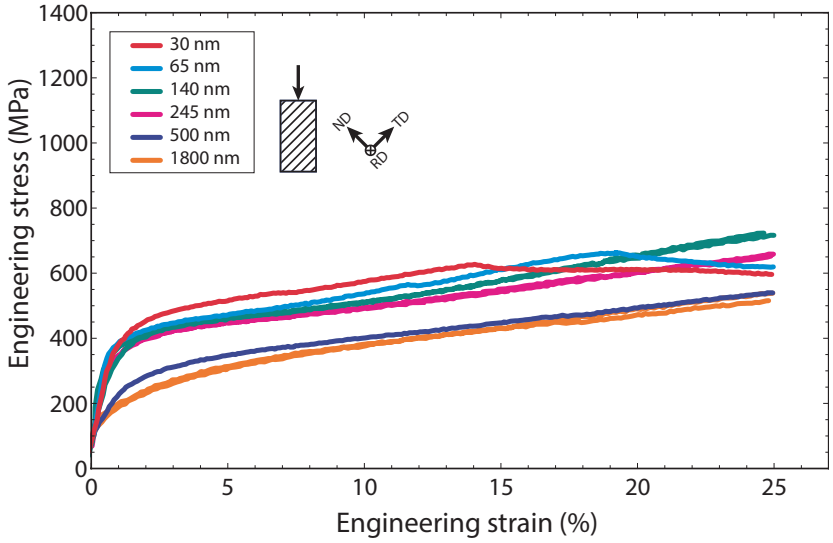

Figure 4.24: Stress-strain curves for 45° compression specimens oriented for layer parallel shear along the TD. (TD45 specimens)

compressive stress). Significantly lower yield and flow stresses are observed for these specimens, compared to the ND, RD, and TD compression specimens previously discussed. Figures 4.24 and 4.25 also provide evidence of in-plane shear strength anisotropy, with the RD45 compression specimens showing a higher flow stress than the TD45 compression specimens, suggesting that the shear strength of the layers along the RD is higher than that along the TD.

Figures 4.26 and 4.27 show images of the specimens at 0, 5, 10, 15, and 20% compressive strain. It is apparent from the asymmetric shape change that compression is largely accommodated by layer parallel shear. At strain levels $<$10%, shearing of the TD45 specimens appears fairly homogeneous outside of

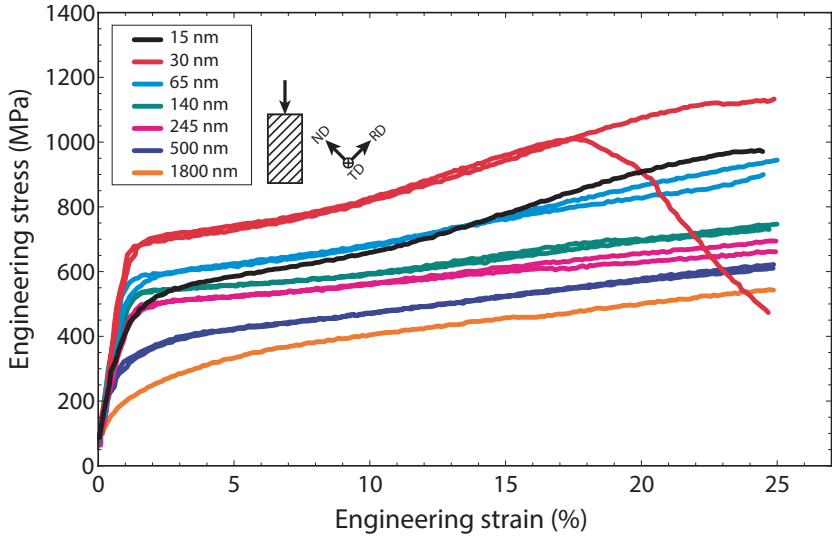

Figure 4.25: Stress-strain curves for 45° compression specimens oriented for shear along the RD (RD45 specimens).

the triangular constrained specimen end regions. Shear appears to be more localized in the RD45 specimens, yet it still occurs over regions that are hundreds of microns wide and contain thousands of layers.

Images from post-test characterization showing a 30 nm and 65 nm TD45 specimen after 25% strain are shown in Figures 4.28 and 4.29. The sheared layers remain inclined to the loading direction and cracks that developed near the end of the compression tests are visible. The cracks, such as the one shown in Figure 4.28(c) frequently do not follow the layers, but rather often lie at a shallow inclination angle with respect to the layer direction. Layers near the bottom corner of the 30 nm specimen that, due to layer parallel shear, impinge on the

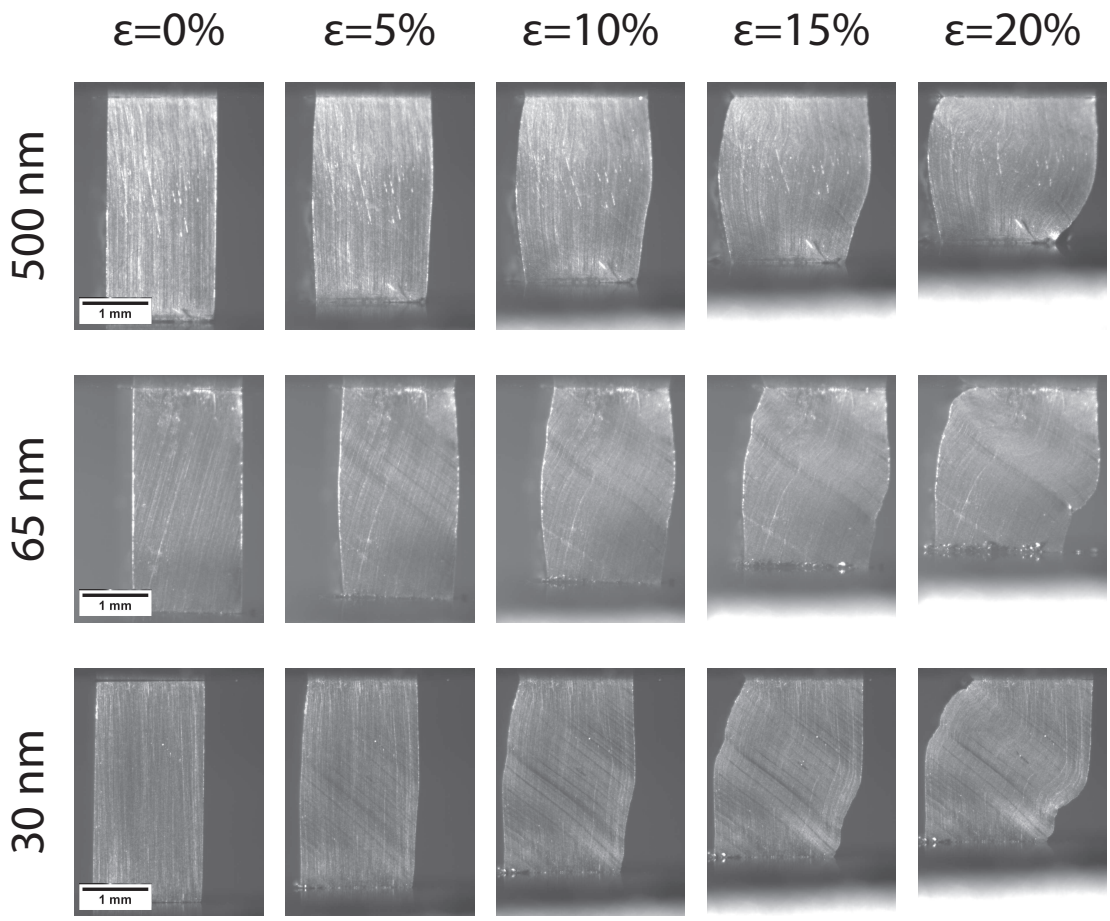

Figure 4.26: Images of TD45 compression specimens at 0, 5, 10, 15, and 20% strain.

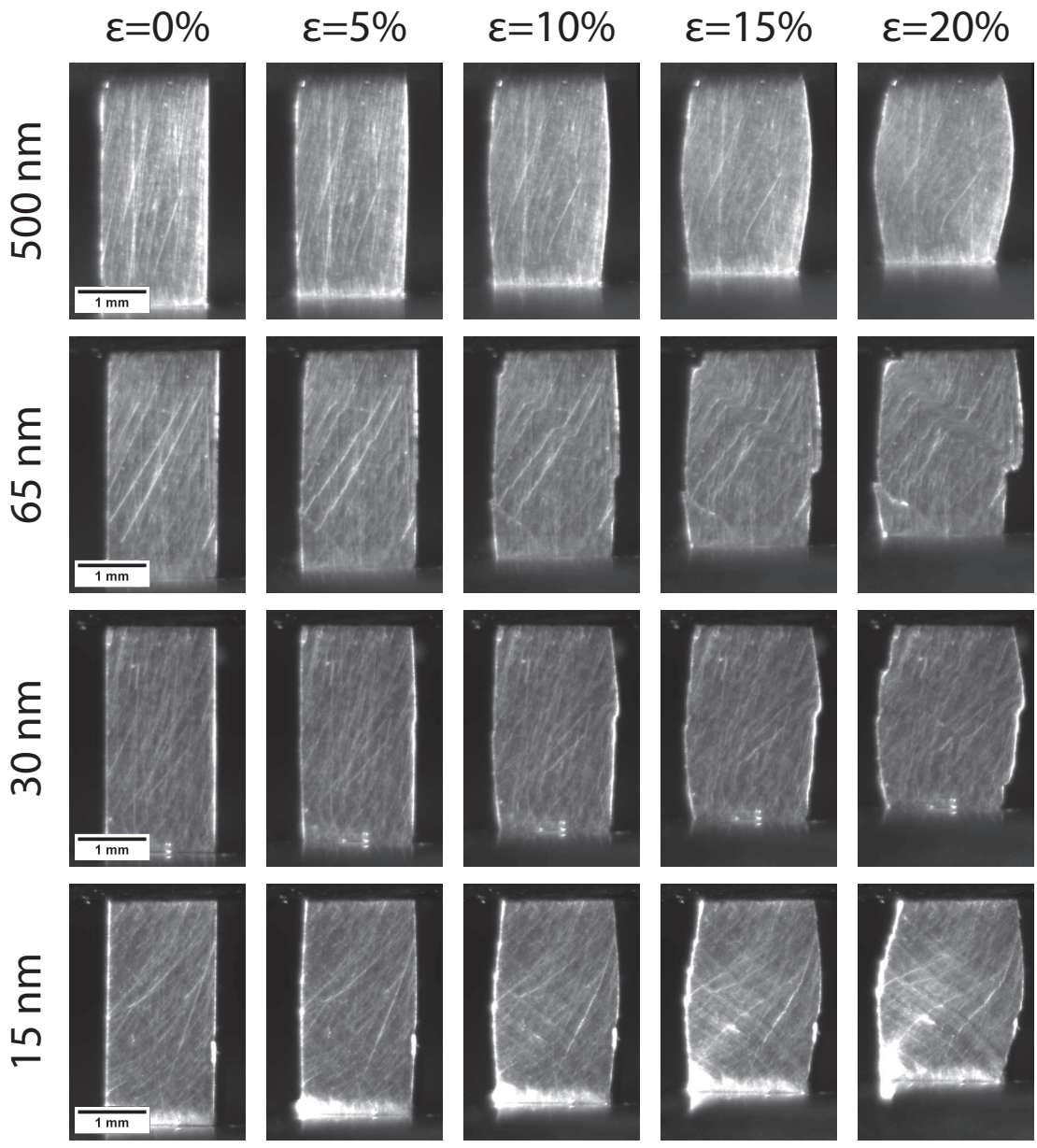

Figure 4.27: Images of RD45 compression specimens at 0, 5, 10, 15, and 20% strain.

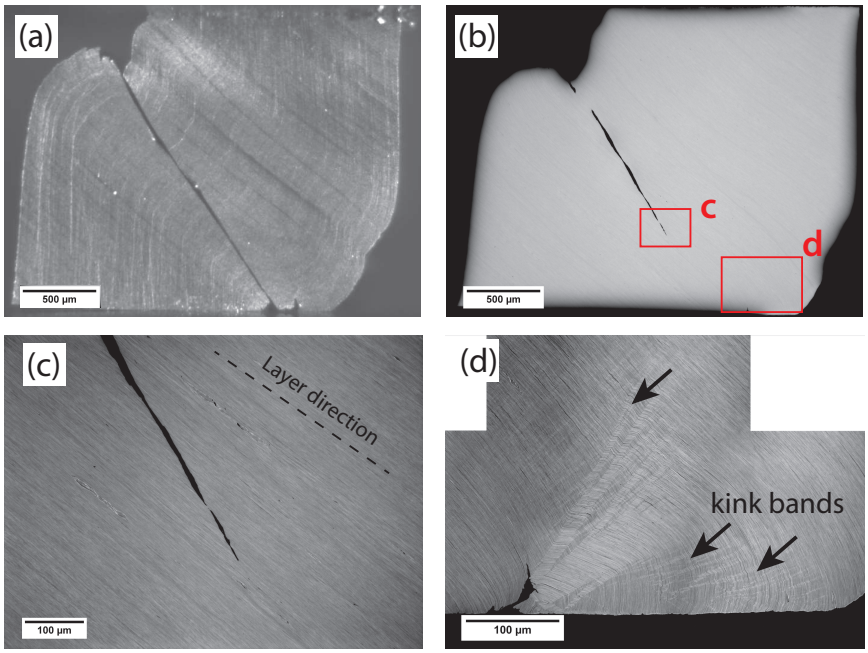

Figure 4.28: Post-test images of a 30 nm TD45 compression test showing an *in situ* image at 25% strain (a), and a bright field photomicrograph of the cross-sectioned specimen (b). Crack formation at a shallow angle with respect to the layer direction occurs at large strain (>20%) (c), and kink bands are observed near the original right hand corner of the specimen where the layers have sheared and impinged on the compression platen.

specimen platen are observed to form kink bands (4.28(d)). Kink band formation in this region results from the layer parallel component of the compressive stress combined with the constraint of the platen which precludes continued layer parallel shear. Due to the formation of both kink band and cracks at large compressive strains, calculations of layer parallel shear stresses from the stress-strain data shown in Figures 4.24 and 4.25 are made using data from small compressive strains (2%).

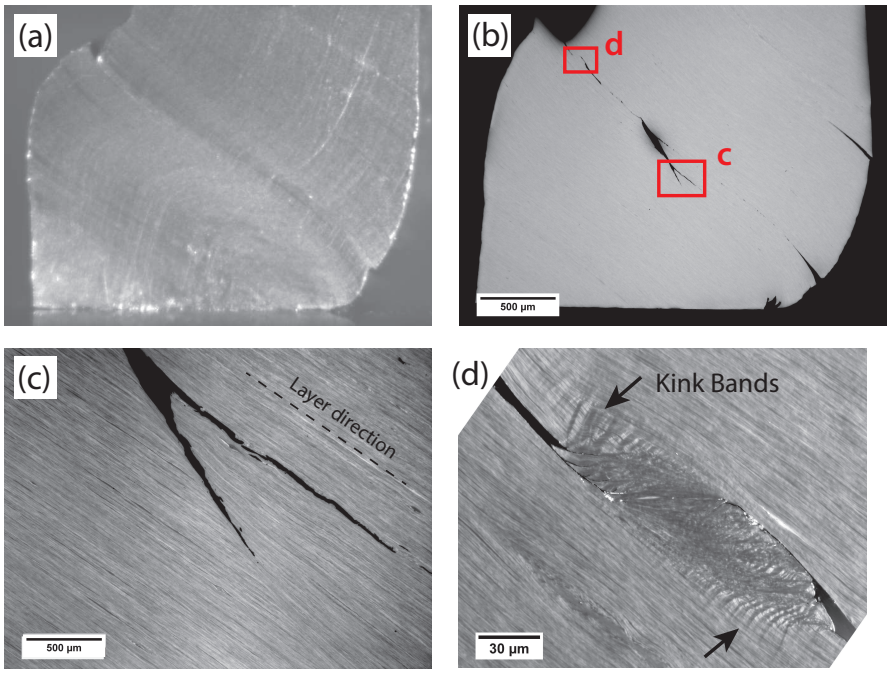

Figure 4.29: Post-test images of a 65 nm TD45 compression test showing an *in situ* image at 25% strain (a), and a bright field photomicrograph of the cross-sectioned specimen (b). Crack formation occurs at large strain (>20%) (c), and kink bands are observed in the wake of the shear crack, where crack surface contact leads to layer parallel compressive stresses.

While the stress-strain results from the 45° compression tests combined with the *in situ* observations indicate that the weak shear plane lies parallel to the layer interfaces, a final confirmation was made by compressing 30 nm Cu-Nb nanolaminate material at various orientations with respect to the layer direction. In all cases, the shear direction was parallel to the TD axis. The resulting flow stresses at 2% compressive strain, shown in Figure 4.30, confirm that the weak shear plane is indeed the plane of the layers. The compressive strength of the off-axis samples decreases as the layer inclination angle moves from 0° to 45° and

increases from 45° to 90°. This matches the behavior expected based on the resolved shear stress acting on the lamellae.

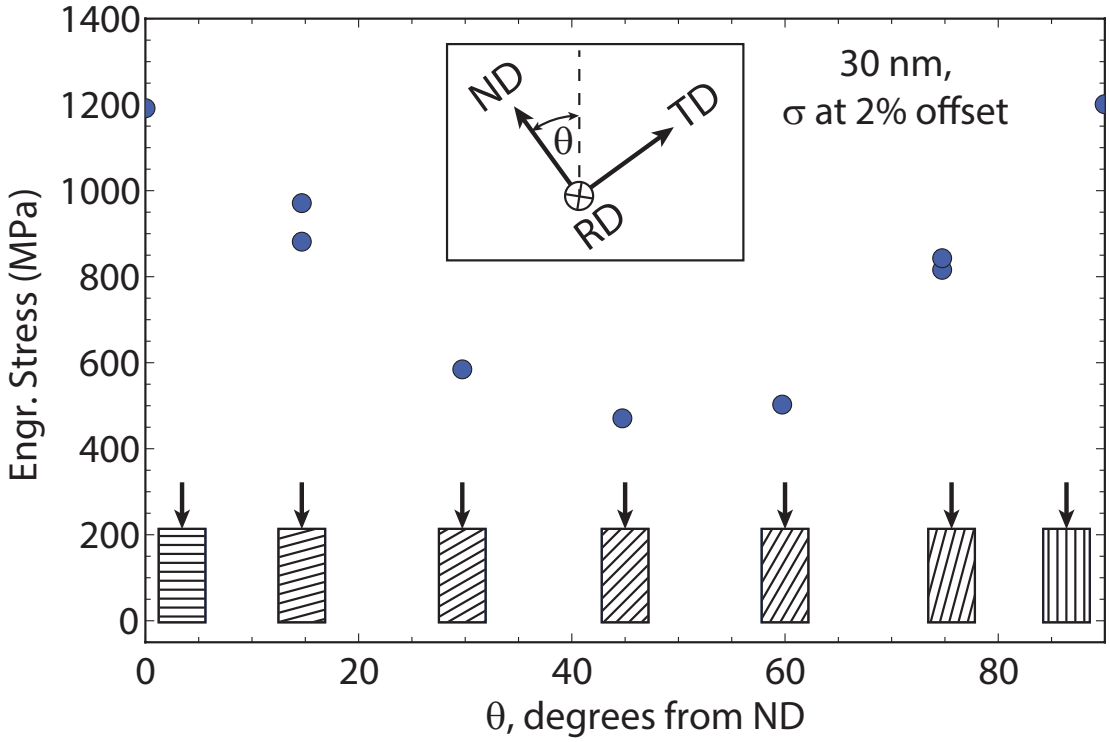

Figure 4.30: Flow stress at 2% offset for 30 nm specimens cut at various angles about the RD (shear direction is the TD).

4.5.2 Compression test anisotropy summary

A comparison of the flow stress at a 2% offset for the ND, TD, RD, TD45, and RD45 compression specimen is shown in Figure 4.31. Variation in plastic anisotropy with layer thickness is evident. At layer thicknesses of 250 nm

and above, the layer parallel shear strength is lower than the layer parallel or layer normal strength, yet no significant effect of layer thickness is observed (all flow stresses appear to increase linearly and commensurate with the decrease in layer thickness). In contrast, as the layer thickness is decreased below 250 nm, the stress required for layer parallel shear diverges from that required for layer parallel stretch (RD, TD, or ND compression). While the Hall-Petch type linear relationship between layer thickness and strength applies to the RD, TD, and ND data, the layer parallel shear strength does not follow this relationship, and in the case of the TD45 compression specimens, remains approximately invariant with respect to layer thickness below 250 nm. As with the RD-TD anisotropy observed for the tensile results presented in Section 4.2, the differences in RD, TD, and ND flow stresses are small and likely attributed to the effects of crystallographic texture. The magnitude of the difference between these flow stresses and the flow stresses of the TD45 and RD45 specimens is very large for sub-100 nm layer thicknesses (differing by 30-60% depending on the layer thickness) and requires additional explanation.

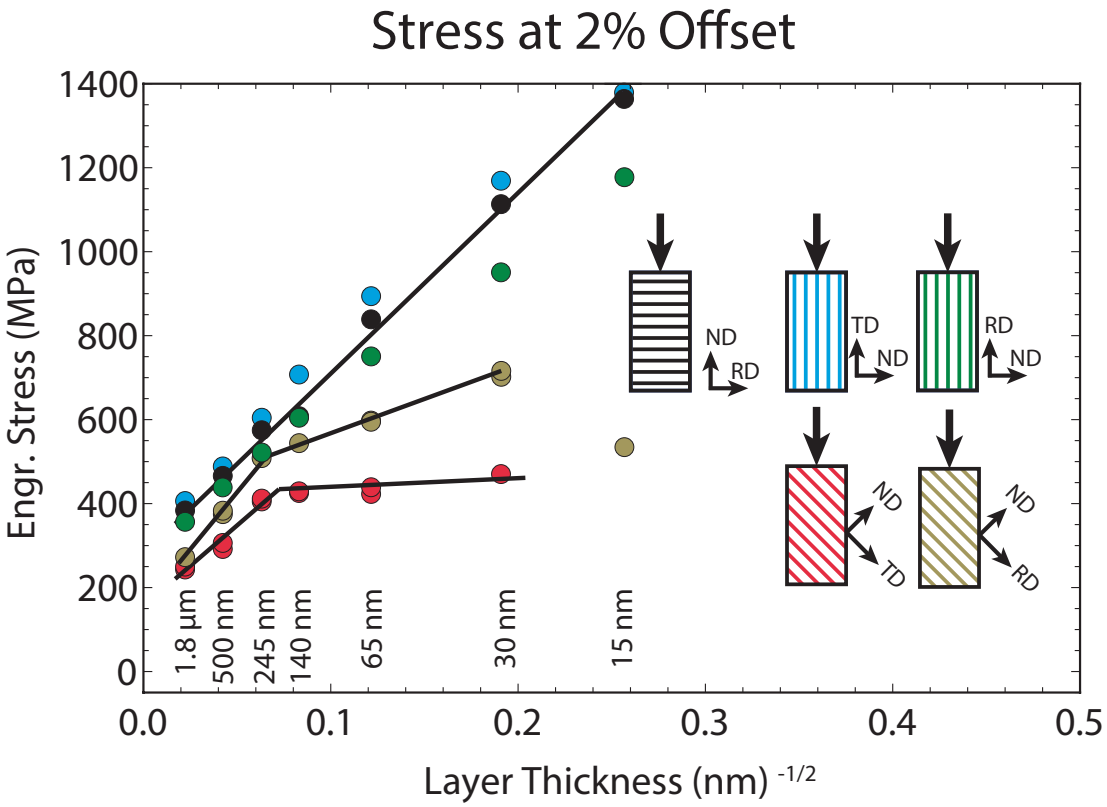

Figure 4.31: Flow stress at a 2% offset for ND, TD, RD, TD45 and RD45 compression specimens.

4.5.3 Microstructural origins of low shear strength

Two aspects of the layer parallel shear response are intriguing: 1) the stress required for layer parallel shear along the RD direction is higher than that for shear along the TD direction (in plane shear strength anisotropy) and 2) the stress required for layer parallel shear is much lower than the stress required for layer parallel stretch (tension or compression parallel to the layer direction, Figures 4.13, 4.19 and 4.20). The effect of various microstructural features on both types of anisotropy will be discussed in the following sections.

Lamellar architecture

Some anisotropy in mechanical response is expected based solely on the lamellar architecture of the nanolaminate material. The layer parallel tensile specimens, layer parallel compression specimens, and layer normal compression specimens all require co-deformation of the Cu and Nb phase. The response of the specimens to the iso-strain loading conditions is expected to be an average of the mechanical response of each phase, as discussed in Section 4.2. Comparison of Figures 4.16, 4.19 and 4.20, and the 2% flow stress data for all compression specimens summarized in Figure 4.31, reveals that the flow stress of each material is roughly comparable in all of these tests, with the dependence of flow stress

on layer thicknesses following a Hall Petch type relationship. Some anisotropy is driven by crystallographic effects on slip system activity, as discussed in Section 4.2, yet the differences are on the order of 10% or less.

The results for the 45° compression specimens are markedly different than the other test orientations: at all layer thicknesses the 2% flow stress for the 45° compression specimens is significantly lower that that of the other specimens (varying from 30-60% lower depending on the layer thickness). The *in situ* imaging shows non-symmetric deformation and indicates that extensive layer parallel shear occurs during compression. For layer parallel shear of a lamellar composite, the co-deformation constraint is removed. That is, the stress-strain response will be governed by the mechanical behavior of the weaker phase while, in theory, the stronger phase could remain elastic. In practice, the slightly wavy interfaces observed in the rolled Cu-Nb nanolaminates result in some degree of mechanical interlocking and preclude such a simple response. Nevertheless, the co-deformation constraint between Cu and Nb is significantly relaxed compared to that required for layer parallel tension/compression.

The effects of constraint and co-deformation may partially explain the flow strength of the 45° compression specimens. While the flow stress of the individual Cu and Nb phases has not been determined for the very fine layer thicknesses studied here, nanoindentation tests performed on ARB processed Cu-Nb

nanolaminates show that, at a layer thickness of 27 μm, the Nb phase is significantly harder than the Cu phase (0.92 versus 1.16 GPa) [89]. This suggests that strain partitioning during layer parallel shear would occur as a result of the relative ease of deformation of the Cu layers.

While a lamellar architecture and phase flow stress mismatch may, in part, explain the difference between the 45° compression flow stress (layer parallel shear) and the RD, TD, and ND compression (layer parallel stretch), it cannot explain the difference in shear strength along the TD versus RD direction. Instead, if this result is to be attributed to the lamellar architecture, layer waviness must be invoked: a difference in layer parallel shear strength for shear in the RD versus TD directions could be the result of varying degrees of layer waviness along these two directions. The layer parallel shear strength of wavy elastic-elastic/perfectly plastic lamellar composites has been explored numerically by Khatam [165]. For a sinusoidal lamellar composite, in-plane shear parallel to the wavy layers requires higher stresses than in-plane shear perpendicular to the direction of waviness (which closely matches the response of a perfectly flat laminate). Characterization of ARB processed Cu-Nb nanolaminates has shown that the layer waviness is greater along the RD than the TD, a result attributed to flow localization during rolling. Thus shear along the RD would be expected to occur at a higher shear stress than shear along the TD, provided the Cu and Nb

phases have different yield or flow stresses. While the effects of layer waviness cannot be quantified without knowledge of the relative mechanical properties of Cu and Nb at the layer thicknesses tested, the flow stress trend expected based on layer waviness matches the observed shear stress anisotropy, where the layer parallel shear strength along the RD is higher than that along the TD.

Crystallographic effects

In addition to the effects of lamellar architecture and layer morphology, the strong crystallographic texture of the Cu-Nb nanolaminates may be responsible for the strength anisotropy. Mean field polycrystal modeling can be employed to determine whether the shear stress anisotropy expected based on crystallographic texture alone is consistent with the experimentally observe shear stress anisotropy. This analysis is similar to the procedure that was used to explain the layer parallel tensile behavior.

Unfortunately, direct comparison of polycrystal modeling results for layer parallel tension/compression with layer parallel shear is not possible due to the lack of information about the relative strengths of the Cu and Nb layers. For a perfectly lamellar composite, the layer parallel shear strength would be governed by the weaker phase while the layer parallel tensile/compressive strength

would be an average of the two individual phase responses (weighted by the relative strength of each phase). Without information about the relative strengths of these very thin layers (30 nm), a weighted average capturing the tensile flow stress cannot be constructed and therefore an accurate comparison between layer parallel stretch and layer parallel shear cannot be made.

Polycrystal modeling can, however, be used to explore the effects of crystallographic texture on the RD versus TD shear anisotropy. The modeling procedure used is identical to that discussed for layer parallel tension (Section 4.2), with the exception that the input velocity gradient corresponded to layer parallel shear along the RD or TD direction instead of plane strain layer parallel tension. The deformation was applied in increments of 1% shear strain, with crystallographic texture and slip system hardening values updated after each increment. The RD shear flow stress (τ_{RD}) was compared to the TD shear flow stress (τ_{TD}) at 5% plastic shear strain as this is the level of shear strain in the unconstrained region of the compression specimens that corresponds to 2% macroscopic compression (shown schematically in Figure 4.32(a)). Single phase simulations were conducted for both the 500 nm and 30 nm material. The results for each phase are presented separately since, without assessing the relative strengths and modeling the effect of waviness on strain partitioning, a satisfactory homogenization scheme cannot be devised.

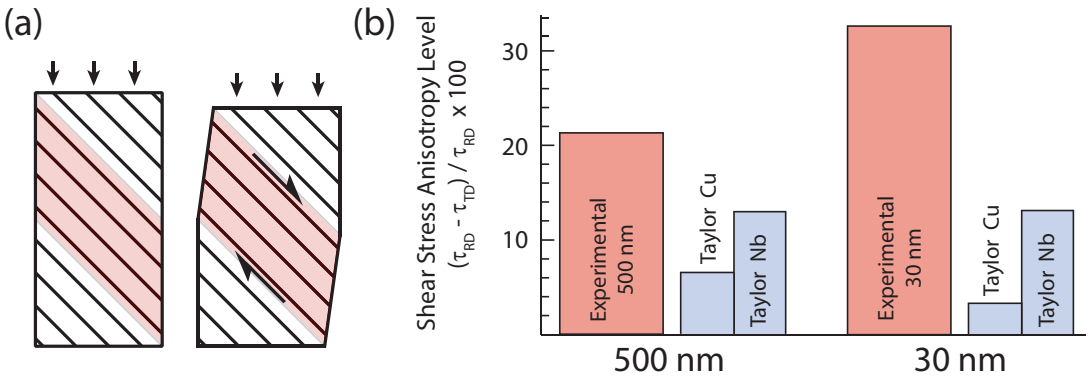

Figure 4.32: Comparison of experimental and modeled shear stress anisotropy. (a) shows a schematic of a 45° compression specimen compressed to 2% compressive strain accommodated *via* 5% shear strain in the unconstrained inclined layers. (b) compares the experimental and modeled shear stress anisotropy for the 500 nm and 30 nm Cu-Nb nanolaminates. Positive values indicate ($\tau_{RD} > \tau_{TD}$).

The predicted anisotropy, show in Figure 4.32(b), was calculated as a percent difference in flow stress for RD shear versus TD shear, where positive values indicate ($\tau_{RD} > \tau_{TD}$). While the degree of anisotropy predicted by polycrystal modeling shows the correct trend for both the Cu and Nb layers (i.e. the predicted τ_{RD} is greater than the predicted τ_{TD}), the difference in magnitude between the experimental anisotropy levels and the predicted anisotropy is significant. While the experimental anisotropy level for the 500 nm and 30 nm laminate material is 21.5% and 33%, the predicted levels for Cu are 6.4% and 3.6% respectively, and the predicted Nb anisotropy levels are 12.8% and 13.2%. The disagreement between experimental and predicted anisotropy is even more severe if it is assumed that the Cu phase is weaker and therefore dictates the

layer parallel shear strength of the composites (as suggested by nanoindentation data of larger layer thickness laminates [89]).

The modeling suggests that the effects of crystallographic texture are insufficient to explain the experimentally observed anisotropy in layer parallel shear strength at either 500 or 30 nm. Further, the model results do not show the experimentally observed increase in RD versus TD shear stress anisotropy as the layer thicknesses decreases. The predicted anisotropy at 30 nm is either equal or less than the anisotropy at 500 nm, depending on the details of the homogenization scheme used. While crystallographic texture effects may contribute in some small part to the observed trend of $\tau_{RD} > \tau_{TD}$, it is clear from Figure 4.32(b) that other factors play a more dominant role in determining the layer parallel shear strength anisotropy.

Interfacial shear strength

The high density of Cu-Nb interfaces in these nanolaminate materials raises the possibility that interfacial shear at the Cu-Nb interfaces controls the material response during layer parallel shear. Interface shear/sliding in PVD Cu-Nb laminates, with planar KS interfaces, has been investigated using atomistic simulations by Wang and coworkers [22, 80]. They found that the interfaces observed

in PVD Cu-Nb had an in-plane anisotropic shear strength that was low compared to the strength of the nanolaminates as estimated from nanoindentation hardness data. For the two types of KS interfaces they considered, the shear strength ranged from 0.4 to 1.1 GPa and 0.06 to 0.18 GPa, with exact interface shear strength depending on the in plane shear direction (due to the crystallographic anisotropy). It was proposed that the sliding mechanism involved dislocation loop nucleation and dislocation glide at the interface. Based on these calculations, the average shear strength of the interfaces in PVD Cu-Nb nanolaminates was taken to be 500 MPa [78]. The low layer parallel shear strength of these PVD laminates was confirmed by 45° micropillar compression tests [163], and direct observation of interfacial shear during TEM nanoindentation suggested that interfacial shear was responsible for the low layer parallel shear strength [163]. The layer parallel shear strength estimated from these experiments was reported as 300 to 550 MPa, within the range of values expected from atomistic simulation of interfacial shearing.

While interface shearing is accepted as a potential deformation mechanism in PVD Cu-Nb nanolaminates, the interface crystallography of ARB processed Cu-Nb nanolaminates is significantly different. The $\{112\}$ KS interfaces observed in ARB Cu-Nb laminates are atomically faceted, and interface sliding is predicted to be very difficult. Wang [21] conducted atomistic modeling (simulation tech-

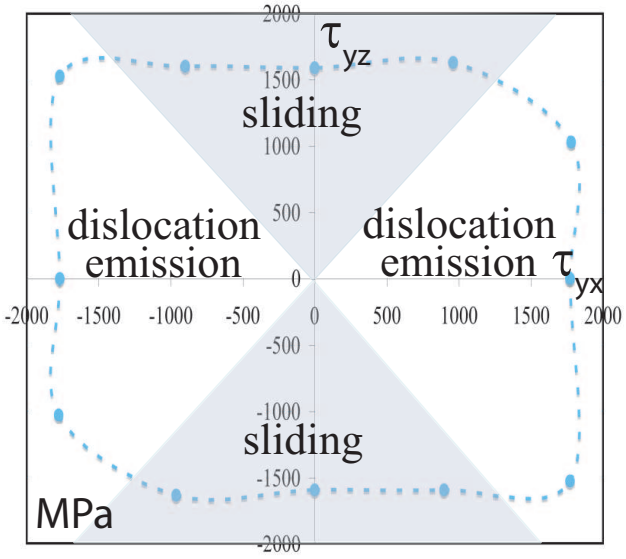

Figure 4.33: Calculated interfacial shear stress map for ARB Cu-Nb $\{112\}$ KS type interfaces. The directions x, y, and z correspond to the RD, ND, and TD directions respectively. Adapted from Reference [21].

niques identical to that used for the earlier work on PVD interfaces) and found that, depending on the shear direction, either 1) shear occurred at the interface at a very high shear stress of approximately 1.5 GPa, or 2) interface shear was not possible and dislocation emission from the interface occurred instead. The two dimensional flow strength map obtained from these calculations is shown in Figure 4.33. While this shear strength has not been experimentally confirmed, the conclusion that interfacial shear of a faceted interface would require much higher stresses than interfacial shear of an atomically flat interface is intuitive.

Given the very high predicted shear strength of the interfaces in ARB Cu-Nb

nanolaminates (1.5 GPa, which would requiring an applied compressive stress of 3 GPa to activate layer parallel shear during compression at 45° to the layers), the experimentally observed low layer parallel shear strength (∼400 MPa for shear along the TD) does not appear to result from shearing of the Cu-Nb interfaces.

Grain Morphology

A final potential cause for the low layer parallel shear strength may be the effects of very high grain aspect ratios in the sub-100 nm layer thickness Cu-Nb nanolaminates. The divergence between the layer parallel shear strength and the layer parallel (or layer normal) compressive strengths appears to begin at a layer thickness of 245 nm (Figure 4.31). This layer thickness marks the point at which the Cu layers become single crystal through thickness, with grains becoming increasingly elongated as the layer thickness is further refined. The correlation between nanoscale, high aspect ratio grains and the observed anisotropy suggests that grain morphology may influence the layer parallel shear strength.

The effects of grain morphology on plastic anisotropy are not well understood and, compared to the effects of crystallographic texture, have received limited attention in the scientific literature. One notable example of grain mor-

phology driven anisotropy is the work of Yoshinaga *et al.* studying the Lankford coefficient, or R-value, of electro-deposited (ED) iron sheets with high aspect ratio needle-shaped grains [166]. The R-value is the ratio of in-plane and through-thickness strains during tension and is commonly used to describe the anisotropic response of sheet metals to tensile straining. Unexpectedly high R-values were observed in the high aspect ratio ED iron and it was shown that the anisotropy exceeded that predicted by considering crystallography alone [166].

This experimental result prompted several theoretical studies, notably by Delannay [144] and Alankar [167]. Both works attributed the plastic anisotropy to the effects of grain shape on slip system activity, with Delannay accounting for the effects of dislocation pile-up backstresses to show that slip systems parallel to the long axis of the grains were favored [144], while Alankar considered the effects of edge and screw dislocation velocities and the effect of grain shape on forest hardening [167]. Both studies concluded that slip system activity on planes lying nearly parallel to the long axis of the grains was enhanced due to the effects of grain shape.

That dislocation motion should occur more readily on slip planes intersecting few obstacles (other dislocations, grain boundaries, twin boundaries, subgrain boundaries, etc.) is intuitive and has been frequently invoked under the idea of a 'effective mean free path' for dislocation glide [144, 168]. Materials that natu-

rally contain a high density of planar oriented boundaries, such as nanotwinned metals, have received particular attention, with dislocation motion parallel to the twin boundaries predicted to be favored [169, 170]. The orientation of slip systems with respect to these twin boundaries has been used to explain the low twin-boundary parallel shear strength that is experimentally observed [171].

While the crystallographic texture of Cu-Nb nanolaminates is considerably more complicated than the nanotwinned metals discussed above, and no single slip plane is predominantly oriented parallel to the Cu-Nb interface, similar arguments based on a dislocation mean free path would suggest that a high density of lamellar Cu-Nb boundaries and a low density of in-plane Cu-Cu and Nb-Nb boundaries should drive plastic anisotropy and a low layer parallel shear strength. This effect from the relative grain boundary/interface densities should become clear when the boundaries are the dominant dislocation obstacles (i.e. when the grain size is sufficiently small that the effects of dislocation entanglement or subgrain dislocation cell formation are minimal). While this argument would require extensive modeling to confirm, the correlation of the experimentally observed low layer parallel shear strength with the transition in grain morphology and aspect ratio, combined with the similar effects demonstrated in nanotwinned metals, lend credence to this proposition. Further work elucidating the role of grain morphology on plastic anisotropy is needed.

4.6 Summary

Microstructural characterization has revealed that significant changes in crystallographic texture, grain size/morphology, and Cu-Nb interface structure occur as the layer thickness of Cu-Nb multilayers is refined using ARB. The crystallographic texture of both Cu and Nb strengthens as the layer thickness decreases, and $\{112\}_{Cu}\|\{112\}_{Nb}\quad[111]_{Cu}\|[110]_{Nb}$ emerges as the predominant and stable interface orientation relationship. Grain refinement occurs during rolling, with even coarse (20 μm) multilayers possessing sub-micron grain sizes. With further processing, both the Cu and Nb layers become predominantly single crystal in the through-thickness direction. This transition occurs at 245 nm in the Cu phase and between 140 and 30 nm in the Nb phase. The grains in these nanolaminates become extremely elongated, with aspect ratios exceeding 1:50:5 (ND:RD:TD) at layer thicknesses $\leq$ 65 nm [123].

Uniaxial tensile tests conducted parallel to the rolling direction (RD) and transverse direction (TD) demonstrate that ductility generally decreases with decreasing layer thickness, however at 30 nm both high strengths (1200 MPa) and significant ductility (8%) are achieved. The yield strength increases monotonically with decreasing layer thickness, consistent with the Hall-Petch relationship, and significant in-plane flow stress anisotropy is observed at all layer

thicknesses. Transverse direction tensile specimens show a higher flow stress compared to rolling direction specimens and polycrystal modeling demonstrates that this anisotropy can be attributed primarily to the effects of crystallographic texture.

Compression tests conducted with the stress axis parallel to the ND, RD, and TD confirm the Hall-Petch type relationship between layer size and strength. The flow strength of samples tested in these orientations is comparable for all layer thicknesses, with the small variations that exist likely resulting from the effects of crystallographic texture (as demonstrated for the tensile specimens). The formation of kink bands is observed during layer parallel compression tests, and will be discussed further in Chapter 5.

The Cu-Nb nanolaminates possess a low layer parallel shear strength, as indicated by compression tests conducted at 45° to the layered structure. The shear strength for RD shear is higher than that for TD shear, an effect that is consistent across all layer thicknesses and may be attributed to the effects of layer waviness. In contrast to the mechanical tests where co-deformation of the Cu and Nb layers is required (layer parallel tension/compression and compression along the ND), the relationship between strength and layer size does not follow a Hall-Petch relationship for layer parallel shear. Instead, the shear strength either plateaus (for TD shear) or shows a weak increase with decreasing layer

size (RD shear) at layer thicknesses below 245 nm. The result is that ARB Cu-Nb nanolaminates become increasingly anisotropic as the layer thickness falls below 245 nm, with the stress required for layer parallel stretch diverging from that required for layer parallel shear. It is proposed that the effects of grain aspect ratio are responsible for the increase in anisotropy with decreasing layer size (and increasing grain aspect ratios). While additional studies elucidating the effects of grain shape on plastic anisotropy are needed, the experimental results indicate that the layer parallel shear versus layer parallel stretch anisotropy increases dramatically below 245 nm and is correlated with an increase in grain aspect ratio. The role of this anisotropy in driving an unusual form of deformation known as kink band formation will be discussed in the following chapter.

Chapter 5

Kink Band Formation

In this chapter, the phenomenon of kink band formation in ARB Cu-Nb nanolaminates will be discussed.[1] Detailed analysis of the kink bands formed during the bulk compression tests shown in Section 4.4 will be presented, with particular emphasis on the microstructural observations that provide insight into the kinematics of kinking. This will include discussion of the geometry of kink bands and the deformation at a kink band boundary. The results from micropillar compression tests conducted at Los Alamos National Laboratory will be discussed. These tests provide a clear view of the mechanism of kink band formation in small scale specimens, where a single kink band is observed to form.

[1] A substantial amount of material in Chapter 5 is reproduced from *Strain fields induced by kink band propagation in Cu-Nb nanolaminate composites* T.J. Nizolek, M.R. Begley, R.J. McCabe, J.T. Avallone, N.A. Mara, I.J. Beyerlein, and T.M. Pollock, Submitted to Composites Part A.

The resulting load-displacement data (corresponding to the formation of a single kink band) quantifies the geometric softening that results from the rotation of material within the band.

The insight into the kinematics of kink band formation gained from these observations is used to construct a simple analytical model of plane strain kink band formation in a perfectly plastic anisotropic material. Bifurcation analysis is not conducted, thus this model attempts to explain the formation of a kink band from an initial material defect. In the model, the stresses are uniform throughout the sample and kink band formation is assumed *a priori*. The strain rates and deviatoric stresses required to form a kink band are obtained as a function of the kink band geometry. Conditions are then sought for which the necessary stresses for kink band formation violate the yield criterion outside of the kink band, a procedure which is found to place bounds on the acceptable kink band inclination angle (β). The stresses and strains during kink band formation are then used to obtain the plastic work rate during kinking. Arguments based on the work rate indicate that continued shear and rotation of a kink band beyond $\phi = 2\beta$ is unfavorable compared to the formation of a new kink band.

While much of this chapter is devoted to analyzing the deformation within a kink band, Section 5.6 is devoted to the phenomena of kink band propagation and analysis of the strain fields generated in the surrounding specimen. *In*

situ SEM compression tests provide high magnification views of kink band propagation in bulk (1 mm$\times$1 mm$\times$2.5 mm) specimens, elucidating the sequence of events leading to kink band formation as well as kink band intersections. Kink band propagation is further analyzed using digital image correlation strain mapping during bulk compression testing. The displacement and strain fields indicate that significant distortion of the specimen is required when kink bands form *via* initiation followed by propagation across a large specimen. DIC strain maps for the material surrounding a propagating kink band will be presented and used to show that the energy dissipated in this material is significant (on the order of that dissipated by the shear within a kink band). Comparisons will be drawn between a propagating kink band and a mode II crack, and the implications for a fracture mechanics based approach to kink band formation will be discussed.

The final section of this chapter is devoted to the geometry of kink band intersections. Rules initially developed for deformation twin intersections are shown to be applicable to kink band intersections. From these rules, a required angular relationship between the crossing kink band and the crossed kink band is obtained. It is also determined that kink bands with a band inclination angle $<22.5^\circ$ cannot be crossed by a second kink band. Even when the orientations of the kink bands are such that one kink band may cross the other, the formation of a kink band intersection results in a constraint that inhibits the crossed kink

band from broadening to accommodate further compressive strain. This analysis of kink band intersections elucidates the sequence of events required to form the complex networks of kink bands observed in Cu-Nb nanolaminates.

5.1 Introduction

5.1.1 Kink band morphology and definition

Kink band formation is a type of strain localization that has been observed in a multitude of anisotropic single phase and composite materials. While significant attention has been given to kink band formation in fiber composites due to the technological importance of these materials [151–153], kink bands have also been observed in oriented polymers [154], geological and mineral samples [172, 173], biological materials such as wood and abalone shell [174, 175], and low symmetry single crystals such as cadmium, ceramic ternary carbide 'MAX' phases, and freshwater ice [155–157]. Figure 5.1 shows images of kink bands in several different material systems. Despite the broad range of material classes and constitutive behaviors, the observed deformation bands possess common features that warrant the use of the general term 'kink band.' A kink band can be defined by the following characteristics: 1) the deformation band consists

of a region that is either microstructurally or crystallographically misoriented from the rest of the sample, 2) the angle of misorientation (ϕ) is approximately uniform across the width of the band, and 3) there exists a specific relationship between the boundary of the deformation band and the rotation of the material within the deformation band such that the boundary nominally bisects the angle made between the deformed and undeformed material ($\phi = 2\beta$ as shown in Figure 5.2(a)). This definition excludes other types of deformation bands such as shear bands, compaction bands, and slip bands. While defining a kink band based on these three morphological characteristics is appealing in that it does not place restrictions on the kinematics or deformation processes of kink band formation (which may vary among material classes), a definition based solely on morphology would necessarily include deformation twins as a type of kink band. Twins are not generally considered kink bands, although the striking geometric similarities have been discussed [176]. While twins, from a continuum mechanics perspective, could be considered to be a special subset of kink bands where the magnitude of shear is prescribed by the need to preserve the crystallographic structure, convention dictates that twins should be excluded. This requires the addition of a somewhat contrived fourth criterion for kink bands: 4) the plane of the kink band boundary must not be restricted to a specific crystallographic plane.

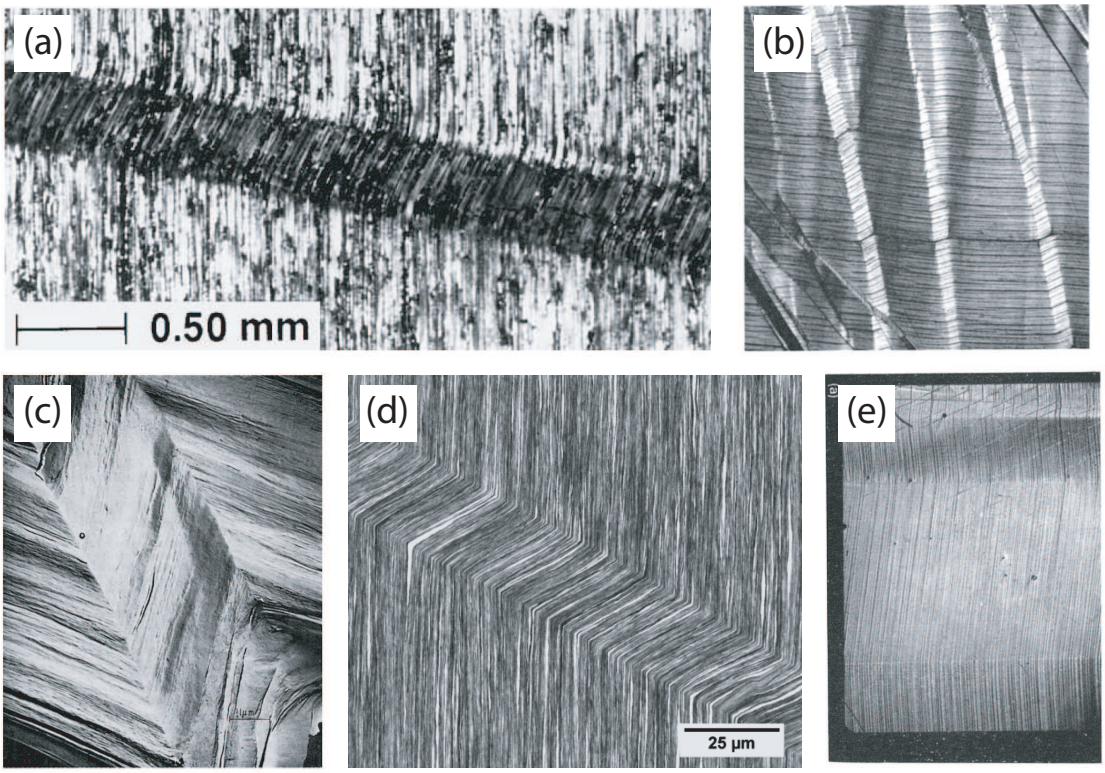

Figure 5.1: Images showing examples of kink bands in several material systems. Kink bands have been observed to form in (a) an AS4-PEEK unidirectional polymer matrix composite (from Reference [177]), (b) pyrolytic graphite (from Reference [178]), (c) oriented polyethylene (from Reference [154]), (d) a 30 nm Cu-Nb nanolaminate, and (e) an Ni-Ni3Al alloy single crystal (from Reference [179]). (a),(b), and (e) are reproduced with permission from Elsevier while (c) is reproduced with permission from John Wiley & Sons.

A common feature of all materials which form kink bands is pronounced mechanical anisotropy. Specifically, the material must possess a set of planes along which the shear strength is very low. For example, in unidirectional fiber or layered composites the necessary anisotropy for kink band formation occurs due to the architecture of the composite; shear on a plane parallel to the fibers or layers requires a much lower stress than shear along any other direction due to the lower strength of the matrix phase [151, 158]. In single phase materials which form kink bands, such as low symmetry single crystals, the anisotropy is inherent to the material, with the planes of low shear strength being the (often single set of) crystallographic slip planes on which dislocation glide readily occurs [159, 160].

When the material is oriented so that the planes of low shear strength are nominally parallel to a compressive stress, a region or band of the material containing slightly misoriented fibers or layers may yield (prior to global yield) as a result of the fiber parallel shear stress. Due to the constraint imposed by the surrounding material, this band shears and rotates the fibers, a process that initially increases the resolved shear stress parallel to the fibers in the misoriented region (Figure 5.2(b)). The resultant geometric softening produced by shear and rotation creates a localized band of misoriented material. The band 'locks up' after a certain amount of rotation (at $\phi = 2\beta$, Figure 5.2(a)), with further

specimen compression being accommodated either by additional kink band formation or by broadening of the original kink band [153, 158]. While kink band formation is most easily visualized by considering the presence of an initial misorientation, bifurcation analysis indicates that kink band formation could occur even in perfectly aligned materials [180].

Kink band formation (achieving a fully rotated ($\phi = 2\beta$) kink band spanning the entire cross-section) can be envisioned to occur in two ways: 1) a region of material shears uniformly across the entire specimen (Figure 5.2(b)), or 2) formation occurs first by nucleation at a stress concentration followed by propagation of the band across the specimen (Figure 5.2(c)). Reports in the literature offer conflicting views of which of these two mechanisms best describes kink band formation, with some experimental studies [158, 177] indicating that kink bands form by propagation across a specimen, while other experimental studies and analytical models [181–183] treat kink band formation as if a kink band occurs through uniform shear and rotation of a band of material.

5.1.2 Origins of the kink band geometry

Previous studies [152, 153, 172–174, 184–187] of kink bands in a wide range of materials have shown that the angle of rotation of material within a

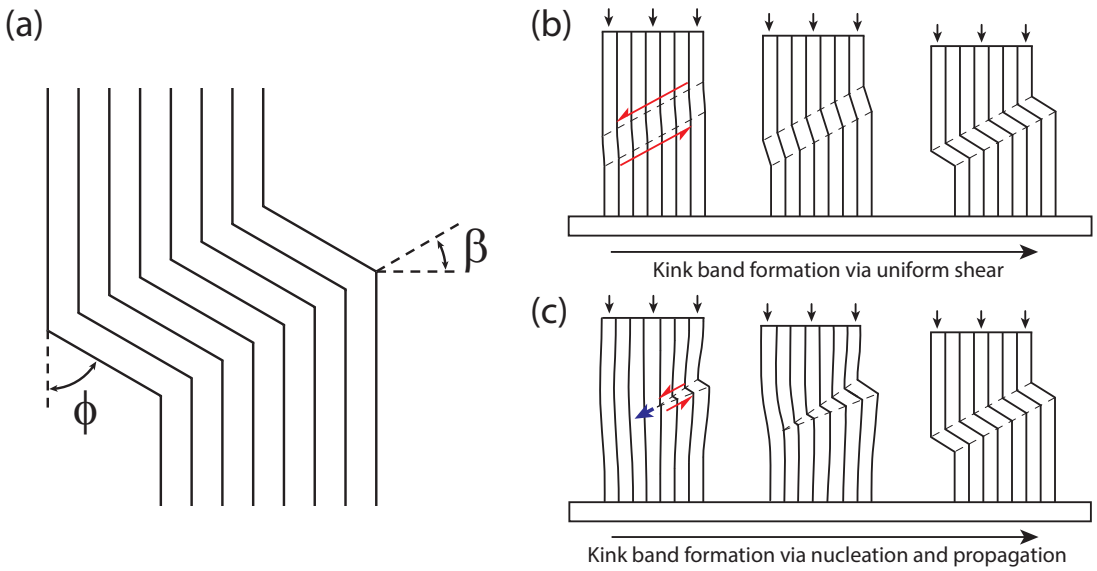

Figure 5.2: (a) Schematic illustrating the morphology of a kink band showing the $\phi = 2\beta$ relationship. The kinked sample can be envisioned to form *via* the uniform shearing of a band of material (b) or by an initiation and propagation sequence (c). The final deformed state may be nearly identical.

kink band (ϕ) is twice the angle made between the band and fiber/layer normal direction (β), as shown in Figure 5.2(a). This condition ($\phi = 2\beta$) imposes a limitation on the shear strain within a kink band and distinguishes kink bands from other forms of localization, such shear bands, were extremely large local strain can occur and lead to failure [140, 188–190].

For many systems that form kink bands, such as fiber composites, the $\phi = 2\beta$ relationship has been explained by considering the layer transverse strains within a kink band. For $\phi < \beta$, dilatation within the kink band is required - the fiber/layer spacing must be larger than the fiber/layer spacing in the non-

kinked material (Figure 5.3(a)). At $\phi = 2\beta$, the fiber/layer spacing within the kink band is required to be equal to the layer spacing outside the kink band, while for $\phi > 2\beta$, the layer spacing within the band would be less than the spacing outside of the band. This is demonstrated schematically in Figure 5.3. For fiber composites materials consisting of high strength fibers in a compliant matrix, kinking is envisioned to occur by the uniform rotation of a band of material traversing the specimen (as shown in Figure 5.2(b)). The fibers are considered to be inextensible during this process, a reasonable assumption given the lack of plasticity in the often studied glass or carbon fiber reinforcement materials. Therefore, the positive layer transverse strains during rotation from $\phi = 0$ to $\phi = \beta$ are accommodated initially by elastic strains in the compliant polymer matrix, followed by debonding at the fiber-matrix interfaces at rotations larger than a few degrees [191]. This debonding is required as, although compliant, the polymer matrix cannot entirely accommodate the large non-isochoric deformations associated with large transverse strains and negligible longitudinal strains along the length of the kinked fibers. The voids between the debonded fibers and matrix reach a maximum size at $\phi = \beta$ (maximum transverse strain) and begin to close up as fiber rotation continues towards $\phi = 2\beta$. When a rotation of $\phi = 2\beta$ is reached, the layer transverse strains go to zero, the fibers are again in intimate contact with the matrix, and further rotation is largely pro-

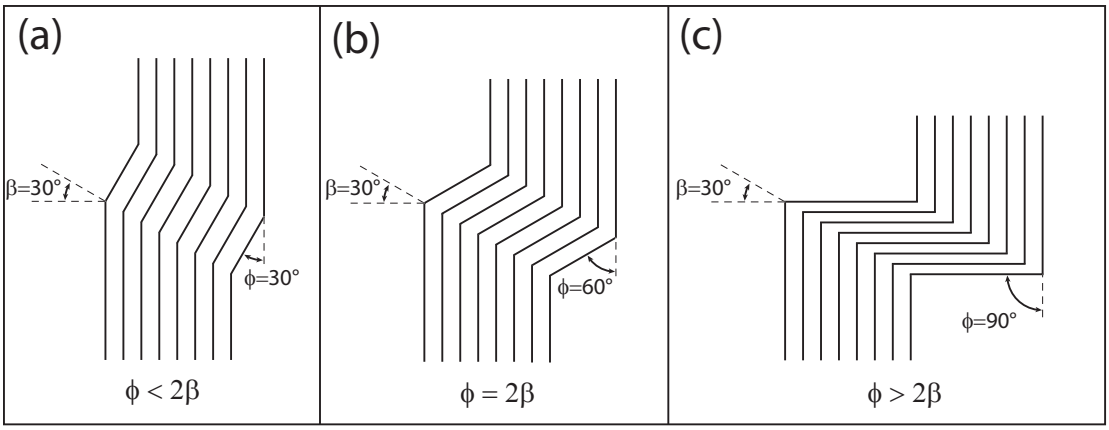

Figure 5.3: Schematic illustrating the transverse strains associated with various ϕ to β relationships.

hibited by incompressibility within the band. That is, while positive transverse strains (Figure 5.3(a)) are accommodated by debonding and void formation, negative transverse strains cannot be accommodated with a volume preserving matrix and inextensible fibers [158].

According to Vogler [187], that minimization of the geometrically necessary transverse strains leads to the $\phi = 2\beta$ condition was first suggested by Paterson and Weiss in 1966 [172], although Paterson cites an even earlier work by Mügge from 1897 [192]. This rationale has been widely accepted and incorporated into kink band analysis, for example, by Evans and Adler [152], Fleck and Budiansky [193], and Moran *et al.* [153]. The explanation for the ubiquitous $\phi = 2\beta$ relationship arrived at by consideration of transverse strains has a sound basis in fiber composite literature where fibers can be treated as essentially rigid.

Kink bands in metallic nanolaminates also display the $\phi = 2\beta$ angular relationship, however the traditional argument for this relationship is difficult to apply to layers consisting of ductile metals. As with fiber composites, the stress required for layer parallel shear in Cu-Nb nanolaminates is much lower than that required for layer parallel tension or compression (Figure 4.31), yet neither phase can be treated as rigid or purely elastic during kinking. Further, the minimal load drop associated with kink band formation in Cu-Nb nanolaminates (Section 4.4) stands in contrast to the response during kinking in fiber composites, where kink band formation often occurs during a tremendous load drop (with the stress frequently falling to one half of the value prior to kink band formation [153], provided complete failure does not occur). Figure 5.4 compares the mechanical response of a 30 nm Cu-Nb TD compression specimen during kink band formation to that of several other materials that form kink bands. The combination of high strengths and large deformability in the Cu-Nb material is striking. These differences in constitutive behavior and mechanical response raise the question of whether the non-volume preserving kinematics (interface debonding followed by the collapse of the band to $\phi = 2\beta$) that are envisioned for kinking in fiber composites is applicable to kinking in ductile metallic nanolaminates.

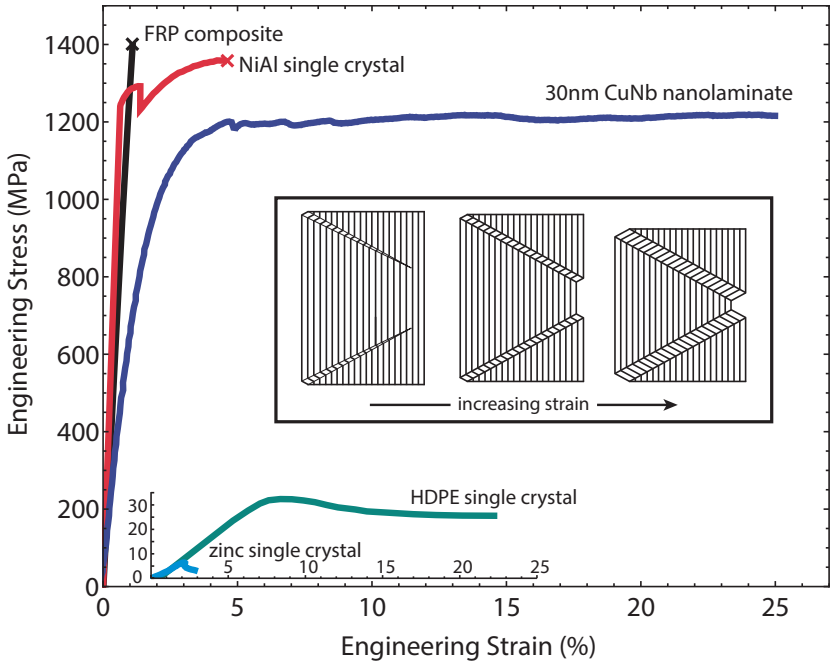

Figure 5.4: Unidirectional fiber reinforced composites [194] and intermetallics such as NiAl [195] form kink bands at high stresses but display low strains to failure while highly oriented polymers [196] and single crystal metals [197] form kink bands at stresses far too low for structural applications (<40 MPa). Kinking in Cu-Nb nanolaminates results in an exceptional combination of very high strength and large deformation when compared to conventional kinking materials. Reproduced from Reference [149] with permission from John Wiley and Sons.

Thus several questions regarding kink band formation in Cu-Nb nanolaminates need to be addressed:

1. Are the non-volume preserving kinematics employed in fiber composite models of kink band formation applicable to kinking in Cu-Nb nanolaminates?

2. Is minimization of transverse strains sufficient to explain the $\phi = 2\beta$ relationship observed in these metallic nanolaminates?

3. Is the formation mechanism of kink bands in Cu-Nb nanolaminates that of uniform shearing of a band of material (Figure 5.2(b)), or one of nucleation followed by propagation of a kink band (Figure 5.2(c))?

These questions will be addressed in the following sections using post-test metallographic analysis of the layer parallel compression tests, *in situ* SEM and micropillar compression tests, and digital image correlation strain mapping during layer parallel compression.

5.2 Post-test analysis of kink bands

In this section, post-test microstructural analysis of kink bands formed in the bulk compression specimens (discussed in Sections 4.4) is presented and used to infer information about the kinematics of kink band formation. As previously noted, kink band formation is the dominant deformation mechanism during layer parallel compression of the sub-100 nm Cu-Nb nanolaminates. Figure 5.5 shows a composite image of a 65 nm TD compression specimen. A bright field low magnification light optical image (Figure 5.5(a)) shows that, despite the

kink bands appearing as dark bands in the *in situ* video recording (Sections 4.4), kink bands do not correspond to cracks or large-scale material damage (although a small delamination crack is evident in the non-kinked material near the top of the specimen). A low magnification polarized light microscopy image (Figure 5.5(b)) highlights the kink bands present in Figure 5.5(a), showing that the pronounced inhomogeneous shape change of the specimen results from kink band formation. While the two large kink bands emanating from the specimen corners at the left are shown in Figure 5.5(b), smaller kink bands have also formed in other regions (Figure 5.5(c)).

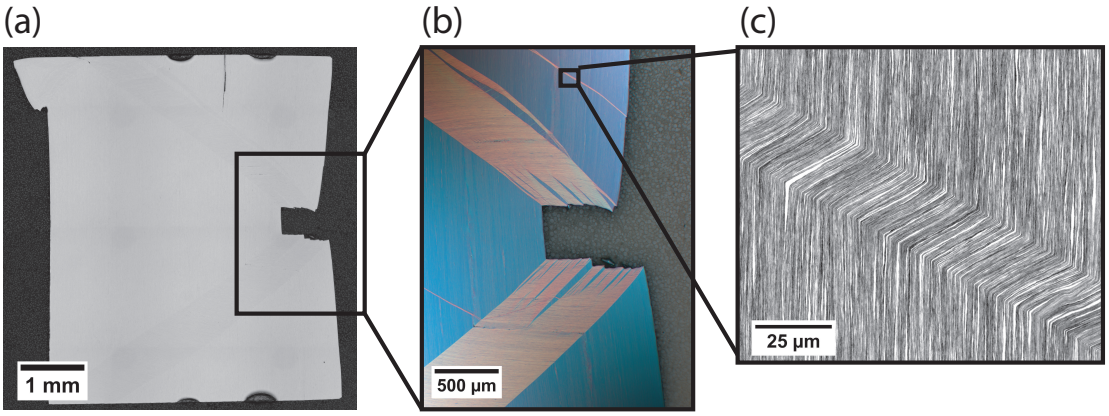

Figure 5.5: Bright field LOM (a), polarized LOM (b), and BSE SEM (c) images of kink bands in a 65 nm TD compression specimen. Adapted from Reference [91] with permission from Springer.

Similar observations of kink bands were made in the 30 nm and 15 nm compression specimens. As noted in Section 4.4, the compressive strain at which kink bands initiated decreased with decreasing layer thickness. As all compres-

sion tests were interrupted at 25% compressive strain, this means that a larger fraction of the total compressive strain was accommodated through kink band formation in the smaller layer thickness samples. Presumably due to this effect, as well as the increasing anisotropy of the 30 and 15 nm specimens, the appearance of these kinked samples tended to be more complex, with kink bands intersecting one another, bifurcating, and forming complicated networks of localized strain. Figure 5.6 shows a single kink band (Figure 5.6(a)), the intersection of two kink bands (Figure 5.6(b)), and a kink band bifurcation (Figure 5.6(c)). Figure 5.6(d) and (e) show some of the complex localized deformation networks that result from combinations of these features in a 15 nm TD compression specimen.

Kink bands observed during post-test analysis of Cu-Nb nanolaminates display the $\phi = 2\beta$ relationship as shown in Figure 5.7. This relationship is shown at the boundary of a kink band in a 30 nm TD compression specimen in Figure 5.7(a). Figure 5.7(b) shows that, while β can vary for different kink bands within a specimen, $\phi = 2\beta$ is observed for both kink bands in the lower right hand corner of a 30 nm compression specimen. This relationship is even observed at the intersection of two kink bands (Figure 5.7(c)), with both kink bands and the 'twice sheared' region where the kink bands overlap showing $\phi = 2\beta$. This relationship can be readily detected by observing that the kink

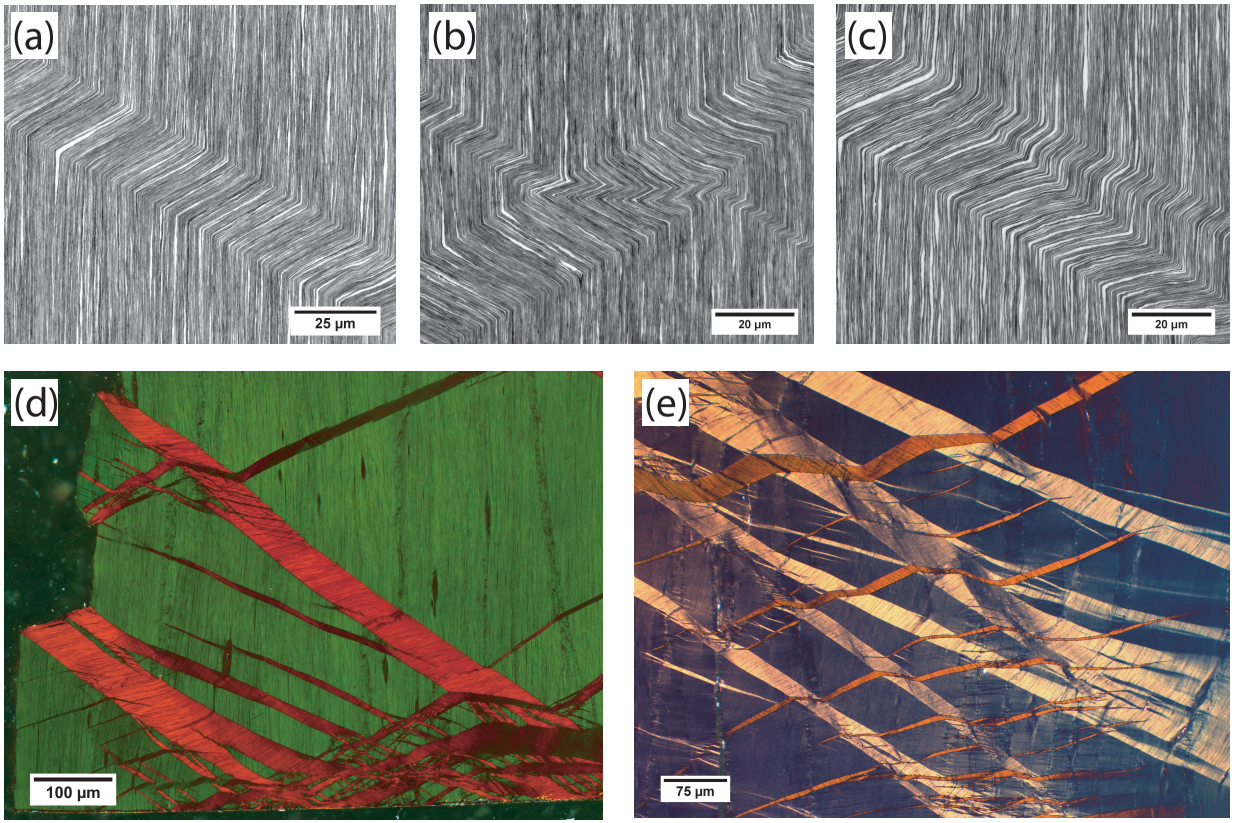

Figure 5.6: Images (a) through (c) show high magnification BSE SEM images of kink bands: a single kink band in a 65 nm TD specimen (a), the intersection of two kink bands in a 30 nm TD specimen (b), and a kink band bifurcation in a 65 nm TD specimen (c). Images (d) and (e) are polarized light optical micrographs showing complex networks of kink bands in a 15 nm TD specimen. (d) and (e) reproduced from Reference [91] with permission from Springer.

band boundary bisects the angle between the kinked and non-kinked layers (i.e. the boundary appears as a mirror plane in the layered structure).

The invariant angle of the layers within a kink band indicates that the shear strain within a kink band is homogeneous. This is also demonstrated by the linear distortion of a FIB deposited series of platinum lines (initially a $4\,\mu$m$\times 4\,\mu$m series of 100 nm thick lines) deposited perpendicular to the layers in a 65 nm TD compression specimen prior to compression and kink band formation. The distortion of these lines is shown in Figure 5.7(d), where approximately one half of the grid has been sheared by a kink band. The $\phi = 2\beta$ relationship states that, given the band angle β, both the rotation ϕ and the shear strain within the kink band are known. The Lagrangian shear strain parallel to the kink band boundary (γ) is given by Equation 5.1, when the $\phi = 2\beta$ relationship is assumed (a detailed discussion of kink band kinematics will be given in Section 5.5).

$$\gamma = 2\tan\beta \tag{5.1}$$

5.2.1 Kink band boundary geometry

While post-test microstructural observations of the material inside a kink band show that $\phi = 2\beta$, they do not provide information regarding whether the

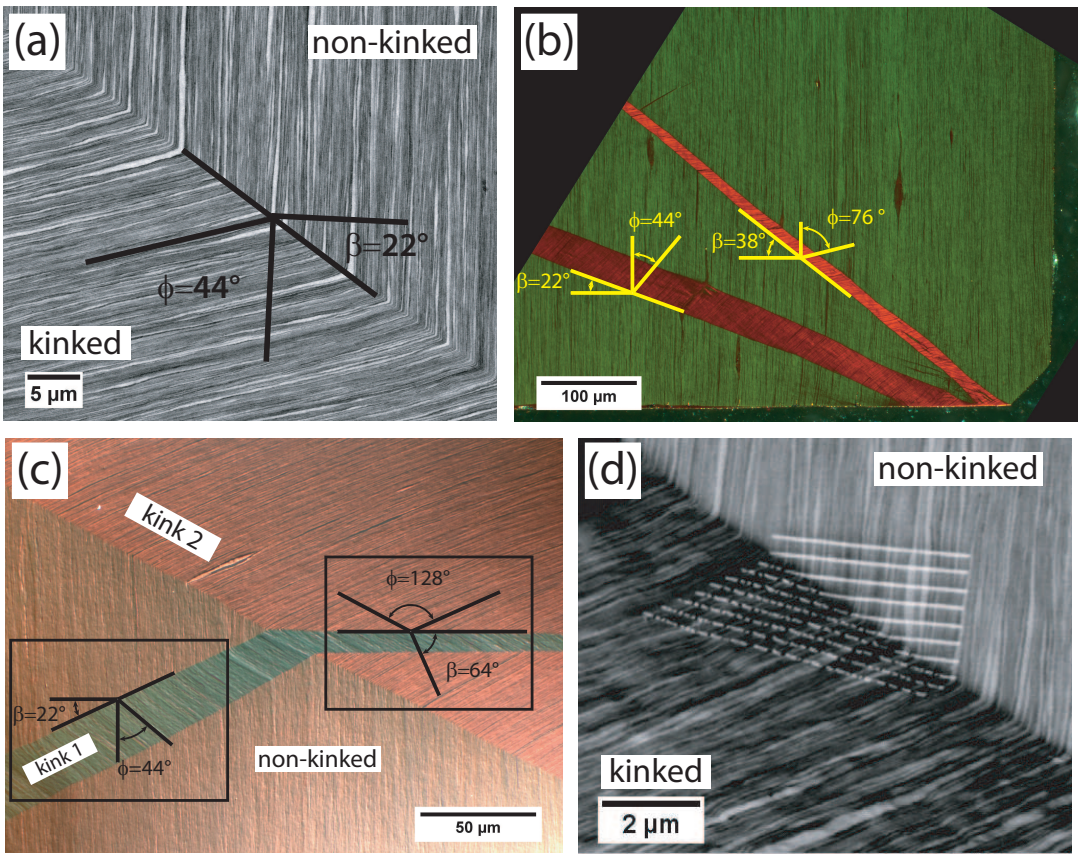

Figure 5.7: Images showing the $\phi = 2\beta$ relationship in kinked nanolaminates. A BSE SEM image of a kink band boundary in a 30 nm TD compression specimen (a), polarized LOM images of kink bands near the corner of a 30 nm TD compression specimen (b) and kink bands intersecting in a 30 nm TD compression specimen (c) all display this relationship. The homogeneous shear within a kink band is indicated by the invariance of the layer orientation within a band, as well as by the linear distortion of a series of FIB deposited platinum lines (d). Images (b) and (c) reproduced from Reference [149] with permission from John Wiley and Sons.

deformation process that achieved this state was isochoric. Even if delamination had occurred during rotation from $\phi = 0$ to $\phi = 2\beta$, any voids or separations between the layers would have closed as the material rotated from $\phi = \beta$ to $\phi = 2\beta$ (as discussed in conjunction with Figure 5.3). However, *in situ* video recording during bulk compression tests (Section 4.4) revealed that kink bands broaden during compression. This observation indicates that non-kinked material is transformed into kinked material by plastic deformation at the kink band boundary during broadening. Thus if non-isochoric deformation occurs during transformation from $\phi = 0$ to $\phi = 2\beta$, some evidence of void formation or fracture should be present at the boundary (although layer fracture is not expected for these ductile phases).

Several mechanisms for the formation of a boundary between kinked and non-kinked material can be envisioned and are shown schematically in Figure 5.8. The only arrangement, other than the infinitely sharp boundary shown in previous schematics, that would allow the layer thickness to remain constant both inside, outside, and at the boundary of the kink band without void formation is that of 'concentric folding' (Figure 5.8(a)). In this arrangement, the apparent boundary width would change along the length of a kink band as each subsequent layer would be bent to a radius of curvature larger than than the previous layer ($r_n = r_{n-1} + h$ where r is the radius of curvature and h is the layer

thickness). If a constant radius of curvature, and therefore boundary width, is required, the boundary could appear as depicted in Figure 5.8(b) or Figure 5.8(c). In Figure 5.8(b), the layer thickness remains constant, and void formation occurs at the boundary. This type of kink band boundary has been reported by Dodwell [198] for kink bands in compressed stacks of paper and has been analyzed in detail in Reference [199].

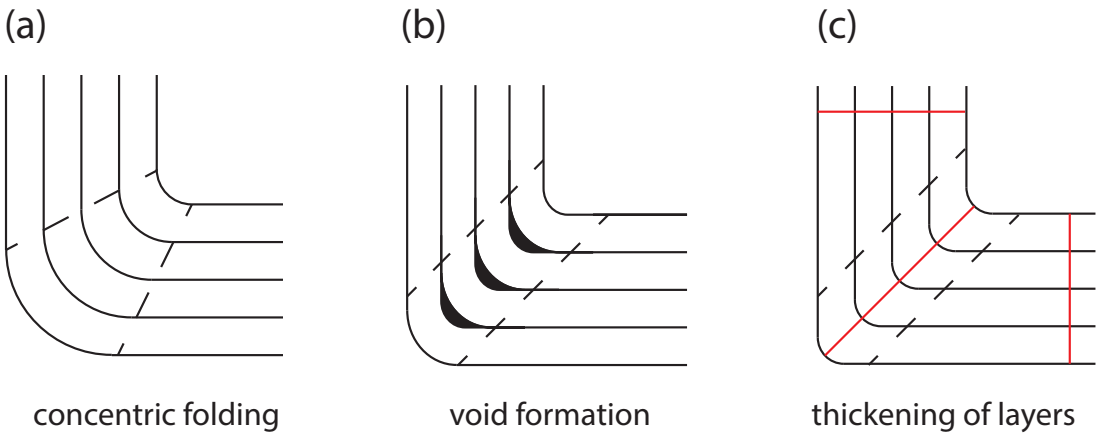

Figure 5.8: Schematic of potential kink band boundary geometries.

If void formation is prohibited, the layers remain continuous, and no change in layer radius occurs along the length of the boundary, the thickness of the layers at the boundary must locally increase (Figure 5.8(c)). For the boundary shown in Figure 5.8(c), all three solid red lines intersect the same number of layers and lie normal to the layer boundaries. The solid line drawn parallel to the boundary is longer (by $\sqrt{2}$) than the other two lines and shows that, in the

absence of void formation, a change in layer thickness is required. The geometry of kink band boundaries and folded multilayers has received particular attention in the geological literature [173, 198–201] as precious minerals, such as gold-rich quartz, have been observed to deposit in voids at the boundaries of kinks and folds in rock strata [198].

Figure 5.9 shows that the geometry of the kink band boundaries in Cu-Nb nanolaminates matches that described in Figure 5.8(c). Figure 5.9(a) shows a high magnification STEM image of the kink band boundary in a 30 nm TD compression specimen [134]. No void formation or delamination is evident, and the layers remain continuous across the kink band boundary. Figure 5.9(b) shows a low magnification polarized light optical micrograph showing that no change in the layer radius or width of the kink band boundary is observed over a length of several hundred microns in a 65 nm TD compression specimen (thus ruling out the concentric folding type boundary). The conclusion drawn from these observations is that both layer transverse strain and layer parallel strain (coupled by layer volume preservation) must occur as the non-kinked material is sheared and the kink band broadens. A schematic of these geometrically required strains is shown in Figure 5.10. Substantial layer transverse strains occur during kinking from $\phi = 0$ to $\phi = 2\beta = \frac{\pi}{2}$, with a maximum layer transverse true strain of 34.6% at $\phi = \beta = \frac{\pi}{4}$.

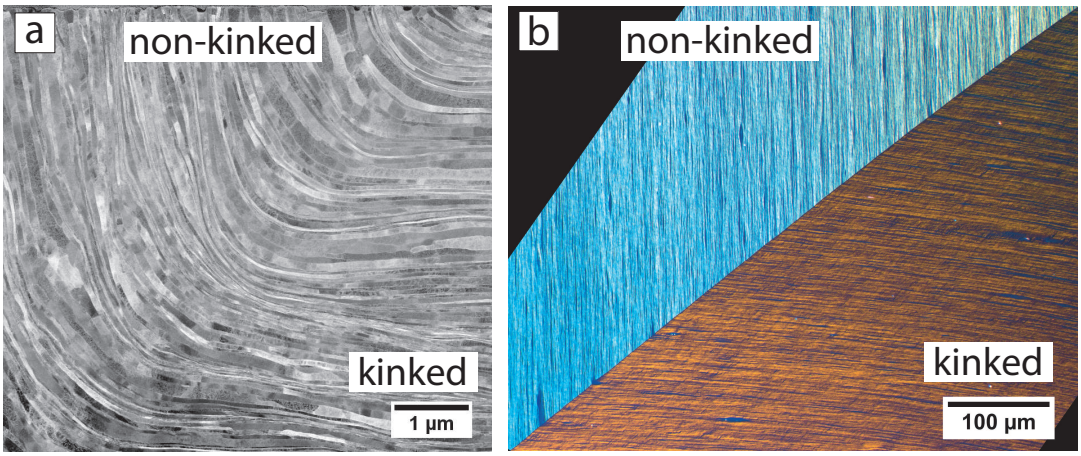

Figure 5.9: STEM and LOM images of kink band boundary geometry. (a) shows a high magnification STEM image showing the absence of voids or debonding at a kink band boundary in a 30 nm TD compression specimen. STEM image from Jaclyn Avallone, UCSB [134]. (b) shows the sharp boundary between kinked and non-kinked material in a 65 nm TD compression specimen.

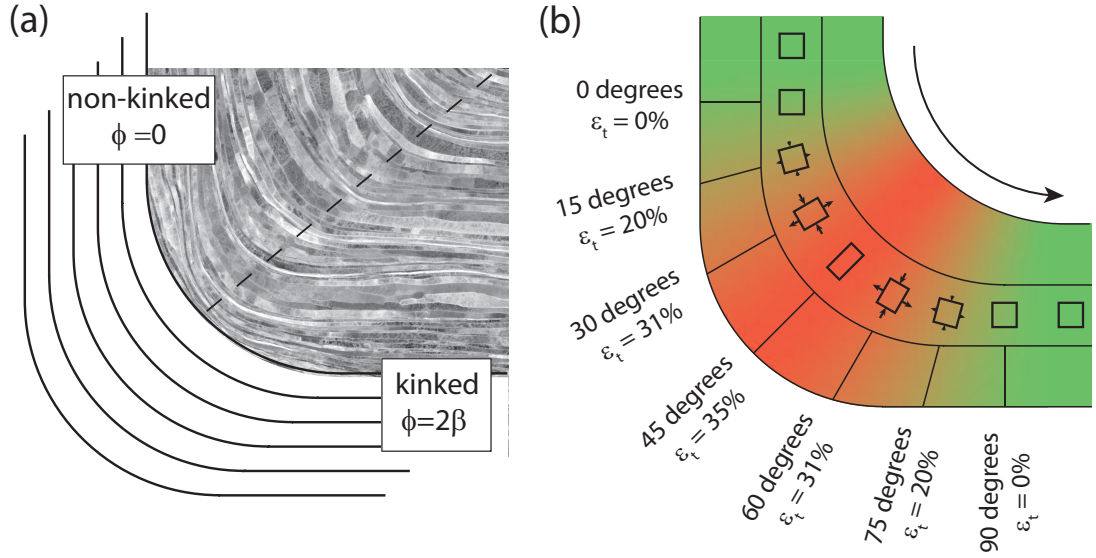

Figure 5.10: The geometry of a kink band boundary (overlaid on the STEM image from Figure 5.9) is shown in (a) and the layer transverse true strains that occur at the kink band boundary during kink band broadening are shown in (b).

These observations indicate that the deformation at a kink band boundary during broadening shears and rotates the non-kinked material outside of the band to $\phi = 2\beta$ without void formation, delamination, or other non-volume preserving deformation. Plastic deformation of the Cu and Nb layers is required, with large layer parallel shear, layer transverse tension/compression, and layer parallel tension/compression progressively occurring during kink band broadening. This stands in contrast to the kinematics developed for kinking in fiber composites, where kink band formation is described using non-isochoric deformation.

The traditional explanation for why the deformation within a kink band ceases at $\phi = 2\beta$ is not applicable when the kinematics of kink band formation or broadening are volume preserving. While lock up at $\phi = 2\beta$ is intuitive when layer transverse dilatation is achieved easily though debonding and layer transverse contraction is strongly resisted by incompressibility, with the adoption of isochoric kinematics it is not clear why the band would lock up at a prescribed rotation angle. As shown in Figure 5.10, thickening followed by thinning of the layers occurs continuously as the layers are reoriented to $\phi = 2\beta$. Why layer thinning would be acceptable from $\phi = \beta$ to $\phi = 2\beta$ but prohibited for rotations past $\phi = 2\beta$ is unclear.

Having determined that the kinematics used in fiber composite kink band

formation models are inappropriate to apply to kink band formation in Cu-Nb multilayers, the micropillar experiments described in the next section were conducted in order to gain further insight into the kinematics of kinking in ductile nanolaminates and to guide modeling of this phenomenon.

5.3 Micropillar compression

The bulk layer parallel compression specimens discussed in Section 4.5 provide information regarding the bulk mechanical response of large specimens which deform *via* kink band formation. However they do not provide insight into the degree of geometric softening that occurs due to the rotation of material within a kink band (since multiple kink bands form in these specimens), nor do they address whether there is a sample size effect on kink band formation as the specimens were very large compared to the layer thickness (over 4 orders of magnitude wider than the nominal layer thickness). In order to determine whether small scale specimens (with dimensions on the order of several microns) also deform by kink band formation, and to obtain information on strain softening during kink band formation, micropillar compression tests of the 65 nm ARB Cu-Nb nanolaminate material were performed at Los Alamos National Laboratory.

Several specimens of 65 nm ARB Cu-Nb nanolaminate material, with square cross-sections measuring $\sim 4\,\mu$m $\times$ $\sim 4\,\mu$m, were prepared and tested as described in Section 2.5. Based on the nominal layer thickness and the specimen dimensions, it is estimated that these pillars contained approximately 60 layers across the width of the specimens.

Figure 5.11 shows images of an initial, undeformed, pillar (Figure 5.11(a)) and the flat tipped diamond indenter aligned with one of the compression specimens at the beginning of a test (Figure 5.11(b)). Figure 5.11(c)-(e) shows views of the same pillar after compression to an engineering strain of 12%. Kink bands are clearly present in the deformed pillar, emanating from both the top specimen corner as well as from the mid-section of the specimen. The width of both kink bands is approximately 1 μm.

Figure 5.12 shows both the stress-strain curve during micropillar compression and a series of images captured during testing at the points labeled on the stress-strain curve. Kink bands in these small specimens appear to form by the near uniform rotation of a band of material inclined across the specimen. Significant load drops occur during the formation of each of the two kink bands (the lower kink band is partially obscured by FIB machining debris in Figure 5.12, but was shown clearly in Figure 5.11). These load drops appear asymmetric, with the softening that occurs at the beginning of kink band formation occur-

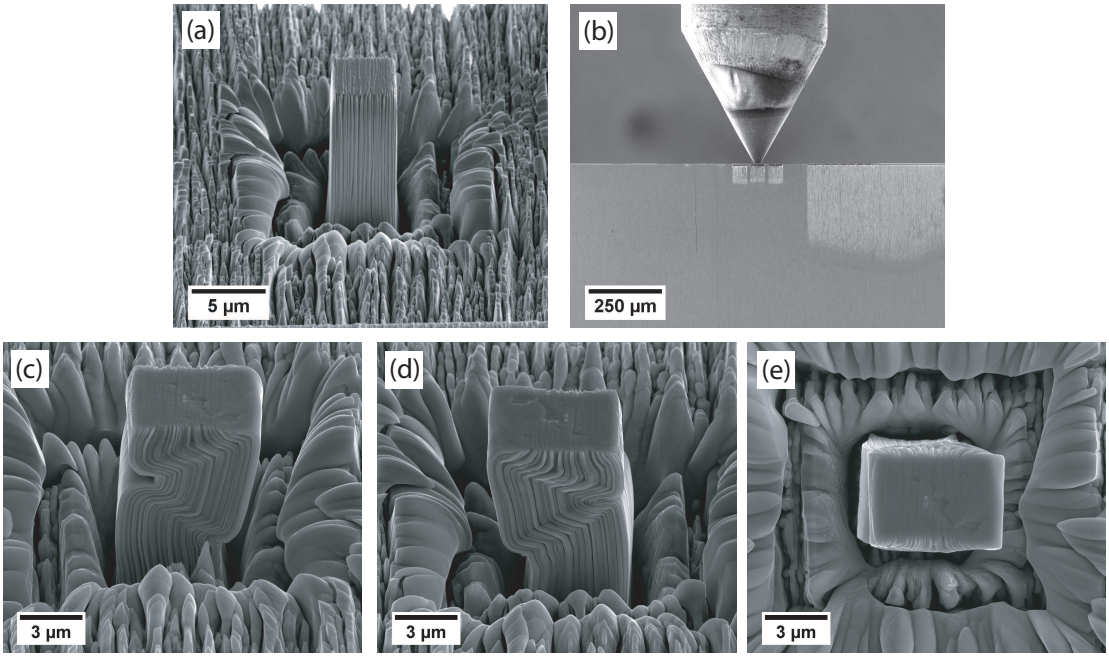

Figure 5.11: SEM images of pre and post-test 65 nm ARB Cu-Nb layer parallel micropillar. (a) shows the FIB milled micropillar prior to testing. (b) shows compression test set-up using a diamond flat punch picoindenter. (c,d,e) show the front, back, and top view of the micropillar after compression to 12% engineering strain.

ring more rapidly than the hardening that increases the load bearing capacity back to the initial, pre-kink band, value. The kink band inclination angle β is approximately 35°, a value in excellent agreement with the previously reported values for kink band formation in 65 nm TD compression specimens (32-37°, Table 4.2). Both the stress-strain behavior and the deformation observed in the *in situ* images were similar for all three pillars tested (data from other pillars not shown). The flow stress of the micropillars at 2% strain ranged from 1 to 1.1 GPa, values that are slightly higher than the 0.9 GPa flow stress obtained from bulk compression tests of the same material (Section 4.4). While the reason for this slight difference in flow stress is not clear, the difference may result from the reduced sample size of the micropillars: micropillars were machined from regions in which the layer thicknesses appeared very uniform, thus excluding the occasional thicker layers found in the bulk compression specimens. The strain at which the load drop and kink band formation occurred in the micropillar specimens (∼4%) is similar to the strain at which kink band initiation occurred in the bulk compression tests discussed in Section 4.4 (∼6%).

Since the rotation of the material that occurs during kink band formation appears near-homogeneous over the small dimension of the micropillar, and a substantial amount of the stress-strain curve corresponds to the formation of a single kink band, the stress-strain data can be used to gain insight into the

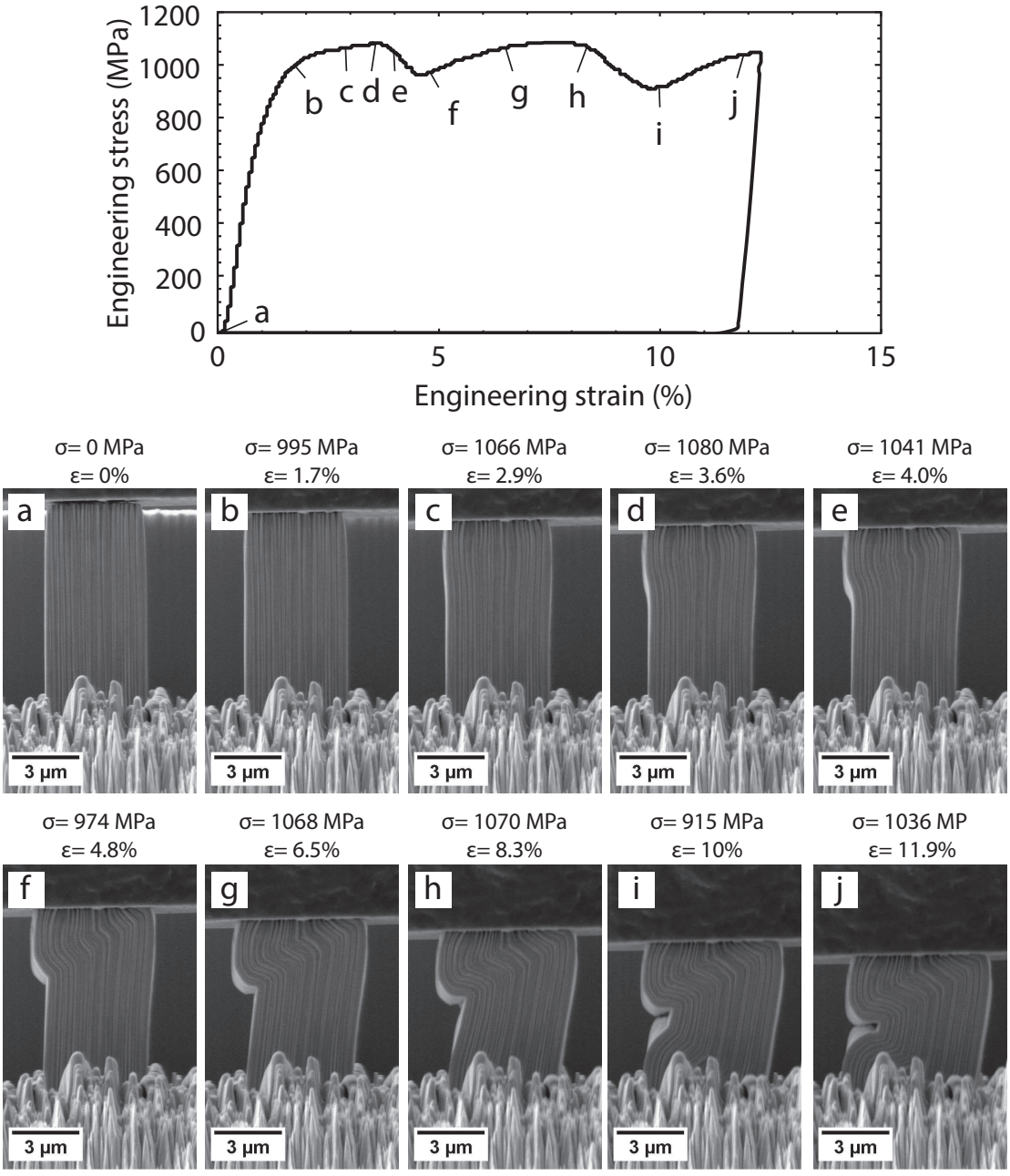

Figure 5.12: Stress-strain curve from a micropillar compression test of 65 nm layer thickness ARB Cu-Nb material. Images corresponding to points (a) through (j) on the stress-strain curve are shown below. Some slight barreling is evident near the specimen end prior to kink band formation, as shown in (c).

geometric softening resulting from layer rotation. Figure 5.13 shows images of the micropillar at the first load maximum, first load minimum, and the point at which the stress increased to a level equal to the first stress maximum (indicated schematically below the images). The geometry of the kink band is measured in order to determine whether the angular relationships at these points correspond to special angular relationships (for example $\phi = \beta$ or $\phi = 2\beta$).

While this analysis is complicated by the slight non-uniform rotation in Figure 5.13(b) and the more pronounced non-uniform rotation in Figure 5.13(c), an estimate of the β and ϕ values is given in the insets in Figure 5.13. The minimum load corresponds to $\phi = \beta$ as shown in Figure 5.13(b). In Figure 5.13(c), the relationship between ϕ and β approximates $\phi = 2\beta$, yet substantial non-uniform rotation is observed. This variation in ϕ could be due to constraint from the compression indenter, as the layers farthest from the indent show a rotation angle closer to 2β. Nevertheless, these results indicate that geometric softening occurs during rotation to $\phi = \beta$ while geometric hardening occurs during shear and rotation towards an orientation near or approximating $\phi = 2\beta$. This result is somewhat surprising given that the resolved shear stress acting on the layers should increase during rotation from $\phi = 0$ to $\phi = \frac{\pi}{4}$. Yet the minimum load during the shear and rotation of kink band formation corresponds to $\phi = \beta$, where $\beta = 35°$.

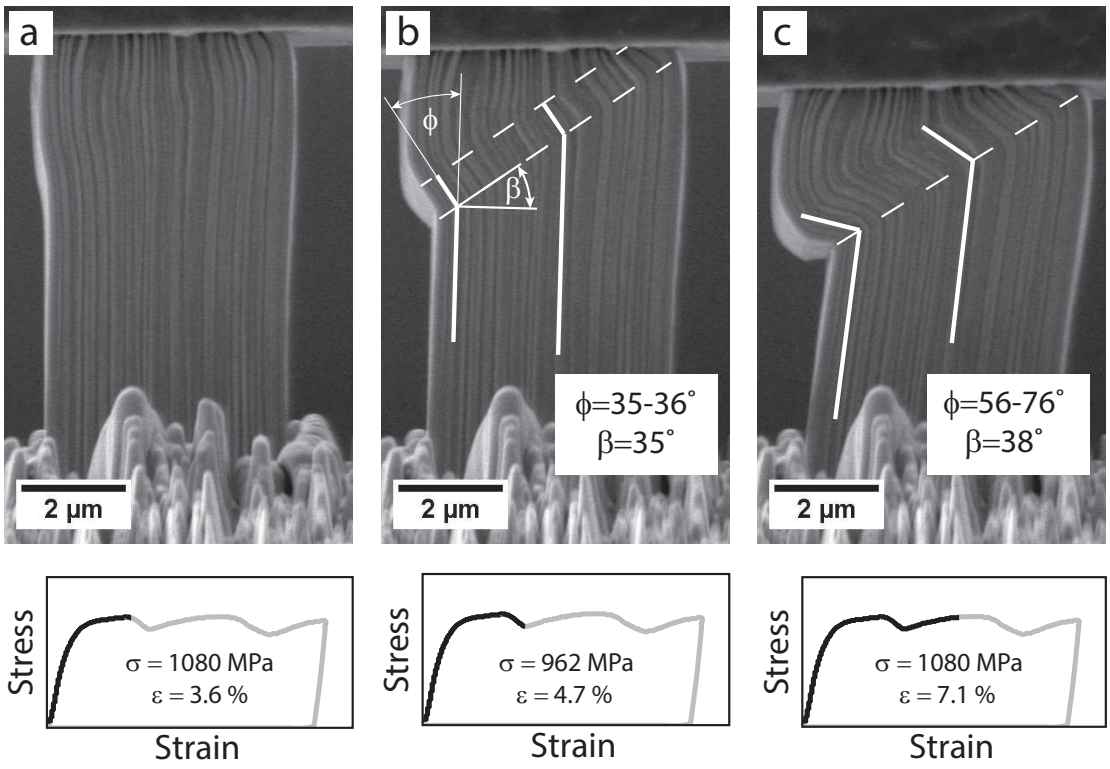

Figure 5.13: Micropillar images corresponding to first stress maximum, first stress minimum, and stress equal to first maximum, as indicated on the schematic stress-strain diagrams.

A final conclusion can be drawn from the micropillar compression tests: when the size of the kink band is on the order of the specimen size, a kink band appears to form by the near-uniform shear and rotation of a band of material. The width of the kink band formed is is approximately 15 times the nominal layer thickness (the width of the sheared band in Figure 5.13 is $\sim$1 μm while the nominal layer thickness is 65 nm).

5.4 Summary of major kink band observations

The experimental results from post-test metallography of kink bands and micropillar compression tests provide insight into the geometry of kink bands as well as the kinematics and stress-strain behavior during kink band formation. While the conclusions drawn from the experimental work were stated throughout the previous sections, they are summarized below:

1. Kink band formation in Cu-Nb is isochoric, with no evidence of void formation or widespread layer debonding either during formation or at the kink band boundary in post-test analysis.

2. The deformation within a kink band ceases once the layers have rotated to $\phi = 2\beta$. Micropillar compression tests suggest a minimum load is attained at $\phi = \beta$.

3. The explanation for the $\phi = 2\beta$ relationship that is presented in models developed for fiber composite kink bands (discussed in Section 5.1.2) cannot be applied to kink bands in Cu-Nb multilayers. Fiber composite models assume kink bands form *via* non-isochoric deformation, and employ kinematics which are inappropriate for the isochoric kink band formation process observed in Cu-Nb nanolaminates.

4. Kink bands displaying different values of ϕ are observed within individual specimens, indicating that ϕ and therefore β likely depend on the local stress state and are not 'fixed' for a given material.

5. No evidence of kink band boundary rotation is observed during kink band formation (β remains fixed while ϕ increases, as was observed in the micropillar compression tests). Therefore the length of a kink band boundary does not change during kink band formation.

6. All experimentally observed kink band boundary angles (β) are $\leq$45°. While β values significantly below 45° are frequently observed (Table 4.2), no similar deviation of the kink band boundary angle to values above 45° is observed.

In the following section, an analytical model of plane strain kink band formation is developed that seeks to explain the observations presented above. As the goal is to provide insight into the phenomenon of kink band formation without introducing unnecessary complexity, the Cu-Nb nanolaminate material is modeled as a perfectly plastic anisotropic material. This approach homogenizes the response of the individual Cu and Nb layers. While work hardening is not considered, incorporation of a work hardening rate into future refinements of the model is likely to provide further insights. This model does not address the

phenomenon of kink band propagation, an aspect of kink band formation that will be analyzed in detail in Section 5.6.

5.5 Analytical kink band model

A model of kink band formation in a perfectly plastic anisotropic material has been developed and is presented in this section. This new model for kink band formation is necessary, as previous models developed for kink band formation in fiber composites can not be applied to kink band formation in Cu-Nb nanolaminates (the previous models assume non-isochoric deformation, as discussed in Section 5.1.2).

In this model, kink band formation is assumed *a priori*. That is, the conditions for bifurcation from a homogeneous velocity gradient to a velocity gradient corresponding to kink band formation are not examined. Instead, the model assumes kink band formation will occur, and calculates the necessary strain rates and deviatoric stresses required to form a kink band (for all possible values of ϕ and β). An evaluation of the conditions for which these stresses violate the yield criterion of the surrounding non-kinked material is conducted. This analysis places bounds on the kink band angle β. In order to determine why shear and rotation past the $\phi = 2\beta$ condition is unfavorable, an analysis of the plastic

work rate during kinking is conducted.

In the following sections, the model is discussed in terms of: 1) kinematics, 2) stresses and yield criteria, and 3) the plastic work rate during kinking. In the kinematics section, the strain and strain rate tensors consistent with the experimental observations presented in the previous sections are calculated. Due to the large rotations involved and the goal of describing strains and strain rates in a coordinate system tied to the layer orientation within the kink band, multiple coordinate transformations are required.

In the second section, a general anisotropic yield surface is constructed that captures the experimentally observed anisotropy of the Cu-Nb nanolaminate material. By invoking normality (plastic strain rates must lie normal to the yield surface) the plastic strain rates associated with the anisotropic yield surface are obtained. These are equated to the plastic strain rates calculated in the kinematics section, allowing determination of the deviatoric stress state required to 1) yield the material in the kink band and 2) provide plastic strain rate increments consistent with the kinematics of kink band formation. While this procedure determines the stress state of the specimen required to induce kink band formation, it is also necessary to verify that this stress state does not violate the yield criterion for the undeformed sample surrounding the kink band. It is found that, for certain values of β and ϕ, the stresses required to yield the material within

the kink band do indeed violate the yield criterion for the undeformed material surrounding the kink band. These stress states are clearly inadmissible, a result that allows bounds to be placed on acceptable values of ϕ and β.

In the final section, the plastic work rate associated with kink band formation is calculated from the deviatoric stresses and plastic strain rates. Analysis of the work rate during kink band formation indicates that the shear and rotation within a kink band initially lead to a lower work rate (as ϕ increases from $\phi = 0$ to $\phi = \beta$). The minimum work rate occurs at $\phi = \beta$, and increasing work rates are predicted as ϕ approaches 2β. The implications of these changes in work rate provide an explanation for the observed $\phi = 2\beta$ relationship.

5.5.1 Kink band kinematics

Combining the requirement that the volume of a kink band be invariant during formation with the requirement that the kink band boundary length does not change (β remains constant), it follows that the width of the kink band does not change during kink band formation. Therefore, if the non-kinked material on one side of a kink band boundary remains stationary, the displacement vectors for the material outside of the other kink band boundary must lie parallel to the kink band boundary plane. Therefore the average deformation gradient within

the kink band must be one of simple shear parallel to the kink band boundary. It is recognized that these kinematics may not apply to the deformation occurring at the length scale of individual layers, where inhomogeneous deformation may occur. Nevertheless, the average or homogenized deformation of the individual layers must conform to the simple shear kinematics of the kink band region. In this section, the kink band is treated as a volume preserving band of simple shear at an angle β to the layer normals.

Figure 5.14 shows the coordinate systems used the following analysis. There is an undeformed (sample) coordinate system, a coordinate system aligned with the band boundary, and a coordinate system aligned with the layer parallel and layer normal directions of the material within the kink band.

The displacement vectors in the kink band are given by Equation 5.2. These correspond to simple shear parallel to the kink band boundary, with the displacement in the $\underline{e}_\zeta$ direction given by the shear strain multiplied by the distance from the kink band boundary (ξ).

$$\begin{aligned} u_\zeta &= \xi\big(\tan\beta + \tan(\phi - \beta)\big) \\ u_\xi &= 0 \end{aligned} \tag{5.2}$$

The displacement gradient tensor (in basis $\underline{e}_\zeta, \underline{e}_\xi$) is given in Equation 5.3 while the deformation gradient tensor is defined in Equation 5.4 and calculated in Equation 5.5.

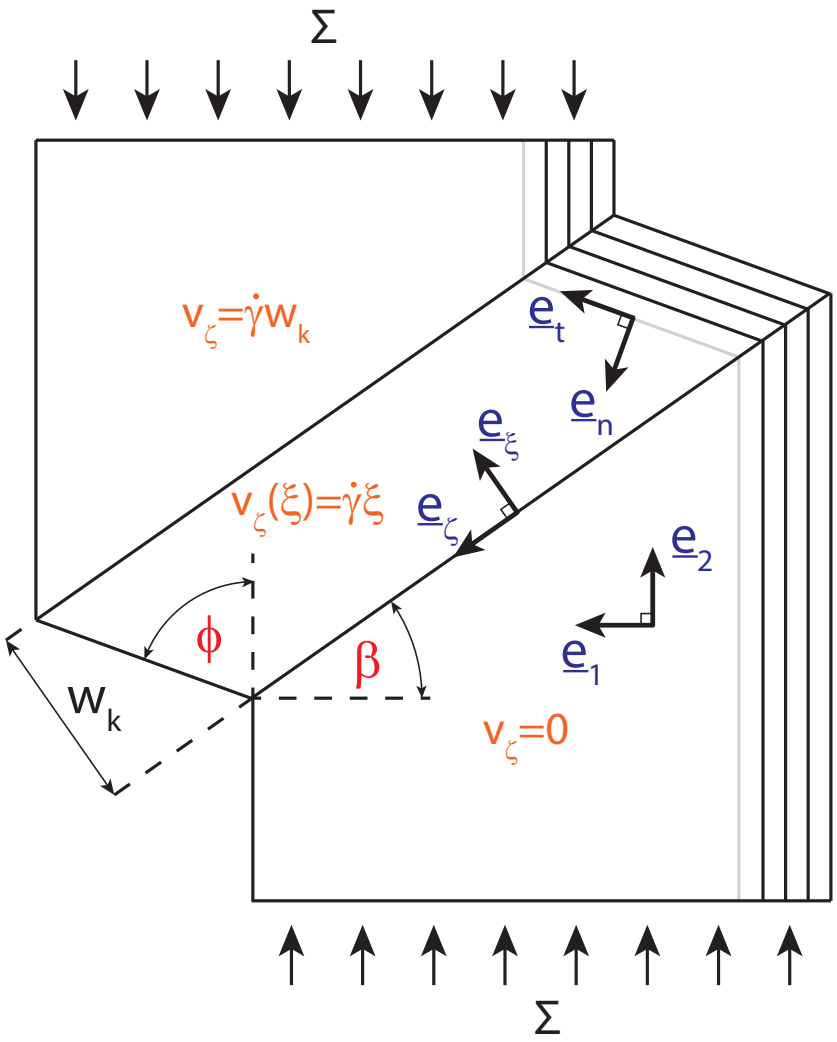

Figure 5.14: Illustration of coordinate systems, kink band angles, and velocity fields used for the kink band analytical model. One coordinate system with basis vectors $\underline{e}_1$ and $\underline{e}_2$ is aligned with the specimen axes. Another coordinate system with basis vectors $\underline{e}_\zeta$ and $\underline{e}_\xi$ is aligned with the kink band boundary. A final coordinate system, which rotates during kink band formation, has basis vectors $\underline{e}_n$ and $\underline{e}_t$ and is aligned with the layer orientation within the kink band. The v_ζ components of the velocity fields for the material inside the kink band and outside of the kink band are indicated for the different regions (the other component (v_ξ) is zero everywhere).

$$\mathbf{u} \otimes \nabla = \begin{bmatrix} 0 & \tan\beta - \tan(\beta - \phi) \\ 0 & 0 \end{bmatrix} \tag{5.3}$$

$$\mathbf{F} = \mathbf{I} - \mathbf{u} \otimes \nabla \tag{5.4}$$

$$[F] = \begin{bmatrix} 1 & \tan\beta - \tan(\beta - \phi) \\ 0 & 1 \end{bmatrix} \tag{5.5}$$

The Lagrangian strain tensor (in basis $\underline{e}_\zeta, \underline{e}_\xi$), defined in Equation 5.6, is given in Equation 5.7.

$$\mathbf{E} = \frac{1}{2}(\mathbf{F}^T \cdot \mathbf{F} - \mathbf{I}) \tag{5.6}$$

$$[E] = \begin{bmatrix} 0 & \frac{1}{2}\big(\tan\beta - \tan(\beta - \phi)\big) \\ \frac{1}{2}\big(\tan\beta - \tan(\beta - \phi)\big) & \frac{1}{2}\big(\tan\beta - \tan^2(\beta - \phi)\big) \end{bmatrix} \tag{5.7}$$

Taking the derivative of $\mathbf{E}$ with respect to time gives the Lagrangian strain rate tensor ($\dot{\mathbf{E}}$), where $\dot{\phi}$ is the rotation rate (time derivative). The Lagrangian strain rate tensor (in basis $\underline{e}_\zeta, \underline{e}_\xi$) is given by Equation 5.8.

$$[\dot{E}] = \begin{bmatrix} 0 & \frac{1}{2}\dot{\phi}\sec^2(\beta - \phi) \\ \frac{1}{2}\dot{\phi}\sec^2(\beta - \phi) & \dot{\phi}\sec\beta\sec^3(\beta - \phi)\sin\phi \end{bmatrix} \tag{5.8}$$

The shear strain rate, $\dot{\gamma}$ is twice the tensorial shear rate and is given by Equation 5.9.

$$\dot{\gamma} = 2\dot{E}_{\zeta\xi} = \dot{\phi}\sec^2(\beta - \phi) \tag{5.9}$$

In experimental displacement rate controlled compression testing, it is the displacement rate of the top surface of the specimen ($\dot{u}_2$), not the rotation rate of the layers ($\dot{\phi}$), that is controlled. Equation 5.10 relates $\dot{\phi}$ to $\dot{u}_2$, where w_k is the width of the kink band.

$$\dot{\phi} = \frac{\dot{u}_2}{w_k}\cos^2(\beta - \phi)\csc\beta \tag{5.10}$$

A change of basis is required to transform the previously described Lagrangian strain and strain rate tensors into those describing the layer parallel shear (E_{nt}), layer transverse strain (E_{nn}), and layer parallel strains (E_{tt}). The three coordinate systems were shown in Figure 5.14 and are the sample (non-kinked) coordinate system, the kinked coordinate system, and the layer coordinate system. The coordinate system basis vectors are related by Equations 5.11 and 5.12.

$$\begin{Bmatrix} e_n \\ e_t \end{Bmatrix} = \mathbf{Q}_1 \begin{Bmatrix} e_1 \\ e_2 \end{Bmatrix} = \begin{bmatrix} \cos\phi & -\sin\phi \\ \sin\phi & \cos\phi \end{bmatrix} \begin{Bmatrix} e_1 \\ e_2 \end{Bmatrix} \tag{5.11}$$

$$\begin{Bmatrix} e_\zeta \\ e_\xi \end{Bmatrix} = \mathbf{Q}_2 \begin{Bmatrix} e_1 \\ e_2 \end{Bmatrix} = \begin{bmatrix} \cos\beta & -\sin\beta \\ \sin\beta & \cos\beta \end{bmatrix} \begin{Bmatrix} e_1 \\ e_2 \end{Bmatrix} \tag{5.12}$$

The transformation matrices $\mathbf{Q}_1$ and $\mathbf{Q}_2^T$ relate the kink band coordinate

basis vectors to the layer coordinate basis vectors as shown in Equation 5.13.

$$\begin{Bmatrix} e_n \\ e_t \end{Bmatrix} = \mathbf{Q}_1 \mathbf{Q}_2^T \begin{Bmatrix} e_\zeta \\ e_\xi \end{Bmatrix} = \mathbf{Q}_3 \begin{Bmatrix} e_\zeta \\ e_\xi \end{Bmatrix} = \begin{bmatrix} \cos(\beta-\phi) & \sin(\beta-\phi) \\ -\sin(\beta-\phi) & \cos(\beta-\phi) \end{bmatrix} \begin{Bmatrix} e_\zeta \\ e_\xi \end{Bmatrix} \tag{5.13}$$

The opposite transformation is achieved using $\mathbf{Q}_3^T$ as shown in Equation 5.14.

$$\begin{Bmatrix} e_\zeta \\ e_\xi \end{Bmatrix} = \mathbf{Q}_3^T \begin{Bmatrix} e_n \\ e_t \end{Bmatrix} = \begin{bmatrix} \cos(\beta-\phi) & -\sin(\beta-\phi) \\ \sin(\beta-\phi) & \cos(\beta-\phi) \end{bmatrix} \begin{Bmatrix} e_n \\ e_t \end{Bmatrix} \tag{5.14}$$

The strain rate in the kink band coordinates is written out in dyadic form in Equation 5.15.

$$\underline{\dot{E}} = \frac{1}{2}\dot{\gamma}(\underline{e}_\xi \underline{e}_\zeta + \underline{e}_\zeta \underline{e}_\xi) \tag{5.15}$$

Using Equation 5.14, $\underline{e}_\xi \underline{e}_\zeta$ and $\underline{e}_\zeta \underline{e}_\xi$, as well as their sum, are given in Equations 5.16, 5.17, and 5.18.

$$\begin{aligned} \underline{e}_\xi \underline{e}_\zeta = \sin(\beta-\phi)\cos(\beta-\phi)\underline{e}_n \underline{e}_n - \sin^2(\beta-\phi)\underline{e}_n \underline{e}_t + \cos^2(\beta-\phi)\underline{e}_t \underline{e}_n \\ - \sin(\beta-\phi)\cos(\beta-\phi)\underline{e}_t \underline{e}_t \end{aligned} \tag{5.16}$$

$$\begin{aligned} \underline{e}_\zeta \underline{e}_\xi = \sin(\beta-\phi)\cos(\beta-\phi)\underline{e}_n \underline{e}_n - \sin^2(\beta-\phi)\underline{e}_t \underline{e}_n + \cos^2(\beta-\phi)\underline{e}_n \underline{e}_t \\ - \sin(\beta-\phi)\cos(\beta-\phi)\underline{e}_t \underline{e}_t \end{aligned} \tag{5.17}$$

$$\begin{aligned} \underline{e}_\xi \underline{e}_\zeta + \underline{e}_\zeta \underline{e}_\xi = \sin\big(2(\beta-\phi)\big)\underline{e}_n \underline{e}_n + \cos\big(2(\beta-\phi)\big)(\underline{e}_t \underline{e}_n + \underline{e}_n \underline{e}_t) \\ - \sin\big(2(\beta-\phi)\big)\underline{e}_t \underline{e}_t \end{aligned} \tag{5.18}$$

Taking these results and Equation 5.15, the strain rate components in the layer coordinate system are obtained as a function of the kink band shear rate:

$$\begin{aligned}\underline{\dot{E}}_{nn} &= \frac{1}{2}\dot{\gamma}\sin\big(2(\beta-\phi)\big)\\ \underline{\dot{E}}_{tt} &= -\frac{1}{2}\dot{\gamma}\sin\big(2(\beta-\phi)\big)\\ \underline{\dot{E}}_{nt} &= \frac{1}{2}\dot{\gamma}\cos\big(2(\beta-\phi)\big)\end{aligned} \tag{5.19}$$

The strain rate components as a function of the rotation rate are obtained by combining Equations 5.9 and 5.19. These strain rates are presented in Equation 5.20.

$$\begin{aligned}\underline{\dot{E}}_{nn} &= \dot{\phi}\tan(\beta-\phi)\\ \underline{\dot{E}}_{tt} &= -\dot{\phi}\tan(\beta-\phi)\\ \underline{\dot{E}}_{nt} &= \frac{1}{2}\dot{\phi}\left(1-\tan^2(\beta-\phi)\right)\end{aligned} \tag{5.20}$$

Integration of these strain rates yields the Lagrangian strains in the layer coordinate system, given in matrix form in Equation 5.21.

$$[E] = \begin{bmatrix}\ln\big(\cos(\beta-\phi)\big)-\ln(\cos\beta) & \frac{1}{2}\big(2\phi-\tan\beta+\tan(\beta-\phi)\big)\\ \frac{1}{2}\big(2\phi-\tan\beta+\tan(\beta-\phi)\big) & \ln(\cos\beta)-\ln\big(\cos(\beta-\phi)\big)\end{bmatrix} \tag{5.21}$$

Using Equations 5.20 and 5.10, the layer parallel shear strain, layer transverse strain, and layer parallel strain rates are obtained as a function of the

vertical displacement rate of the specimen end ($\dot{u}_2$). Note that $\dot{E}_{tt}$ is simply the negative of $\dot{E}_{nn}$, as the deformation is isochoric. Figure 5.15 shows $\dot{E}_{nn}$ and $\dot{E}_{nt}$, (normalized by $\frac{\dot{u}_2}{w_k}$) plotted as a function of ϕ for several β values. For all values of β, the layer parallel shear strain rate is maximum at $\phi = \beta$, increasing from $\phi = 0$ to $\phi = \beta$ and decreasing from $\phi = \beta$ to $\phi = 2\beta$ (Figure 5.15(a)). The layer transverse strain rate is zero at $\phi = \beta$, decreasing from $\phi = 0$ to $\phi = \beta$ and becoming negative from $\phi = \beta$ to $\phi = 2\beta$.

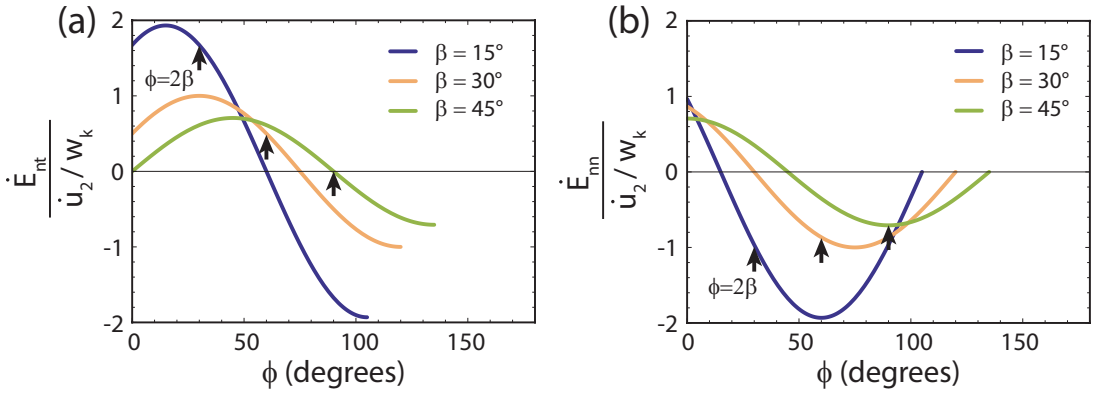

Figure 5.15: Plots of normalized strain rate ($\frac{\dot{E}}{\dot{u}_2/w_k}$) versus kink band rotation angle (ϕ). (a) shows the normalized layer parallel shear strain rate while (b) shows the normalized layer transverse strain rate. Note that $\dot{E}_{tt}$ (not plotted) is simply the negative of $\dot{E}_{nn}$, as the deformation is isochoric. Black arrows indicate the $\phi = 2\beta$ condition based on the β value of each curve.

The layer parallel shear and layer transverse Lagrangian strains are plotted for several values of β in Figure 5.16. The layer transverse strain equals zero at both $\phi = 0$ and $\phi = 2\beta$, with the maximum strain occurring at $\phi = \beta$. The magnitude of these transverse strains are large, with a maximum transverse

layer strain of 3.4%, 14% and 34.7% for a β of 15°, 30°, and 45° respectively. Thus the layer transverse strain at $\phi = \beta$ increases rapidly and non-linearly with increasing β.

The layer parallel shear is maximal at $\phi = \frac{\pi}{4} + \beta$, a rotation that lies outside of the experimentally observed range of ϕ values (limited by $\phi = 2\beta$) for all $\beta \leq \frac{\pi}{4}$. Therefore, during kinking and rotation from $\phi = 0$ to $\phi = 2\beta$, the layer parallel shear strain increases monotonically. The tensorial shear strain (E_{nt}) at $\phi = 2\beta$ for β =15°, 30°, and 45° is 15.5%, 47%, and 57% respectively.

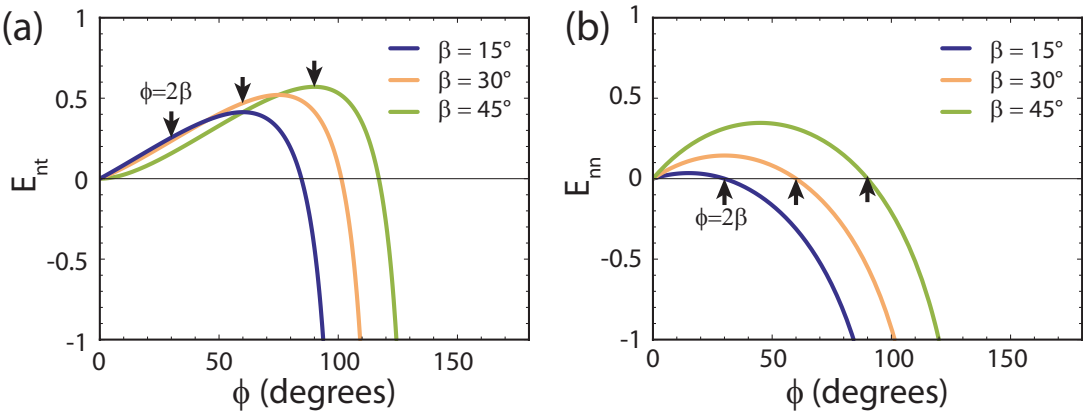

Figure 5.16: Plots of Lagrangian strain versus kink band rotation angle (ϕ). (a) shows the layer parallel shear strain (E_{nt}) while (b) shows the layer transverse strain (E_{nn}). Note that E_{tt} (not plotted) is simply the negative of E_{nn}, as the deformation is isochoric. Black arrows indicate the $\phi = 2\beta$ condition based on the β value of each curve.

These calculations allow the observed kink band angles β and ϕ to be related to the shear strain, transverse strain, and layer parallel strain that occurs within

a kink band. They also provide a picture of the complexity of the deformation within a kink band. Absent the debonding and non-isochoric deformation that is reported for kink band formation in fiber composites, the layers must undergo extensive transverse and layer parallel straining during kink band formation.

While the layer parallel shear and layer transverse strains are substantial, these is no reason why these strains should set conditions on the range of ϕ or β values allowed for kink bands in Cu-Nb nanolaminates. Particularly for the case of a narrow kink band embedded in a specimen, where significant hydrostatic stress may occur, these strain levels are plausible for ductile Cu-Nb nanolaminates. Thus unlike the transverse strain-based arguments used to explain the $\phi = 2\beta$ relationship in fiber composite kink bands (Section 5.1.2), examination of the strains alone do not preclude certain values of β or ϕ for ductile nanolaminates.

Yet the strain rates appear to offer some insight. For all values of β, the shear strain rate is maximal at $\phi = \beta$ while the layer transverse and layer parallel strain rates are zero. Layer parallel shear is the easiest deformation mode for these anisotropic nanolaminates while layer transverse strain is much more difficult and requires higher stresses (as was shown in Chapter 4). This hints that an examination of the work rate is necessary to gain insight into kink band formation in these materials.

5.5.2 Stresses within a kink band at yield

In order to calculate the work rate associated with the kinematics described above, the stresses within the kink band are needed. These stresses must satisfy equilibrium as well as the yield criterion for the material within the kink band. Equilibrium is satisfied by specifying that the stresses are uniform everywhere in the specimen (both inside and outside of the kink band). The stresses required to form a kink band will be obtained by constructing a yield surface and solving for the stress state required to both 1) keep the material within the kink band at yield and 2) provide the strain rates corresponding to shear parallel to the kink band boundary. Normality is assumed and therefore the plastic strain rate increments lie normal to the yield surface. By specifying that the plastic strain rate increments from the flow law must equal the plastic strain rates from the observed kinematics (Equation 5.20), the deviatoric stresses can be obtained.

A simple elliptical yield surface, suitable for plane strain deformation of a perfectly plastic anisotropic material will be used. This yield surface captures the main aspects of the experimentally observed anisotropy of Cu-Nb nanolaminates (a high flow stress for layer parallel/layer normal compression and a low flow stress for layer parallel shear). The yield surface is smooth and convex.

For the two-dimensional plane strain model considered, all coordinate sys-

tems shown in Figure 5.14 share a common out of plane direction ($\underline{e}_{33}$). For plane strain, the out of plane stress (σ_{33}) is given by Equation 5.22

$$\sigma_{33} = \frac{1}{2}(\sigma_{nn} + \sigma_{tt}) \tag{5.22}$$

so that:

$$\frac{1}{3}\sigma_{kk} = \frac{1}{2}(\sigma_{nn} + \sigma_{tt}) \tag{5.23}$$

The components of the deviatoric stress tensor (defined in Equation 5.24) are given by Equation 5.25.

$$S_{ij} = \sigma_{ij} - \frac{1}{3}\sigma_{kk}\delta_{ij} \tag{5.24}$$

$$\begin{aligned} S_{nn} &= \frac{1}{2}(\sigma_{nn} - \sigma_{tt}) \\ S_{tt} &= \frac{1}{2}(\sigma_{tt} - \sigma_{nn}) \\ S_{33} &= 0 \end{aligned} \tag{5.25}$$

The yield function in terms of the deviatoric stresses is given by Equation 5.26, where σ_0 and τ_0 are the yield stresses in uniaxial tension and layer parallel shear respectively. The material yields when the deviatoric stresses satisfy $F = 0$.

$$F = \left(\frac{2S_{nn}}{\sigma_0}\right)^2 + \left(\frac{\sigma_{nt}}{\tau_0}\right)^2 - 1 \tag{5.26}$$

Figure 5.17 shows this yield criterion plotted for a variety of different σ_0 to τ_0 ratios, including the isotropic case in which $\tau_0 = \frac{1}{2}\sigma_0$. The experimental anisotropy observed in Cu-Nb nanolaminates is a function of the layer size, and therefore different σ_0 to τ_0 ratios are needed to describe the different nanolaminate materials. Estimates of the various levels of anisotropy appropriate for modeling different nanolaminates can be obtained from the discussion in Chapter 4 and Figure 4.31. For later analysis, a σ_0 to τ_0 ratio of 4:1 will be used. This anisotropy level corresponds to the approximate anisotropy of the 30 nm material as was determined through layer parallel/normal compression tests and compression tests at 45° to the layer direction (TD45 compression tests).

Assuming normality, the associated flow rule is obtained from differentiating the yield function, as shown in Equations 5.27 and 5.28. The resulting plastic strain rates are given in Equation 5.29, where λ is the plastic strain rate multiplier.

$$\dot{E}_{ij} = \lambda \frac{\partial F}{\partial \sigma_{ij}} \tag{5.27}$$

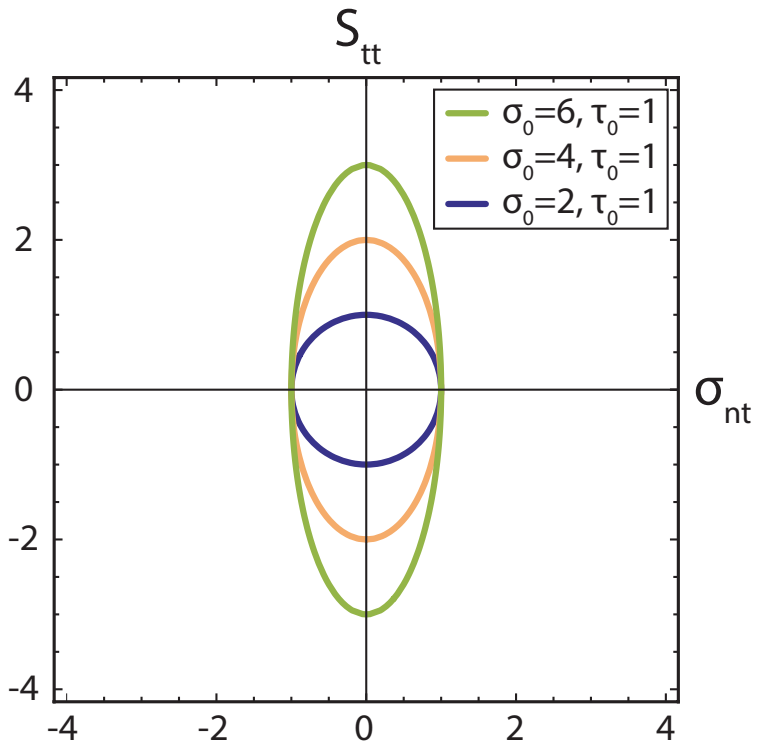

Figure 5.17: An elliptic, plane strain yield surface is shown for various combinations of τ_0 and σ_0. The blue yield surface corresponds to the isotropic case, while the orange and green surfaces demonstrate the effect of increasing anisotropy. Plot axes are the deviatoric stresses.

$$\begin{aligned}\dot{E}_{nn} &= \lambda\frac{\partial F}{\partial \sigma_{nn}} = \lambda\frac{\partial F}{\partial S_{nn}}\frac{\partial S_{nn}}{\partial \sigma_{nn}} + \lambda\frac{\partial F}{\partial S_{tt}}\frac{\partial S_{tt}}{\partial \sigma_{tt}} \\ \dot{E}_{nt} &= \lambda\frac{\partial F}{\partial \sigma_{nt}}\end{aligned} \tag{5.28}$$

$$\begin{aligned}\dot{E}_{nn} &= \lambda\frac{4}{\sigma_0^2}\left(\frac{1}{2}S_{nn} - \frac{1}{2}S_{tt}\right) = \lambda\frac{4S_{nn}}{\sigma_y^2} \\ \dot{E}_{nt} &= \lambda\frac{\sigma_{nt}}{\tau_y^2}\end{aligned} \tag{5.29}$$

Setting these strain rates obtained from the flow law (Equation 5.29) equal to the strain rates obtained from the assumed kinematics (Equation 5.20), the deviatoric stresses shown in Equation 5.30 are obtained.

$$\begin{aligned}S_{nn} &= \frac{\sigma_0^2}{4\lambda}\,\dot{\phi}\tan(\beta-\phi) \\ \sigma_{nt} &= \frac{\tau_0^2}{2\lambda}\,\dot{\phi}\big(1-\tan^2(\beta-\phi)\big)\end{aligned} \tag{5.30}$$

Rearranging Equation 5.30 gives Equation 5.31:

$$\begin{aligned}\left(\frac{S_{nn}}{\frac{\sigma_0}{2}}\right)^2 &= \left(\frac{\sigma_0}{2}\right)^2\left(\frac{\dot{\phi}}{\lambda}\right)^2\tan^2(\beta-\phi) \\ \left(\frac{\sigma_{nt}}{\tau_0}\right)^2 &= \tau_0^2\left(\frac{\dot{\phi}}{\lambda}\right)^2\frac{1}{4}\big(1-\tan^2(\beta-\phi)\big)^2\end{aligned} \tag{5.31}$$

Putting the results from Equation 5.31 into the yield function (Equation 5.26) results in Equation 5.32.

$$\left(\frac{\sigma_0}{2}\right)^2 \left(\frac{\dot{\phi}}{\lambda}\right)^2 \tan^2(\beta-\phi) + \tau_0^2 \left(\frac{\dot{\phi}}{\lambda}\right)^2 \frac{1}{4}\left(1-\tan^2(\beta-\phi)\right)^2 = 1 \tag{5.32}$$

Solving for λ yields Equation 5.33.

$$\lambda = \dot{\phi}\sqrt{\left(\frac{\sigma_0}{2}\right)^2 \tan^2(\beta-\phi) + \frac{1}{4}\tau_0^2\left(1-\tan^2(\beta-\phi)\right)^2} \tag{5.33}$$

Putting the solution for λ into Equation 5.30 and re-arranging, the deviatoric stresses needed to satisfy the yield criterion and provide the desired plastic strain rate increments are obtained. These stresses are given in Equation 5.34.

$$\begin{aligned} S_{nn} &= \frac{\sigma_0^2 \tan(\beta-\phi)}{2\sqrt{\sigma_0^2 \tan^2(\beta-\phi) + \tau_0^2\left(1-\tan^2(\beta-\phi)\right)^2}} \\ \sigma_{nt} &= \frac{\tau_0^2\left(1-\tan^2(\beta-\phi)\right)}{\sqrt{\sigma_0^2 \tan^2(\beta-\phi) + \tau_0^2\left(1-\tan^2(\beta-\phi)\right)^2}} \end{aligned} \tag{5.34}$$

It is critical to note that these deviatoric stresses (Equation 5.34) are arrived at by simply considering what stress state is needed to yield and shear a kink band with a particular value of ϕ and β. That is, it is assumed that the kink band must yield. While equilibrium is guaranteed by the assumption of a uniform stress state both inside and outside of a kink band, the stress state in Equation 5.34 may still be ruled inadmissible if it exceeds the yield criterion for the

non-kinked material outside of the kink band. Therefore, the deviatoric stresses required to shear the kink band (Equation 5.34) must be transformed from the layer coordinate systems into the specimen coordinate system and checked using the non-kinked material yield criterion. Any stress state resulting from a combination of ϕ, β, τ_0, and σ_0 that would violate the non-kinked material yield function (fall outside of the yield surface) is physically unrealistic.

Transforming the deviatoric stresses S_{nn} and σ_{nt} into the basis $\underline{e}_1, \underline{e}_2$ results in S_{11} and σ_{12} as shown in Equation 5.35.

$$\begin{aligned} S_{11} &= \frac{\sigma_0^2 \cos(2\phi)\tan(\beta-\phi) + 2\tau_0^2 \sin(2\phi)\big(1-\tan^2(\beta-\phi)\big)}{-2\sqrt{\tau_0^2 + (\sigma_0^2 - 2\tau_0^2)\tan^2(\beta-\phi) + \tau_0^2 \tan^4(\beta-\phi)}} \\ \sigma_{12} &= \frac{\sigma_0^2 \sin(2\phi)\tan(\beta-\phi) - 2\tau_0^2 \cos(2\phi)\big(1-\tan^2(\beta-\phi)\big)}{-2\sqrt{\tau_0^2 + (\sigma_0^2 - 2\tau_0^2)\tan^2(\beta-\phi) + \tau_0^2 \tan^4(\beta-\phi)}} \end{aligned} \tag{5.35}$$

The yield criterion for the non-kinked material is given in Equation 5.36. The same values of τ_0 and σ_0 apply to both the kinked and the non-kinked material, as the material behavior is taken to be perfectly plastic.

$$F = \left(\frac{S_{11}}{\frac{1}{2}\sigma_0}\right)^2 + \left(\frac{\sigma_{12}}{\tau_0}\right)^2 - 1 \tag{5.36}$$

Combining the deviatoric stresses in Equation 5.35 with the yield function in Equation 5.36, conditions are sought for which $F > 0$. This would correspond to

the prohibited scenario in which the stresses required to deform the kink band exceed the stresses required to deform the non-kinked material (and would lie outside of the yield surface).

Figure 5.18 shows region plots with axes of ϕ and β, that indicate that there are combinations of ϕ, β, τ_0, and σ_0 that would result in stresses that would violate the yield function of the non-kinked material surrounding the band. Maps corresponding to various ratios of σ_0 to τ_0 are shown, with $\frac{\sigma_0}{\tau_0}$ ranging from that of a nearly isotropic material ($\frac{\sigma_0}{\tau_0} = 2.2$) to that of a strongly anisotropic material ($\frac{\sigma_0}{\tau_0} = 6.6$). The isotropic case is not shown as no violation of the non-kinked yield surface occurs (both the kinked and non-kinked material would be exactly at yield for an isotropic material). Interestingly, for any level of anisotropy, attempting to satisfy yield within the kink band for $\phi = 0$ and $\beta > 45°$ results in an immediate violation of the non-kinked material yield surface. This indicates that kink bands with $\beta > 45°$ will never be able to form.

The maps in Figure 5.18 also show that, for a given $\beta < 45°$, the initial stages of kink band formation are acceptable (an initial increase in ϕ can occur without violating the yield function of the non-kinked material surrounding the band). However, these plots also show that, as ϕ increases for a given β, yield of the non-kinked material would occur prior to the kink band attaining $\phi = 2\beta$. For the near isotropic case ($\frac{\sigma_0}{\tau_0} = 2.2$) the kink band can continue to yield until ϕ

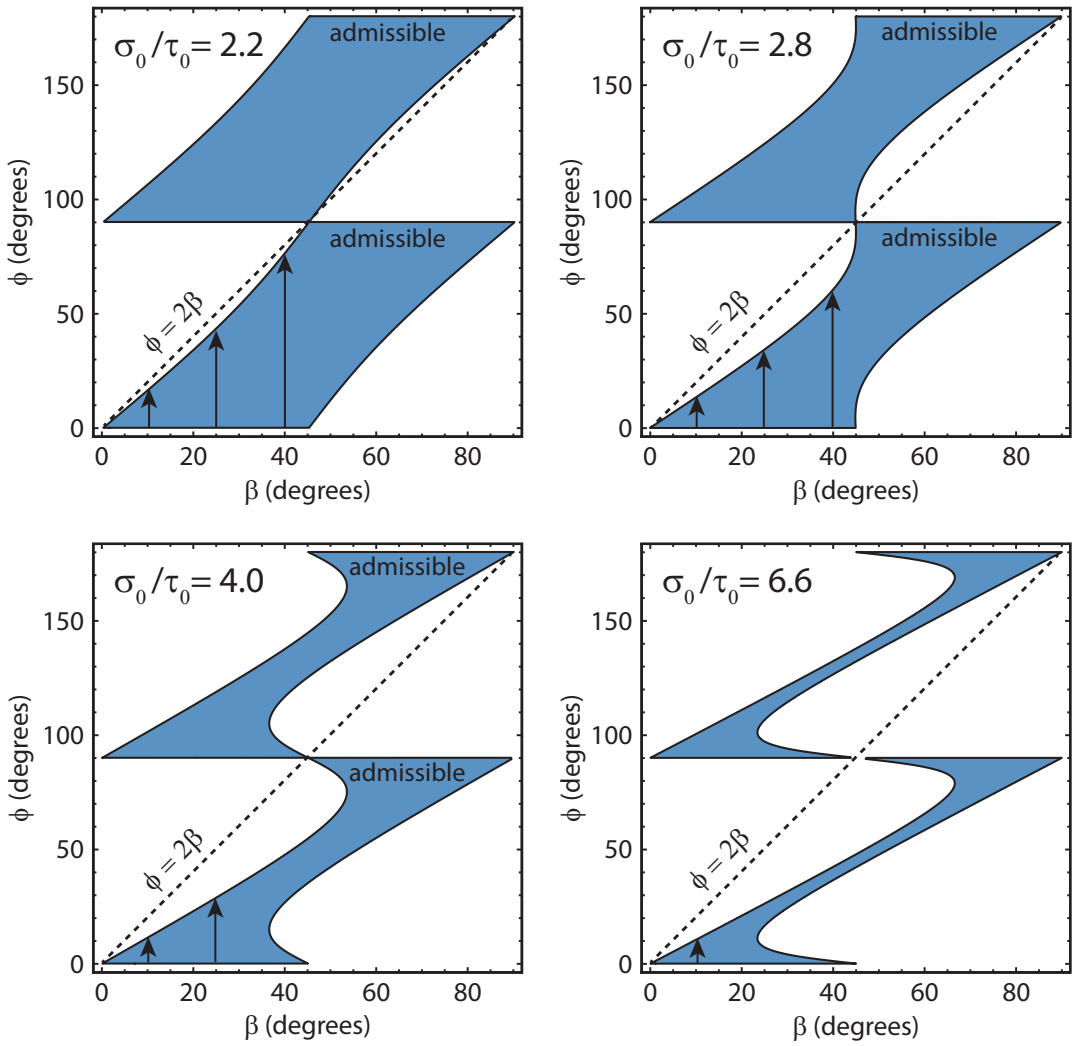

Figure 5.18: Maps indicating the effect of ϕ and β on whether the stress state required to yield the kink band is below the yield surface of the surrounding non-kinked material (F<0). Regions that are shaded blue correspond to yield within the kink band and no yield in the specimen (F<0), indicating an acceptable stress state for continued deformation within the kink band. Regions that are white correspond to a stress state exceeding the yield surface of the non-kinked material (F>0) and are prohibited. At the boundary of these regions, both the kink band and non-kinked material are at yield. The σ_0 to τ_0 ratios used for each map are indicated in the top left corner.

is nearly equal to 2β without the yield function outside of the kink band being satisfied (without encountering the boundary in Figure 5.18). Yet for increasing levels of anisotropy, the angle ϕ at which both the yield functions for the material within the kink band and outside of the kink band are satisfied decreases significantly below the $\phi = 2\beta$ line. This does not necessarily mean that continued kinking to $\phi = 2\beta$ is prohibited, but merely indicates that, at this boundary in Figure 5.18, both the kink band and the surrounding material are at yield. Further analysis of this boundary is needed to determine whether compatible plastic strain rate increments both outside of the kink band and inside of the kink band can be obtained.

The results from analysis of the yield criteria place a constraint on the acceptable values of β, namely that β must be less that 45° at the onset of kink band formation. It is also apparent that additional analysis is needed of the condition at which both the kinked and non-kinked material is yielded (the boundaries of the shaded region in Figure 5.18). The restriction placed on β agrees with the experimental observation that β is never greater than 45° for kink bands in Cu-Nb nanolaminates. Thus consideration of the yield criteria provides a theoretical explanation for this observation. While kink band formation can proceed from $\phi = 0$ to the value of ϕ given by the upper boundary in Figure 5.18, further analysis is needed to determine the behavior of the specimen at this point.

In the remainder of this analysis, the plastic work rates during kink band formation will be calculated. The restriction of $\beta \leq 45^\circ$ will be carried forward, however the effects of all possible ϕ values will be examined. The angle ϕ will not be restricted to a particular range, as the analysis of the yield criteria has not definitively ruled out ϕ values falling outside of the regions shown in Figure 5.18.

5.5.3 Work rate in a kink band

Combining the stresses and plastic strain rates allows the rate of work during kink band formation to be calculated. The objective of this section is to provide insight into why deformation within a kink band should cease at $\phi = 2\beta$, as experimentally observed. It is expected that the work rate required to deform a kink band past $\phi = 2\beta$ should be greater than that required to initially form a kink band. Such a result would indicate a driving force for the formation of a new kink band, rather than continued shear past $\phi = 2\beta$.

The plastic work rate ($\dot{W}^p$) is defined in Equation 5.37. As both the stresses and strains have the same sign, it is not necessary to take absolute values of the stresses or strains. Further simplification is possible as $S_{tt} = -S_{nn}$ and, for isochoric plane strain deformation, $\dot{E}_{tt} = -\dot{E}_{nn}$ (as shown in Equation 5.20).

$$\begin{aligned}\dot{W}^p &= S_{nn}\dot{E}_{nn} + S_{tt}\dot{E}_{tt} + 2\sigma_{nt}\dot{E}_{nt} \\ &= 2S_{nn}\dot{E}_{nn} + 2\sigma_{nt}\dot{E}_{nt}\end{aligned} \tag{5.37}$$

Making appropriate substitutions, an expression for the work rate in the band is given by Equation 5.38.

$$\dot{W}^p = \dot{\phi}\sqrt{\sigma_0^2 \tan^2(\beta-\phi) + \tau_0^2\left(1-\tan^2(\beta-\phi)\right)^2} \tag{5.38}$$

A check of the work rate equation can be conducted by considering the case of an isotropic material, where the work rate should be simply $\dot{W}^p = \tau_o\dot{\gamma}$. Setting $\tau_0 = \frac{\sigma_0}{2}$ (for an isotropic material), Equation 5.38 reproduces this result (where the shear rate is that given in 5.9).

Figure 5.19 shows the work rate (normalized by the rotation rate $\dot{\phi}$ and layer parallel yield strength (σ_0)) as a function of ϕ for several cases of β ($\beta = 15°$, $30°$, and $45°$). The initial work rate (for a constant $\dot{\phi}$) increases monotonically with increasing β, a trend confirmed by calculating (not shown) the derivative of Equation 5.38 with respect to β and noting that it is always positive for $\phi = 0$. Interestingly, for a given β, the work rate decreases from $\phi = 0$ to $\phi = \beta$ and increases monotonically past $\phi = \beta$. The work rate approaches infinity as ϕ approaches $\beta + 90°$, a result of the highly non-linear relationship between the

shear strain rate in the band ($\dot{\gamma}$) and $\dot{\phi}$ (Equation 5.9). The condition $\phi = \beta + 90°$ would correspond to the layers having been sheared and rotated to lie parallel to the kink band boundary: as this condition is approached, the rotation rate ($\dot{\phi}$) approaches zero and $\frac{\dot{W}}{\dot{\phi}\sigma_0}$ becomes infinite.

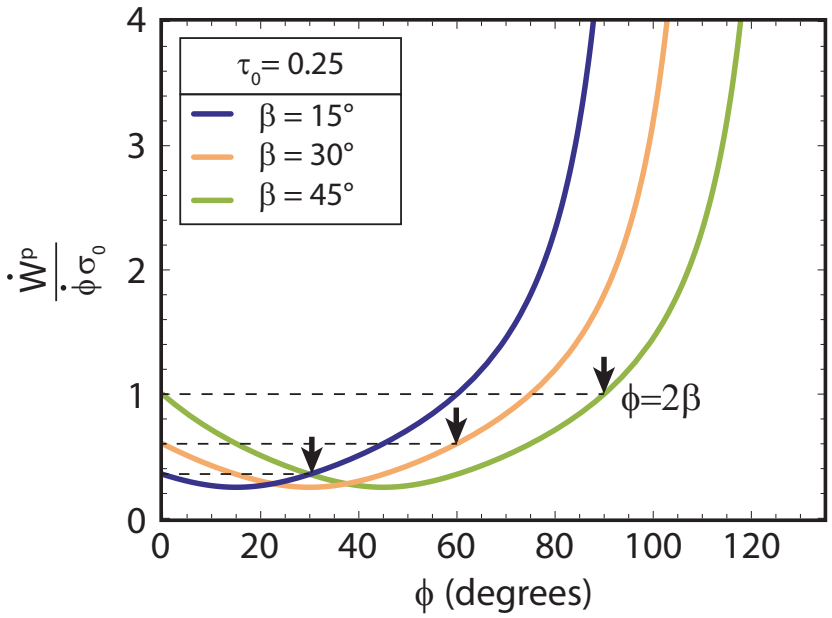

Figure 5.19: Plot showing the work rate (normalized by the rotation rate ($\dot{\phi}$) and the layer parallel yield strength (σ_0)) as a function of ϕ for several different kink band β values. The ratio of σ_0 and τ_0 shown is 1:4, a value that corresponds approximately to that of the 30 nm Cu-Nb nanolaminate material.

Figure 5.19 and Equation 5.38 provide a potential explanation as to why, experimentally, the deformation within a kink band ceases once $\phi = 2\beta$. During kink band formation, the work rate from $\phi = 0$ to $\phi = 2\beta$ is lower than the initial work rate, indicating that continued localized deformation should be favorable.

However, if $\phi = 2\beta$ is reached, further deformation within the kink band would require higher work rates than the initial work rate. This suggests that continued shear past $\phi = 2\beta$ would not be favorable and that, provided the yield functions discussed in the previous section can be satisfied, either the formation of a new kink band or broadening of the $\phi = 2\beta$ kink band can be expected.

While Figure 5.19 shows the work rate (normalized by $\dot{\phi}\sigma_0$), this plot is somewhat non-intuitive as $\dot{\phi}$ is a highly non-linear function of the shear rate within the band ($\dot{\gamma}$). Experimentally, it is not the rotation rate of the layers, but rather the displacement rate of the specimen end that is held constant (for displacement controlled layer parallel compression testing). The relationship between the $\dot{\gamma}$ and $\dot{\phi}$ was given in Equation 5.10. Substituting the expression for $\dot{\phi}$ into Equation 5.38, Equation 5.39 is obtained.

$$\dot{W}^p = \frac{\dot{u}_2}{w_k} \cos^2(\beta - \phi) \csc\beta \sqrt{\sigma_0^2 \tan^2(\beta - \phi) + \tau_0^2 \left(1 - \tan^2(\beta - \phi)\right)^2} \tag{5.39}$$

Note that, for a constant $\dot{u}_2$, the work rate in Equation 5.39 is infinite for $\beta = 0$. This corresponds to the physically unrealistic scenario in which the shear within a kink band is perpendicular to the layers in the specimen and there are no vertical displacements ($\frac{\dot{W}^p}{\dot{u}_2}$ becomes infinite). Nevertheless, for any non-zero value of β, Equation 5.39 provides a description of the work rate as a function

of ϕ and β that can be more readily compared to constant displacement rate experiments.

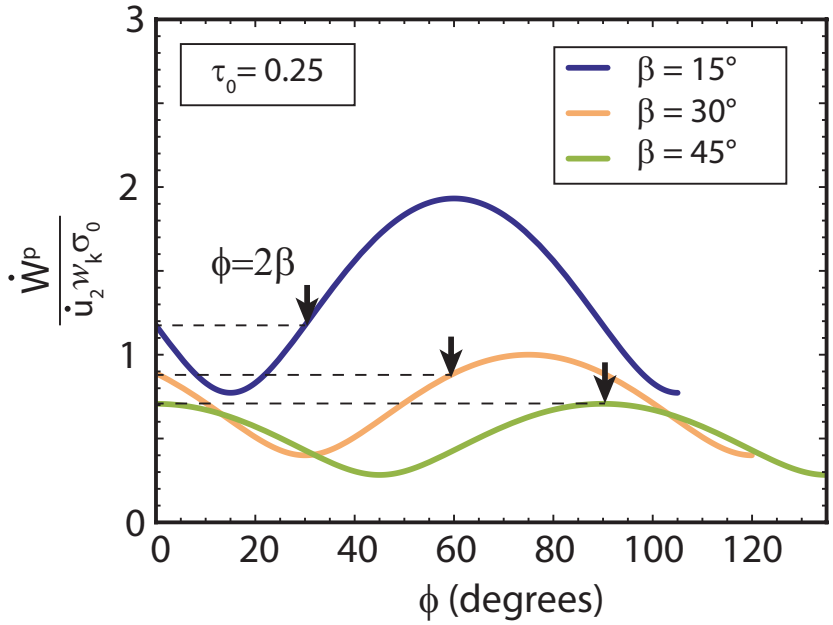

Figure 5.20: Plot showing the work rate (normalized by $\dot{u}w_k\sigma_0$) as a function of ϕ for several different kink band β values. The 1:4 ratio of σ_0 to τ_0 shown corresponds approximately to that of the 30 nm Cu-Nb nanolaminate material.

Figure 5.20 shows the work rate (normalized by $\dot{u}_2 w_k \sigma_0$) for several cases of β ($\beta = 15°$, $30°$, and $45°$). Again, the work rate decreases from $\phi = 0$ to $\phi = \beta$ and increases from $\phi = \beta$ to $\phi = 2\beta$. For all cases, the work rate at $\phi = 0$ and $\phi = 2\beta$ are equal and, for $\beta < 45°$, further rotation past $\phi = 2\beta$ would require higher work rates. While the work rate decreases again past $\phi = \beta + 45°$, the higher work rates between $\phi = 2\beta$ and $\phi = \beta + 45°$ represent a barrier, and $\phi = \beta + 45°$ is never reached for $\beta < 45°$. A special case appears to be $\beta = 45°$,

where the work rate for further rotation past $\phi = 2\beta$ would decrease. This suggests that kink bands with $\beta \approx 45°$ may be nearly able to shear past the $\phi = 2\beta$ condition. The presence of any strain hardening would alter the work rates shown in Figure 5.20 and raise the work rate at $\phi = 2\beta$ slightly higher than the work rate at $\phi = 0$. The presence of a small strain hardening rate may be critical for preventing the further localized deformation in kink bands with $\beta = 45°$ that would be predicted to be possible for a perfectly plastic material.

5.5.4 Kink band model summary

Despite the simplicity of this analytical model for kink band formation (the use of homogeneous stress and strain fields combined with a general anisotropic yield surface), the results provide insight into the geometry and deformation behavior of kink bands. The model provides an upper bound on β that is in excellent agreement with experimental observations. Kink band formation with $\beta > 45°$ cannot occur, as the material outside of the kink band would yield before the necessary stresses for kink band formation are developed.

The condition that the work rate during kink band formation must not exceed the work rate at kink band initiation provides a compelling argument for why deformation of a kink band past $\phi = 2\beta$ does not occur. While this argu-

ment shows that ϕ should never exceed 2β, further analysis of the yield criteria and plastic strain rate increments are needed at values of ϕ nearly equal to 2β. The results shown in Figure 5.18 indicate that the initial stages of kink band formation (rotation from $\phi = 0$) can occur without yield of the surrounding specimen. Yet as ϕ increases towards 2β, the yield function of the surrounding material is satisfied at values significantly below $\phi = 2\beta$ for highly anisotropic materials. The behavior of the specimen when both the yield function of the kink band and the specimen are simultaneously satisfied remains unknown. It is possible that compatible plastic strain rate increments may be found that allow the continued deformation of the kink band to $\phi = 2\beta$. Alternatively, this condition may correspond to the specimen undergoing a compatible deformation (shear and rotation of the layers outside of the kink band) so that the $\phi = 2\beta$ relationship is attained in the final deformed state. Further analysis of the behavior when both the kink band and the surrounding material are at yield is needed.

5.6 Kink band propagation

In this section the phenomenon of kink band propagation will be considered. While the micropillar compression experiments discussed in Section 5.3

showed that kink band formation in small specimens appears to occur by the near-uniform shearing of a band of material, the *in situ* images recorded during bulk layer parallel compression testing (Figure 4.21 in Section 4.4) showed evidence of localized deformation initiating at a specimen corner and growing across the specimen. In this section, *in situ* SEM compression tests are conducted in order to determine whether kink band propagation occurs within bulk specimens. This phenomenon is indeed observed, and the results from several *in situ* SEM experiments showing high magnification views of kink band propagation, as well as the interaction and intersection of propagating kink bands, will be presented.

While the previous sections of this chapter have focused on the deformation occurring within the kink band, the phenomenon of kink band propagation introduces and additional consideration: heterogeneous deformation of the sample surrounding a propagating kink band. Strains surrounding a propagating wedge shaped or 'crack-like' kink band may arise both from compatibility (continuity of the layered structure across a wedge shaped kink band) and stress concentration resulting from a band of near uniform shear strain terminating in a specimen. This is indeed an indication that yielding outside of the kink band occurs and suggests that future analysis of the work rates during kinking should consider this aspect of the problem.

In order to investigate both the strain fields surrounding a propagating kink band and the stability of kink band propagation, strain mapping *via* digital image correlation was conducted during layer parallel compression of bulk (3.6 $\times$ 3.6 $\times$ 7.2 mm) 30 nm Cu-Nb specimens. Kink bands are observed to initiate at specimen edges, propagate across the sample during a rising global stress, and induce extended strain fields in the non-kinked material surrounding the propagating kink band. It is proposed that these stress/strain fields significantly contribute to the total energy dissipated during kinking and, analogous to crack tip stress/strain fields, influence the direction of kink propagation and therefore the kink band inclination angle (β).

5.6.1 Motivation

Most theoretical and experimental studies have focused exclusively on the deformation occurring within the kink band. If a kink band forms by uniform shear across the entire specimen, as was assumed for the kinematics description in Section 5.5, the kink band is the only region that experiences significant deformation; the material on either side of the kink band undergoes only a rigid translation during formation of the kink band. However, significant experimental evidence [153, 154, 158, 177, 186, 202–205] has shown that kink bands

in many material systems form by initiation at a inhomogeneity or stress concentration followed by propagation across the sample. The propagation stage is evident provided that the specimen is large relative to the width of the kink band. The occurrence of kink band propagation was recognized early on: Chaplin, in a 1977 study of kinking in glass reinforced polymers, stated 'Anyone who has watched a compression test on a material which demonstrates this compression crease [kinking] type failure be it fibre reinforced composite, wood or some other natural material, will have noticed that it does not fail simultaneously across the section. The failure starts in one region and propagates, often very rapidly, across the sample' [206]. The propagation of kink bands in oriented polyethylene was recorded during *in situ* tests as early as 1969 [154] yet, presumably due the experimental difficulties of working with high strength fiber composites, similar results were not published in composites literature until decades later [177, 186, 202–204].

While the deformation (shear and rotation to $\phi = 2\beta$) within a propagating kink band may be nearly identical to that proposed in models that assume uniform kink band formation, the deformation of the specimen surrounding a propagating kink band is markedly different. Compatibility between the kinked and non-kinked material (continuity of fibers or layers) geometrically requires distortion of the material surrounding the kink band. In a semi-infinite spec-

imen, the material remains undistorted far in advance of the kink band tip, while behind the kink band tip the specimen is displaced parallel to the kink band by an amount proportional to the width of the kink band and the uniform shear strain within the kink band. This gradient in displacements naturally requires an accommodation strain field in the material surrounding the kink band. Additionally, stress concentration at the kink band tip leads to local strain fields extending in advance of the kink band that are analogous to crack tip strain fields. The presence of these distortions has been noted by observing fiber bending near the tip of a propagating kink band [154, 177]. However, only limited quantitative measures of the extent or magnitude of these strain fields have been reported. An early study [207] used speckle interferometry to map displacements surrounding a kink band in a carbon fiber/PEEK composite, yet only displacement contour plots were reported and no further analysis was conducted. A more recent investigation [208] used digital image correlation (DIC) strain mapping during kink band formation in glass-fiber/epoxy composites and showed a decrease in the elastic strains behind the propagating kink band, indicating softening and unloading. Unfortunately the large size of the kink band compared to the specimen size did not permit careful study of strain fields at the kink band tip. Kink band propagation was shown more clearly in a 2010 DIC study of failure modes during off-axis compression of unidirectional

carbon-fiber/epoxy composites [205], however the focus of that investigation was the construction of a failure envelope and therefore the details of kink band propagation were not analyzed.

The local strain and stress fields in the material surrounding a propagating kink band have not been considered in modeling efforts, yet they are important in that they clearly contribute to the total work of kink band formation and likely influence the direction of kink band propagation. Previous investigators have attempted to explain why certain kink band inclination angles (β) should be preferred by considering the effects of preexisting defects or by considering only the deformation within the kink band [158, 181–183, 193]. Budiansky [182] proposed that β was controlled by the elastic effects of preexisting local imperfections, while Wadee [181] invoked non-isochoric deformation (during multi-axial loading of paper stacks) and proposed that β was set by the layer transverse compressibility. Several investigators [158, 183, 193] have assumed or derived a relationship between β and ϕ and suggest that β evolves through band boundary rotation as the material within the kink band shears. The question of what determines the angle β has proved difficult to answer, with Budiansky concluding that prospects for 'a simple theoretical criteria for β based only on analysis of final, uniform, kinked states are not promising' [191]. The difficulty that has been encountered in efforts to predict β may be attributed to

the lack of attention that has been paid to the propagation stage of kink band formation. During kink band propagation, the interaction of the stress fields driven by compatibility, as well as those arising from the stress concentration at the tip of a kink band, with the anisotropic composite material should be expected to influence the kink band propagation direction. By identifying the factors that influence the propagation direction, and recognizing that the propagation direction determines the boundary angle of the fully formed kink band, an alternative explanation for what sets β may be found.

In the following sections, *in situ* SEM compression tests are used to demonstrate that kink band formation in large Cu-Nb specimens occurs through the initiation of a kink band at a stress concentration, followed by propagation of the kink band across the specimen. The SEM images obtained during kink band propagation reveal the rotation of the material within a propagating kink band and demonstrate that the morphology of a propagating kink band is 'crack-like' (the kink band appears as a slender wedge shaped band). The results from DIC strain mapping of bulk compression specimens are then presented and used to quantify the strain fields associated with kink band propagation. The influence of these strain fields on the kink band angle β and the total energy dissipated during kink band propagation will be discussed.

5.6.2 *In situ* SEM observations

In situ SEM compression tests were conducted in order to determine whether kink band propagation occurs in Cu-Nb nanolaminates. Additionally, these tests were expected to provide insight into the sequence of events leading to the complex networks of strain localization observed in post-test metallographic analysis of the bulk compression specimens (Figure 5.6). Unlike the previous *in situ* video recording using reflected light, SEM imaging using a BSE detector allows the structure within a kink band to be observed clearly (due to both the higher magnifications possible and the relative insensitivity of SEM imaging to the small amount of surface relief that accompanies localized deformation).

Specimens with dimensions of 1 mm $\times$ 1 mm $\times$ 2.5 mm of either 30 nm or 65 nm Cu-Nb were prepared and tested as described in Section 2.5. The stress axis for all tests was parallel to the transverse direction of the rolled material. Imaging was conducted using an accelerating voltage of 25 kV, a spot size of 3, a working distance of 10 mm, and a 40 μm aperture. Due to the position of the BSE detector, some 'shadowing' resulted from the surface relief generated during kink band formation: one side of the ridge that forms on a polished specimen surface during kink band formation appeared brighter than the other side due to its orientation with respect to the BSE detector. Nevertheless, the

lamellar structure within the kink bands was successfully revealed in most cases.

While the specimen dimensions for the *in situ* SEM tests differed from those used for the bulk layer parallel mechanical tests (Section 4.4), the specimens were still many orders of magnitude larger than the layer size: the 30 nm SEM compression specimens contained over 33,000 individual layers over the width of the specimen. Thus no specimen size effect was expected; the results described below are consistent with the appearance of kink band formation in the larger specimens used for bulk layer parallel mechanical tests.

Figure 5.21 shows a sequence of low magnification BSE SEM images taken during kink band formation in a 30 nm compression specimen. The entire width of the lower end of the specimen is shown in the first frame, although due to kink band formation and lateral straining of the specimen, the edges of the specimen move out of the field of view in subsequent frames. The few dark spots on the specimen surface are specks of dust, however these do not obscure the view of kink band formation. A kink band is observed to initiate at the lower left specimen corner and grow across the specimen, eventually intersecting the opposite free surface. The angle of inclination (β) varies slightly during growth, but is a nominal 29°: a value that lies near the range of β values (24°-27°) observed in the larger bulk compression specimens (Section 4.4). A discussion of why certain β values may be preferred is reserved for Section 5.6.3.

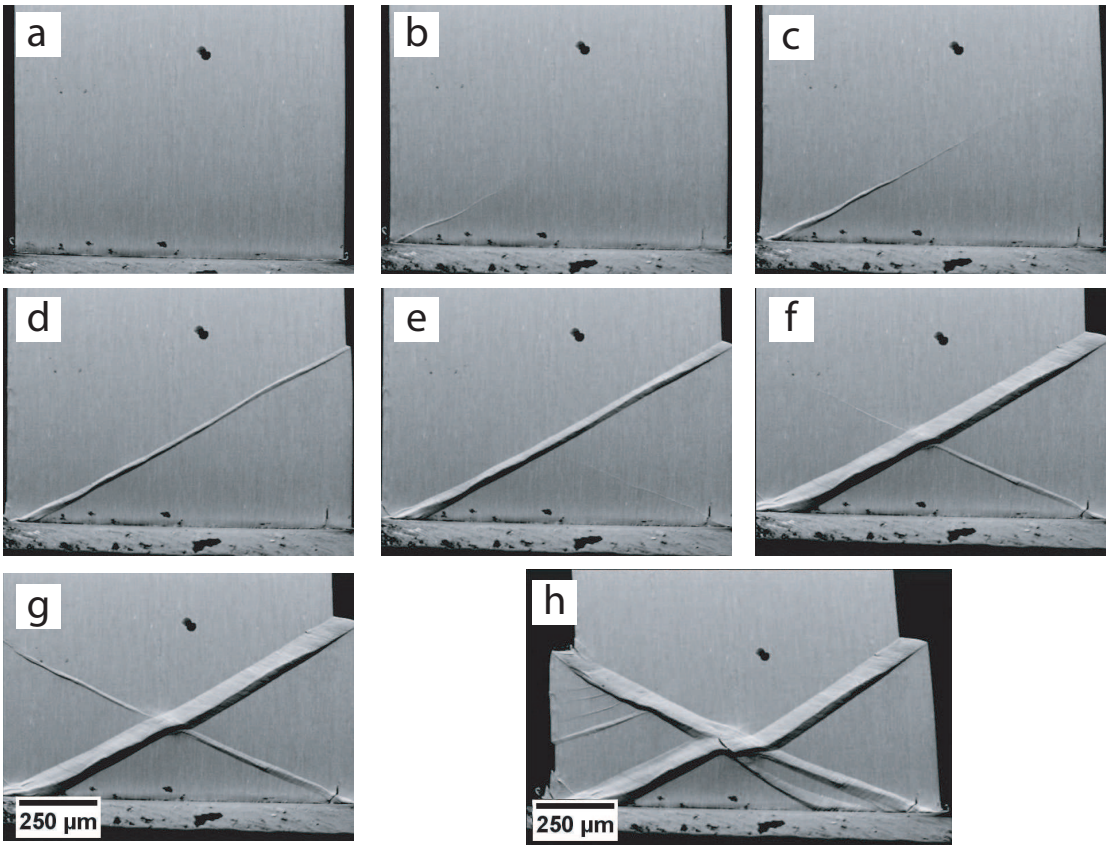

Figure 5.21: *In situ* SEM image sequence of kink band formation in a 30 nm compression specimen. Kink band propagation as well as the intersection of kink bands is evident.

Once the kink band grows across the specimen, kink band broadening occurs (Figure 5.21(d) and (e)). While the original kink band broadens to accommodate additional compressive strain, a second kink band emanating from the right hand corner propagates and intersects the first kink band. This second kink band shears the original kink band, creating an offset between the two halves of the first kink band. Subsequent compression causes the second kink band to broaden, yet interestingly no addition broadening of the initial kink band is observed. This suggests that a kink band intersection may 'lock' the crossed kink band, an idea that will be discussed further in Section 5.7. The last frame shown in Figure 5.21 is a slightly lower magnification image from the end of the compression test and shows the entire width of the specimen end. As mentioned, some shadowing results from the peaked ridge of surface relief that occurs during kinking. The highest point of this shallow triangular ridge corresponds to the original propagation path and thus the different widths of the light and dark sides of the kink bands shown in Figure 5.21 indicate that the kink bands broaden preferentially in the direction away from the end of the specimen. This observation is consistent with the constraint expected from the specimen ends. Demonstration that the peak in the surface relief corresponds to the initial kink band path provides a useful tool for analyzing kink band formation in specimens where *in situ* imaging is not possible.

The initiation of a kink band at a stress concentrating specimen corner in a 30 nm TD sample is shown at a higher magnification in Figure 5.22. The first clearly distinguishable sign of a kink band emanating from the specimen corner occurs in Figure 5.22(b), with the kink band becoming even more clear in Figure 5.22(c). The origin of the band appears to be slightly to the left of the actual specimen corner, perhaps due to slight polishing-induced edge rounding on the top face of the specimen (which would move the actual point of contact between the specimen and the compression platen inward from the specimen corner). The kink band propagates away from the corner in subsequent frames, appearing to bifurcate in Figure 5.22(e) (shown at a higher magnification in Figure 5.22(1)). Ultimately the lower branch becomes dominant as propagation continues, broadening in Figure 5.22(f) and Figure 5.22(g). The nominal propagation angle β is 23°, a value in the range of previously noted β values.

A final series of frames from the *in situ* SEM tests is shown in Figure 5.23. In this experiment, two similarly inclined kink bands were observed to propagate towards one another, resulting in the configuration shown in Figure 5.23(a). During additional straining, the kink bands connect (Figure 5.23(b)) and broaden. Further compression results in the formation of additional small kink bands (Figure 5.23(e,f)) surrounding the broadening kink band and its intersection with a preexisting oppositely inclined kink band. Figure 5.23 provides

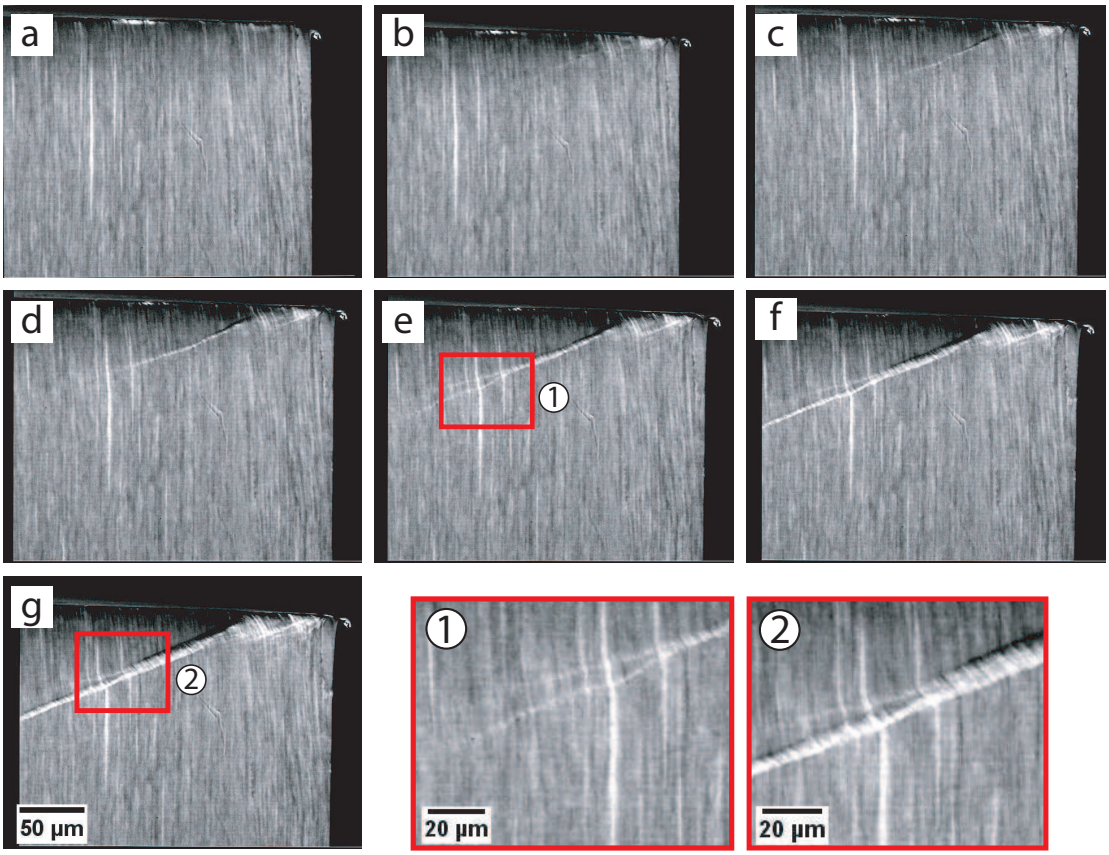

Figure 5.22: *In situ* SEM image sequence of kink band initiation at the corner of a 30 nm TD compression specimen.

an indication of how the complex networks of kink bands observed in Figure 5.6 arise.

The results from *in situ* SEM compression provide evidence that kink band formation occurs through propagation from a stress concentrating feature (specimen corners), followed by band broadening. Intersections with other kink bands are observed, and it is clear that the 'crossed kink band' is sheared by the crossing kink band.

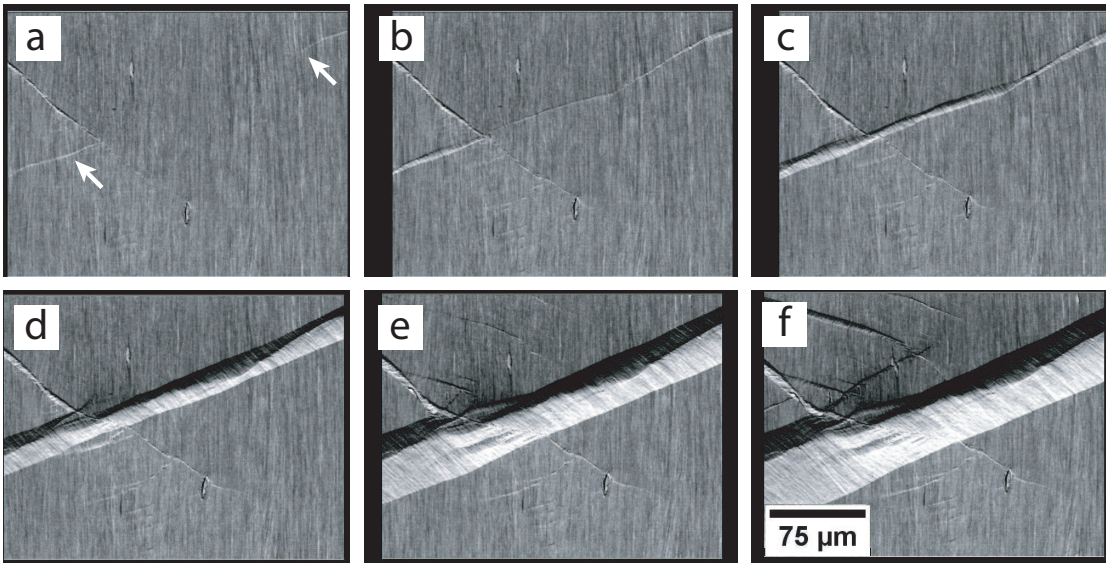

Figure 5.23: *In situ* SEM image sequence of several kink bands in a 30 nm compression specimen interacting. Two similarly inclined kink bands that propagated towards one another are indicated with arrows in (a).

The kink band propagation phenomenon described above requires deformation of the specimen surrounding the propagating kink band (as layer continuity across the wedge shaped kink band is maintained). Additionally, there is

likely a stress concentration associated with a narrow wedge shaped kink band terminating in a specimen. In order to obtained a quantitative measure of the deformation surrounding a propagating kink band, DIC strain mapping was conducted on bulk compression specimens.

5.6.3 Mechanical testing and DIC

In order to investigate the strain fields associated with kink band propagation, DIC strain mapping was conducted on bulk layer parallel compression specimens of the 30 nm layer thickness ARB Cu-Nb material. Several features make this material attractive for the study of kink band propagation: 1) the load drops associated with kinking are small relative to the high stresses at which kink bands initiate, suggesting stable or near stable growth, 2) layer debonding during kink band formation is infrequent, and 3) the layer length scale and therefore minimum kink band length scale is orders of magnitude smaller than the specimen size. This facilitates *in situ* observations of kink band propagation and allows for high resolution DIC strain mapping of the strain fields surrounding a narrow, propagating, kink band.

Specimens for compression testing and DIC analysis were prepared as described in Section 2.6. The specimens were compressed along the TD material

direction at a strain rate of $10^{-4}s^{-1}$ between rigid, non-rotatable platens. A laser extensometer was used to record the nominal compressive strain throughout the tests. In situ images were recorded at a rate of 2 images per second during compression, allowing the surface strains to be obtained through DIC analysis as described in Section 2.6.1.

5.6.4 Global stress-strain response and kink band initiation

Figure 5.24 shows the stress-strain response of a compression specimen, with the strain calculated using the laser extensometer data. The results generally match the mechanical behavior expected based on prior mechanical tests of the same material (Chapter 4). Examination of the *in situ* images of the specimen surface allows the stress-strain curve to be divided into two regimes: one prior to the initiation of a visible kink band and labeled 'uniform compression' and one regime corresponding to and labeled 'kink band propagation.' The stress-strain curve does not display any sharp change of slope at the point of kink band initiation, making determination of these regimes dependent on *in situ* observations. Kink band propagation occurs initially under a rising load (from 1142 MPa to the maximum of 1205 MPa), however a sharp load drop (near the end of the stress-strain curve) corresponds to the final propagation of the kink band across

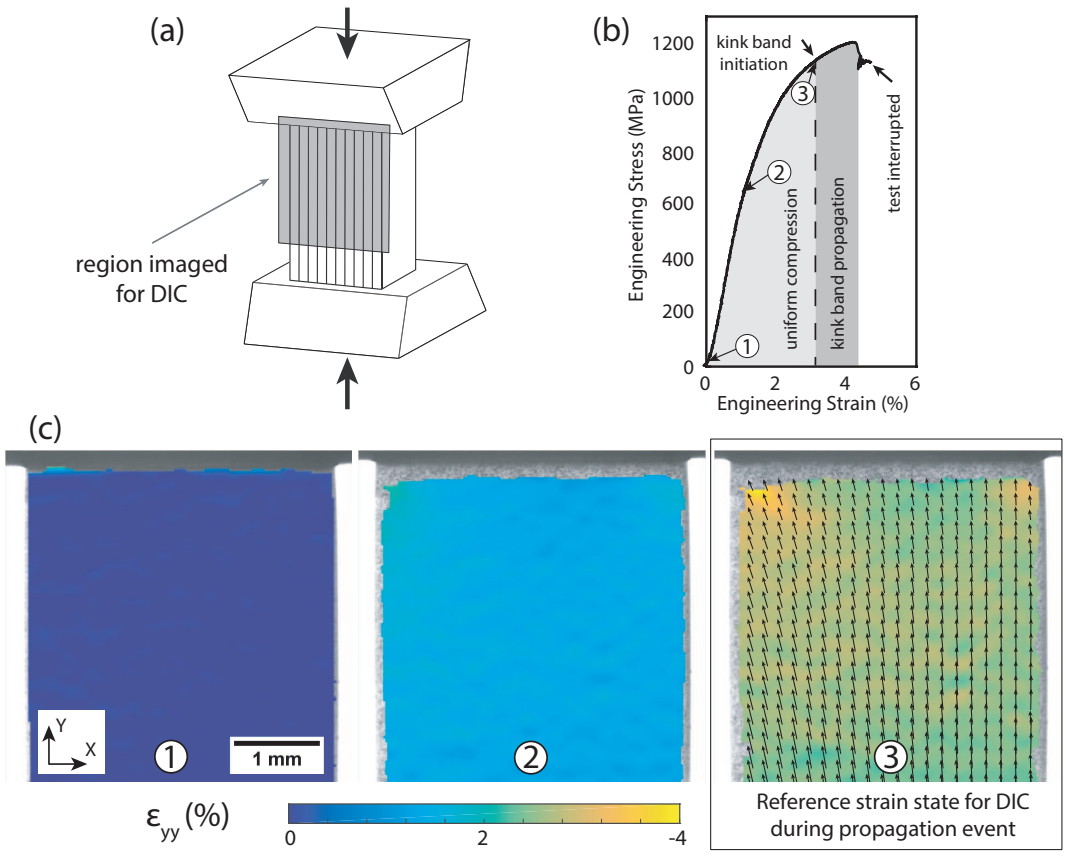

Figure 5.24: (a) Schematic of compression setup and DIC region. (b) Stress-strain curve annotated to show uniform compression regime, kink band initiation, and kink band propagation regime. Points 1, 2, and 3 prior to kink band initiation correspond to DIC strain maps (ϵ_{yy}) shown in (c). The displacement vector map overlay in (c3) indicates non-symmetric displacements which bias kink band formation to occur from the upper left corner. The strain distribution in part (c3) is taken to be the reference configuration for subsequent DIC analysis of the strains during kink band propagation, Figures 5.25 and 5.26.

the specimen. The rising load during the initial stages of kink band propagation suggest that propagation is more difficult than the initiation of a kink band in these samples. Based on the behavior of other DIC specimens and prior layer parallel compression experiments (Chapter 4), continued compression would be expected to induce kink band broadening at a near constant stress.

Compressive strain (ϵ_{yy}) maps of the imaged region of the specimen corresponding to points '1,' '2,' and '3' labeled on the stress-strain curve are shown in Figure 5.24(c). As the specimen is loaded in the elastic range local strains appear fairly homogeneous although, due to the effects of friction at the specimens ends, a triangular constrained region near the specimen end and slight specimen barreling are expected. Elevated strain values are observed at the stress-concentrating specimen corners (evident in Figure 5.24(c3)), with the left hand corner showing higher local strains than the right hand corner. The overlaid displacement vector map shows non-symmetric displacements which can be attributed to either non-uniform friction or a slight misalignment of the specimen. The asymmetric displacements are presumably responsible for kink band nucleation occurring at the left rather than right hand corner. Point '3' is taken to correspond to the beginning of kink band propagation as this frame precedes the first frame in which a kink band can be clearly seen to extend from the top left corner. It is likely that the true initiation point occurs slightly earlier

and would have been detected earlier had high magnification microscopy been conducted on that corner. As the focus of this section is kink band propagation and not initiation, it is reasonable to take point 3 as the beginning of kink band propagation. In order to distinguish small local strains during the subsequent kink band propagation, all DIC analysis of propagation uses the specimen state at point 3 as the reference state. This effectively zeros out the local strain values shown in Figure 5.24(c3) and allows the shape of the strain field in front of the propagating kink band to be shown clearly using the change in strain state from the reference configuration ($\Delta\epsilon_{xy}$ and $\Delta\epsilon_{yy}$). This referencing also minimizes the difference between the deformed and undeformed coordinate system, providing a more accurate representation of the strain fields.

5.6.5 Kink band propagation

Figures 5.25 and 5.26 show the stress-strain curve, specimen image, and $\Delta\epsilon_{xy}$ and $\Delta\epsilon_{yy}$ strain maps during kink band propagation. The instantaneous stress, total specimen strain (from laser extensometer data), and time since initiation are shown on the stress-strain curve. The kink band is evident as a dark band on the full resolution specimen images due to deformation induced surface relief, and an arrow is used to indicate the kink band tip location. The

nominal angle of propagation and therefore kink band inclination angle (β) was $\sim$27° however the propagation across the last quarter of the specimen occurred at a more shallow angle of $\sim$21° . These values are in good agreement with the previously reported values for β in 30 nm TD compression specimens (24-27° in Table 4.2 and 23-29° for *in situ* SEM tests).

The 2-D Lagrange strain tensor obtained from DIC has been transformed into a coordinate system in which the x-axis is aligned with the nominal direction of kink band propagation (a 27.5° rotation from the coordinate system used in Figure 5.24) and $\Delta\epsilon_{xy}$ lies parallel to the shearing action of the kink band. Continued uniform straining of the specimen during compression is evident in Figure 5.25, however the inhomogeneous strains adjacent to and in front of the kink band become clear as the kink band length increases. While some elevated local strains are present near the right hand corner, as expected due to the stress singularity at that location, no visible kink band is observed. The pronounced $\Delta\epsilon_{xy}$ strain field in front of the kink band shown in the bottom of Figure 5.25 extends across the entire specimen (millimeters ahead of the kink band tip), becoming more diffuse and lower in magnitude as the distance from the tip increases. The shear strain field is aligned with the eventual propagation path.

During the second half of propagation, Figure 5.26, the strain fields in front of the kink band continue to increase in magnitude and spatial extent and the

kink band propagation rate accelerates. No evidence of unloading is seen in the material behind the kink band tip during propagation. The kink band morphology during propagation is that of a very slender wedge (appearing crack-like), with the kink band width tapering from approximately $\sim$30 μm near the initiation site to below 5 μm at the visible kink band tip. This is seen more clearly in Figure 5.27 which shows an image of the specimen taken one second before the kink band reaches the specimen edge. While the kink band taper is somewhat non-uniform, the nominal taper angle is $\sim$0.5°.

By identifying the kink band tip location, the strain fields obtained though DIC can be plotted in polar coordinates and compared to those of an inclined crack. Based on the inclination angle of the kink band ($\sim$27°), a similarly inclined crack might be expected to have both a mode I and mode II component, however the mode I stress intensity factor would be negated by tractions arising from crack face closure. Therefore the kink band tip strain fields will be compared to those of a pure mode II crack. In addition to the elevated strains near the kink band tip (Figure 5.26(a,b)), significant homogeneous compression is observed during kink band propagation (as seen from comparing Figure 5.25(a) to Figure 5.25(b)). Therefore it is expected that the experimentally observed kink band strain field consists of a superposition of a uniform far field strain and the strains associated with the stress singularity at the kink band tip.

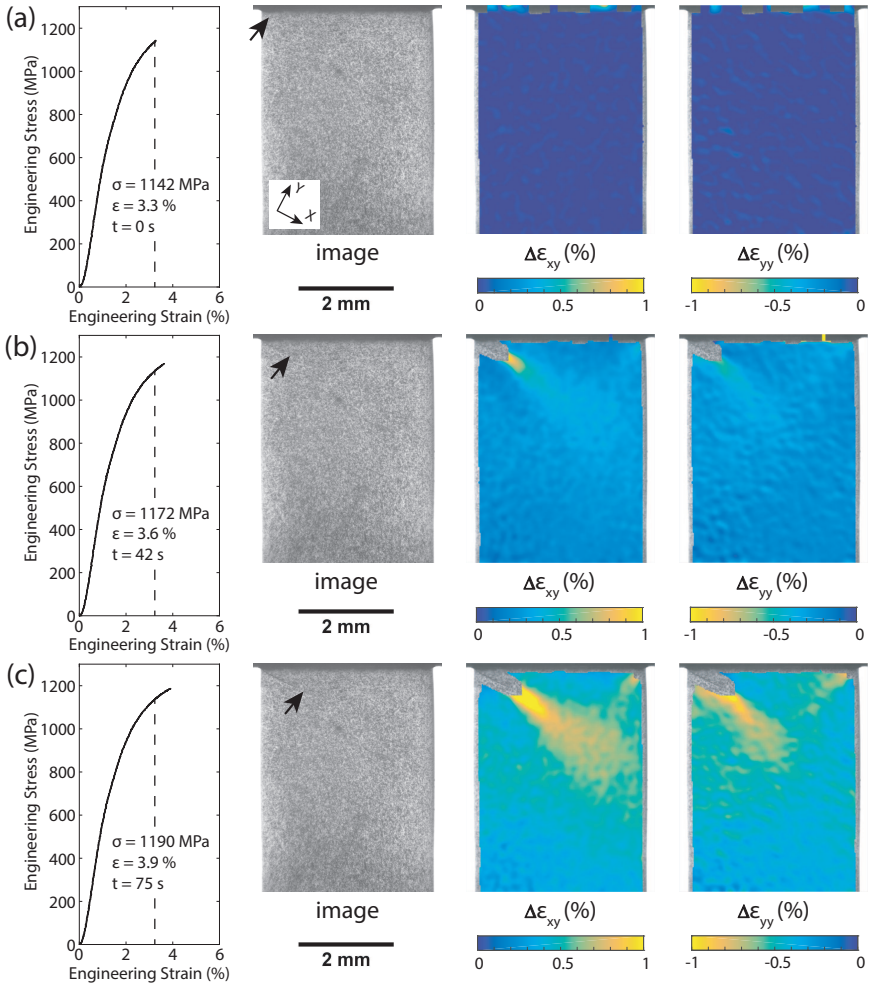

Figure 5.25: Kink band propagation, part 1: Stress-strain curve, in-situ image, $\Delta\epsilon_{xy}$ strain map, and $\Delta\epsilon_{yy}$ strain map during the initial stages of kink band propagation. The arrow indicates the tip of the kink band as determined from the full resolution optical images. Note that the coordinate system is rotated to align with the kink band propagation direction and that different scales are used for $\Delta\epsilon_{xy}$ and $\Delta\epsilon_{yy}$. All calculated strains are referenced to the state of the sample at the beginning of kink band propagation (dashed line on stress-strain curve) and therefore do not include the nearly homogeneous compression that occurred prior to kink band nucleation. Inset on the stress-strain diagram gives stress, total sample strain (ϵ), and time (t) relative to start of kink band propagation.

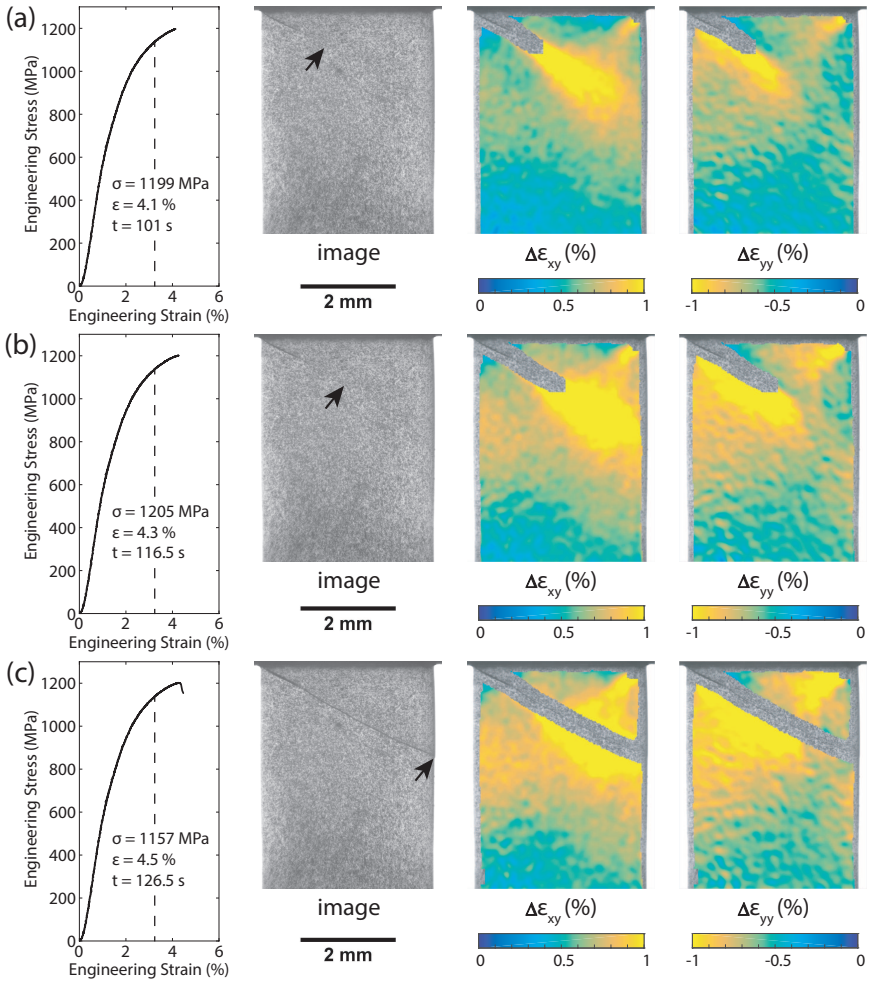

Figure 5.26: Kink band propagation, part 2: Stress-strain curve, in-situ image, $\Delta\epsilon_{xy}$ strain map, and $\Delta\epsilon_{yy}$ strain map during the later stages of kink band propagation. The arrow indicates the tip of the kink band as determined from the full resolution optical images. Note that the coordinate system is rotated to align with the kink band propagation direction and that different scales are used for $\Delta\epsilon_{xy}$ and $\Delta\epsilon_{yy}$. All calculated strains are referenced to the state of the sample at the beginning of kink band propagation (dashed line on stress-strain curve) and therefore do not include the nearly homogeneous compression that occurred prior to kink band nucleation. Inset on the stress-strain diagram gives stress, total sample strain (ϵ), and time (t) relative to start of kink band propagation.

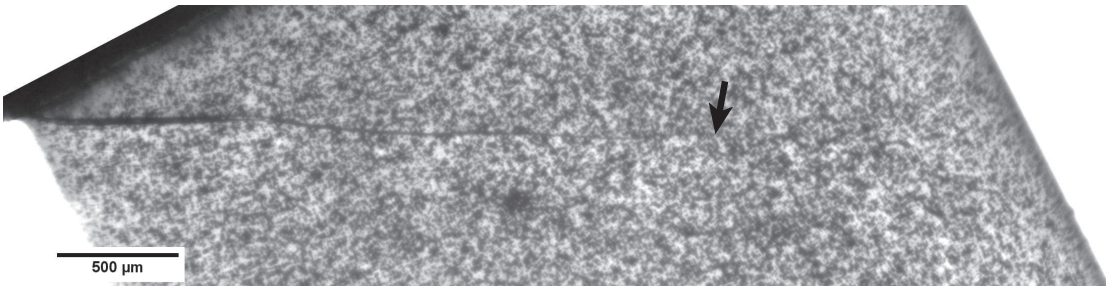

Figure 5.27: Full resolution image showing kink band extending from the specimen corner initiation site and terminating in the specimen (tip location is marked with an arrow). Image has been rotated 27.5°. The kink band appears as a very slender wedge, tapering from approximately ∼30 μm to below 5 μm over a length of 2.8 mm (a nominal wedge angle of ∼0.5°).

Figure 5.28 compares the experimental kink band polar strain fields to those resulting from the combination of the analytical linear elastic fracture mechanics (LEFM) solution for a mode II crack and a small (0.4%) homogeneous compression. The LEFM strain field solution is given in Equation 5.40, where Y is the elastic modulus and ν is the Poisson's ratio. As with Figures 5.25 and 5.26, the large uniform strain prior to kink band initiation is not included in the strains presented in Figure 5.28. The magnitude of the small homogeneous strain that was included in the calculation was obtained from the difference between the experimentally measured 'far field' strain value at the lower end of the specimen (3.6 mm from the kink band tip) and the theoretical contribution of the mode II crack strains at the same location. While the stress intensity factor K_{II} was experimentally fit to the data, Figure 5.28 shows remarkably good agreement in the angular distributions of strain as well as the radial dependence of ϵ_{rr}, $\epsilon_{\theta\theta}$,

and $\epsilon_{r\theta}$. Material anisotropy may be responsible for the differences in the angular strain distributions between the kink band fields and the isotropic LEFM solution, although the discrepancies and therefore potential effects of material anisotropy do not appear pronounced. Figure 5.29 provides a plot of the radial distribution of strains along the $\theta = 0$ and $\theta = -62.5^\circ$ lobes and indicates generally good agreement between the kink band fields and the $r^{-\frac{1}{2}}$ singularity in the elastic crack tip solution.

$$\begin{aligned}
\epsilon_{rr} =& \frac{K_{II}}{2Y\sqrt{2\pi r}} * (1+\nu)(-1+4\nu+3\cos\theta)\sin\frac{\theta}{2} \\
\epsilon_{\theta\theta} =& \frac{K_{II}}{2Y\sqrt{2\pi r}} * (1+\nu)(-3+4\nu-3\cos\theta)\sin\frac{\theta}{2} \\
\epsilon_{r\theta} =& \frac{K_{II}}{4Y\sqrt{2\pi r}} * (1+\nu)(\cos\frac{\theta}{2}+3\cos\frac{3\theta}{2})
\end{aligned} \tag{5.40}$$

The agreement between the mode II elastic crack tip fields and the experimental kink band strain fields may seem surprising given that at a macroscopic strain of $\sim 4\%$ these strain fields are expected to be fully plastic. While a more appropriate comparison would be that between the kink band and the Hutchinson, Rice, and Rosengren (HRR) plastic crack tip fields, analytical solutions for the mode II HRR field angular dependencies are, to the best of the author's knowledge, unavailable. Therefore the analytical LEFM solutions are plotted, with the only modification being that volume preservation was enforced by setting the Poisson's ratio equal to 0.5. While the LEFM solution was used in place of the

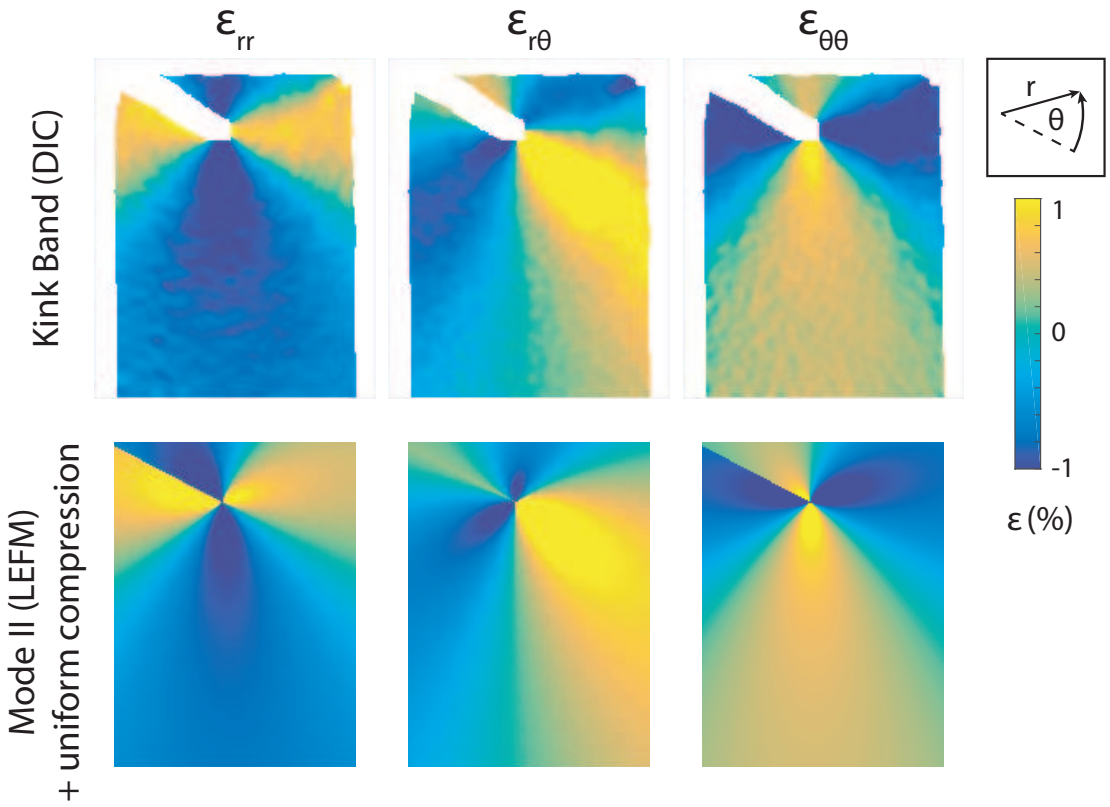

Figure 5.28: Polar strain fields during propagation are similar to those obtained from the superposition of the LEFM analytical solution for an inclined mode II crack and a uniform far field compressive strain. The polar coordinate system is rotated so that $\theta = 0$ is aligned with the kink band propagation direction. The elastic modulus was taken as 115 GPa (the average of Cu and Nb moduli), a Poisson's ratio of 0.5 was used, and the mode II stress intensity factor was fit to the experimental data, resulting in $K_{II} = 53$ MPa m$^{1/2}$.

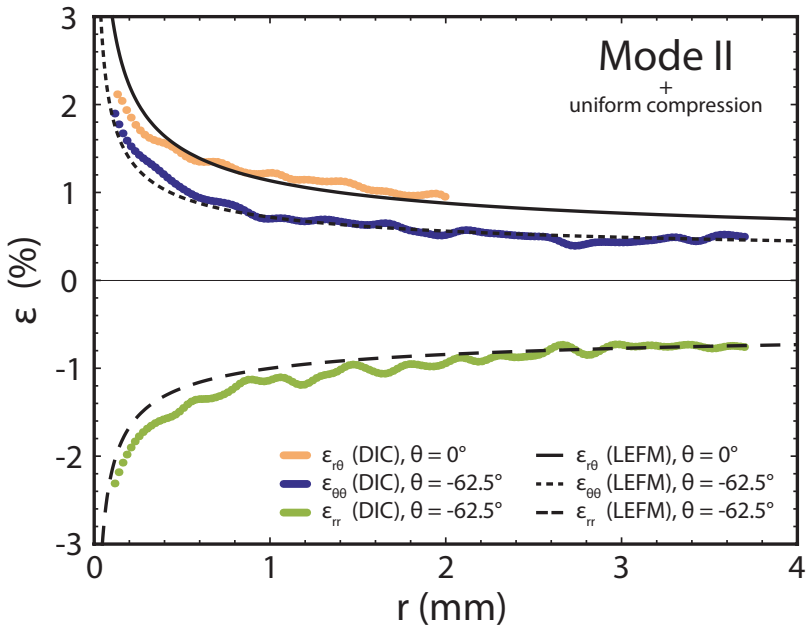

Figure 5.29: Radial dependence of kink band and mode II crack polar strain fields shown in Figure 5.28. ϵ_{rr} and $\epsilon_{\theta\theta}$ are plotted at $\theta = 90°$ while $\epsilon_{r\theta}$ is plotted along $\theta = -27.5°$. These angles correspond to the two lobes in Figure 5.28 that are oriented away from the compression platens and are therefore least likely to be influenced by end constraints.

HRR solution, the difference between the two is slight when K_{II} is taken as a fit parameter. The HRR solutions show similar angular dependencies of strain and the HRR strain fields follow $r^{-\frac{n}{n+1}}$ [209], where n is the stress hardening exponent relating plastic strain (ϵ^p) to a material constant (α) and stress (σ): $\epsilon^p = \alpha\sigma^n$. For a near linear work hardening material ($n \approx 1$), the strain associated with the dominant singularity follows a relationship approximating $r^{-\frac{1}{2}}$. The small nonlinearity in the portion of the stress-strain curve corresponding to kink propagation (Figure 5.24(b)) suggests that the strain associated with the dominant singularity would show an r dependence close to that obtained from LEFM (as observed in Figure 5.29). Thus, despite the strain fields at a macroscopic strain of $\sim 4\%$ being fully plastic, the subtle differences in r dependence between LEFM and HRR fields would not be distinguishable.

While the strain field maps in Figures 5.25, 5.26, and 5.28 provide a quantitative description of the distortion of the specimen, a more intuitive picture is provided by exaggerating and applying the displacements obtained through DIC to a series of lines representing the layered sample. This approach is modeled on the work of Sun [208]. An image containing a series of vertical lines is generated with image dimensions matching the dimensions of the DIC displacement data array (see Figure 5.30(a)). Each pixel of the original image is displaced according to the DIC displacement data multiplied by a scaling factor (in the

present case, 100). This large scaling factor, and therefore large exaggeration of the displacement, is employed to amplify the small strains observed during kink propagation. Due to this, it is only possible to apply the horizontal displacements; applying equally exaggerated vertical displacements would cause the image to collapse to nearly a line. Since only horizontal displacements are applied, angles are not reproduced faithfully and the small region around the kink band where displacement data are missing appears as if it were a material discontinuity. Nevertheless, Figure 5.30 provides an indication of the deformation pattern surrounding a propagating kink band and points out features such as the 'reverse shear' in the region below the kink band (Figure 5.30 (b,c)) that is present, but not as apparent, in the strain maps in Figures 5.25 and 5.26. The deformation of this region indicates that significant layer parallel shear occurs adjacent to the kink band flank to accommodate the kink band.

5.6.6 Implications of DIC results

The *in situ* observations presented in Figures 5.25 and 5.26 show that kink band propagation in Cu-Nb laminates can occur under a rising load during uniaxial compression. The strain fields ahead of and surrounding the propagating kink band are significant in magnitude and spatial extent: in Figure 5.26(b) a

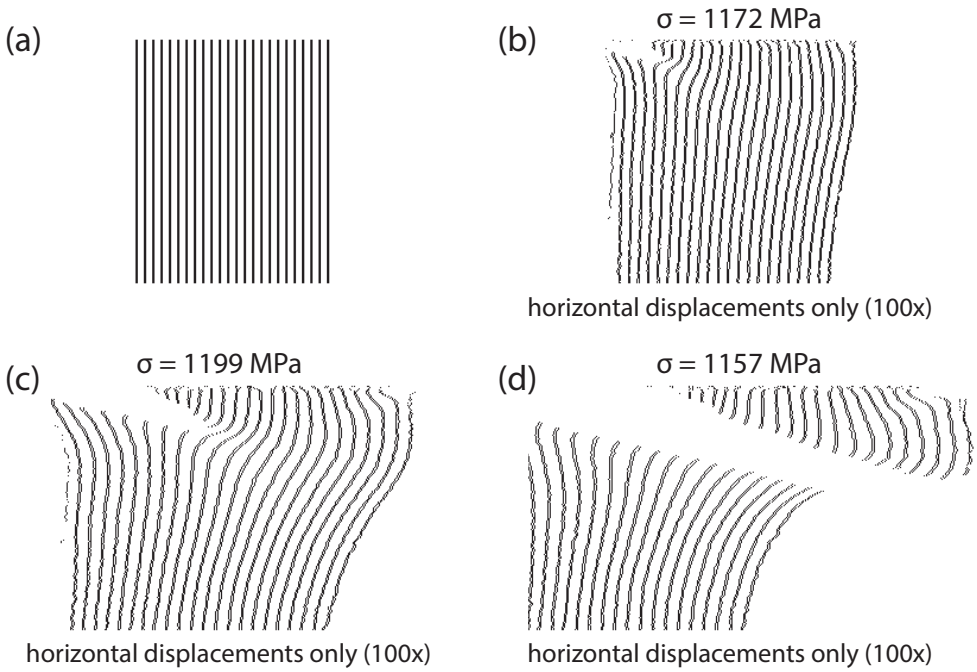

Figure 5.30: Exaggerated (100x) horizontal displacements are applied to an image containing vertical lines and representing the specimen (a). Images in (b), (c), and (d), correspond to Figure 5.25(b), Figure 5.26(a), and Figure 5.26(c) respectively. While vertical displacements are not included, these exaggerated representations point out features of the specimen distortion such as the reverse shear below the kink band in (b,c) that are mapped quantitatively in Figures 5.25 and 5.26.

1.5 mm^2 area of the strain field ahead of the kink band contains $\Delta\epsilon_{xy}$ values in excess of 1%. While the shear strain within the kink band is very large ($\gamma = 1.12$ given $\beta = 27.5°$ and $\phi = 2\beta$), the area of the kink band in Figure 5.26(b) is no greater than 0.03 mm^2. The work of deformation (Φ) is proportional to the area (A), plastic strain (ϵ_{ij}^p), and stress (σ_{ij}) of the material assuming plane strain fully plastic deformation (Equation 5.41).

$$\begin{aligned} \Phi &= \int \sigma_{ij}\epsilon_{ij}^p dV \\ &\propto \sigma_{ij}\epsilon_{ij}^p A \end{aligned} \tag{5.41}$$

Although simplistic, comparing the relative areas and strain magnitudes and assuming equal stresses inside and outside of the kink band indicates that the energy required to form the strain field extending in front of the kink band is approximately one half of the energy required to deform the material within the kink band. That is, despite the large strain within the kink band, the much larger area of the surrounding material allows the small strains in the kink band tip strain field to contribute significantly to the total energy dissipated. This evaluation almost certainly underestimates plastic dissipation in the strain field as the contributions of material sheared less than 1% are neglected. While previous studies have examined the work contributions from deformations within a kink band and sought to explain the geometry of kink bands using energy mini-

mization arguments [181, 183, 210], any prediction of total energy dissipation during kink band formation must include consideration of the deformation field in front of a propagating kink band.

Two distinct factors responsible for the local strain fields during kink band propagation can be identified: 1) compatibility between the wedge shaped kink band and non-kinked 'matrix' (accommodation strains) and 2) the stress concentration at the tip of a kink band terminating in a specimen. Accommodation strains around a wedge shaped kink band arise due to the variation in kink band width and continuity of layers across the kink band. The homogeneous local shear strain in the material within a kink band with inclination β and rotation ϕ (Figure 5.2) is given by Equation 5.42.

$$\gamma = \sec^2(\beta - \phi) \tag{5.42}$$

The displacement of the layered structure across the kink band is a function of the width of the kink band and the shear strain within the kink band. The slightly wedge shaped kink band morphology shown in Figure 5.27 indicates a gradient in kink band width and therefore a gradient in displacements along the kink band boundary. This displacement gradient, combined with the previously observed layer continuity across kink bands, requires a corresponding displace-

ment gradient in the non-kinked material adjacent to the band boundary. The necessity of an accommodation strain field surrounding a wedge shaped kink band has been pointed out in work on oriented polymers [211], and a close analogy is found in the strain field surrounding a deformation twin terminating in a single crystal [212]. Given the wedge shaped morphology of the propagating kink band (Figure 5.27) and the numerous non-parallel kink band boundaries observed post-test in compression specimens (Figure 5.6(d)), it appears that accommodation strain fields are commonly associated with kink bands in Cu-Nb laminates.

While accommodation strains are clearly required for a wedge shaped kink band, these strains are necessary in the material surrounding a propagating kink band regardless of the shape of the propagating band. They are an unavoidable result of compatibility between the kinked and non-kinked material when a kink band terminates in a specimen. Figure 5.31 shows several possibilities for the shape of a kink band propagating through a layered material. These schematics are drawn so that the layers outside of the kink band remain vertical, a simplifying representation that emphasizes the layer transverse component of the geometrically required strain field. Here it is assumed that the kink band need not grow in a self similar manner: the kink band 'tip zone' may have a different morphology than the portions of the kink band far removed from the tip. The

uniform wedge shape, Figure 5.31(a), requires a linear displacement gradient at the boundary and leads to accommodation strains that are uniform along the length of the kink band. Figures 5.31(b), (c), and (d) show kink bands with parallel sides and various tip morphologies that result in accommodation strains present only near the tip zone. Varying the width of the kink band tip zone (Figure 5.31(b)) and varying the rotation ϕ in a kink band tip zone (Figure 5.31(c)) results in similar accommodation strains while a non-uniform wedge or elliptical kink band tip zone requires nonlinear displacement gradients at the boundary and results in non-uniform accommodation strains. Various morphologies of propagating kink bands have been reported in the literature: a self-similar wedge is consistent with the experimental observations of Robertson on kinks in oriented polymers [154], a parallel sided band terminating in a wedge shaped tip zone was considered by Pertsev [213, 214], and a parallel sided band terminating in a zone of variable fiber rotation ϕ matches the observations of Vogler for kink bands in polymer matrix fiber composites [177]. Other experimental work points towards a combination of variations in ϕ and gradients in kink band width at the tip zone of a kink band [153].

A clear difference in the distribution of accommodation strains is evident between a self-similar wedge (Figure 5.31(a)) and a band possessing parallel sides and a district tip zone (Figure 5.31(b), (c), and (d)). The question re-

mains, however, of why one morphology should be preferred over another and whether the constitutive behavior of the material influences the morphology of a propagating kink band. Consider the two kink band morphologies shown in Figure 5.31(a) and (b) propagating through either an elastic or plastic specimen. The self-similar wedge shaped kink band 5.31(a) has accommodation strains adjacent to the kink band. An incremental advance of the kink band (Figure 5.31(e)) subjects additional material now adjacent to the newly created kink band segment to the geometrically required accommodation strain. The material that was adjacent to the kink band boundary prior to its advance remains distorted. In contrast, the advance of a kink band with parallel sides and a wedge shaped tip zone (Figure 5.31(c)) requires both distortion of the material adjacent to the newly created kink band tip zone and a reversal of the accommodation strains in material that now lies next to the parallel boundary. This is illustrated in Figure 5.31(f). In the case of purely elastic accommodation strain fields, such a reversal of the accommodation strains behind the tip of the kink band would lower the strain energy in the material and should be preferred. If, however, the accommodation strain fields are predominantly plastic, such a reversal would be dissipative and require additional (redundant) plastic deformation. Thus a uniform wedge shape should be preferred when the accommodation strains are predominately plastic. This argument agrees with

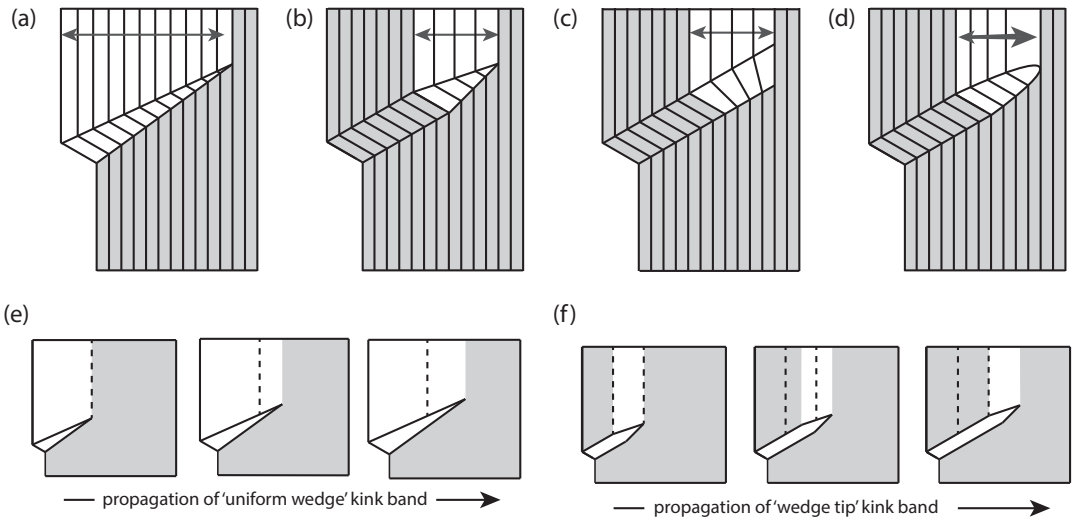

Figure 5.31: Schematic illustrating potential geometries for a kink band terminating in a specimen (a-d) and resultant accommodation strains. (e) and (f) show kink bands with either a uniform wedge shape (e) or a wedge shaped tip (f) advancing through the specimen. The dashed lines denote the original boundaries of the accommodation strain region.

the observation that kink bands propagating through yielded Cu-Nb nanolaminates and compliant polymers posses a fairly uniform wedge morphology [154], while kink bands propagating through fiber composites (in which the fibers remain elastic) tend to have parallel sided kink bands with a district tip zone [153, 177].

The second factor responsible for local strain fields during kink band propagation is the stress concentration that occurs at the tip of the kink band. The long, narrow, propagating kink band shown in Figure 5.27 has strong similarities to a mode II type shear crack and is found to have similar strain fields in

front of the kink tip (Figure 5.28). Several investigators have proposed fracture mechanics based approaches to modeling kink band propagation. Moran and Shih [153] proposed modeling kink band propagation as growth of a predominantly mode II crack with bridging tractions through an anisotropic material, yet they did not have the experimental fields in hand to motivate such a modeling effort. Bažant [215] proposed and conducted an analysis treating the kink band as a crack with a significant fracture process zone at the kink band tip. While no existing theoretical analysis accounting for material anisotropy, bridging tractions, and displacements prescribed by the kink band geometry is available to be compared with the experimental results shown in Figures 5.25, 5.26, and 5.28, the similarities to the mode II crack strain fields in Figure 5.28 are compelling. With the experimental kink band tip strain field data to serve as validation, the development of a fracture mechanics based approach to kink band propagation in metallic multilayers appears promising.

Both compatibility driven accommodation strains along the kink band flank and the extensive strain fields emanating from the kink band tip are expected to influence the direction of kink band propagation and therefore the kink band inclination angle β. The observed kink band inclination angle of 21-27° is far from the 45° angle expected from bifurcation analysis of plane strain shear localization in perfectly plastic isotropic materials [216], suggesting that these factors

may have significant influence. In the case of the accommodation strains, the magnitude of the accommodation strain component parallel to the kink band boundary is set by the angle of the wedge shaped kink band and the shear strain within the kink band. The kink band inclination angle, β, determines how this strain component is oriented with respect to the anisotropic material through which the kink band propagates. Various kink band inclination angles would result in different distributions of the accommodation strains in the surrounding anisotropic material and presumably different energy penalties associated with the accommodation strain fields. Likewise, the energy of the strain field in front of a propagating kink band should depend both on the constitutive behavior of the composite material and the orientation of the kink band. Attempts to predict why certain kink band inclination angles (β) should be preferred without consideration of the details of kink band propagation neglect the effects of these extensive strain fields. Just as the prediction of crack propagation paths requires consideration of material anisotropy, it is likely that successful prediction of the kink band propagation angle requires consideration of the anisotropy and local deformation of the material surrounding the propagating kink band.

5.7 Kink band intersections

The previous sections have addressed both the deformation inside of a kink band and the deformation of the specimen surrounding a propagating kink band. However a final aspect of kink band formation must be discussed: kink band intersections. The formation of the complex networks of intersecting kink bands observed in post-test metallographic analysis (Figure 5.32) occurs through many individual kink band crossing events; events in which a propagating kink band crosses a preexisting kink band. The *in situ* SEM compression tests discussed in Section 5.6.2 indicate that the two segments of a crossed kink band are offset from one another by the shear within the crossing kink band. While broadening of a crossing kink band during further specimen compression is observed, broadening of a crossed kink band appears to be inhibited by the presence of the other kink band. In this section, the geometry of kink band intersections is analyzed using information obtained from post-test metallographic analysis of the bulk layer parallel compression specimens discussed in Section 4.4.

Figure 5.33 shows two high magnification BSE SEM images of a kink band intersection in a 30 nm TD compression specimen as well as a schematic of the region where these images were taken. The *in situ* SEM results showed that a

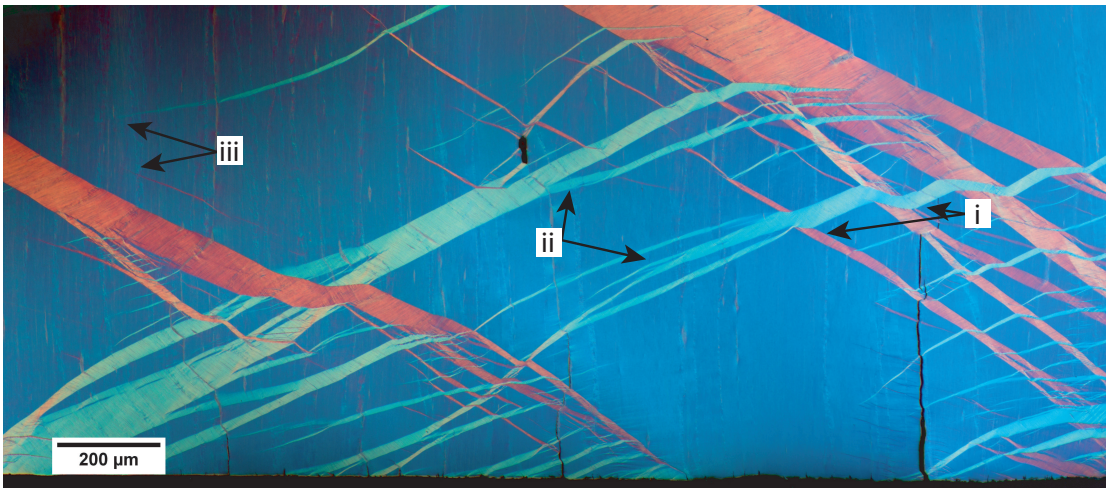

Figure 5.32: A polarized light optical image of a complex network of kink bands in a 15 nm Cu-Nb compression specimen. Kink band intersections (i), bifurcations (ii), and terminations (iii) are evident. The original layer orientation and compression direction is vertical.

crossed kink band is sheared by the crossing kink band, a result that allows the crossed and the crossing kink band to be identified (these kink bands are labeled 'A' and 'B' respectively in Figure 5.33). The region of A that is intersected and sheared by B creates a third 'twice sheared' region labeled 'C'. Both A and B show the $\phi = 2\beta$ relationship (the boundary bisects the angle between the kinked and non-kinked layers). If the non-kinked material is considered to be the 'matrix', both the A/matrix and B/matrix boundaries follow $\phi = 2\beta$. Interestingly, the A-C boundary also shows $\phi = 2\beta$: the angle between the layers in A and C are bisected by the A/C boundary. Despite the material in C having been sheared along the shear direction of A, the layers in C remains parallel to the layers in B. Thus C has deformed by simple shear parallel to the layers, which does

not produce any rotation of the layers. This can only occur if the kink band boundary of A (and therefore the invariant plane of shear in A) lies parallel to the layer orientation in B.

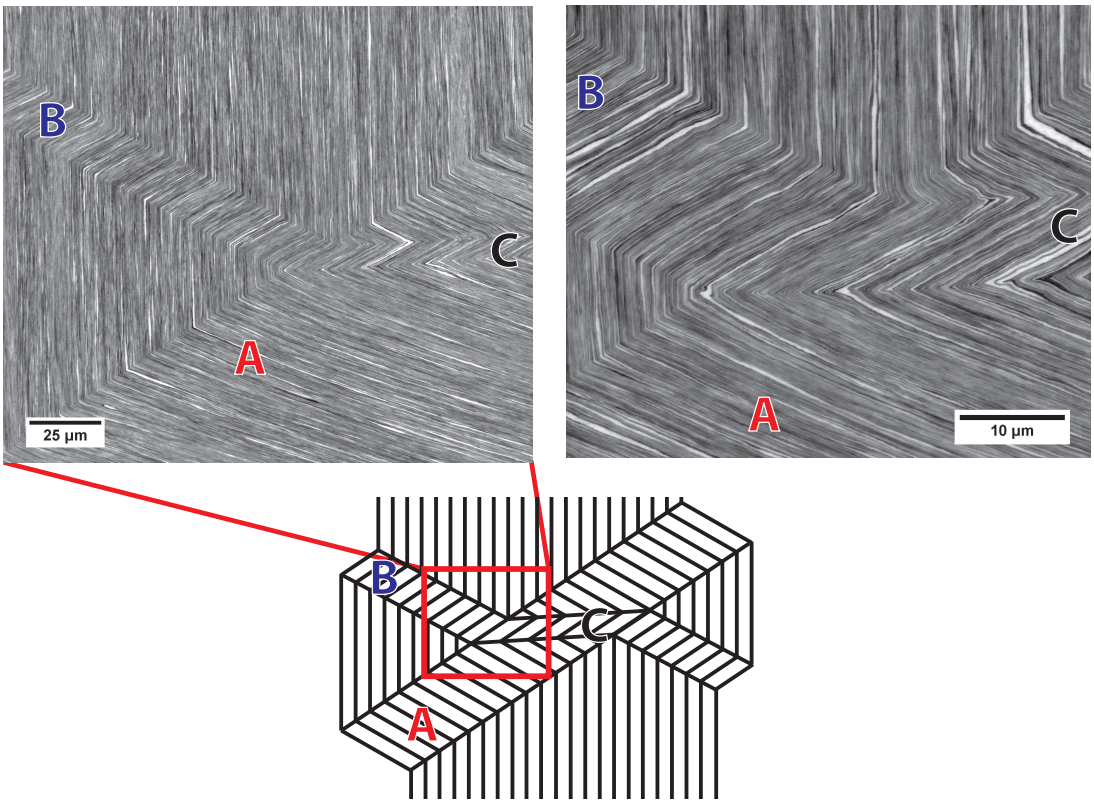

Figure 5.33: SEM micrographs of a kink band intersection in a 30 nm TD compression specimen and a schematic showing a larger view of where the micrographs were taken from.

Due to the geometrical similarities between kink bands and deformation twins (as discussed in Section 5.1), it is worth exploring whether previously developed rules for deformation twin intersections may be applied to kink band intersections. The geometry of a deformation twin, adapted from Reference

[212], is presented in Figure 5.34. According to the classical theory of deformation twinning, deformation twins can be considered to form by the homogeneous shear of a band of material in a crystal. The boundary of the twin is the 'invariant shear plane' (K_1) and the shear direction (η_1) lies in this plane. K_2 is the second undistorted plane of shear (the shear deformation rotates, but does not leave the K_2 plane distorted in the final twined geometry). Finally, the direction η_2 is referred to as the conjugate shear direction. Figure 5.35 shows a more clear illustration of how the (rotated) twin geometry relates to the geometry of a kink band: K_1 is the kink band boundary plane while K_2 is the plane of the kinked layers.

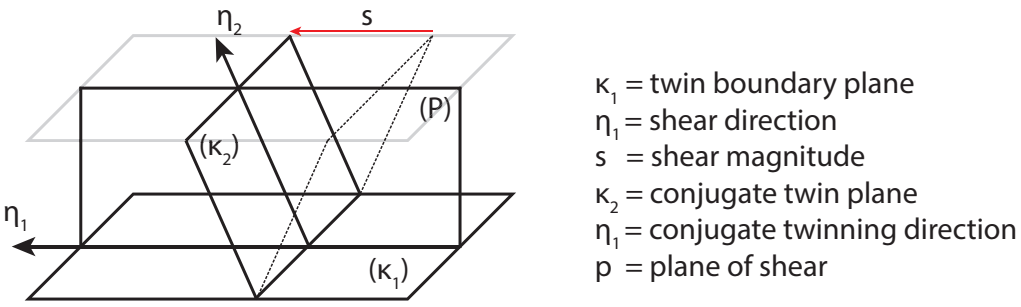

Figure 5.34: A schematic indicating the K_1 and K_2 planes and the η_1 and η_2 direction of a deformation twin, adapted from Reference [212].

Crystallographically admissible deformation twin intersections have been observed in several materials including uranium [212]. These intersections arise when a deformation twin crosses a preexisting twin, resulting in the formation of a 'secondary twin' in the crossed region [217, 218]. The following discussion

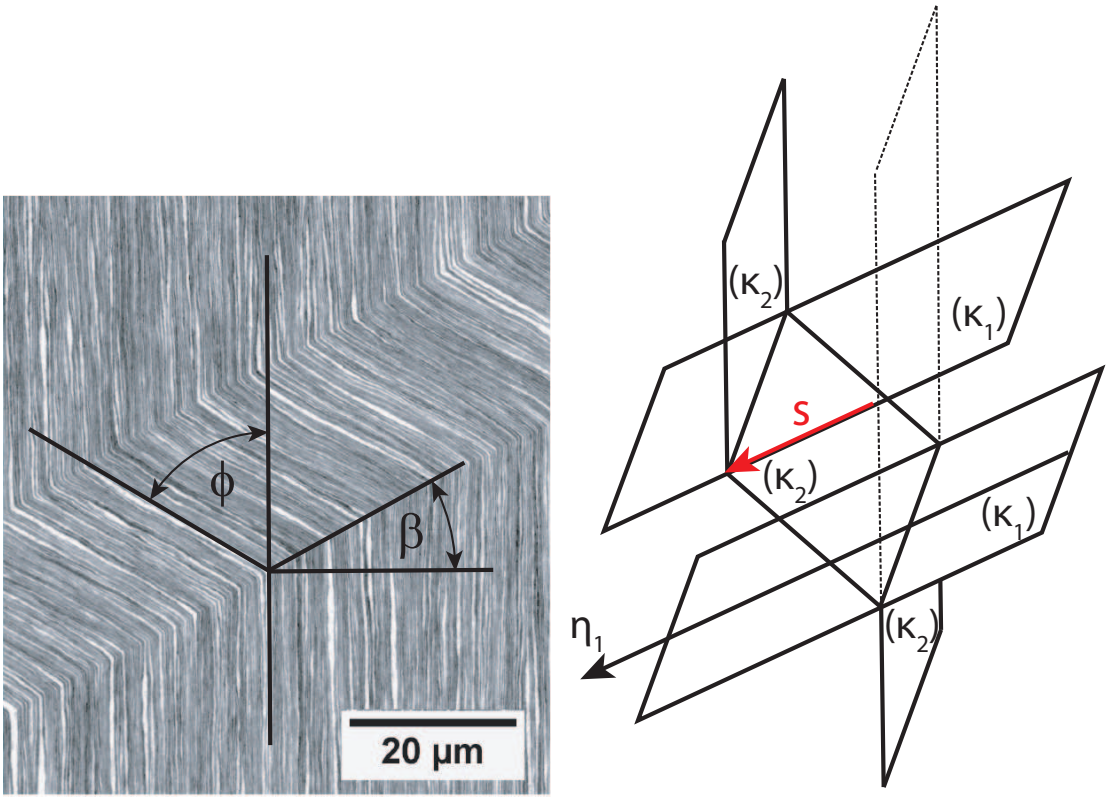

Figure 5.35: An image of a kink band accompanied by a rotated schematic of the deformation twin geometry, showing how the twin geometry relates to kink bands.

will refer to the 'crossing twin (A)' (the twin that propagates across the initial twin), the 'crossed twin (B),' and the 'secondary twin (C)' (the segment corresponding to overlap of the crossed and crossing twin). Cahn [217] developed a set of rules, based solely on compatibility across the twin-matrix and twin-twin boundaries formed during twin crossing. These rules are:

1. The traces of the crossing twin A and the secondary twin C in the K_1 plane of the crossed twin B must be parallel.

2. The direction (η_1) and magnitude (s) of shear in the crossing and secondary twin must be identical.

These conditions can be met if η_1 of the crossing twin is contained in the plane K_1 of the crossed twin. This geometry, proposed by Cahn, is shown in Figure 5.36(a), where the twin plane and direction notation is depicted again (Figure 5.36(b)). In Figure 5.36(a), the twin boundaries (K_1) of the crossed twin remains undeflected, as the shear direction of the crossing twin lies parallel to these boundaries. This geometry accurately describes twin intersections in uranium, and allows determination of the crossed twin and crossing twin (and therefore the sequence of twin growth) by inspection [218].

The geometry for twin intersections shown in Figure 5.36(a) is not applicable to kink bands. The *in situ* SEM experiments clearly show that the crossed

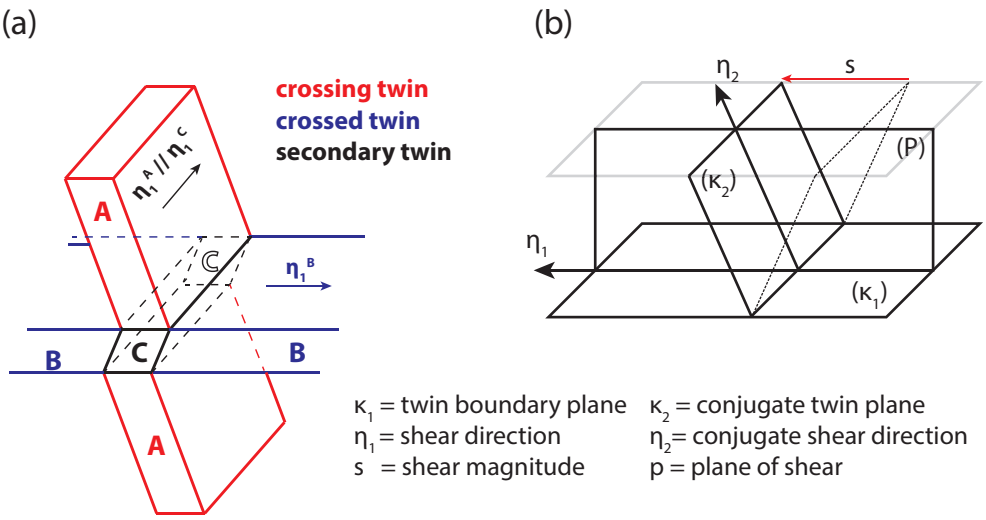

Figure 5.36: Geometry of deformation twin intersections proposed by Cahn [217].

kink band is sheared by the crossing kink band (Figure 5.21), in disagreement with Cahn's twin intersection geometry. However, a second geometry for twin intersections that also follows Cahn's compatibility rules was proposed by Liu [219]. In this twin intersection geometry, shown in Figure 5.37, the crossing twin (A) remains straight while the crossed twin (B) is deflected (η_1 of A is not contained in K_1 of B). While according to Christian [212], Liu's proposed geometry is 'not generally compatible with the crystallography of twinning,' it accurately describes the geometry of kink band intersections.

As was shown in Figure 5.33, and applying the notation for twins to kink bands, the geometry of kink band intersections is such that the shear direction

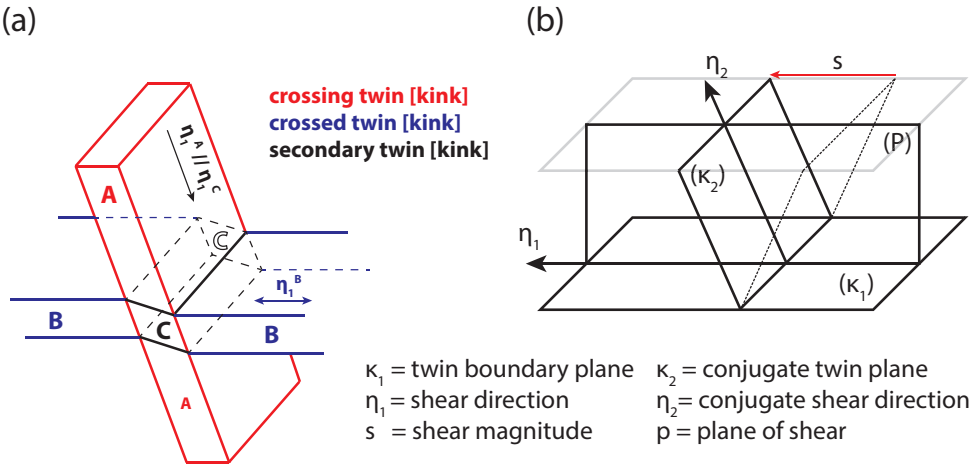

Figure 5.37: Geometry of deformation twin intersections proposed by Liu [219].

(η_1) of the crossing kink band (A) lies parallel to the layer planes (K_2) in the crossed kink band (B). This provides the condition:

$$\phi^B + \beta^A = \frac{\pi}{2} \tag{5.43}$$

Assuming that $\phi = 2\beta$ in both A and B, the condition becomes:

$$\beta^A = \frac{\pi}{2} - 2\beta^B \tag{5.44}$$

It is assumed that, consistent with experimental observations and in accordance with the modeling results described in Section 5.5, β must be $\leq \frac{\pi}{4}$ for kink bands in Cu-Nb nanolaminates. Combining this restriction with the con-

dition in Equation 5.44, it is clear that β of the crossed kink band (B) must lie within a certain angular range: $\frac{\pi}{8} \leq \beta^B \leq \frac{\pi}{4}$. Thus any kink band with $\beta < \frac{\pi}{8}$ (or equivalently $\phi < \frac{\pi}{4}$) cannot be crossed by a second kink band.

While not obvious from inspection alone, if $\phi = 2\beta$ in both kink bands (A and B) and Equation 5.44 is satisfied, it is geometrically required that $\phi^C = 2\beta^C$. That is, the A/matrix, B/matrix, and A/C boundaries are all mirror planes and there is no layer orientation change across the boundary A/B, as experimentally shown in Figure 5.33. Thus the only condition that needs to be satisfied for kink band intersections is Equation 5.44.

One final aspect of kink band intersections should be considered: does the intersection of two kink bands result in a constraint that limits the ability of one of the kink bands to broaden during subsequent compression? This was suggested by the *in situ* SEM compression test shown in Figure 5.21, where the crossing kink band, but not the crossed kink band, broadened during further compression.

Figure 5.38 shows a schematic of a kink band intersection in which both kink bands A and B follow the $\phi = 2\beta$ relationship, and the condition for kink band intersections given in Equation 5.44 is satisfied. If the crossing kink band (A) broadens (Figure 5.38(a)), shear would occur along the A-matrix interfaces

in the same manner as if kink band B was not present, and an identical shear displacement would occur along the B/C boundary. This B/C boundary lies parallel to the layer orientation in B and C, allowing this shear displacement to be accomplished through pure layer parallel shear, an easy deformation mode for these materials. Thus the intersection of two kink bands places no restriction on band broadening of the crossing kink band.

The situation is different if band broadening of the crossed kink band is envisioned (Figure 5.38(b)). In this case, shear along the lower boundary of the left half of kink band B requires shear at the B/matrix interface and layer parallel shear in A but would also require the formation of a new kink band on the right hand side of the diagram (in order for shear displacements to be continuous). If B is envisioned to broaden instead along the upper left B-matrix interface, this would require shear along the B-matrix interface, shear at an angle nearly perpendicular to the layers in C, layer parallel shear in a small region of A, and the formation of a new kink band immediately below the right half of kink band B. In both scenarios, nucleation of a new kink band would be required and is expected to require higher stresses than those required for band broadening of the crossing kink band (Figure 5.38(a)). Thus from a simple geometrical argument, kink band intersections appear to provide a constraint that inhibits band broadening of the crossed kink band.

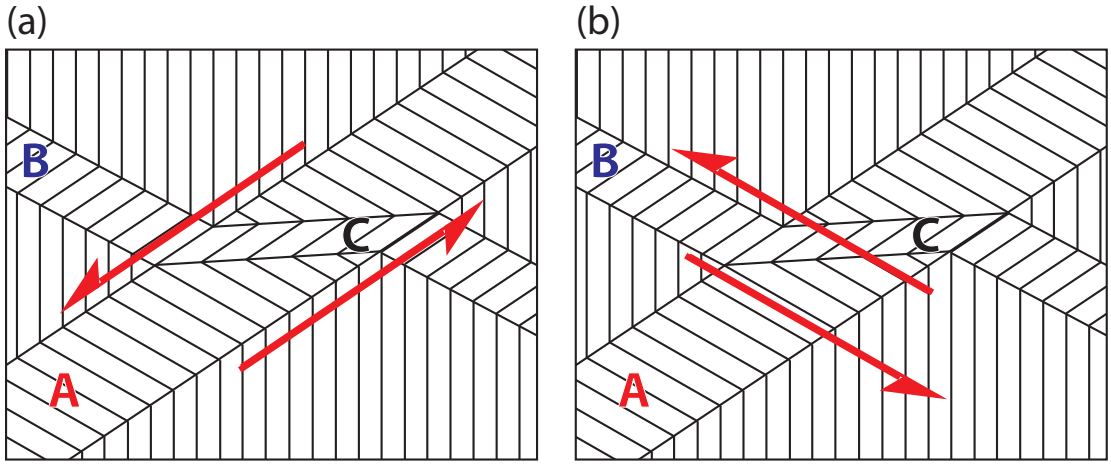

Figure 5.38: Schematic illustrating the constraint that a kink band intersections has on continued kink band broadening. Broadening of the crossing kink band (labeled A) is permitted, but broadening of the crossed kink band (labeled B) requires the formation of an additional kink band.

5.8 Summary

In this chapter, experimental results from post-test analysis of bulk layer parallel compression specimens, *in situ* SEM compression tests, micropillar compression tests, and digital image correlation strain mapping of the strain fields surrounding a propagating kink band have been presented. These results provide insight into the mechanism of kink band formation in bulk specimens and micron scale specimens, elucidate the kinematics of deformation within the kink band, and indicate that both significant deformation and energy dissipation occur in the specimen surrounding a propagating kink band. From the experi-

mentally observed deformation behavior, the kinematics necessary to construct a model of kink band formation have been been obtained. This model has successfully applied bounds to the possible range of kink band inclination angles (β) and provided a plastic work rate argument that indicates that deformation beyond the $\phi = 2\beta$ condition is unfavorable compared to the formation of a new kink band.

The $\phi = 2\beta$ relationship is consistently observed in post-test analysis of kink bands in Cu-Nb nanolaminates. The nearly constant ϕ observed in post-test specimens, as well as the distortion of platinum markers applied prior to kink band formation, indicate that the transformation from $\phi = 0$ to $\phi = 2\beta$ results in a macroscopically homogeneous strain within the kink band (straight lines in the undeformed configuration remain straight in the final deformed configuration). Analysis of the kink band boundary geometry indicates a lack of voids or delamination, an observation from which it is concluded that the deformation associated with the transformation from $\phi = 0$ to $\phi = 2\beta$ is isochoric.

The simplest description of kink band formation that reproduces the final kinked state through volume preserving deformation is one of simple shear parallel to the kink band boundary. While undoubtedly an approximation to the real kinematics of kink band formation, a homogeneous simple shear parallel to the kink band boundary appears to be a reasonable description of kink band

formation as observed in micropillar compression experiments. The load drop observed during micropillar compression provides an indication of the geometric softening that occurs as the layers within the kink band are rotated, yet the minimum in load does not occur at $\phi = 45^\circ$ as would be expected based on a simple analysis of resolved shear stress on the layers. Instead, this load minimum occurs at $\phi = \beta$.

The analytical model developed for kink band formation in a perfectly plastic anisotropic material indicates that the work rate during kink band formation would decrease from $\phi = 0$ to $\phi = \beta$. A minimum work rate occurs at $\phi = \beta$, a condition that corresponds to the minimum load in the micropillar compression experiments. The model also indicates that the work rate at $\phi = 2\beta$ is equal to the work rate at $\phi = 0$, and increases beyond this condition for all $\beta < 45^\circ$. This suggests a driving force for the formation of a new kink band, as this would require less work than the continued shear and rotation past $\phi = 2\beta$ of the original kink band.

The most important conclusion from the model developed for kink band formation is that neither the non-isochoric deformation, delamination, or inextensible fibers/layers assumed in models developed for fiber composites are required to explain why deformation within a kink band would cease at $\phi = 2\beta$ relationship. The work rate argument for 'lock up' at $\phi = 2\beta$, assuming only per-

fectly plastic deformation of an anisotropic material, is sufficient. This provides a theoretical underpinning to a much more general understanding of kink band formation, one that is not dependent on highly restrictive assumed constitutive behavior (such as inextensible fibers). While anisotropy is still required, this broad model is more easily reconciled with the tremendous range of material classes in which the phenomenon of kink band formation has been observed.

While the initial results and predictions that have been made with the kink band model are encouraging, additional work is needed to determine the behavior of the specimen when the yield functions of both the material inside of the kink band and the non-kinked specimen surrounding the kink band are satisfied. Additionally, the description of kink band formation is significantly complicated by consideration of the propagation stage observed in specimens that are large relative to the layer size. In the large specimens used for *in situ* SEM compression and DIC strain mapping compression tests, kink bands are observed to initiate at stress concentrations at the specimen corners and propagate across the specimens. A significant fraction of this propagation event occurs stably during a rising global load. Spatially extended strain fields resembling those expected for a mode II crack are observed in front of the kink band during propagation. The size of these fields is on the order of the kink band length, with the magnitude of distortion decreasing with distance from the kink band tip.

Analysis of the deformation surrounding a propagating kink band reveals important additional aspects of kink bands formation. First, the wedge shaped morphology of the propagating kink band indicates the presence of an accommodation strain field adjacent to the kink band. Secondly, there is a stress singularity associated with a kink band terminating in a specimen. Analysis of the strain field in front of a propagating kink band indicates very good agreement with the analytical solution for the dominant singularity at the tip of a mode II crack, suggesting that a fracture mechanics based analysis of kink band propagation is appropriate. Finally, while the strain level in the kink band tip strain field is approximately two orders of magnitude smaller than the strains within the kink band, the much larger volume of the kink band tip strain field results in a significant contribution to the total work of kink band formation. The energy of the kink band tip strain field must be considered in any accurate calculation of energy dissipation during kink band propagation. These strain fields should also be considered for a more complete description of kink band kinematics, where first a large volume of material in front of a kink band is deformed as a result of the kink band tip stress field, followed by the formation of a narrow region of high shear strain associated with the advance of the kink band.

Chapter 6

Conclusions and Recommendations for Future Work

The objectives of this research were to synthesize bulk Cu-Nb nanolaminates using the ARB process, to determine the influence of the nanolamellar microstructures on mechanical behavior and flow stress anisotropy, and to explore the deformation behavior of these bulk nanocrystalline materials. Significant improvements to the ARB process were required in order to produce material with the large dimensions and microstructural homogeneity required to obtain reliable mechanical test data. In addition to facilitating layer parallel tension, layer normal compression, and off-axis compression tests to char-

acterize flow stress anisotropy, the bulk ARB produced material allowed layer parallel compression tests to be conducted. In these tests, deformation of metallic nanolaminates by kink band formation was observed for the first time. The kinematics of kink band formation in ductile nanolaminates were determined through post-test metallographic analysis, *in situ* SEM, and micropillar compression tests. These kinematics enabled the construction of an analytical model for kink band formation in perfectly plastic anisotropic materials, a model that has provided bounds on the acceptable kink band angles and angular relationships ($\phi \leq 2\beta$). It is expected that both the model and insights from the experimental characterization of kink bands, most notably the characterization of the strain field surrounding a propagating kink band, can be applied to the general phenomena of kink band formation and will inform future studies of kink band formation in other material systems.

The key findings from these investigations are summarized below, with recommendations for future work discussed in Section 6.1.

1. The accumulative roll bonding process has greatly facilitated the synthesis of metallic multilayers, with bulk (4 mm $\times$ 10 mm $\times$ 100 mm) sheets of Cu-Nb nanolaminates containing >200,000 individual layers being routinely processed. Significant improvements in the microstructural homo-

geneity of metallic nanolaminates has been achieved by altering processing parameters, including introducing intermediate annealing steps into the ARB processing of Zr-Nb nanolaminates.

(a) Multistack and clad ARB processing methods have been implemented to decrease the required processing time and eliminate the creation of new interphase interfaces during ARB synthesis of Cu-Nb nanolaminates.

(b) The formation of pure Nb as well as intermixed Cu-Nb inclusions in ARB processed material was found to result from surface damage and burr formation during wirebrushing. The use of a wirebrush with smaller diameter bristles, combined with the implementation of the clad ARB process, largely eliminated these defects.

(c) While room temperature processing of Zr-Nb multilayers resulted in loss of layer continuity at cumulative rolling strains >3, the introduction of a 575°C annealing step after every other ARB processing step suppressed layer fragmentation and allowed for successful ARB processing and synthesis of Zr-Nb nanolaminates with nominal layer thickness of 88 nm.

(d) The high rolling loads and roll diameters required for successful

ARB processing result from the large minimum threshold reductions needed to achieve cold roll bonding. For Cu and Nb, successful cold roll bonding required percent reductions exceeding 50%.

2. Significant changes in crystallographic texture, grain size, and grain morphology occur throughout ARB processing of Cu-Nb multilayers.

   (a) The crystallographic texture of the Cu and Nb phase strengthens as the layer thickness is decreased, with the texture of the $<$100 nm nanolaminates differing from the conventional Cu and Nb rolling textures observed in the $>$20 μm layer thickness multilayers.

   (b) Grain refinement is observed in coarse multilayers (layer thickness of 500-40 μm). Sub-micron grain sizes are attained in both phases even at a layer thickness of 20 μm.

   (c) The grain structure of the layers transitions from polycrystalline to single crystal through thickness as the layer size is reduced. The Cu layers become predominately single crystal though thickness at 245 nm while the Nb layers become single crystal through thickness between 140 and 30 nm.

   (d) Once the layers become predominantly single crystalline through thickness, grain aspect ratios increase dramatically as the layer thick-

ness is refined. Grain aspect ratios in both phases exceed 1:50:5 (ND:RD:TD) at layer thicknesses below 58 nm.

3. The layer parallel tensile flow strength and both layer parallel and layer normal compressive flow strengths increase monotonically with decreasing layer thickness over the range of layer thicknesses tested (1800-15 nm).

   (a) The layer parallel tensile tests indicate that the relationship between yield strength and the inverse square root of the layer thickness is linear, in agreement with the Hall-Petch equation. The Hall-Petch coefficients calculated from RD and TD tensile data are 0.078 and 0.080 MPa $m^{1/2}$.

   (b) The observed TD versus RD flow stress anisotropy is attributed to the effects of crystallographic texture, as determined though polycrystal modeling. The degree of anisotropy varies between 8 and 13%, with TD tension specimens showing a higher flow strength than RD tension specimens.

   (c) As with the tensile tests, compression specimens tested along the RD, TD, and ND show an approximately linear increase in the flow strength with the inverse square root of layer thickness.

4. Cu-Nb nanolaminates possess a low layer parallel shear strength, as indicated by compression tests conducted at 45° to the layered structure. The stress required for layer parallel shear versus layer parallel/normal compression diverges (the material becomes increasingly anisotropic) as the layer thickness is refined below 245 nm.

   (a) The stress required for layer parallel shear, as measured *via* off-axis compression specimens, is lower than the stress required for ND, TD, or RD compression at all layer thicknesses. This is consistent with the relaxed constraints on co-deformation associated with layer parallel shear of a laminate.

   (b) The flow strength for RD shear is greater than that for TD shear. This result may be partially attributed to crystallographic texture but requires consideration of other factors such as layer waviness to fully explain the in-plane shear strength differences.

   (c) The divergence between the stress required for layer parallel shear and layer parallel/normal compression and tension begins at a layer thickness of 245 nm, with the anisotropy becoming more pronounced as the layer thickness decreases. At a layer thickness of 30 nm, the resolved shear stress required for TD shear is $<$25% of the stress re-

quired for RD, TD, or ND parallel compression.

(d) The low layer parallel shear strength cannot be attributed to interfacial sliding or interfacial shear, based on the very high ($>$1.5 GPa) predicted shear strength of these interfaces. The increase in layer parallel shear versus layer parallel stretch anisotropy correlates with the significant increase in grain aspect ratios, suggesting that this trend in anisotropy results from the effects of highly elongated grains and the resulting disparities in dislocation obstacle spacing.

5. Kink band formation is the dominant deformation mode during layer parallel compression of sub-100 nm layer thickness Cu-Nb nanolaminates. This form of strain localization results in bands of large local deformation in which the layers are uniformly misoriented from the surrounding material. In contrast to the ND compression specimens, the layer parallel compression specimens that deform by kink band formation show no evidence of failure at compressive strains less than 25%.

(a) Kink bands observed in post-test specimens display the $\phi = 2\beta$ relationship, a geometry that is maintained even at kink band intersections.

(b) The deformation resulting in kink band formation appears to be iso-

choric, with no evidence of widespread layer debonding or void formation. This indicates that substantial (∼35% for β =45°) layer transverse strain occurs during kink band formation.

(c) A model based on the observed kinematics of kink band formation has been developed. This model applies to plane strain kink band formation in a perfectly plastic anisotropic material and confirms that kink band formation (rotation from $\phi = 0$ towards $\phi = 2\beta$) can occur even when kinking is approximated as a homogeneous shear parallel to the kink band boundary.

(d) The analytical kink band model indicates that kink bands with $\beta > 45°$ should never form, a result in excellent agreement with experimental observation of kink band β values in Cu-Nb nanolaminates. The kink band model also indicates that rotation past $\phi = 2\beta$ should be unfavored, as the plastic work rate would increase above that required to form a new kink band.

(e) Micropillar compression experiments indicate that the geometric softening that occurs during kink band formation is maximal at $\phi = \beta$, a condition that corresponds to the minimum work rate as determined from the kink band model.

(f) While kink band formation in micropillar compression specimens ap-

pears to occur through the near homogeneous shear of a band of material, *in situ* SEM compression and bulk DIC compression tests indicate that kink band formation in large specimens involves propagation of the band.

(g) Kink band propagation results in spatially extended strain fields in front of the kink band tip. These fields show good agreement with those expected for a mode II crack, suggesting that a fracture mechanics approach to kink band formation may be appropriate. These fields also indicate that, in large specimens, the plastic dissipation due to deformation outside of a kink band is on the order of that due to the deformation within the kink band.

6.1 Recommendations for future work

Several promising areas for further investigation have been identified in this work. These include the effects of elevated ARB processing temperature, the role of grain shape on plastic anisotropy, and several matters related to kink band formation. Recommendations for future research are presented below.

While the improvements made to the ARB process discussed in Chapter 3 have enabled significant advances in the quality and quantity of nanolaminate

material that can be produced, the challenges associated with truly industrial scale ARB processing remain daunting. Due to the high flow strength of the workpiece, the large threshold reductions needed to achieve cold roll bonding, and the low coefficient of friction for cold rolling, rolling mills with very high load capacities and large roll diameters are needed for room temperature ARB synthesis of even modest sheets of nanolaminates. Further, attempts at Los Alamos National Laboratory to ARB process high strength materials such as duplex stainless steel resulted in the unfortunate and costly scenario in which plastic deformation occurs both in the workpiece and in the rolling mill rolls. ARB processing at elevated temperatures would serve to decrease the flow stress of the workpiece, decrease the threshold reduction for bonding, and reduce the tendency for edge cracking and the associated material losses. Therefore, the effects of ARB processing at elevated temperature should be explored, with particular emphasis on the effects of temperature on the co-deformation of material systems of interest. For the case of Cu-Nb laminates, the disparity in melting point and the different temperature dependencies of the flow stresses may increase the tendency for loss of layer continuity, yet there may be a temperature range which substantially lowers the flow stress and the threshold reduction for bonding without promoting layer instabilities. Further, for material combinations that cannot be processed at room temperature without layer fragmenta-

tion, high temperature processing may enable successful nanolaminate synthesis. For systems where diffusion or intermetallic formation is expected, either careful selection of processing temperature or the addition of a third material to serve as a diffusion barrier may be necessary.

Additional investigation is also required to explore the role of extreme grain aspect ratios in altering slip system activity and imparting mechanical anisotropy. Compared to the effects of crystallographic texture, the effects of grain morphology are not well understood. While the correlation of increasing grain aspect ratio with increasing anisotropy in Cu-Nb nanolaminates is suggestive, analysis of this system is complicated by the dual-phase microstructure and the presence of heterophase interfaces. Analysis of simpler model systems, such as severely deformed single phase Nb would be desirable. The high threshold for dynamic recrystallization would enable significant grain aspect ratios to develop during either single phase ARB processing or other SPD processing such as equal channel angular extrusion. While the use of mean field, or even crystal plasticity, modeling would still be required to decouple the effect of grain morphology from that of deformation texture, this modeling would be considerable simpler for a single phase material. A better understanding of the effects of grain morphology would enable more accurate predictions of the constitutive behavior of severely deformed materials.

Finally, additional analysis of the kink band formation process, as well as further development of the analytical kink band model, is needed. While the work described in Chapter 5 has laid the groundwork for future investigations by showing that the deformation associated with kink band formation is volume preserving and, in an average sense, must conform to simple shear parallel to the kink band boundary, the effects of potential inhomogeneous strains at the layer length scale must be explored. The stable growth of kink bands in these nanolaminates suggests that this information could be obtained experimentally through high magnification *in situ* DIC SEM tests. Alternatively, numerical studies using tools such as finite element analysis could provide insight into potential heterogeneous deformation at the layer length scale, work that is in fact already underway. Conducting *in situ* observations of dislocation motion during kink band formation would also be desirable, potentially providing insight into the sources of the plastic anisotropy that drives kink band formation as well as the mechanisms through which this nanolaminate material accommodates the large strains during kinking.

Further development of the analytical model presented in Section 5.5 is also needed. A pressing question is what happens when, for high levels of anisotropy, the yield functions of both the material within the kink band and the non-kinked material surrounding the kink band are satisfied. Compatible plastic strain rate

increments must be obtained for the entire sample and analyzed to determine whether a fully formed ($\phi \rightarrow 2\beta$) kink band can develop. Finally, while the analytical model has shown remarkable success in predicting the observed features of kink bands, it should be determined whether relaxation of the constraint that deformation be homogeneous changes the model predictions. This model validation would likely require the use of numerical tools to simulate inhomogeneous deformation at the layer length scale.

Bibliography

[1] A. Misra, Mechanical behavior of metallic nanolaminates, in: R. H. Hannink, A. J. Hill (Eds.), Nanostructure control of materials, Woodhead Publishing, 2006, pp. 146–176.

[2] A. S. Edelstein, R. C. Cammaratra, Nanomaterials: synthesis, properties and applications, CRC Press, 1998.

[3] A. Misra, M. Verdier, Y. Lu, H. Kung, T. E. Mitchell, M. Nastasi, J. D. Embury, Structure and mechanical properties of Cu-X (X=Nb, Cr, Ni) nanolayered composites, Scr. Mater. 39 (1998) 555–560.

[4] B. M. Clemens, H. Kung, S. A. Barnett, Structure and strength of multilayers, Mater. Res. Bull. 24 (1999) 20–26.

[5] N. A. Mara, D. Bhattacharyya, P. Dickerson, R. G. Hoagland, A. Misra, Deformability of ultrahigh strength 5 nm Cu/Nb nanolayered composites, Appl. Phys. Lett. 92 (2008) 231901.

[6] N. A. Mara, D. Bhattacharyya, R. G. Hoagland, A. Misra, Tensile behavior of 40 nm Cu/Nb nanoscale multilayers, Scr. Mater. 58 (2008) 874 – 877.

[7] T. Nizolek, I. J. Beyerlein, N. A. Mara, J. T. Avallone, T. M. Pollock, Tensile behavior and flow stress anisotropy of accumulative roll bonded Cu-Nb nanolaminates, Appl. Phys. Lett. 108 (2016) 051903.

[8] A. Misra, R. G. Hoagland, Effects of elevated temperature annealing on the structure and hardness of copper/niobium nanolayered films, J. Mater. Res. 20 (2005) 2046–2054.

[9] S. Zheng, I. J. Beyerlein, J. S. Carpenter, K. Kang, J. Wang, W. Han, N. A. Mara, High-strength and thermally stable bulk nanolayered composites due to twin-induced interfaces, Nat. Commun. 4 (2013) 1696.

[10] J. S. Carpenter, S. J. Zheng, R. F. Zhang, S. C. Vogel, I. J. Beyerlein, N. A. Mara, Thermal stability of Cu-Nb nanolamellar composites fabricated via accumulative roll bonding, Philos. Mag. 93 (2013) 718–735.

[11] A. Misra, R. G. Hoagland, H. Kung, Thermal stability of self-supported nanolayered Cu/Nb films, Philos. Mag. 84 (2004) 1021–1028.

[12] W. Z. Han, A. Misra, N. A. Mara, T. C. Germann, J. K. Baldwin, T. Shimada, S. N. Luo, Role of interfaces in shock-induced plasticity in Cu/Nb nanolaminates, Philos. Mag. 91 (2011) 4172–4185.

[13] X. Zhang, E. G. Fu, N. Li, A. Misra, Y.-Q. Wang, L. Shao, H. Wang, Design of radiation tolerant nanostructured metallic multilayers, J. Eng. Mater. Technol. 134 (2012) 041010.

[14] T. Höchbauer, A. Misra, K. Hattar, R. G. Hoagland, Influence of interfaces on the storage of ion-implanted He in multilayered metallic composites, J. Appl. Phys. 98 (2005) 123516.

[15] X. Zhang, E. Fu, A. Misra, M. Demkowicz, Interface-enabled defect reduction in He ion irradiated metallic multilayers, JOM 62 (2010) 75–78.

[16] A. Misra, M. J. Demkowicz, X. Zhang, R. G. Hoagland, The radiation damage tolerance of ultra-high strength nanolayered composites, JOM 59 (2007) 62–65.

[17] A. Misra, J. P. Hirth, R. G. Hoagland, Length-scale-dependent deformation mechanisms in incoherent metallic multilayered composites, Acta Mater. 53 (2005) 4817–4824.

[18] I. J. Beyerlein, N. A. Mara, J. Wang, J. S. Carpenter, S. J. Zheng, W. Z. Han, R. F. Zhang, K. Kang, T. Nizolek, T. M. Pollock, Structure-property-functionality of bimetal interfaces, JOM 64 (2012) 1192–1207.

[19] S. Simões, R. Calinas, M. T. Vieira, M. F. Vieira, P. J. Ferreira, In situ TEM study of grain growth in nanocrystalline copper thin films, Nanotechnology 21 (2010) 145701.

[20] D. J. Chakrabarti, D. E. Laughlin, The Cu-Nb (copper-niobium) system, J. Phase Equilib. 2 (1982) 455–460.

[21] J. Wang, K. Kang, R. F. Zhang, S. J. Zheng, I. J. Beyerlein, N. A. Mara, Structure and property of interfaces in ARB Cu/Nb laminated composites, JOM 64 (2012) 1208–1217.

[22] J. Wang, R. G. Hoagland, A. Misra, Mechanics of nanoscale metallic multilayers: From atomic-scale to micro-scale, Scr. Mater. 60 (2009) 1067–1072.

[23] I. J. Beyerlein, J. R. Mayeur, S. Zheng, N. A. Mara, J. Wang, A. Misra, Emergence of stable interfaces under extreme plastic deformation, PNAS 111 (2014) 4386–4390.

[24] C. W. Sinclair, J. D. Embury, G. C. Weatherly, Basic aspects of the co-deformation of bcc/fcc materials, Mater. Sci. Eng. A 272 (1999) 90–98.

[25] L. Thilly, M. Veron, O. Ludwig, F. Lecouturier, J. P. Peyrade, S. Askénazy, High-strength materials: in-situ investigations of dislocation behaviour in Cu-Nb multifilamentary nanostructured composites, Philos. Mag. A 82 (2002) 925–942.

[26] I. Bakonyi, L. Péter, Electrodeposited multilayer films with giant magnetoresistance (GMR): progress and problems, Prog. Mater Sci. 55 (2010) 107–245.

[27] S. Kashiwabara, Y. Jyoko, Y. Hayashi, Structure and magnetic properties of electrodeposited metallic multilayers, Physica B 239 (1997) 47–49.

[28] D. M. Tench, J. T. White, Enhanced tensile strength for electrodeposited nickel-copper multilayer composites, Metall. Trans. A 15 (1984) 2039–2040.

[29] D. M. Tench, J. T. White, Tensile properties of nanostructured Ni-Cu multilayered materials prepared by electrodeposition, J. Electrochem. Soc. 138 (1991) 3757–3758.

[30] J. Yahalom, D. F. Tessier, R. S. Timsit, A. M. Rosenfeld, D. F. Mitchell, P. T. Robinson, Structure of composition-modulated Cu/Ni thin films prepared by electrodeposition, J. Mater. Res. 4 (1989) 755–758.

[31] A. S. M. A. Haseeb, J.-P. Celis, J. R. Roos, Dual-bath electrodeposition of Cu/Ni compositionally modulated multilayers, J. Electrochem. Soc. 141 (1994) 230–237.

[32] S. Menezes, D. P. Anderson, Wavelength-property correlation in electrodeposited ultrastructured Cu-Ni multilayers, J. Electrochem. Soc. 137 (1990) 440–444.

[33] W. Blum, The structure and properties of alternately deposited metals, Trans. Am. Electrochem. Soc 40 (1921) 307–320.

[34] M. Schlesinger, M. Paunovic, Modern electroplating, volume 55, John Wiley & Sons, 2011.

[35] C. A. Ross, Electrodeposited multilayer thin films, Annu. Rev. Mater. Sci. 24 (1994) 159–188.

[36] P. M. Anderson, J. S. Carpenter, M. D. Gram, L. Li, Mechanical properties of nanostructured metals, in: Handbook of Nanomaterials Properties, Springer, 2014, pp. 495–553.

[37] K. Yasuna, M. Terauchi, A. Otsuki, K. N. Ishihara, P. H. Shingu, Bulk metallic multilayers produced by repeated press-rolling and their perpendicular magnetoresistance, J. Appl. Phys. 82 (1997) 2435–2438.

[38] C. M. Emmerson, T.-H. Shen, S. D. Evans, H. Allinson, A combined in situ optical reflectance–electron diffraction study of Co/Cu and Co/Au multilayers grown by molecular beam epitaxy, Appl. Phys. Lett. 68 (1996) 3740–3742.

[39] A. Misra, H. Kung, Deformation behavior of nanostructured metallic multilayers, Adv. Eng. Mater. 3 (2001) 217–222.

[40] N. Li, A. Misra, Y. Q. Wang, L. Shao, Design of radiation tolerant nanostructured metallic multilayers, J. Eng. Mater. Technol. 134 (2012) 041010.

[41] F. Wang, P. Huang, M. Xu, T. J. Lu, K. W. Xu, Shear banding deformation in Cu/Ta nano-multilayers, Mater. Sci. Eng. A 528 (2011) 7290–7294.

[42] J. M. Wheeler, R. Raghavan, V. Chawla, J. Zechner, I. Utke, J. Michler, Failure mechanisms in metal–metal nanolaminates at elevated temperatures: Microcompression of Cu–W multilayers, Scr. Mater. 98 (2015) 28–31.

[43] E. G. Fu, N. Li, A. Misra, R. G. Hoagland, H. Wang, X. Zhang, Mechanical properties of sputtered Cu/V and Al/Nb multilayer films, Mater. Sci. Eng. A 493 (2008) 283–287.

[44] Y. P. Li, G. P. Zhang, On plasticity and fracture of nanostructured Cu/X (X= Au, Cr) multilayers: the effects of length scale and interface/boundary, Acta Mater. 58 (2010) 3877–3887.

[45] Q. Wei, A. Misra, Transmission electron microscopy study of the microstructure and crystallographic orientation relationships in V/Ag multilayers, Acta Mater. 58 (2010) 4871–4882.

[46] S. S. Sahay, K. S. Ravichandran, J. G. Byrne, Nanoscale brass/steel multilayer composites produced by cold rolling, Metall. Mater. Trans. A 27 (1996) 2383–2385.

[47] J. C. M. Kampe, T. H. Courtney, Y. Leng, Shape instabilities of plate-like structures - I. experimental observations in heavily cold worked in situ composites, Acta Metall. 37 (1989) 1735–1745.

[48] J. D. Embury, R. M. Fisher, The structure and properties of drawn pearlite, Acta Metall. 14 (1966) 147–159.

[49] G. Frommeyer, G. Wassermann, Microstructure and anomalous mechanical properties of in situ-produced silver-copper composite wires, Acta Metall. 23 (1975) 1353–1360.

[50] Y. Saito, N. Tsuji, H. Utsunomiya, T. Sakai, R. G. Hong, Ultra-fine grained bulk aluminum produced by accumulative roll-bonding (ARB) process, Scr. Mater. 39 (1998) 1221–1227.

[51] N. Tsuji, Production of ultra-fine grained bulk steel by accumulative roll-bonding (ARB) process, Current Advances in Materials and Processes 11 (1998) 560–560.

[52] Y. Saito, H. Utsunomiya, N. Tsuji, T. Sakai, Novel ultra-high straining process for bulk materials - development of the accumulative roll-bonding (ARB) process, Acta Mater. 47 (1999) 579–583.

[53] N. Tsuji, Y. Saito, S.-H. Lee, Y. Minamino, ARB (accumulative roll-bonding) and other new techniques to produce bulk ultrafine grained materials, Adv. Eng. Mater. 5 (2003) 338–344.

[54] S. C. V. Lim, A. D. Rollett, Length scale effects on recrystallization and texture evolution in Cu layers of a roll-bonded Cu-Nb composite, Mater. Sci. Eng. A 520 (2009) 189–196.

[55] Ö. Yazar, T. Ediz, T. Öztürk, Control of macrostructure in deformation processing of metal/metal laminates, Acta Mater. 53 (2005) 375–381.

[56] G. P. Chaudhari, V. Acoff, Cold roll bonding of multi-layered bi-metal laminate composites, Compos. Sci. Technol. 69 (2009) 1667–1675.

[57] D. Yang, P. Cizek, P. Hodgson, C. Wen, Ultrafine equiaxed-grain Ti/Al composite produced by accumulative roll bonding, Scr. Mater. 62 (2010) 321–324.

[58] M. Eizadjou, A. K. Talachi, H. D. Manesh, H. S. Shahabi, K. Janghorban, Investigation of structure and mechanical properties of multi-layered Al/Cu composite produced by accumulative roll bonding (ARB) process, Compos. Sci. Technol. 68 (2008) 2003–2009.

[59] R. N. Dehsorkhi, F. Qods, M. Tajally, Investigation on microstructure and mechanical properties of Al–Zn composite during accumulative roll bonding (ARB) process, Mater. Sci. Eng. A 530 (2011) 63–72.

[60] Y. F. Sun, N. Tsuji, H. Fujii, F. S. Li, Cu/Zr nanoscaled multi-stacks fabricated by accumulative roll bonding, J. Alloys Compd. 504 (2010) S443–S447.

[61] M. Danaie, C. Mauer, D. Mitlin, J. Huot, Hydrogen storage in bulk Mg–Ti and Mg–stainless steel multilayer composites synthesized via accumulative roll-bonding (ARB), Int. J. Hydrogen Energy 36 (2011) 3022–3036.

[62] S. M. Gilbert, E. Gillam, Deformation of cold-rolled wire-reinforced copper composites, Composites 14 (1983) 41–51.

[63] G. Min, J.-M. Lee, S.-B. Kang, H.-W. Kim, Evolution of microstructure for multilayered Al/Ni composites by accumulative roll bonding process, Mater. Lett. 60 (2006) 3255–3259.

[64] P. J. Hsieh, Y. P. Hung, J. C. Huang, Transformation into nanocrystalline or amorphous materials in Zr–X binary systems using ARB route, Scr. Mater. 49 (2003) 173–178.

[65] L. B. Freund, S. Suresh, Thin film materials: stress, defect formation and surface evolution, Cambridge University Press, 2004.

[66] D. Tabor, The hardness of metals, Oxford University Press, 1951.

[67] M. Mata, M. Anglada, J. Alcalá, Contact deformation regimes around sharp indentations and the concept of the characteristic strain, J. Mater. Res. 17 (2002) 964–976.

[68] G. P. Zhang, Y. Liu, W. Wang, J. Tan, Experimental evidence of plastic deformation instability in nanoscale Au/Cu multilayers, Appl. Phys. Lett. 88 (2006) 013105.

[69] Y. P. Li, X. F. Zhu, J. Tan, B. Wu, W. Wang, G. P. Zhang, Comparative investigation of strength and plastic instability in Cu/Au and Cu/Cr multilayers by indentation, J. Mater. Res 24 (2009) 728–735.

[70] Y. P. Li, X. F. Zhu, G. P. Zhang, J. Tan, W. Wang, B. Wu, Investigation of deformation instability of Au/Cu multilayers by indentation, Philos. Mag. 90 (2010) 3049–3067.

[71] T. E. Mitchell, Y. C. Lu, M. Nastasi, H. Kung, et al., Structure and mechanical properties of copper/niobium multilayers, J. Am. Ceram. Soc. 80 (1997) 1673–1676.

[72] E. O. Hall, The deformation and ageing of mild steel: III discussion of results, Proc. Phys. Soc. London, Sect. B 64 (1951) 747–753.

[73] G. E. Dieter, Mechanical metallurgy, McGraw Hill Book Company, 1961.

[74] L. B. Freund, The stability of a dislocation threading a strained layer on a substrate, J. App. Mech. 54 (1987) 553–557.

[75] W. D. Nix, Mechanical properties of thin films, Metall. Trans. A 20 (1989) 2217–2245.

[76] P. M. Anderson, T. Foecke, P. M. Hazzledine, Dislocation-based deformation mechanisms in metallic nanolaminates, MRS Bull. 24 (1999) 27–33.

[77] N. A. Mara, A. Misra, R. G. Hoagland, A. V. Sergueeva, T. Tamayo, P. Dickerson, A. K. Mukherjee, High-temperature mechanical behavior/microstructure correlation of Cu/Nb nanoscale multilayers, Mater. Sci. Eng. A 493 (2008) 274–282.

[78] N. A. Mara, D. Bhattacharyya, J. P. Hirth, P. Dickerson, A. Misra, Mechanism for shear banding in nanolayered composites, Appl. Phys. Lett. 97 (2010) 021909.

[79] N. Li, N. A. Mara, J. Wang, P. Dickerson, J. Y. Huang, A. Misra, Ex situ and in situ measurements of the shear strength of interfaces in metallic multilayers, Scr. Mater. 67 (2012) 479–482.

[80] J. Wang, R. G. Hoagland, J. P. Hirth, A. Misra, Atomistic simulations of the shear strength and sliding mechanisms of copper–niobium interfaces, Acta Mater. 56 (2008) 3109–3119.

[81] U. F. Kocks, C. N. Tomé, H. R. Wenk, Texture and anisotropy: preferred orientations in polycrystals and their effect on materials properties, Cambridge University Press, 2000.

[82] J. D. Splett, D. F. Vecchia, L. F. Goodrich, A comparison of methods for computing the residual resistivity ratio of high-purity niobium, J. Res. Natl. Inst. Stand. Technol. 116 (2011) 489.

[83] E. Cerreta, G. T. Gray, R. S. Hixson, P. A. Rigg, D. W. Brown, The influence of interstitial oxygen and peak pressure on the shock loading behavior of zirconium, Acta Mater. 53 (2005) 1751–1758.

[84] E. C. W. Perryman, J. M. Lack, Examination of metals by polarized light, Nature 167 (1951) 479–479.

[85] G. F. Vander Voort, Metallography, principles and practice, ASM International, 1984.

[86] W. S. Rasband, ImageJ. US National Institutes of Health, Bethesda, MD, 1997.

[87] M. A. Sutton, J. J. Orteu, H. Schreier, Image correlation for shape, motion and deformation measurements: basic concepts, theory and applications, Springer Science & Business Media, 2009.

[88] R. A. Lebensohn, C. N. Tomé, A self-consistent anisotropic approach for the simulation of plastic deformation and texture development of polycrystals: application to zirconium alloys, Acta Metall. Mater. 41 (1993) 2611–2624.

[89] B. L. Hansen, J. S. Carpenter, S. D. Sintay, C. A. Bronkhorst, R. J. McCabe, J. R. Mayeur, H. M. Mourad, I. J. Beyerlein, N. A. Mara, S. R. Chen, G. T. Gray, Modeling the texture evolution of Cu/Nb layered composites during rolling, Int. J. Plast. 49 (2013) 71–84.

[90] Z. Q. Wang, I. J. Beyerlein, An atomistically-informed dislocation dynamics model for the plastic anisotropy and tension–compression asymmetry of BCC metals, Int. J. Plast. 27 (2011) 1471–1484.

[91] T. Nizolek, N. A. Mara, I. J. Beyerlein, J. T. Avallone, J. E. Scott, T. M. Pollock, Processing and deformation behavior of bulk Cu–Nb nanolaminates, Metall. Micro. Anal. 3 (2014) 470–476.

[92] J. Wadsworth, W. K. Dong, O. D. Sherby, Welded damascus steels and a new breed of laminated composites, Metal Progress 129 (1986) 61–67.

[93] M. A. Meyers, A. Mishra, D. J. Benson, Mechanical properties of nanocrystalline materials, Prog. Mater Sci. 51 (2006) 427–556.

[94] J. Wadsworth, D. R. Lesuer, Ancient and modern laminated composites - from the Great Pyramid of Gizeh to Y2K, Mater. Charact. 45 (2000) 289–313.

[95] C. S. Smith, A History of Metallography: the development of ideas on the structure of metals before 1890, The University of Chicago Press, 1960.

[96] D. R. Lesuer, C. K. Syn, O. D. Sherby, J. Wadsworth, J. J. Lewandowski, W. H. Hunt, Mechanical behaviour of laminated metal composites, Int. Mater. Rev. 41 (1996) 169–197.

[97] H. E. McGannon (Ed.), The making, shaping and treating of steel, United States Steel, 8th edition, 1964.

[98] B. Dodd, The making of old japanese swords, J. Mech. Work Technol. 2 (1978) 75–84.

[99] J. Aston, E. B. Story, Wrought iron, its manufacture, characteristics and applications, AM Byers Company, 1939.

[100] I. T. Ferguson, B. Derby, Diffusion bonded Mokumé Gane decorative metal laminates, Mater. Sci. Technol. 14 (1998) 510–517.

[101] O. D. Sherby, J. Wadsworth, R. D. Caligiuri, L. E. Eiselstein, B. C. Snyder, R. T. Whalen, Superplastic bonding of ferrous laminates, Scripta Metall. 13 (1979) 941–946.

[102] O. D. Sherby, S. Lee, R. Koch, T. Sumi, J. Wolfenstine, Multilayered composites based on ultrahigh carbon steel and brass, Mater. Manuf. Process. 5 (1990) 363–376.

[103] Y. Ohashi, J. Wolfenstine, R. Koch, O. D. Sherby, Fracture behavior of a laminated steel-brass composite in bend tests, Mater. Sci. Eng. A 151 (1992) 37–44.

[104] I. D. Choi, D. K. Matlock, D. L. Olson, Creep behavior of nickel-copper laminate composites with controlled composition gradients, Metall. Trans. A 21 (1990) 2513–2520.

[105] K. K. Chawla, C. E. Collares, The stress-strain behavior of aluminum/ stainless steel laminate composites, in: Proc. of the 1978 International Conference on Composite Materials, pp. 1237–1245.

[106] H. Li, H. Choo, Y. Ren, T. A. Saleh, U. Lienert, P. K. Liaw, F. Ebrahimi, Strain-dependent deformation behavior in nanocrystalline metals, Phys. Rev. Lett. 101 (2008) 015502.

[107] J. A. Forster, S. Jha, A. Amatruda, The processing and evaluation of clad metals, JOM 45 (1993) 35–38.

[108] L. Li, K. Nagai, F. Yin, Progress in cold roll bonding of metals, Sci. Technol. Adv. Mater. 9 (2008) 023001.

[109] S. Kalpakjian, S. R. Schmid, Manufacturing processes for engineering materials, Prentice Hall, 4th edition, 2003.

[110] B. Dodd, P. Boddington, The causes of edge cracking in cold rolling, J. Mech. Work Technol. 3 (1980) 239–252.

[111] S. L. Semiatin, H. R. Piehler, Formability of sandwich sheet materials in plane strain compression and rolling, Metall. Trans. A 10 (1979) 97–107.

[112] A. G. Atkins, A. S. Weinstein, The deformation of sandwich materials, Int. J. Mech. Sci. 12 (1970) 641–657.

[113] P. S. Steif, Interfacial instabilities in an unbonded layered solid, Int. J Solids Struct. 26 (1990) 915–925.

[114] P. S. Steif, On deformation instabilities in clad metals subjected to rolling, Journal of Applied Metalworking 4 (1987) 317–326.

[115] Y.-M. Hwang, H.-H. Hsu, H.-J. Lee, Analysis of plastic instability during sandwich sheet rolling, Int. J. Mach. Tool Manu. 36 (1996) 47–62.

[116] N. V. Govindaraj, J. G. Frydendahl, B. Holmedal, Layer continuity in accumulative roll bonding of dissimilar material combinations, Materials & Design 52 (2013) 905–915.

[117] J.-M. Lee, B.-R. Lee, S.-B. Kang, Control of layer continuity in metallic multilayers produced by deformation synthesis method, Mater. Sci. Eng. A 406 (2005) 95–101.

[118] F. Nowicke, A. Zavaliangos, H. C. Rogers, The effect of roll and clad sheet geometry on the necking instability during rolling of clad sheet metals, Int. J. Mech. Sci. 48 (2006) 868–877.

[119] A. M. Russell, L. S. Chumbley, Y. Tian, Deformation processed metal–metal composites, Adv. Eng. Mater. 2 (2000) 11–22.

[120] J. S. Carpenter, T. Nizolek, R. J. McCabe, M. Knezevic, S. J. Zheng, B. P. Eftink, J. E. Scott, S. C. Vogel, T. M. Pollock, N. A. Mara, I. J. Beyerlein, Bulk texture evolution of nanolamellar Zr-Nb composites processed via accumulative roll bonding, Acta Mater. 92 (2015) 97–108.

[121] A. Yahiro, T. Masui, T. Yoshida, D. Doi, Development of nonferrous clad plate and sheet by warm rolling with different temperature of materials., ISIJ Int. 31 (1991) 647–654.

[122] R. Liang, A. S. Khan, A critical review of experimental results and constitutive models for BCC and FCC metals over a wide range of strain rates and temperatures, Int. J. Plast. 15 (1999) 963–980.

[123] J. S. Carpenter, R. J. McCabe, S. J. Zheng, T. A. Wynn, N. A. Mara, I. J. Beyerlein, Processing parameter influence on texture and microstructural evolution in Cu-Nb multilayer composites fabricated via accumulative roll bonding, Metall. Mater. Trans. A 45 (2014) 2192–2208.

[124] J. S. Carpenter, S. C. Vogel, J. E. LeDonne, D. L. Hammon, I. J. Beyerlein, N. A. Mara, Bulk texture evolution of Cu-Nb nanolamellar composites during accumulative roll bonding, Acta Mater. 60 (2012) 1576–586.

[125] J. S. Carpenter, X. Liu, A. Darbal, N. T. Nuhfer, R. J. McCabe, S. C. Vogel, J. E. LeDonne, A. D. Rollett, K. Barmak, I. J. Beyerlein, N. A. Mara, A comparison of texture results obtained using precession electron diffraction and neutron diffraction methods at diminishing length scales in ordered bimetallic nanolamellar composites, Scr. Mater. 67 (2012) 336–339.

[126] S.-B. Lee, J. E. LeDonne, S. C. V. Lim, I. J. Beyerlein, A. D. Rollett, The heterophase interface character distribution of physical vapor-deposited and accumulative roll-bonded Cu–Nb multilayer composites, Acta Mater. 60 (2012) 1747–1761.

[127] J. S. Carpenter, R. J. McCabe, I. J. Beyerlein, T. A. Wynn, N. A. Mara, A wedge-mounting technique for nanoscale electron backscatter diffraction, J. Appl. Phys. 113 (2013) 094304.

[128] R. J. McCabe, J. S. Carpenter, S. Vogel, N. A. Mara, I. J. Beyerlein, Recrystallization and grain growth in accumulative roll-bonded metal composites, JOM 67 (2015) 2810–2819.

[129] X. Liu, N. T. Nuhfer, A. D. Rollett, S. Sinha, S.-B. Lee, J. S. Carpenter, J. E. LeDonne, A. Darbal, K. Barmak, Interfacial orientation and misorientation relationships in nanolamellar Cu/Nb composites using transmission-electron-microscope-based orientation and phase mapping, Acta Mater. 64 (2014) 333–344.

[130] I. J. Beyerlein, N. A. Mara, J. S. Carpenter, T. Nizolek, W. M. Mook, T. A. Wynn, R. J. McCabe, J. R. Mayeur, K. Kang, S. Zheng, J. Wang, T. M. Pollock, Interface-driven microstructure development and ultra high strength of bulk nanostructured Cu-Nb multilayers fabricated by severe plastic deformation, J. Mater. Res. 28 (2013) 1799–1812.

[131] S. J. Zheng, I. J. Beyerlein, J. Wang, J. S. Carpenter, W. Z. Han, N. A. Mara, Deformation twinning mechanisms from bimetal interfaces as revealed by in situ straining in the TEM, Acta Mater. 60 (2012) 5858–5866.

[132] I. Beyerlein, J. Mayeur, R. McCabe, S. Zheng, J. Carpenter, N. Mara, Influence of slip and twinning on the crystallographic stability of bimetal

interfaces in nanocomposites under deformation, Acta Mater. 72 (2014) 137–147.

[133] C. L. Trybus, W. A. Spitzig, Characterization of the strength and microstructural evolution of a heavily cold rolled Cu-20% Nb composite, Acta Metall. 37 (1989) 1971–1981.

[134] J. T. Avallone, STEM investigation of as-rolled and kinked Cu-Nb nanolaminates, 2013. Unpublished.

[135] F. Bachmann, R. Hielscher, H. Schaeben, Texture analysis with MTEX - free and open source software toolbox, Solid State Phenom. 160 (2010) 63–68.

[136] W. Z. Han, J. S. Carpenter, J. Wang, I. J. Beyerlein, N. A. Mara, Atomic-level study of twin nucleation from face-centered-cubic/body-centered-cubic interfaces in nanolamellar composites, Appl. Phys. Lett. 100 (2012) 011911.

[137] K. J. Hemker, W. N. Sharpe Jr, Microscale characterization of mechanical properties, Annu. Rev. Mater. Res. 37 (2007) 93–126.

[138] D. Josell, D. Van Heerden, D. Read, J. Bonevich, D. Shechtman, Tensile testing low density multilayers: aluminum/titanium, J. Mater. Res. 13 (1998) 2902–2909.

[139] L. Thilly, S. V. Petegem, P. Renault, F. Lecouturier, V. Vidal, B. Schmitt, H. V. Swygenhoven, A new criterion for elasto-plastic transition in nanomaterials: application to size and composite effects on Cu-Nb nanocomposite wires, Acta Mater. 57 (2009) 3157–3169.

[140] M. Dao, L. Lu, R. J. Asaro, J. T. M. De Hosson, E. Ma, Toward a quantitative understanding of mechanical behavior of nanocrystalline metals, Acta Mater. 55 (2007) 4041–4065.

[141] E. Ma, Instabilities and ductility of nanocrystalline and ultrafine-grained metals, Scr. Mater. 49 (2003) 663–668.

[142] M. A. Adams, A. C. Roberts, R. E. Smallman, Yield and fracture in polycrystalline niobium, Acta Metall. 8 (1960) 328–337.

[143] N. Hansen, B. Ralph, The strain and grain size dependence of the flow stress of copper, Acta Metall. 30 (1982) 411–417.

[144] L. Delannay, M. R. Barnett, Modelling the combined effect of grain size and grain shape on plastic anisotropy of metals, Int. J. Plast. 32 (2012) 70–84.

[145] P. Pant, K. W. Schwarz, S. P. Baker, Dislocation interactions in thin FCC metal films, Acta Mater. 51 (2003) 3243–3258.

[146] J. Wang, A. Misra, An overview of interface-dominated deformation mechanisms in metallic multilayers, Curr. Opin. Solid State Mater. Sci. 15 (2011) 20–28.

[147] S. Lotfian, M. Rodríguez, K. E. Yazzie, N. Chawla, J. Llorca, J. M. Molina-Aldareguía, High temperature micropillar compression of Al/SiC nanolaminates, Acta Mater. 61 (2013) 4439–4451.

[148] D. R. P. Singh, N. Chawla, G. Tang, Y.-L. Shen, Micropillar compression of Al/SiC nanolaminates, Acta Mater. 58 (2010) 6628–6636.

[149] T. Nizolek, N. A. Mara, I. J. Beyerlein, J. T. Avallone, T. M. Pollock, Enhanced plasticity via kinking in cubic metallic nanolaminates, Adv. Eng. Mater. 17 (2015) 781–785.

[150] E9-09 standard test method for compression testing of metallic materials at room temperature, ASTM international, 2002.

[151] A. S. Argon, Fracture of composites, in: H. Herman (Ed.), Treatise on Materials Science and Technology, volume 1, Academic Press, New York, 1972, pp. 79–114.

[152] A. G. Evans, W. F. Adler, Kinking as a mode of structural degradation in carbon fiber composites, Acta Metall. 26 (1978) 725–738.

[153] P. M. Moran, C. F. Shih, Kink band propagation and broadening in ductile matrix fiber composites: experiments and analysis, Int. J Solids Struct. 35 (1998) 1709–1722.

[154] R. E. Robertson, Formation of kink bands in oriented polymers, J. Polym. Sci: Part A-2: Polym. Phys. 7 (1969) 1315–1328.

[155] E. Orowan, A type of plastic deformation new in metals, Nature 149 (1942) 463–464.

[156] M. W. Barsoum, T. Zhen, S. R. Kalidindi, M. Radovic, A. Murugaiah, Fully reversible, dislocation-based compressive deformation of Ti_3SiC_2 to 1 GPa, Nat. Mater. 2 (2003) 107–111.

[157] M. E. Manley, E. M. Schulson, Kinks and cracks in S1 ice under across-column compression, Philos. Mag. Lett. 75 (1997) 83–90.

[158] P. M. Moran, X. H. Liu, C. F. Shih, Kink band formation and band broadening in fiber composites under compressive loading, Acta Metall. Mater. 43 (1995) 2943–2958.

[159] J. B. Hess, C. S. Barrett, Structure and nature of kink bands in zinc, Trans. Am. Inst. Min. Met. Eng. 185 (1949) 599–606.

[160] F. C. Frank, A. N. Stroh, On the theory of kinking, Proc. Phys. Soc. B 65 (1952) 811–821.

[161] C. C. Chiao, R. L. Moore, T. T. Chiao, Measurement of shear properties of fibre composites: part 1. evaluation of test methods, Composites 8 (1977) 161–169.

[162] C. C. Hays, C. P. Kim, W. L. Johnson, Microstructure controlled shear band pattern formation and enhanced plasticity of bulk metallic glasses containing in situ formed ductile phase dendrite dispersions, Phys. Rev. Lett. 84 (2000) 2901–2904.

[163] N. Li, J. Wang, A. Misra, J. Y. Huang, Direct observations of confined layer slip in Cu/Nb multilayers, Microsc. Microanal. 18 (2012) 1155–1162.

[164] C. R. Mayer, L. W. Yang, S. S. Singh, J. Llorca, J. M. Molina-Aldareguia, Y. L. Shen, N. Chawla, Anisotropy, size, and aspect ratio effects on micropillar compression of Al-SiC nanolaminate composites, Acta Mater. 114 (2016) 25–32.

[165] H. Khatam, M.-J. Pindera, Parametric finite-volume micromechanics of periodic materials with elastoplastic phases, Int. J. Plast. 25 (2009) 1386–1411.

[166] N. Yoshinaga, N. Sugiura, S. Hiwatashi, K. Ushioda, O. Kada, Deep drawability of electro-deposited pure iron having an extremely sharp (111)//ND texture, ISIJ Int. 48 (2008) 667–670.

[167] A. Alankar, D. P. Field, D. Raabe, Plastic anisotropy of electro-deposited pure α-iron with sharp crystallographic $\langle 111 \rangle$ texture in normal direction: analysis by an explicitly dislocation-based crystal plasticity model, Int. J. Plast. 52 (2014) 18–32.

[168] G. Winther, D. J. Jensen, Deformation induced dislocation boundaries: alignment and effect on mechanical properties, Comput. Mater. Sci. 9 (1997) 251–260.

[169] I. Shabib, R. E. Miller, Deformation characteristics and stress–strain response of nanotwinned copper via molecular dynamics simulation, Acta Mater. 57 (2009) 4364–4373.

[170] T. Zhu, H. Gao, Plastic deformation mechanism in nanotwinned metals: an insight from molecular dynamics and mechanistic modeling, Scr. Mater. 66 (2012) 843–848.

[171] Z. You, X. Li, L. Gui, Q. Lu, T. Zhu, H. Gao, L. Lu, Plastic anisotropy and associated deformation mechanisms in nanotwinned metals, Acta Mater. 61 (2013) 217–227.

[172] M. S. Paterson, L. E. Weiss, Experimental deformation and folding in phyllite, Geol. Soc. Am. Bull. 77 (1966) 343–374.

[173] T. B. Anderson, The relationship between kink–bands and shear fractures in the experimental deformation of slate, J. Geol. Soc. 130 (1974) 367–382.

[174] L. Benabou, Predictions of compressive strength and kink band orientation for wood species, Mech. Mater. 42 (2010) 335–343.

[175] R. Menig, M. H. Meyers, M. A. Meyers, K. S. Vecchio, Quasi-static and dynamic mechanical response of *Haliotis rufescens* (abalone) shells, Acta Mater. 48 (2000) 2383–2398.

[176] A. G. Crocker, J. S. Abell, The crystallography of deformation kinking, Philos. Mag. 33 (1976) 305–310.

[177] T. J. Vogler, S. Kyriakides, On the initiation and growth of kink bands in fiber composites: part I. experiments, Int. J Solids Struct. 38 (2001) 2639–2651.

[178] R. D. Reiswig, L. S. Levinson, T. D. Baker, Optical and electron microscopy of carbonaceous materials, Carbon 5 (1967) 603–606.

[179] L. R. Cornwell, J. D. Embury, G. R. Purdy, The deformation of single crystals of the Ni–Ni_3Al system, Acta Metall. 18 (1970) 1217–1223.

[180] I. Pane, H. M. Jensen, Plane strain bifurcation and its relation to kinkband formation in layered materials, Eur. J. Mech. A-Solids 23 (2004) 359–371.

[181] M. A. Wadee, G. W. Hunt, M. A. Peletier, Kink band instability in layered structures, J. Mech. Phys. Solids 52 (2004) 1071–1091.

[182] B. Budiansky, Micromechanics, Comput. Struct. 16 (1983) 3–12.

[183] R. A. E. Zidek, C. Völlmecke, Analytical studies on the imperfection sensitivity and on the kink band inclination angle of unidirectional fiber composites, Comp. Part A 64 (2014) 177–184.

[184] T. B. Anderson, The geometry of a natural orthorhombic system of kink bands, in: A. J. Baer, D. K. Norris (Eds.), Proceedings, conference on

research in tectonics (kink bands and brittle deformation), volume 68, Department of Energy Mines and Resources (Canada), 1968, pp. 200–220.

[185] G. E. Attenburrow, D. C. Bassett, Compliances and failure modes of oriented chain-extended polyethylene, J. Mater. Sci. 14 (1979) 2679–2687.

[186] N. A. Fleck, S. Sivashanker, M. P. F. Sutcliffe, Compressive failure of composites due to microbuckle growth, Eur. J. Mech. A - Solids 16 (1997) 65–82.

[187] T. J. Vogler, S. Kyriakides, On the axial propagation of kink bands in fiber composites: part I experiments, Int. J Solids Struct. 36 (1999) 557–574.

[188] Q. Wei, D. Jia, K. T. Ramesh, E. Ma, Evolution and microstructure of shear bands in nanostructured Fe, Appl. Phys. Lett. 81 (2002) 1240–1242.

[189] D. Jia, K. T. Ramesh, E. Ma, Effects of nanocrystalline and ultrafine grain sizes on constitutive behavior and shear bands in iron, Acta Mater. 51 (2003) 3495–3509.

[190] S. Cheng, E. Ma, Y. M. Wang, L. J. Kecskes, K. M. Youssef, C. C. Koch, U. P. Trociewitz, K. Han, Tensile properties of in situ consolidated nanocrystalline Cu, Acta Mater. 53 (2005) 1521–1533.

[191] B. Budiansky, N. A. Fleck, J. C. Amazigo, On kink-band propagation in fiber composites, J. Mech. Phys. Solids 46 (1998) 1637–1653.

[192] O. Mügge, Über translationen und verwandte erscheinungen in krystallen, Nachrichten von der Gesellschaft der Wissenschaften zu Göttingen, Mathematisch-Physikalische Klasse 1897 (1897) 102–109.

[193] N. A. Fleck, B. Budiansky, Compressive failure of fibre composites due to microbuckling, in: Inelastic deformation of composite materials, Springer, 1991, pp. 235–273.

[194] T. Yokozeki, T. Ogasawara, T. Ishikawa, Nonlinear behavior and compressive strength of unidirectional and multidirectional carbon fiber composite laminates, Comp. Part A 37 (2006) 2069–2079.

[195] R. T. Pascoe, C. W. A. Newey, The mechanical behaviour of the intermediate phase NiAl, Metal Sci. 2 (1968) 138–143.

[196] Z. Bartczak, A. S. Argon, R. E. Cohen, Deformation mechanisms and plastic resistance in single-crystal-textured high-density polyethylene, Macromolecules 25 (1992) 5036–5053.

[197] E. G. Tapetado, M. H. Loretto, A study of kinking and buckling in zinc single crystals, Philos. Mag. 30 (1974) 515–526.

[198] T. J. Dodwell, G. W. Hunt, Periodic void formation in chevron folds, Math. Geosci. 46 (2014) 1011–1028.

[199] J. G. Ramsay, Development of chevron folds, Geol. Soc. Am. Bull. 85 (1974) 1741–1754.

[200] S. K. Ghosh, Experiments of buckling of multilayers which permit interlayer gliding, Tectonophysics 6 (1968) 207–249.

[201] M. J. Fleuty, The description of folds, Proceedings of the Geologists' Association 75 (1964) 461–492.

[202] A. M. Waas, C. D. Babcock, W. G. Knauss, An experimental study of compression failure of fibrous laminated composites in the presence of stress gradients, Int. J Solids Struct. 26 (1990) 1071–1098.

[203] M. P. F. Sutcliffe, N. A. Fleck, Microbuckle propagation in carbon fibre-epoxy composites, Acta Metall. Mater. 42 (1994) 2219–2231.

[204] J. L. Wind, A. M. Waas, H. M. Jensen, Initiation of failure at notches in unidirectional fiber composites, Compos. Struct. 122 (2015) 51–56.

[205] H. Koerber, J. Xavier, P. P. Camanho, High strain rate characterisation of unidirectional carbon-epoxy IM7-8552 in transverse compression and in-plane shear using digital image correlation, Mech. Mater. 42 (2010) 1004–1019.

[206] C. R. Chaplin, Compressive fracture in undirectional glass-reinforced plastics, J. Mater. Sci. 12 (1977) 347–352.

[207] F. P. Chiang, F. Jin, Q. Wang, N. Zhu, Speckle interferometry, in: IUTAM Symposium on Advanced Optical Methods and Applications in Solid Mechanics, Springer, pp. 177–190.

[208] W. Sun, A. P. Vassilopoulos, T. Keller, Experimental investigation of kink initiation and kink band formation in unidirectional glass fiber-reinforced polymer specimens, Compos. Struct. 130 (2015) 9–17.

[209] J. W. Hutchinson, Plastic stress and strain fields at a crack tip, J. Mech. Phys. Solids 16 (1968) 337–342.

[210] M. A. Wadee, C. Völlmecke, J. F. Haley, S. Yiatros, Geometric modelling of kink banding in laminated structures, Phil. Trans. R. Soc. A 370 (2012) 1827–1849.

[211] D. C. Martin, E. L. Thomas, Micromechanisms of kinking in rigid-rod polymer fibres, J. Mater. Sci. 26 (1991) 5171–5183.

[212] J. W. Christian, S. Mahajan, Deformation twinning, Prog. Mater Sci. 39 (1995) 1–157.

[213] N. A. Pertsev, A. E. Romanov, Instability of front profiles of kink bands in oriented polymers, Mech. Compos. Mater. 19 (1984) 565–570.

[214] N. A. Pertsev, V. A. Marikhin, L. P. Myasnikova, Z. Pelzbauer, Incomplete kink bands in fully oriented high-density polyethylene, Polym. Sci. (USSR) 27 (1985) 1611–1620.

[215] Z. P. Bažant, J.-J. H. Kim, I. M. Daniel, E. Becq-Giraudon, G. Zi, Size effect on compression strength of fiber composites failing by kink band propagation, in: Fracture Scaling, Springer, 1999, pp. 103–141.

[216] J. W. Hutchinson, V. Tvergaard, Shear band formation in plane strain, Int. J Solids Struct. 17 (1981) 451–470.

[217] R. W. Cahn, Plastic deformation of alpha-uranium; twinning and slip, Acta Metall. 1 (1953) 49–70.

[218] R. D. Field, R. J. McCabe, D. J. Alexander, D. F. Teter, Deformation twinning and twinning related fracture in coarse-grained α-uranium, J. Nucl. Mater. 392 (2009) 105–113.

[219] Y. Liu, Intersections of (112) twins in bcc crystals, T. Metall. Soc. AIME 227 (1963) 775–776.